Modified Cu-based Catalysts for Electrochemical Reduction of CO2 to Multicarbon Products

by

Quhan Chen *BEng*

Thesis submitted to University of Nottingham

for the degree of Doctor of Philosophy

October 2024

Abstract

The electrochemical reduction of carbon dioxide to produce valuable chemicals is widely recognized as a promising strategy for mitigating the environmental impact of CO_2. This research focuses on the development of Cu-based materials, particularly oxide-derived copper (OD-Cu), as efficient electrocatalysts for the conversion of CO_2 to multicarbon products. Normally, the electrocatalytic reduction of CO_2 involves a complex reaction pathway and the simultaneous occurrence of the hydrogen evolution reaction (HER), which subsequently results in poor selectivity of the carbonaceous products. Furthermore, the deactivation of catalysts has a significant impact on their long-term stability. Therefore, various electrode preparation methods and modification techniques have been used to improve the catalytic performance and deepen our understanding of the underlying mechanism.

The surface hydrophobicity of CuO electrodes was controlled by coating PVDC to suppress the hydrogen evolution reaction and promote the conversion of CO_2 to ethylene, a value-added bulk chemical. The systematic investigation of different coating materials, amounts and sequences revealed that the CuO electrode with a PVDC coating of only 50 μg/cm^2 optimizes hydrophobicity (WCA = 122°). It is found that the modified electrode led to highly efficient production of ethylene ($|j|_{C2H4}$ = 6.8 mA/cm^2, FE_{C2H4} = 41.4%) at -0.89 V vs. RHE while effectively suppressing hydrogen evolution (FE_{H2} = 22.7%). The catalytic activity of CO_2RR to ethylene of the PVDC-modified CuO electrode is inherently a 50.8% increase in comparison to that of the CuO electrode. PVDC modification balances proton transfer and CO_2 availability. In addition, PVDC affects CuO reduction by increasing the proportion of Cu^+ species on the CuO-

PVDC surface and facilitating C-C coupling. The PVDC-modified electrode retains durable hydrophobic properties without affecting conductivity, which facilitates efficient CO_2 conversion.

Besides, CuO was prepared using precursors with different mass ratios, both with and without microwave heating. The microwave-assisted synthesized CuO (MW-CuO) showed similar morphology but smaller particle size than the conventionally prepared CuO. MW-CuO exhibited a higher defect site density and significantly more grain boundaries (GBs). At a reactant ratio of Cu^{2+} and CO_3^{2-} of 1.1, MW-CuO exhibited superior catalytic performance and achieved a remarkable FE of C_{2+} products (71.9% at -1.04 V vs. RHE, corresponding to a partial current density of about 11.2 mA/cm^2). This performance, which is among the highest reported for OD-Cu catalysts, is attributed to the significantly higher Cu^+ to Cu^0 ratio of MW-CuO on the surface. These factors, an appropriate ratio of Cu^+ and Cu^0 species, and defective surface features improved the CO_2RR selectivity for multi-carbon products and emphasized the sustainable approach in catalyst preparation.

Another modification strategy involves electrochemical deposition on the Cu_2O-C_3N_4 electrode, resulting in a captivating dendritic 3D Cu structure that significantly enhances the catalytic activity. Electrochemical analysis revealed a fourfold increase in current density. Electrochemical analysis revealed a fourfold increase in current density for multicarbon products after electrodeposition with a peak value of 12.7 mA/cm^2 (with $|j|_{ethylene}$ = 7.2 mA/cm^2) at -1.04 V vs. RHE. Furthermore, the reduction and restructuring of Cu species during the electrocatalytic CO_2 reduction reaction led to a high Cu^+/Cu^0 ratio on the Cu@Cu_2O-C_3N_4 electrode, which correlates with enhanced C-C coupling as

evidenced by higher product ratios of C_2H_4/CH_4. The electrodeposition increased the electrochemically active sites by 1.5 times and reduced the charge transfer resistance by 0.4-fold. In particular, the intrinsic electrocatalyst in the original electrode contributed significantly to the improvement of the electrochemical performance of various electrodes during the deposition process. Furthermore, the mechanism of electrode deactivation was investigated, revealing that carbon deposition was the primary cause.

This thesis covers several relevant works, including the preparation of Cu-based catalysts and the regulation of the gas-liquid-solid interface. It presents universal strategies to improve the performance of oxide-derived Cu electrodes for electrochemical CO_2 reduction reactions to multi-carbon products. The research findings indicate that maintaining a moderate level of hydrophobicity facilitates proton transfer while preserving unhindered CO_2 adsorption. In addition, the presence of porous 3D structures, an optimal ratio of Cu^0 to Cu^+ and abundant surface defects accelerate C-C coupling processes. It contributes to a better understanding of the reaction process.

Keywords: Cu-based catalysts, electrochemical CO_2 reduction, surface modification, multi-carbon products, inhibited hydrogen evolution.

Publication during candidature

The following peer-reviewed journal articles have either been published or are in preparation to be published as a result of the work undertaken as part of this thesis:

- **CHEN, Q.,** ZHU, H., GUO, Z., YAN, Z., YANG, G., ZHENG, Y., XING, Y., YIN, H. & WU, T. (2024). Enhanced Electrochemical Reduction of CO2 to Ethylene using Boosted Hydrophobicity of Polyvinyl Dichloride-Coated CuO Electrodes. *Journal of Alloys and Compounds*, 991, 174475. (https://doi.org/10.1016/j.jallcom.2024.174475)
- **CHEN, Q.**, ZHU, H., MAO, X., GUO, Z., XING, Y., YAN, Z., YANG, G., ZHENG, Y., YIN, H. & WU, T. (2023). Hdrophobicity-controlled CuO Electrode for Enhanced Electrochemical CO2 Reduction to Ethylene. *Energy Proceedings*, Vol 32. (https://doi.org/10.1016/j.jallcom.2024.174475)
- **CHEN, Q.,** LUO, X., MU, G., MAO, X., YIN, H. & WU, T. (2024). Microwave-Assisted Synthesis of a Defect-Rich CuO Electrode for Selective Electrochemical CO2 Reduction to C2+ Products. *ACS Sustainable Chemistry & Engineering*. (https://doi.org/10.1021/acssuschemeng.4c05008)
- **CHEN, Q.**, YIN, H. & WU, T. Cu-Electrodeosition Modified Electrodes for Enhanced CO2 Electrochemical Reduction Towards C2+ Products. (Under preparation)

The following peer-reviewed journal articles have either been published or are in preparation to be published but not as part of this thesis:

- WANG, F., ZHENG, Y., **CHEN, Q.**, YAN, Z., LAN, D., LESTER, E. & WU, T. (2024). A critical review of facets and defects in different MnO2 crystalline phases and controlled synthesis – Its properties and applications in the energy field. *Coordin Chem Rev*, *500*.
- GUO, Z., ZHU, H., YANG, G., WU, A., **CHEN, Q**., YAN, Z., LOON FOW, K., DO, H., HIRST, J. D., WU, T. & XU, M. (2023). Synergistic engineering of heteronuclear Ni-Ag dual-atom catalysts for high-efficiency CO2 electroreduction with nearly 100% CO selectivity. *Chemical Engineering Journal*, 476.
- MAO, X., GUO, R., **CHEN, Q**., ZHU, H., LI, H., YAN, Z., GUO, Z. & WU, T. (2023). Recent Advances in Graphitic Carbon Nitride Based Electro-Catalysts for CO(2) Reduction Reactions. *Molecules*, 28.
- ZHU, H., LIU, S., YU, J., **CHEN, Q.**, MAO, X. & WU, T. (2023). Computational screening of effective g-C(3)N(4) based single atom electrocatalysts for the selective conversion of CO(2). *Nanoscale*, 15, 8416-8423.
- LAN, D., ZHU, H., ZHANG, J., LI, S., **CHEN, Q.**, WANG, C., WU, T. & XU, M. (2022). Adsorptive removal of organic dyes via porous materials for wastewater treatment in recent decades: A review on species, mechanisms and perspectives. *Chemosphere*, 293.

Acknowledgements

This thesis marks the conclusion of a profound and memorable journey, a feat made possible by the unwavering support of my supervisors and colleagues. I extend my deepest gratitude to Professor Tao Wu, my supervisor, whose invaluable guidance, rigorous academic attitude, outstanding scholarly achievements, and selfless dedication played a pivotal role in my doctoral research. His insightful suggestions and guidance on topic selection, conceptualization, and thesis writing have been instrumental in my academic growth.

I would also like to express my appreciation to my co-supervisors, Professor Hongfeng Yin and Professor Edward Lester, for their care and assistance during my doctoral study. Their commitment to academic excellence, extensive experience, and high sense of responsibility have significantly enriched my research endeavours.

Special thanks to the University of Nottingham Ningbo China, Nottingham New Material Institute, and the China Beacons Institute for fostering an excellent academic atmosphere and providing superior research conditions. Gratitude to fellow students, staff at the Center of New Energy and Environmental Materials, and friends from the University of Nottingham, Ningbo, China, for sharing research experiences. I appreciate the invaluable contributions of individuals like Dr. Xiang Luo and Dr. Gang Yang to experimental design. Engaging conversations with Dr. Huiwen Zhu, Mr. Zijun Yan, Mr. Zeyu Guo, Ms. Xinyi Mao, and all fellow students in my research group played a crucial role in refining my systematic thoughts and completing the research presented in this thesis.

I thank my boyfriend, Guohao Mu, for our shared journey of progress, mutual encouragement, and unwavering companionship. Additionally, I express my gratitude to my friends, Xiangbei Guo, Zixuan Guo, Qianhui Zhao, Youchen Sun, Dandan Zhang and Danhua Wang for their steadfast support throughout my PhD journey.

My most profound appreciation goes to my beloved family, especially my parents and grandparents, who have been my pillars of strength. Their unwavering support and love propelled me forward, giving me the confidence to move ahead without any reservations or concerns.

Thank all of you, and may you enjoy today's supreme happiness and joy, and may you have every opportunity and joy for tomorrow.

Table of Contents

List of Figures

List of Tables

List of Abbreviation

Ar = Argon

C_{2+} = Multicarbon

CCS = CO_2 capture and storage

C_{dl} = Double-layer capacitance

CH_4 = Methane

C_2H_4 = Ethylene

C_2H_6 = Ethane

C_2H_5OH = Ethanol

C_3H_7OH = n-Propanol

CO = Carbon monoxide

CO_2 = Carbon dioxide

CO_2RR = Carbon dioxide reduction reaction

Cu = Copper

Cu_2O = Cuprous oxide

CuO = Copper oxide / cupric oxide

CV = Cyclic voltammetry

DMSO = Dimethylsulfoxide

D_2O = Deuteroxide

eCO_2RR = Electrochemical carbon dioxide reduction reaction

ECSA = Electrochemical Active Surface Area

EDS = Energy Dispersive X-Ray Spectrometer

EIS = Electrochemical Impedance Spectroscopy

EtOH = Ethanol

FE = Faradaic efficiency

FID = Flame ionization detectors

GC = gas chromatography

H_2 = Hydrogen

HCOOH = Formic acid

HER = Hydrogen evolution reaction

^{1}H-NMR = Proton nuclear magnetic resonance

H_2O = Water

HRTEM = High-Resolution Transmission Electron Microscope

|j| = Current density

LSV = Linear sweep voltammetry

N_2 = Nitrogen

O_2 = Oxygen

P-ED = Pulse electrodeposition

R_{ct} = Charge transfer resistance

R_s = Solution resistance

PTFE = Polytetrafluoroethylene

PVDC = Polyvinyl Dichloride

PVDF = Polyvinylidene Fluoride

RHE = Reversible hydrogen electrode

SCE = Saturated calomel electrode

SEM = Scanning electron microscope

SWP = Square-wave potential

TCD = Thermal conductivity detector

TEM = Transmission electron microscopy

UPD = Underpotential deposition

VASP = Vienna ab initio Simulation Package

WCA = Water contact angle

XPS = X-Ray Photoelectron Spectroscopy

XRD = X-Ray Diffraction

Chapter 1. Introduction

1.1 Background

The emission of carbon dioxide has many causes and poses a considerable environmental risk [1]. In particular, the burning of fossil fuels such as coal, oil and natural gas for electricity generation [2-5], transportation [6, 7], and industrial processes [8-11] is the main cause of CO_2 emissions [12, 13]. The accumulation of CO_2 in the atmosphere triggers the greenhouse effect and thus leads to global warming [14]. This phenomenon has negative effects, such as a rise in global temperatures, a disruption of the usual weather patterns, an increase in extreme weather events and the progressive retreat of glaciers and polar ice caps [15-18]. To mitigate climate change and preserve the delicate balance of our planet, it is of utmost importance to tackle the sources and threats of CO_2 emissions [19-21].

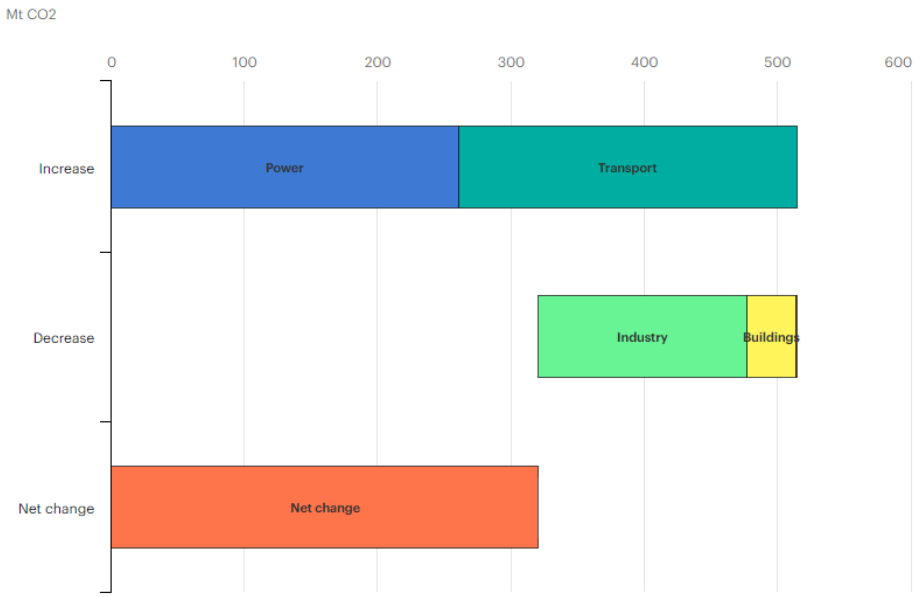

Figure 1.1 Changes in CO_2 emissions by sector, 2021-2022 [22].

The conversion of CO_2 into fuels has attracted considerable attention as a promising strategy for energy storage and the promotion of a sustainable carbon-neutral economy [23, 24]. Scientists and researchers have explored various effective conversion techniques, including photocatalytic conversion, biological conversion, and electrocatalytic reduction [25-27]. Among these methods, electrocatalytic CO_2 reduction powered by renewable energy sources has emerged as an attractive approach due to its mild reaction conditions and environmentally friendly nature [28-30].

When considering the products obtained from eCO_2RR, a variety of compounds can be generated, including carbon monoxide (CO), methane (CH_4), formic acid (HCOOH), ethylene (C_2H_4), ethane (C_2H_6), ethanol (C_2H_5OH), and n-propanol (n-C_3H_7OH) [31]. However, there is actually a preference for C_2 and C_{2+} compounds consisting of two or more carbon atoms. This preference stems from the higher volumetric energy density of these compounds compared to the simpler C_1 products. The ability of C_2 and C_{2+} products to offer convenient transportation and improved energy storage properties makes them particularly desirable [32]. In addition, C_2 and C_{2+} offer a wide range of applications in numerous industries. These versatile compounds are valuable starting materials for chemical synthesis and are promising alternatives to conventional fossil fuels [33-35].

When considering the sustainable development and environmental impact of the CO_2RR process for synthesizing multi-carbon products, several notable considerations come to the fore. The choice of an energy source to drive the CO_2RR process proves to be a critical factor in promoting sustainable development. Utilizing renewable energy sources, such as solar or wind energy,

has the potential to significantly reduce the carbon footprint and environmental impact associated with the process [36, 37]. By limiting fossil fuels, the overall sustainability of the CO_2RR process can be improved.

The design and selection of catalysts and the optimization of reaction conditions are crucial for sustainable CO_2RR. Highly active, selective and stable catalysts improve process efficiency and minimize waste [38, 39]. Controlling factors such as temperature, pH, and electrolyte composition improve reaction efficiency and selectivity, increasing the yield of multi-carbon products while reducing by-products and waste [40]. Maximizing selectivity for the desired multi-carbon products improves process efficiency and economic viability.

In addition, a comprehensive life cycle assessment for the CO_2RR process provides insights into its environmental impact [41, 42]. The LCA considers the entire life cycle of the process, from raw material extraction to catalyst synthesis, reaction, product separation and waste management. Identifying and remediating environmental hotspots improves the overall sustainability of CO_2RR [43-46]. Incorporating these considerations into the development and implementation of CO_2RR for multi-carbon products enables a more sustainable and environmentally friendly process that contributes to the reduction of greenhouse gases and the transition to a low-carbon economy.

Catalysts play a crucial role in facilitating chemical reactions. Factors such as temperature, pressure, and the composition of catalysts used would influence the performance of the entire process. These factors determine the outcome of the reaction and lead to the production of a wide range of hydrocarbon products [47-49]. Copper has moderate adsorption energy towards key reaction intermediates,

which contributes to its unique properties as an electrocatalyst for the production of multi-carbon products compared to other metals [50]. During the CO_2 reduction process, at least 16 different C_1-C_3 products can form on the surface of copper [51]. Table 1.1 shows the standard equilibrium potentials for the electrochemical conversion of CO_2 into specific carbon products, together with the number of electrons transferred. This table shows that the main product potentials for eCO_2RR overlap with those of H_2, which can affect the eCO_2RR performance of catalysts [52]. The overlapping potentials between CO_2 reduction and HER pose a challenge for achieving high selectivity and activity in CO_2RR.

In addition, the formation of different C_1-C_3 products can be attributed to the different bond strengths and reaction kinetics of the various intermediates on the copper surface [53]. The process of CO_2 reduction involves multiple proton and electron transfers to form complex reaction intermediates, which can lead to slow kinetics. The formation of these intermediates and the subsequent conversions determine the selectivity and efficiency of the CO_2 electroreduction process. Therefore, controlling the binding of intermediates is a crucial approach to improve product selectivity [54, 55].

Table 1.1 Electrochemical reactions yielding different products with thermodynamic equilibrium potentials in a 0.1 M $KHCO_3$ solution at 1.0 atm and 25°C [56, 57].

	Chemical formula	Chemical reaction	E^0/V vs. RHE
C_1	**CO**	$CO_2 + 2H^+ + 2e^- \rightarrow CO(g) + H_2O$	-0.10
	HCOOH	$CO_2 + 2H^+ + 2e^- \rightarrow HCOOH(aq)$	-0.12
	CH_3OH	$CO_2 + 6H^+ + 6e^- \rightarrow CH_3OH(aq) + H_2O$	0.03
	CH_4	$CO_2 + 8H^+ + 8e^- \rightarrow CH_4(g) + 2H_2O$	0.17
C_{2+}	**CH_3CHO**	$2CO_2 + 10H^+ + 10e^- \rightarrow CH_3CHO(aq) + 3H_2O$	0.06
	C_2H_4	$2CO_2 + 12H^+ + 12e^- \rightarrow C_2H_4(g) + 4H_2O$	0.08
	C_2H_5OH	$2CO_2 + 12H^+ + 12e^- \rightarrow CH_3CH_2OH(aq) + 3H_2O$	0.09
	C_2H_6	$2CO_2 + 14H^+ + 14e^- \rightarrow C_2H_6(g) + 4H_2O$	0.14
	C_2H_5CHO	$2CO_2 + 16H^+ + 16e^- \rightarrow C_2H_5CHO(aq) + 5H_2O$	0.09
	C_3H_7OH	$3CO_2 + 18H^+ + 18e^- \rightarrow C_3H_7OH(aq) + 5H_2O$	0.10
Hydrogen evolution reaction		$2H^+ + 2e^- \rightarrow H_2(g)$	0.00
Oxygen Evolution Reaction		$2H_2O \rightarrow O_2(g) + 4H^+ + 4e^-$	1.23

Improving the durability and stability of copper-based catalysts is a major challenge in CO_2 electroreduction. Several actors contribute to the gradual degradation of copper-based catalysts during prolonged operation (Figure 1.2). The dissolution/re-deposition of copper ions from the catalyst surface into the electrolyte leads to the loss of active sites and changes in the surface morphology of the catalyst [58-60]. At the same time, the accumulation of reaction by-products or intermediates on the catalyst surface hinders the accessibility of the

active sites and makes the interaction of the reactant with the catalyst more difficult [61, 62]. As a result, copper-based catalysts experience surface erosion, changes in the lattice structure and deactivation of the catalytic sites, leading to a deterioration in overall performance.

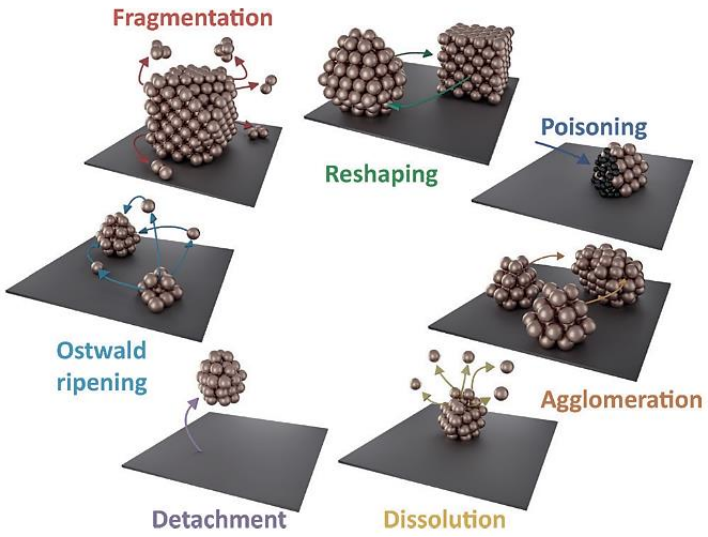

Figure 1.2 Summary of nanoscale degradation mechanism of Cu-based nanostructures during CO_2RR [58].

Researchers have explored various strategies to overcome the challenges associated with CO_2 emissions reduction. The aim is to improve the activity, selectivity, durability and stability of copper-based catalysts for the production of multi-carbon products (Figure 1.3). A critical approach is to suppress the HER and favour the desired CO_2 reduction pathway by modifying the composition, surface structure and electronic structure of the catalyst and tuning the coordination environment [52, 63-65]. In addition, understanding the scaling relationship between the adsorption energies of similar intermediates enables the development of catalysts with higher selectivity for carbon products while minimizing hydrogen formation [66]. Strategies such as surface modifications and the use of stable support materials contribute to making copper-based

catalysts more durable and efficient in the long term. In addition, optimization of reaction conditions, including temperature, pH and electrolyte composition, helps to reduce catalyst degradation and improve stability [67-69]. Addressing these challenges requires in-depth research and innovation in catalyst design, interfacial engineering, and crystal structure modulation, among others, to develop efficient, selective, and stable copper oxide catalysts for CO_2RR [70, 71].

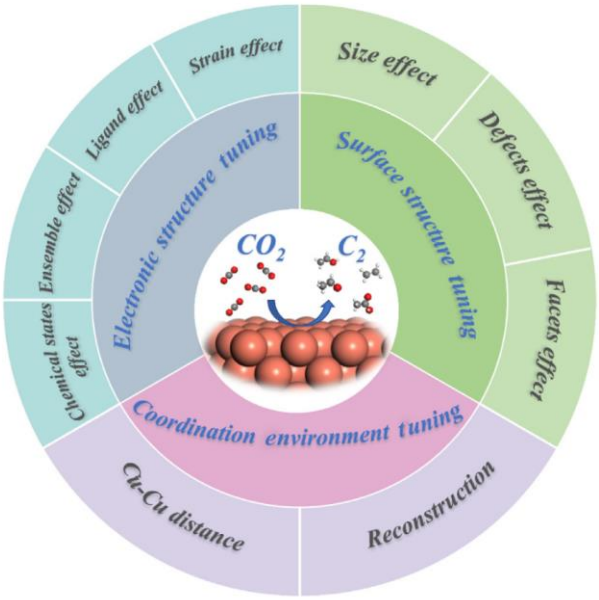

Figure 1.3 Strategies for the design of Cu-based catalysts for CO_2RR to produce multi-carbon products [72].

In situ characterization and operando studies are crucial for understanding catalyst behaviour during CO_2RR and essential for rational catalyst design [73, 74]. Techniques such as spectroscopy, microscopy and electrochemical methods provide insights into the surface structure, adsorption behaviour, and reaction kinetics under realistic conditions [75-77]. Computational modelling, including density functional theory calculations [78-81] and machine learning [82-84], enables the prediction of reaction energetics, identification of active sites and

screening of catalyst composition. This cost-effective approach helps to identify promising candidates for experimental validation. By integrating these methods, catalyst design can be accelerated, providing a viable route to customize catalysts for optimal performance in CO_2RR.

1.2 Aim and objectives

This research plan focuses on the application of Cu-based material in the electrocatalytic reduction of CO_2 to C_{2+} products. Based on this main topic, the specific objectives are listed as follows:

1. To analyse the relationship between hydrophobicity and proton transfer and search for an optimal hydrophobic material to suppress the hydrogen evolution reaction without affecting the CO_2RR.
2. Investigate the formation of defects on the CuO nanoparticles and study the effects of a rough surface on the electrochemical performance of CO_2 reduction to a multi-carbon product.
3. To study the evolution of electrodes and to find out the active species during the test, to study the degradation of electrodes comparatively, and to improve the stability and durability of catalysts.
4. To improve the selectivity and activity of multi-carbon products, to accelerate C-C coupling, and to enhance the charge and mass transfer.

In order to improve the selectivity and efficiency of CO_2RR for multi-carbon products, this work focuses on the development of different electrode modifications. Three main approaches are used: PVDC-modified CuO

electrodes, microwave-assisted synthesis of CuO electrodes, and Cu-electrodeposited Cu_2O-C_3N_4 electrodes. The CuO electrode is hydrophobically modified with different hydrophobic materials, coating amounts and methods to determine the optimal hydrophobicity for controlled proton transfer. In addition, CO_2 permeability calculations are performed to investigate the effects of hydrophobicity. DFT calculations are used to investigate the binding energy of key intermediates on the modified electrode. In addition, the surface roughness of CuO is investigated by introducing defects during synthesis by microwave treatment. The evolution of species on the electrode surface is analyzed to elucidate the degradation mechanism. In the final work, the surface roughness can be adjusted by electrodeposition. Cu is deposited on the Cu_2O-C_3N_4 electrode to create a porous structure and increase the active sites. The ratio of Cu^0 and Cu^+ on the electrode is evaluated to study the C-C coupling process. The overall goal of this work is the modification of Cu-based electrodes for electrochemical CO_2RR, with the aim of producing C_{2+} products.

1.3 Structure of thesis

This thesis comprises seven chapters, accompanied by pertinent references, which establish a logical progression of the research undertaken in this study. It delves into the significant strides made in electrochemical CO_2 reduction reaction stemming from comprehensive investigations conducted during this program (Figure 1.4).

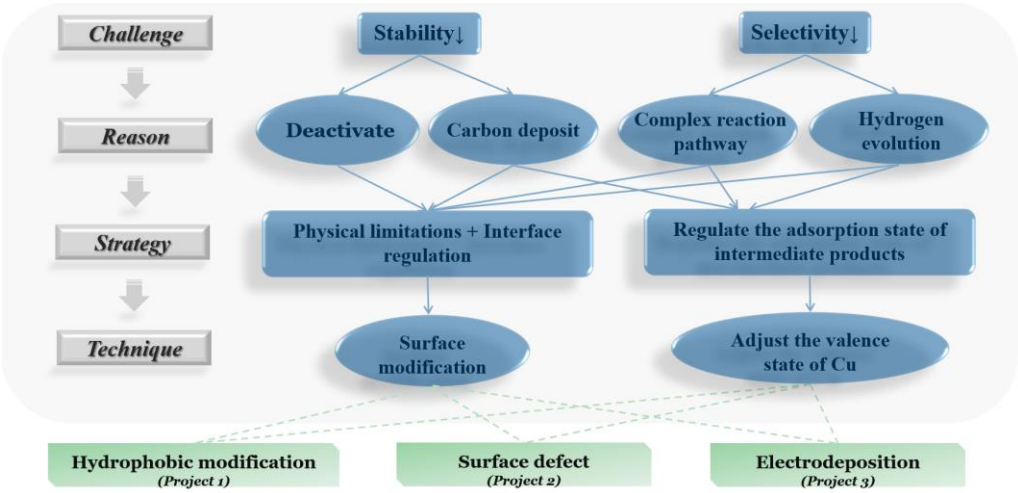

Figure 1.4 The research gap of eCO$_2$RR.

Chapter 1 introduced Cu-based electrocatalysts to develop electrochemical reduction of carbon dioxide. The topic is directly relevant to the overall thesis and planned technical approach presented in the thesis. The chapter also outlined the objectives that would be pursued in the study.

An introduction to the mechanisms and factors influencing the performance of copper-based catalysts in the electrochemical reduction of carbon dioxide, with a special focus on the generation of C_{2+} products, is the main topic of Chapter 2. More attention is paid to these catalysts' preparation, modification, and performance within the context of an H-cell setup.

A detailed description of the experimental equipment and procedures employed was provided in Chapter 3. It covers the synthesis methods for PVDC-modified CuO, microwave-assisted CuO synthesis and Cu electrodeposition of Cu_2O-C_3N_4. The mechanisms and processes underlying the different characterization techniques have been elucidated to allow a better understanding of the experimental results. The catalytic reaction process is also presented, highlighting the most critical factors and parameters. In addition, the

computational process using density functional theory (DFT) is mentioned in this chapter, which provided theoretical insights into the reaction mechanisms and helped in the experimental design and interpretation of the results.

The effect of PVDC modification on the CuO electrodes was investigated in Chapter 4. The effects of PVDC modification on the proton transfer and the stability of the electrocatalysts were systematically investigated by varying the coating material, coating amount and coating order. Comparative tests and calculations were carried out to determine the influence of PVDC on CO_2 availability and CO_2RR performance.

Besides, the synthesis of grain boundary-rich CuO using microwave heating was described and compared with conventionally heated CuO based on morphology and defect density in Chapter 5. The catalytic performance in electrochemical CO_2 reduction for C_{2+} products, as well as the degradation mechanism, is investigated through a series of characterizations.

The electrodeposition method was employed to modify the Cu_2O-C_3N_4 electrode, with the goal of regulating the reaction pathway in Chapter 6. This chapter extensively details the impact of Cu electrodeposition on the electrode by comparing morphology, catalytic activity, and efficiency. Additionally, electrochemical analysis for the Cu@Cu_2O-C_3N_4 electrode is conducted to discern changes in active sites and resistance.

Finally, in Chapter 7, the overarching findings and results drawn from this research are presented, along with suggestions for future work in this field.

Chapter 2. Literature review

2.1 Introduction

Carbon dioxide sequestration and utilization are the two promising approaches to reduce the net CO_2 content of the atmosphere. Among these methods, the conversion of CO_2 into valuable fuels such as carbon monoxide, methane, ethylene and alcohols offers great potential for the development of a sustainable, carbon-neutral economy. There are several effective techniques for CO_2 conversion, including thermocatalytic, photocatalytic, biocatalytic and electrocatalytic CO_2 reduction [85]. Among these methods, electrocatalytic CO_2 reduction is characterized by its mild operating conditions at ambient temperature and pressure. In addition, the electrochemical reaction is environmentally friendly and produces no hazardous waste. This makes electrocatalytic CO_2 reduction a promising and sustainable approach to tackle the challenges of energy storage and environmental issues while creating a pathway to a carbon-neutral future [28, 86-88].

In electrochemical CO_2 reduction, the abundant and inexpensive H_2O is often used as a source of electrons and protons. The extensive use of electrolyte solutions containing bicarbonate ensures a neutral pH and promotes an equilibrium between HCO_3^- and dissolved CO_2 [68, 89]. This equilibrium ensures effective contact between the cathode and the saturated carbon dioxide. At the same time, hydrogen evolution has become the main side reaction. Previous studies have investigated the addition of organic solvents and ionic liquids to water to inhibit the hydrogen evolution reactions and improve Faradaic efficiency [69, 90]. Organic solvents have better CO_2 solubility than water, but

their high cost and limitations in anodic reactions in non-aqueous systems hinder broad applicability. The CO_2 reduction reaction in a water-based system follows the following general formulas:

$$xCO_2 + yH_2O \rightarrow product + zO_2 \qquad \text{Equation 2.1}$$

H-cells, microfluidic cells, membrane-based flow reactors and solid oxide electrolyzers have been developed to perform the electrochemical CO_2 reduction reaction [67, 91-93]. The H-cell is commonly used in the laboratory to evaluate the catalytic performance of electrodes and to perform some basic research [94]. In the H-cell, a membrane separates the cathode chamber and the anode chamber to avoid mixing the electrocatalytic products. The proton exchange membrane Nafion 117, for example, is one of the membranes commonly used. The oxygen evolution reaction (OER) takes place at the anode and follows the reaction equation 2.2.

A wide range of carbonaceous products can be produced at the cathode. The typical carbon products in the CO_2RR are CO, formic acid, hydrocarbons, aldehydes and alcohols [95]. It is more likely that CO is produced with only two electron transfers among these products. At present, the efficiency of CO_2RR to CO could reach more than 95% if modified electrocatalysts with good stability are used [96, 97]. However, due to the low energy density of CO, it is not an ideal product. Figure 2.1 shows the possible market prices and the energy content of the products in CO_2RR. Ethylene, ethanol and propanol have enormous research potential due to their high volumetric energy densities and high market prices [33].

$$\text{Anode: } 6H_2O - 12e^- \rightarrow 12H^+ + 3O_2 \quad E^0 = 1.23V \; vs \; RHE \qquad \text{Equation 2.2}$$

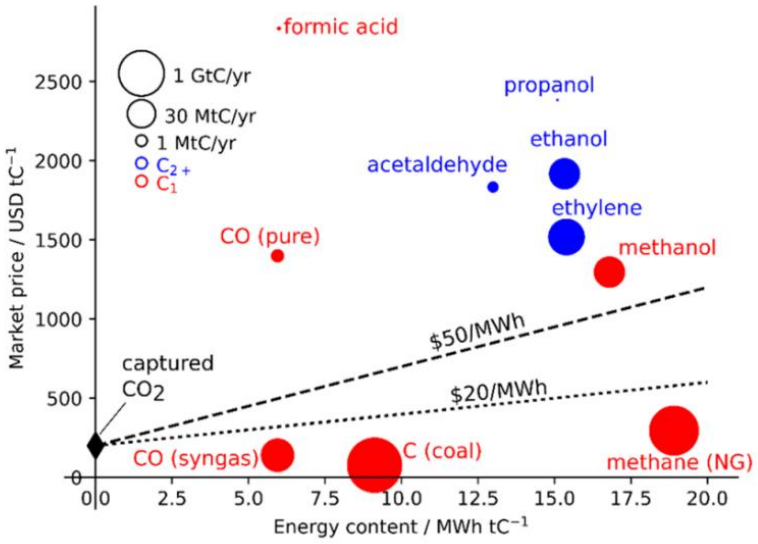

Figure 2.1 Market price and energy content of the desired products in the electrochemical CO_2 reduction reaction.

2.2 Basic Principles of CO_2 Electrocatalytic Reduction

2.2.1 Reaction process of CO_2RR.

The electrocatalytic reduction of carbon dioxide is a complex and intricate reaction process that requires the creation of a comprehensive and unified theoretical framework to develop catalysts with high activity and selectivity (Figure 2.2). In an aqueous environment, this reaction process unfolds as a multi-layered and multi-step journey involving multiple proton-coupled electron transfer events between reactive surface-bound species at the three-phase interface [98].

When carbon dioxide is electrolyzed, it undergoes a series of reduction reactions at the electrode surface. Although the exact reaction mechanism has not been generally explained, the following four steps are widely accepted in heterogeneous catalysis. The overall reaction process can be summarized as

follows: Carbon dioxide molecules are adsorbed on the surface of the electrode, where they interact with the catalyst [99, 100]. Subsequently, the adsorbed carbon dioxide molecules are activated by accepting electrons from the electrode and forming intermediates such as $CO_2^{\bullet-}$, CO* and HCOO* (where * stands for the adsorption site) [101]. The process of linearly bound CO_2 molecules on the catalyst surface in the sp1-hybridized state and their initial electron transfer activation to $*CO_2$ is typically a rate-determining step, as it usually involves spatial changes in the geometric structure and requires a significant amount of reorganization energy [102]. This energy contribution is also a major factor influencing the slow dynamics of electrochemical reduction. Protons from the electrolyte participate in the reduction process and lead to the formation of products such as carbon monoxide (CO), formate ($HCOO^-$) and hydrocarbons by proton-coupled electron transfer [103].

C-C coupling is the crucial step for multi-carbon products. The C-C coupled intermediates can undergo further hydrogenation reactions, in which additional hydrogen atoms are added to the carbon backbone. This leads to the formation of hydrocarbons with different chain lengths, such as ethylene, ethanol, or products with a higher carbon number. Finally, the reaction products desorb from the electrode surface, making room for new CO_2 molecules to pass through the process. The specific pathways and selectivity of the reduction depend on the catalyst, the electrode potential and the reaction conditions [104, 105].

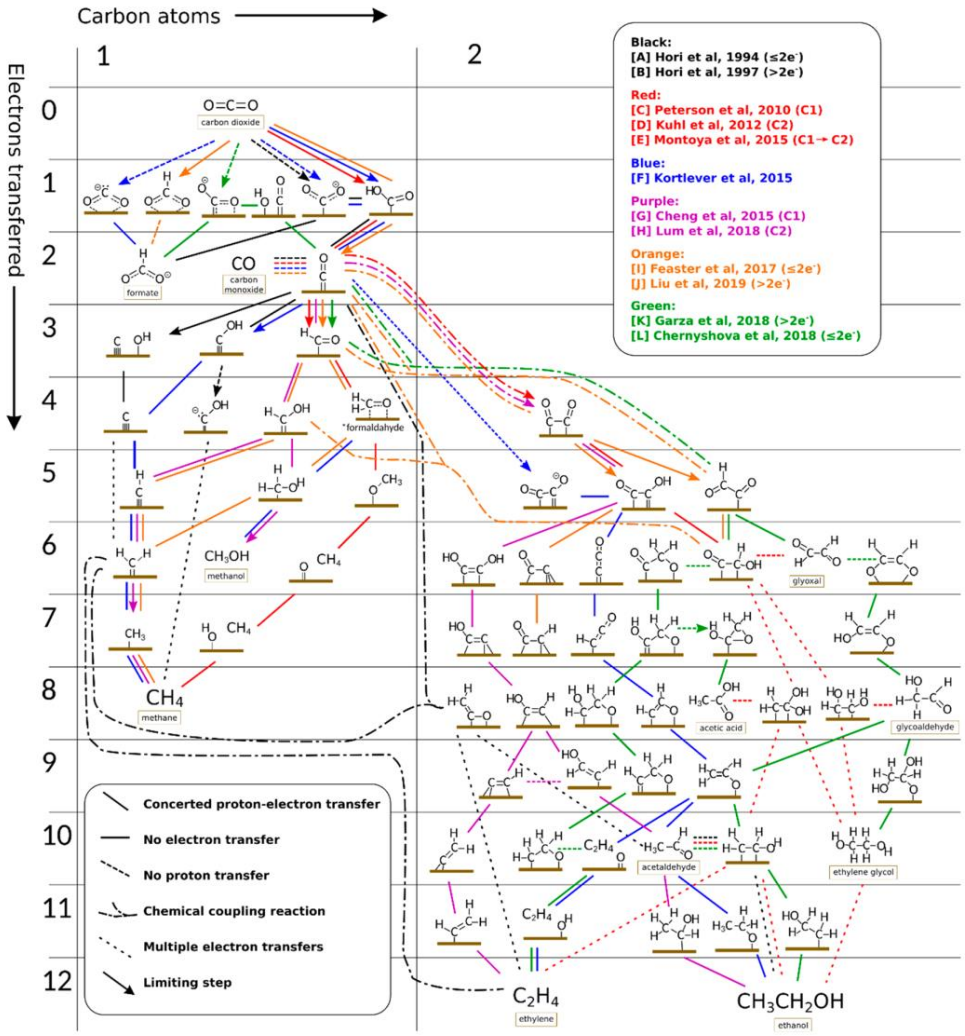

Figure 2.2 The possible pathways of CO_2RR on polycrystalline copper [106].

The difference in production selectivity usually depends on the strength of the bond between the electrocatalyst and the main intermediate, mainly CO*. If the bond between the catalyst and CO* is weak, CO* will be released from the catalyst surface as soon as it is formed. In this case, CO becomes the main product. If the bond is too strong, the hydrogen evolution reaction would dominate, and CO_2 reduction would also be inhibited as the occupied metal sites are not available for further CO_2RR [107]. Therefore, the adsorption and desorption energy of the key intermediates is one of the decisive factors for the efficiency of the final product.

In the production of multi-carbon products, a crucial step is the dimerization of CO*. However, this reaction competes with the hydrogenation of CO*. Based on the data presented in Table 2.1, the possible reactions leading to the formation of COCO* and COCHO* and their respective free energies were documented on three Cu-based electrocatalysts. The COCO* intermediates can be generated by the reaction between CO* and either CO or CO*. It can be deduced that the adsorption of CO next to an existing CO* site occurs spontaneously, but the approach of two neighbouring CO* molecules requires overcoming a small barrier.

On the other hand, the formation of the intermediate COCHO* differs from that of COCO*. While the adsorption of CO next to an existing CHO* site or the approximation of existing CO* and CHO* can contribute to it, it can also be formed by the hydrogenation of COCO*. However, due to their high reaction energies, this hydrogenation process is challenging for the Cu-AGNR and Cu-βB catalysts. In addition, maintaining adequate CO* coverage plays an essential role in achieving high selectivity for C_{2+} products. This coverage helps to inhibit the decomposition of COCHO* and is crucial for the desired result [108].

Table 2.1 The free energies of the C_2-related reactions on Cu-AGNR, Cu-ZGNR and Cu-βB [108].

Reaction	$\Delta G_{Cu\text{-}AGNR}$ [ev]	$\Delta G_{Cu\text{-}ZGNR}$ [ev]	$\Delta G_{Cu\text{-}\beta B}$ [ev]
CO + * → CO*	-0.45	-0.77	-0.60
CO* + H^+ + e^- → CHO*	0.59	0.62	0.61
CO* + CO → COCO*	-0.38	-0.26	-0.55
CO* + CO* → COCO*	0.06	0.17	0.05
CHO* + CO → COCHO*	0.20	-0.38	0.26
CHO* + CO* → COCHO*	0.34	0.15	0.46
COCO* + H^+ + e^-→ COCHO*	1.17	0.50	1.42

2.2.2 Factors influencing the kinetics of CO_2RR

The pathways from CO_2 to C_2 products are very complex, and several factors can influence these reactions. These factors include operating conditions, which include parameters such as temperature, pressure and flow rate [109, 110]. These factors can modulate the reaction rates of both CO_2RR and HER and consequently affect the selectivity of CO_2RR.

pH effect

Upon dissolution in water, CO_2 exists in three inorganic forms: CO_2(aq.), HCO_3^-, and CO_3^{2-}, along with carbonic acid. The concentrations of these species are pH-dependent, affecting the availability of CO_2 for reactions [69].

Aside from the pH of the aqueous solution, the local pH significantly influences the electrochemical reaction in several ways. Changes in pH can alter the surface charge and electrochemical potential of the electrode, influencing the adsorption

and activation of CO_2 molecules [111]. It affects the stability and transformation pathways of reaction intermediates, with alkaline conditions often favouring the stability of intermediates that promote C-C bond formation [112]. Additionally, different electrocatalysts exhibit varying catalytic activities under different local pH conditions, with some being more effective in alkaline environments. Furthermore, Local pH also impacts proton availability, appropriate local pH can suppress hydrogen evolution, thereby enhancing the selectivity for target multi-carbon products[57]. Overall, optimizing local pH is key to improving the efficiency and yield of multi-carbon products in CO_2RR.

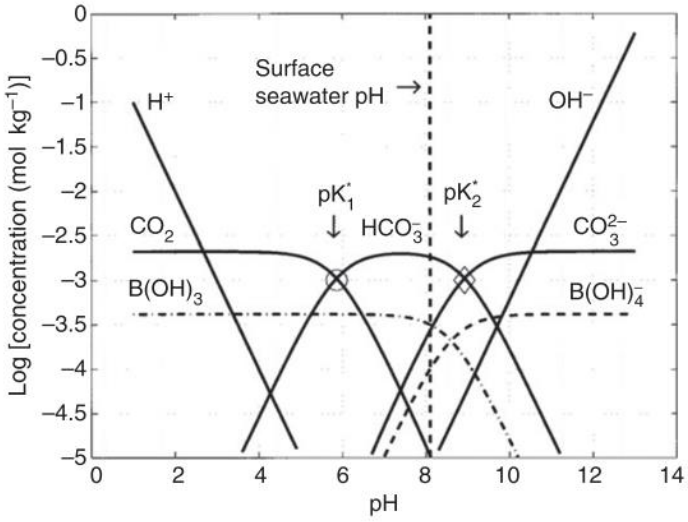

Figure 2.3 Variations in concentration of CO_2, HCO_3^-, and CO_3^{2-} [69].

Electrolyte

The choice of electrolyte is crucial for the performance of CO_2 reduction reactions. Studies have shown that halide ions, introduced through salts like KCl, KBr, and KI, can significantly affect product selectivity. The addition of certain cations or anions can improve CO_2 adsorption and facilitate the formation of the desired products [113-116]. However, there is a significant lack of understanding

regarding the fundamental mechanisms involved in real-time reactions. Advanced operando techniques are essential for revealing the influence of halide anions and provide insights into the fundamental reaction pathways in real-time electrocatalysis.

Catalyst

Another decisive factor is the properties of the catalysts [117-119]. The selection of suitable electrode materials, as well as the design and optimization of catalysts, are of great importance in CO_2RR [120]. The performance of electrocatalysts can be evaluated based on their selectivity, activity, and stability. The faradaic efficiency serves as a measure of the selectivity of electrocatalysts towards a specific product. Equation 2.3 provides the calculation formula where m is the number of electrons transferred, n is the actual number of moles of product, F is Faraday's constant (equal to 96485.3 C/mol), and Q is the total charge consumed [105]. The overpotential, which is the difference between the actual reaction potential and the thermodynamic potential, plays a crucial role in evaluating the activity of catalysts at a given partial current density. A higher overpotential, which is required to reach a certain partial current density, indicates a lower activity of the catalyst and leads to a waste of electrical energy [121]. In addition, the cost efficiency and durability of the catalysts are crucial for industrial production. The desired electrocatalyst should, therefore, not only have activity and selectivity but also cost-effectiveness and stability [122].

$$FE = mnF/Q \qquad \text{Equation 2.3}$$

2.3 Development of Cu-based electrocatalyst

2.3.1 Cu metals electrocatalysts

Pure metals were widely used as electrocatalysts in CO_2RR. Since the main products vary with the bond strength between metal catalysts and the main CO_2RR and HER intermediates such as *H, *OCHO and *CO, metal electrocatalysts can be classified into four groups [106]. The first group mainly includes Au, Ga, Ag, Zn and Pd, on which *CO can be easily desorbed so that CO is selectively produced [122, 123]. The metals of the second group (e.g. Pb, Hg, In, Sn, Cd and Tl) could catalyze the formation of formic acid [124]. The third group plays a decisive role in the formation of hydrocarbons, aldehydes and alcohols. It currently includes only one metal element, Cu, which is highlighted in the following section [125]. The metals of the last group, such as Pt, Fe, Co, Ni, and Ti, are rarely used in CO_2RR. Due to the tight bonding of the metals to the intermediate *CO, the hydrogen evolution reaction would predominate over the CO_2RR [107].

Due to the exclusive performance of copper in catalyzing the reduction of CO_2 to valuable hydrocarbons and alcohols, Cu has been tested in various fields for its performance in ethanol production. In the copper-catalyzed CO_2 reduction reaction, 16 different C_1-C_3 products were detected on the surface of Cu, including 12 C_2 and C_3 products containing hydrocarbons, ketones, aldehydes, alcohols and carboxylic acids [126]. The variety of products observed in CO_2RR can be attributed to the adsorption energies between the catalyst and key intermediates such as *CO and *H. In the case of copper catalysts, the moderately negative adsorption energy between Cu and *CO, combined with the

positive adsorption energy for *H, contributes to the formation of a variety of products [106, 127].

Extensive testing of Cu catalysts with different particle sizes and morphologies has been performed to understand their CO_2RR performance [60, 128, 129]. Interestingly, Cu catalysts with different crystal orientations exhibit different properties in terms of CO_2RR. In particular, Cu(100) surfaces consistently show a relatively high yield of multi-carbon products. If, for example, the faradaic efficiencies of different products on a Cu(100) electrode are considered, the faradaic efficiency for ethanol is below 10%. However, the faradaic efficiencies for ethylene and C_{2+} products are significantly higher, reaching 40.4% and 57.8%, respectively [130]. This underlines the importance of crystal orientation in determining the selectivity and efficiency of CO_2RR on Cu catalysts.

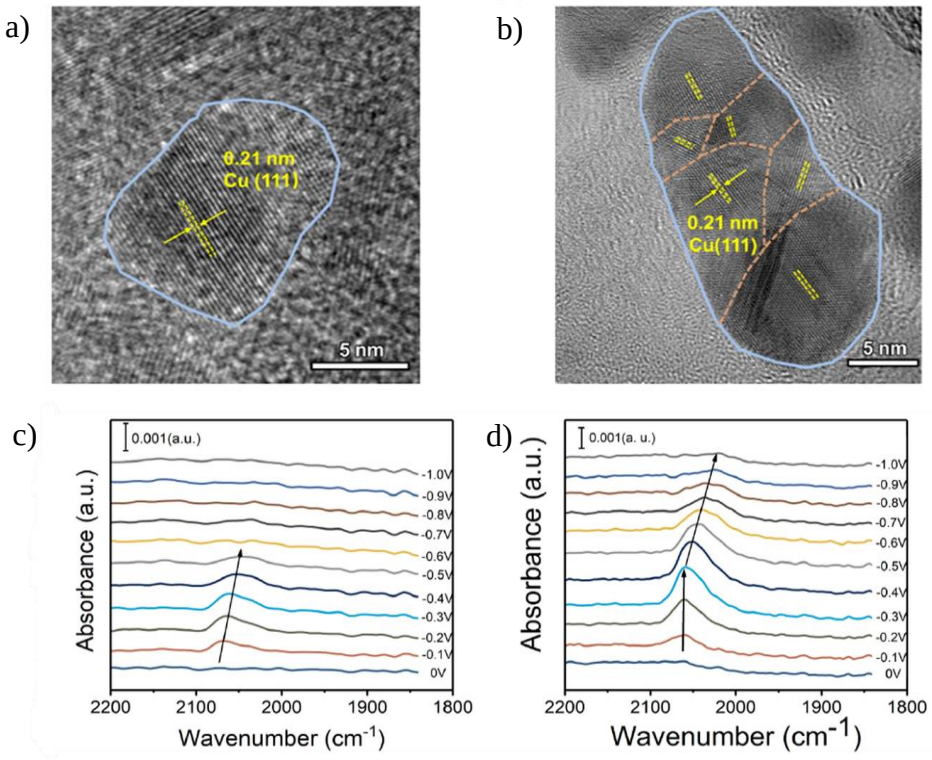

Figure 2.4 HRTEM images and in situ ATR-SEIRAS spectra of a,c) ED-Cu catalysts and b,d) GB-Cu catalysts [131].

Chen's group added poly(vinylpyrrolidone) (PVP) in the electrodeposition step and successfully enriched the grain boundaries. The GB-Cu could effectively prevent carbon contamination and reduce the crystal size. According to the DFT calculations and the in situ ATR-SEIRAS spectra, the presence of grain boundaries enhanced *CO adsorption, further supporting CO dimerization (Figure 2.4c, d). This electrocatalyst shows a high faradaic efficiency of about 31.7% for ethanol and 70.0% for C_2 products at a potential of -1.3 V vs. RHE [131]. This work attracted the great attention of Cu-based electrocatalysts. An extensive body of work focusing on copper-containing materials for CO_2RR continues in order to optimize the production of multi-carbon products (Table 2.2) [106].

Table 2.2 The performance of Cu for CO_2RR to multi-carbon products.

Catalyst	Product	FE	Electrolyte	Potential	Ref.
Cu (100)	**EtOH**	**9.7%**	**0.1 M $KHCO_3$**	**-1.4 V vs. SHE**	**[130]**
	C_2H_4	**40.4%**			
	C_{2+}	**57.8%**			
Anodised copper	**C_2H_4**	**38.1%**	**0.1 M $KHCO_3$**	**-1.08 V vs. RHE**	**[132]**
Electroredeposited copper	**C_2H_4**	**38.0%**	**0.1 M $KHCO_3$**	**-1.2 V vs. RHE**	**[133]**
GB-Rich Copper	**EtOH**	**31.7%**	**0.1 M KOH**	**-1.3 V vs. RHE**	**[131]**
	C_{2+}	**70.0%**			
EC Cu	**C_{2+}**	**56.4%**	**0.1 M $KHCO_3$**	**-1.0 V vs. RHE**	**[134]**
HQ-Cu	**C_{2+}**	**68.2%**	**0.1 M $KHCO_3$**	**-1.05 V vs. RHE**	**[135]**
Porous Hollow Copper Microspheres	**C_{2+}**	**67.3%**	**0.1 M $KHCO_3$**	**-0.82 V vs. RHE**	**[136]**
Nanosheet structure derived Cu	**C_{2+}**	**67.5%**	**0.1 M $KHCO_3$**	**-1.5 V vs. RHE**	**[137]**
Cu nanofoam, co-cata:1-butyl-3-methyl-imidazolium bromide	**EtOH**	**49.0%**	**0.1 M $KHCO_3$**	**-1.6 V vs. Ag/AgCl**	**[138]**

2.3.2 Compound-derived copper electrocatalysts

The electrocatalytic performance of copper nanoparticles derived from halides and oxides has been extensively studied. Cui's group synthesized CuO nanoparticles with different structures and morphologies and studied their electrocatalytic performance in a 0.2 M KI solution. Among the various CuO nanoparticles tested, spherical nanoparticles with a size of about 4 μm and an average surface area of 45.4 m^2/g showed superior performance, achieving a faradaic efficiency of 33% for ethanol production at -1.7 V vs. SCE. Notably, the percentage of ethanol in the carbon-based products of this CuO nanoparticle exceeded 95%. This work emphasizes the high selectivity of the CuO nanoparticle for ethanol production [139].

In another study, another research group analyzed the yields of ethylene and ethanol on Cu_2O film electrodes with different thicknesses from 0.2 μm to 8.8 μm in a 0.1 M $KHCO_3$ solution at -0.99 V vs. RHE (Figure 2.5). Cu_2O films with different thicknesses and different densities of steps and edges were obtained by adjusting the deposition time. The highest ethylene FE of 40.3% was obtained on a 0.9 μm Cu_2O catalyst at a current density of -25 mA/cm^2, while the FE of ethanol was 8.7%. The best FE of 16.4% for ethanol production was observed on a 3.6 μm film at a current density of -35 mA/cm^2, while the ethylene FE was 34.3%. During the CO_2RR process, CuO and Cu_2O were reduced to metallic Cu, and Cu^0 particles were identified as the active species for CO_2 reduction. However, a significant drawback of both CuO and Cu_2O catalysts is the uncontrolled hydrogen evolution reaction, as shown by the FE of H_2 between

26% and 68% on the 0.2-8.8 µm Cu_2O catalyst, which is sometimes even higher than the combined FE of C_2 products, indicating energy waste [140].

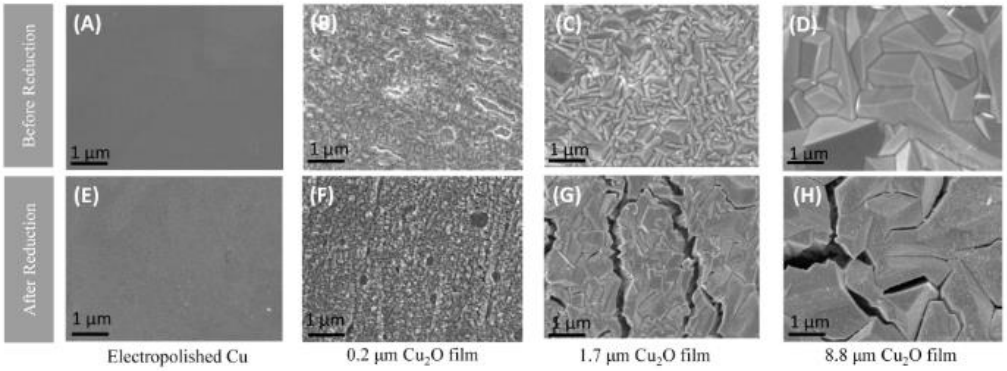

Figure 2.5 SEM images of Cu catalysts before and after CO_2 reduction at −0.99 V: a, e) electropolished Cu; b, f) 0.2 µm, c, g) 1.7 µm, and d, h) 8.8 µm Cu_2O films deposited on Cu disc [140].

CuCl, CuI and CuBr were prepared by electrochemical cycling of an electropolished Cu foil in potassium salt solutions. The prepared CuX samples exhibited both Cu_2O and CuX compounds (CuCl, CuI or CuBr) on their surfaces (Figure 2.6i). The surface morphology varied considerably between the different samples (Figure 2.6a-d). Of particular interest is the iodine-modified Cu sample, which exhibited a rough surface, a greater amount of Cu^+ species, and subsurface oxygen. This iodine modification resulted in the best performance in the production of multi-carbon products during CO_2RR, achieving FEs of about 80% at -0.9 V vs. RHE. During the CO_2RR process, most Cu species in the CuX samples were reduced to metallic Cu. This reduction of Cu species to metallic Cu led to a decrease in the faradaic efficiency of ethylene production (Figure 2.6j). Therefore, the presence of Cu_2O and Cu^+ species and the surface morphology played a crucial role in determining the CO_2RR performance and selectivity towards multi-carbon products [141]. Overall, this study emphasizes

the importance of surface modification and the presence of specific Cu species in controlling CO_2RR performance and product selectivity.

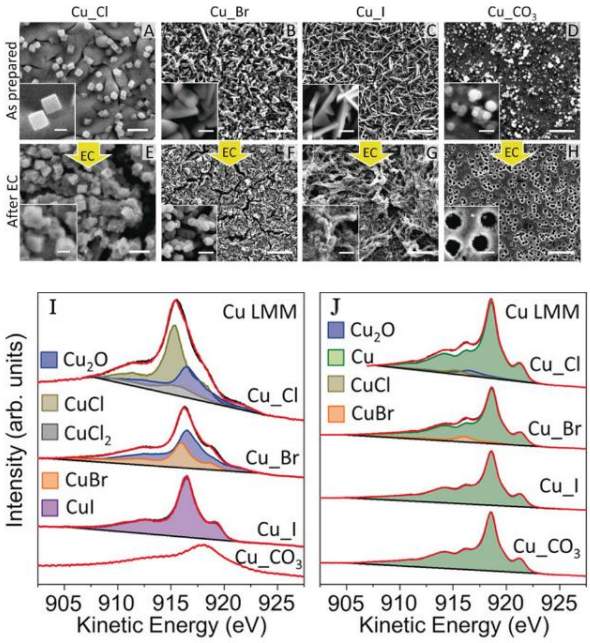

Figure 2.6 SEM images of Cu catalysts before and after CO_2 reduction: a, e) CuCl; b, f) CuBr, c, g) CuI, and d, h) $CuCO_3$. XPS Cu LMM for the electrodes i) before and j) after CO_2 reduction [141].

Table 2.3 The performance of compound-derived copper catalysts for CO_2RR to multi-carbon products.

Catalyst	Product	FE	Electrolyte	Potential	Ref.
Mesoporous CuO	**C_{2+}**	**60.0%**	**1.0 M KI**	**-1.0 V vs. RHE**	**[142]**
Cu_2O-derived Cu NP	**C_2H_4**	**33.5%**	**0.1 M $KHCO_3$**	**-1.1 V vs. RHE**	**[143]**
CuO nanoparticles	**EtOH**	**36.1%**	**0.2 M KI**	**−1.7 V vs. SCE**	**[139]**
PVDF modified CuO	**C_2H_4**	**40.6%**	**0.5 M $KHCO_3$**	**-1.22 V vs. RHE**	**[144]**
Cu_2O film (0.9 μm)	**C_2H_4**	**40.3%**	**0.1 M $KHCO_3$**	**−0.99 V vs. RHE**	**[140]**
	EtOH	**8.7%**			

CuBr	**C_{2+}**	**66.0%**	**0.1 M $KHCO_3$**	**-1.0 V vs. RHE**	**[141]**
CuI	**C_{2+}**	**80.0%**	**0.1 M $KHCO_3$**	**−0.9 V vs. RHE**	**[141]**
CuCl	**C_{2+}**	**73.0%**	**0.5 M $KHCO_3$**	**−2.6 V vs. Ag/AgCl**	**[145]**

2.3.3 Bimetallic electrocatalysts

To compensate for the limitations of pure Cu, researchers have explored alloying Cu or Cu_2O with other metals such as Ag, Au and Zn to produce electrodes with improved electrocatalytic properties [107]. A CuAg electrode was prepared by electrodepositing CuAg onto a carbon paper substrate coated with Cu. The resulting CuAg electrode exhibited a significantly larger electroactive surface area and a smaller crystal size of 3.6 nm, which contributed to its high activity and selectivity in the production of C_2 products [146].

Another group utilized a similar method of electrodeposition in an NH_3-based electrolyte or KCN solution to prepare phase-separated and phase-mixed Ag-incorporated Cu_2O electrodes, namely Ag-Cu_2O_{PS} and Ag-Cu_2O_{PB}. Electrochemical reduction tests showed that the Ag-Cu_2O_{PB} electrode achieved a faradaic efficiency of 34.2% for ethanol production at a potential of -1.2 V vs. RHE and effectively suppressed the hydrogen evolution reaction with Cu_2O [147].

In another study, Ag nanoparticles were embedded in Cu nanopores by in situ reduction with silver nitrate, with ascorbic acid added as a reducing agent, resulting in the formation of Ag@Cu hybrid arrays. The modification of silver at the Cu/Ag interface regulated the electronic structure, improved the adsorption of *CO and facilitated the dimerization of *CO to ethylene (FE =

41.3%) [148]. In addition, the density and length of Cu-Ag interfaces were found to influence ethanol production and possibly affect the migration of CO [149]. These impressive results provide a practical approach to control the desired product pathway by exploring the diversity of bonding configurations [150].

Gold nanoparticles can catalyze the reduction of CO_2 to CO in close proximity to the copper surface, resulting in high coverage of *CO. Nanostructured Cu-Au electrodes have been used in electrochemical reduction. For example, $Cu_{63.9}Au_{36.1}$/NCF showed high selectivity for ethanol and methanol with a faradaic efficiency of 12 and 15.9%, respectively [151]. In another experiment, a bimetallic Cu/Au electrocatalyst was used, which showed high selectivity for C_{2+} products. The activity of the gold-copper tandem catalyst was significantly better than that of the single Cu, Au and Au-Cu catalysts, highlighting the promising future of tandem catalyst applications [152].

Besides, AuCu nanoparticles were embedded in Cu submicron arrays by electrodeposition and chemical reduction, resulting in a more selective electrocatalyst with 29% FE for ethanol and 16% FE for ethylene at -1.0 V vs. RHE. In this case, the Au atoms acted as cocatalysts and altered the adsorption energy of the intermediates, while the unique structure of the Cu submicron provided undercoordinated Cu and Au active sites [153].

To further improve the ability of bimetallic AuCu catalysts for ethanol production, Zhang's group has prepared Au@Cu_2O yolk-shell nanoparticles using a hydrazine hydrogenation reduction method. The Au core wrapped with a copper shell efficiently reduced CO_2 to CO, and the high CO concentration inside the cavity further facilitated ethanol production in the copper shell.

To investigate the spatial confinement effect of the CO intermediates, three samples with different cavity sizes of Cu_2O nanocavities (radius 14, 35, 48 nm) were prepared by adjusting the amount of the reducing agent and the reaction time (Figure 2.7). Electrochemical measurements showed that the catalyst with a moderate cavity size of 35 nm exhibited the highest faradaic efficiency for ethanol with 52.3% at -0.3 V vs. RHE, which can be attributed to the moderate CO concentration in the cavity. These results emphasize the potential of the yolk-shell structure in the development of bimetallic electrocatalysts [154].

Metals of the Pd group have also been used to modify Cu electrodes in electrochemical reduction processes. In one study, Cu overlays were prepared on tetrahexahedral Pd nanocrystals with high index planes. The Pd and Cu overlayers were electrodeposited successively on glassy carbon using the programmed square wave potential and underpotential deposition methods, respectively. Pd on the Cu electrode led to a high density of low-coordinated step atoms, which exhibited strong CO adsorption and favoured CO_2 electroreduction [155].

Studies have shown that for Pd- and Au-doped M@Cu catalysts, the free energy change for OC-COH coupling is lower than that for OC-CHO coupling, which favours the production of alcohols [156]. $Ce(OH)_X$-doped Cu was another efficient electrocatalyst for ethanol production. The exceptional performance is attributed to the presence of hydroxide, which increases the adsorption energy for hydrogen. This promotes the hydrogenation of *HCCOH to *HCCHOH instead of *CCH in the ethylene pathway, leading to the formation of ethanol. However, the accelerated water decomposition simultaneously leads to the formation of H_2 [157].

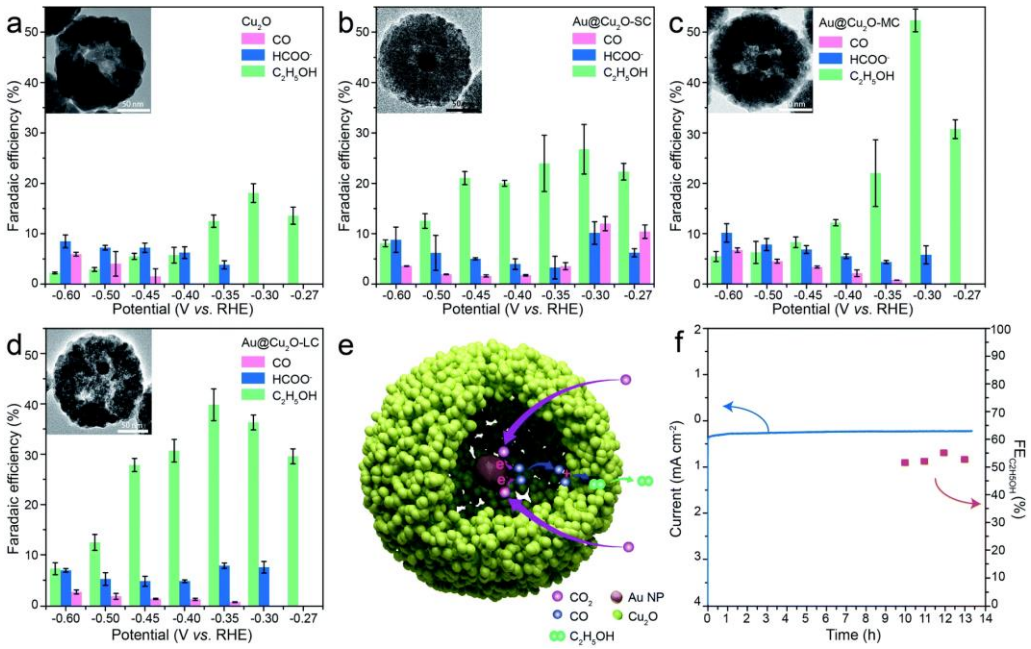

Figure 2.7 Schematic illustration in the Au@Cu$_2$O cavity and the FE of ethanol at -0.3 V vs. RHE [154].

In summary, incorporating a second metal, particularly silver or gold, significantly enhances the performance of copper-based catalysts for ethylene production. These metals fine-tune the catalyst's electronic properties, creating a more favorable environment for improved catalytic efficiency.

Table 2.4 The performance of bimetallic copper-based catalysts for CO_2RR to the multi-carbon products.

Catalyst	Product	FE	Electrolyte	Potential (V vs. RHE)	Ref.
Ag@Cu composite	**C_2H_4**	**41.3%**	**0.5 M $KHCO_3$**	**−1.2**	**[148]**
Zn@Cu composite	**C_2H_4**	**38.3%**	**0.5 M $KHCO_3$**	**−1.2**	**[148]**
Ag-Cu_2O_{PB}	**EtOH**	**34.2%**	**0.2 M KCl**	**−1.2**	**[147]**
$Ag_{0.14}/Cu_{0.86}$	**EtOH**	**41.0%**	**1.0 M $KHCO_3$**	**-0.7**	**[150]**
Cu overlayers on THH Pd NCs	**EtOH**	**20.4%**	**0.1 M $NaHCO_3$**	**-0.5**	**[155]**
Au@Cu_2O	**EtOH**	**52.3%**	**0.1 M $KHCO_3$**	**-0.3**	**[154]**
Ce(OH)x-doped-Cu	**EtOH**	**43.0%**	**1.0 M KOH**	**-0.7**	**[157]**
Ni-Cu NW	**C_{2+}**	**44.0%**	**0.5 M $NaHCO_3$**	**-0.8**	**[158]**

2.3.4 Cu-based heteroatomic carbon electrocatalysts

MOF materials are normally used as electrical insulators. However, various carbon-based MOF electrocatalysts have been synthesized, which are characterized by a large surface area, unique porous structure, and uniformly distributed metal nanoparticles [159-161]. Cu-based MOFs such as HKUST-1 can be carbonized at high temperatures (900-1100°C) to produce OD Cu/C electrocatalysts. At 1000°C, the resulting catalyst achieves a Faradaic efficiency of 34.8% for ethanol at -0.7 V vs. RHE.

This efficiency is due to several factors. First, carbonization forms Cu_2O in the catalyst, which increases its electrocatalytic activity and facilitates CO_2 reduction to ethanol. Secondly, the electronic interactions between Cu and

carbon improve the catalytic performance by promoting CO_2 adsorption and activation and improving ethanol selectivity. The high active surface area and porous structure of OD Cu/C enable efficient mass and electron transfer during electrochemical reduction, which improves reactant accessibility and facilitates the conversion of CO_2 to ethanol. Carbonization of Cu-based MOFs to obtain OD Cu/C catalysts represents a promising approach for efficient electrocatalytic CO_2 to ethanol conversion, taking advantage of Cu_2O formation, electronic interactions and favourable structural properties [162].

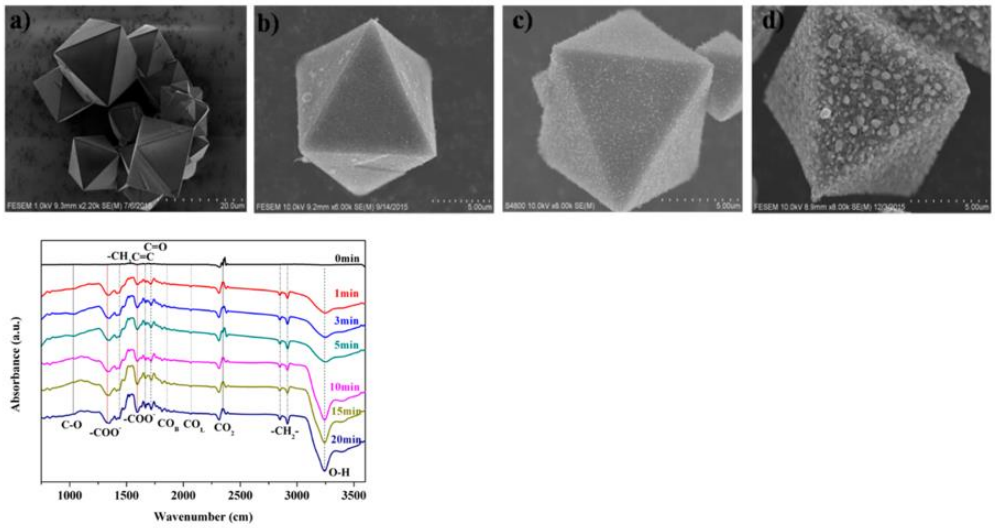

Figure 2.8 SEM images of a) HKUST-1; b) OD Cu/C-900; c) OD Cu/C-1000; d) OD Cu/C-1100; e) In situ FTIR spectrum of CO_2 reduction on OD Cu/C-1000 at −0.7 V vs RHE [162].

Graphene-based materials have attracted considerable attention for improving the electrochemical reduction of CO_2 due to their excellent electronic and thermal conductivity and unique structure [163].

One example is the carbon nanospike electrode (CNS) with electro-nucleated Cu nanoparticles (Cu/CNS), which has a nitrogen doping density of 5.1%. This

catalyst exhibits a remarkable ethanol production (FE = 63%). The nitrogen-doped graphene in Cu/CNS plays a crucial role in achieving these results. The π-electron states in the nitrogen-doped graphene polarize the carbon atoms associated with the nitrogen and provide active sites for C_2 intermediates involved in ethanol formation. In addition, the unique corrugated and crimped structure of CNS enhances the interaction with C_2 intermediates and promotes ethanol selectivity [164].

Another research group developed a Cu GNC-VL nanocomposite for CO_2RR by anchoring Zeolitic Imidazolate Framework-L (ZIF-L) on graphene oxide and incorporating copper into the structure. After carbonization at 1000°C, the resulting MOF electrocatalyst showed remarkable performance. It achieved an impressive ethanol FE of 70.5% at a potential of -0.87 V vs. RHE. In the Cu-GNC-VL nanocomposite, copper is present in the form of a mixture of Cu^0 and Cu^+ species, with Cu^+ atoms accounting for a significant proportion (70.6%). The presence of Cu^+ facilitates the dimerization of CO* intermediates. In addition, the nitrogen in the catalyst provides abundant active sites that effectively reduce the binding energy [165]. The outstanding performance of Cu GNC-VL, compared to OD Cu/C, emphasizes the great potential of nitrogen-containing electrocatalysts in CO_2RR.

A similar graphene-based electrocatalyst with Cu nanoparticles on pyridoxine-modified graphene oxide sheets (GO-VB_6-Cu) was also used. The resulting catalyst showed efficient ethanol production with a faradaic efficiency of 56.3% at a low potential of -0.25 V vs. RHE. Various nitrogen species were functionalized in the N-doped graphene of GO-VB_6-Cu, including pyridine-N, pyrrole-N, graphite-N, and oxidized N [166]. Pyridoxine was used to achieve a

pyridine-N content of 2.3%. The Incorporation of pyridinic N into the N-doped graphene of GO-VB_6-Cu provides additional sites for the CO_2 reduction reaction, resulting in improved ethanol production. Furthermore, it contributes to improved charge transfer and higher mobility within the catalyst, which enhances its catalytic performance [86, 167].

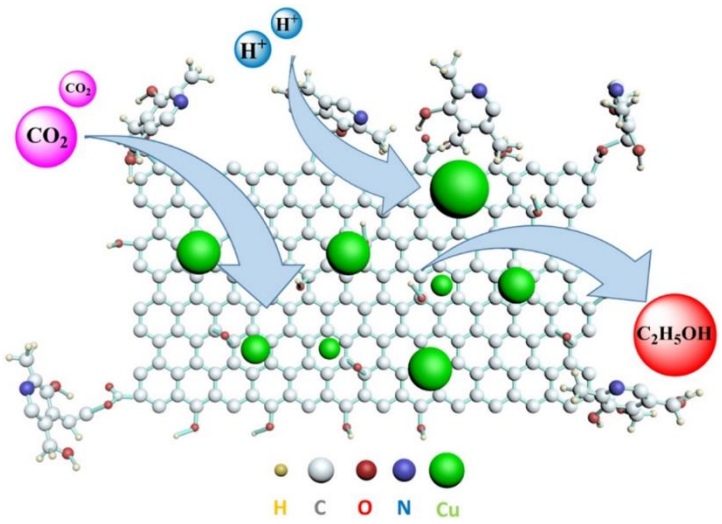

Figure 2.9 Schematic illustration of the proposed process of the CO_2RR on the GO-VB_6-Cu catalyst [166].

Nitrogen species in the catalyst, such as pyridinic N, play a crucial role in the enrichment and activation of CO_2 and facilitate the reorganization processes of the bonds. Here, a nitrogen-doped carbon shell was generated over the Cu surface. The resulting Cu@N_xC electrode exhibits a favourable CO_2RR compared to the HER. The pore structure and the N-containing sites in the nitrogen-doped carbon shell contribute to a high surface coverage of CO intermediates during CO_2RR. This increased surface coverage promotes the formation of C_{2+} products, leading to an impressive 80% FE for C_{2+} products. In particular, the Cu@N_xC electrode shows a faradaic efficiency of over 40% in ethylene production at a potential of -1.1 V [168]. These results emphasize the

importance of the catalyst substrate and the environment for electrocatalysis. The presence of nitrogen species in the catalyst and the resulting nitrogen-doped carbon shell contribute to the improved CO_2RR performance and emphasize the importance of catalyst design and the role of the environment for efficient electrocatalysis.

Table 2.5 The performance of Cu-based heteroatomic carbon catalysts for CO_2RR to multi-carbon products.

Catalyst	Product	FE	Electrolyte	Potential (V vs. RHE)	Ref.
Cu/CNC	**EtOH**	**63.0%**	**0.1 M $KHCO_3$**	**-1.2**	**[164]**
GO-VB_6-Cu	**EtOH**	**56.3%**	**0.1 M $KHCO_3$**	**-0.3**	**[167]**
OD Cu/C	**EtOH**	**34.8%**	**0.1 M $KHCO_3$**	**-0.7**	**[162]**
Cu GNC-VL	**EtOH**	**70.5%**	**0.5 M $KHCO_3$**	**-0.9**	**[165]**
Cu-on-Cu_3N	**C_2H_4**	**39.0%**	**0.1 M $KHCO_3$**	**-1.0**	**[36]**
Cu@N_xC	**C_{2+}**	**80.0%**	**0.1 M $KHCO_3$**	**-1.1**	**[168]**

2.3.5 Cocatalyst applied to enhance CO_2RR

Cocatalysts play a crucial role in CO_2RR by increasing the conversion rate of CO_2 and facilitating the separation and transport of electron-hole pairs. They also improve the activity, stability and product selectivity of the electrocatalyst and help control the reaction pathway by inhibiting side reactions. The composition, surface area, structure and dispersibility of cocatalysts can significantly affect their performance [169].

In Zarandi's research, 1-butyl-3-methyl-imidazolium bromide (BMIMB) was used as a homogeneous cocatalyst in a 0.1 M $KHCO_3$ electrolyte. CO_2 reduction

was carried out on a simple electrodeposited copper nanofoam electrode. The addition of BMIMB improved the CO_2 conversion to 83%. The faradaic selectivity for ethanol was 49%. The synergistic effect between the copper nanofoam and the BMIMB cocatalyst contributed to the stabilization of the intermediates, which significantly increased the ethanol yield [138]. Although further improvements are needed, the use of cocatalysts shows promise as a method for large-scale ethanol production by CO_2RR. The use of cocatalysts can increase the selectivity and yield of the desired products, making them an essential factor in the development of efficient electrocatalytic CO_2 systems.

2.4 The valence state of Cu

The valence states of copper have long been recognized as crucial factors in the performance of copper-based catalysts for CO_2 reduction [170]. A combination of experimental techniques and DFT calculations was employed to elucidate the role of mixed-valence copper active sites in catalysis. The complexity of base materials, which often feature a myriad of structural motifs such as grain boundaries, high-index facets, stepped terraces, and corrugated surfaces, presents a challenge in untangling the contributions of these features to the CO_2 reduction performance. As a result, achieving a clear mechanistic understanding becomes inherently difficult.

To address this challenge, CuLs with various dihedral angles of adjacent $Cu^{I}Cu^{II}$L-metalloligands transformed, ultimately yielding the most stable variant with a 180° dihedral angle. This variant demonstrates outstanding performance in CO_2 reduction, achieving a methane FE of 67.8% and an ethylene FE of 17.3%.

Additionally, DFT calculations corroborate that isolated Cu(I) sites predominantly catalyze methane generation, whereas synergistic interactions between adjacent Cu(II) sites favour ethylene production(Figure 2.10a) [171].

Besides, single-crystal Cu(111) foils, characterized by minimal morphological and crystallographic heterogeneities, were utilized. These foils were then subjected to varying degrees of oxidation to obtain OD-Cu with distinct crystalline and valence states. The postelectrolytic and operando characterizations revealed that the CuO_x were gradually reduced and fragmented during the CO_2RR. The transition state $Cu^{\delta+}$ ($0 < \delta < 1$) between the initial oxide and the ultimately reduced copper phases, along with its stability over time, significantly influences the catalytic performance of CO_2RR to multicarbon products (Figure 2.10b) [172].

Indeed, stabilizing the transition state of copper is crucial for improving the selectivity towards C_{2+} products. The utilization of 0.9 nm Cu_2O nanosheets with abundant oxygen vacancies has shown promising results, achieving an exceptionally high C_{2+} FE of approximately 81%. Both experimental and computational findings suggest that the presence of abundant Cu^+ species in the ultrathin 2D Cu_2O nanosheets is the most favourable oxidation state for *CO adsorption and coverage on the catalyst surface. This, in turn, promotes the C−C coupling reaction in CO_2 reduction [173]. Therefore, in the transition state, the presence of $Cu^{\delta+}$, where δ is close to 1, is crucial for achieving excellent performance in producing C_{2+} products.

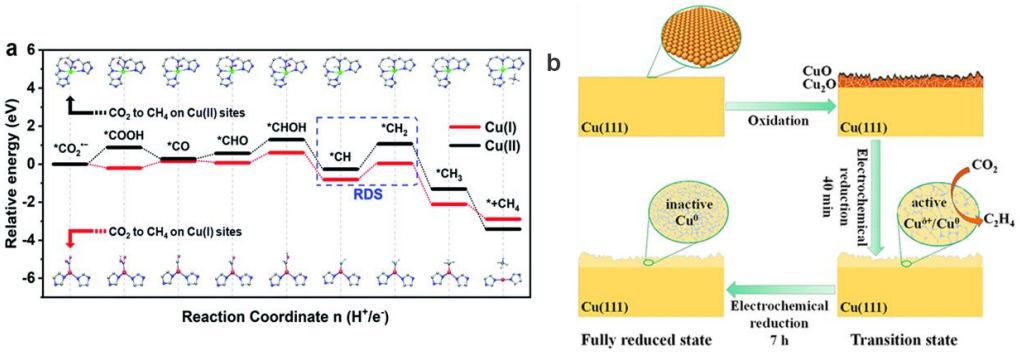

Figure 2.10 a) Calculated free energy diagram for CO_2 electrocatalytic reduction to CH_4 on the Cu(I) sites and Cu(II) sites of the CuL catalyst [171], b) valence change of copper at each reaction stage [172].

2.5 Stability

In recent years, considerable efforts have been dedicated to understanding how nanoscale structures influence the activity and selectivity of electrocatalytic CO_2 reduction. Nevertheless, the stability of catalysts during electrolysis stands out as a key consideration for advancing practical applications. Despite breakthroughs in improving reaction activity and selectivity, research on the stability of copper-based electrodes and the underlying nanoscale degradation mechanisms remains at a preliminary stage[58]

The commonly available copper-based catalysts in the market can only maintain stable electrocatalytic activity for a short period (around 10 hours) [174, 175]. Even with the most stable catalysts available in an H-cell reactor, the ethylene yield can only be sustained for up to 40 hours [132, 176]. Copper-based electrocatalysts used in CO_2 electroreduction encounter challenges related to catalyst stability, influenced by a range of factors (Figure 1.2). Examining the nanoscale degradation mechanisms has unveiled key processes that play a vital

role in this degradation. During the reaction, reshaping and fragmentation occur, leading to shape variations and potential breakage of copper nanostructures [174]. These alterations directly impact the catalyst's active surface area and overall structure. Detachment and dissolution of catalyst nanoparticles can also occur, resulting in a decreased number of active sites and undermining the catalyst's stability. Ostwald agglomeration, another degradation mechanism, involves the rearrangement of nanoparticles, causing aggregation or enlargement of specific particles and affecting the catalyst's surface properties [61, 177].

Moreover, the occurrence of poisoning, where impurities or their byproducts adhere to active sites, can lead to a decrease in the activity and selectivity of the catalyst [178]. Together, these degradation mechanisms profoundly influence the activity, selectivity, and stability of copper electrocatalysts during CO_2RR by altering their active surface area, structure, and morphology.

Table 2.6 The stability of Cu-based catalysts for CO_2RR to multi-carbon products.

Catalyst	Product	FE	Electrolyte	Potential (V vs. RHE)	Stability	Ref.
Cubic Cu_2O NPs	**C_2H_4**	**57.3%**	**0.1 M $KHCO_3$**	**-1.1**	**10 h**	**[174]**
Branched CuO NPs	**C_2H_4**	**65.0%**	**0.1 M $KHCO_3$**	**-1.05**	**12 h**	**[175]**
Anodized $Cu(OH)_2$	**C_2H_4**	**38.1%**	**0.1 M $KHCO_3$**	**-1.08**	**40 h**	**[132]**
CuAg composite	**EtOH**	**16.4%**	**0.1 M $KHCO_3$**	**-1.1**	**5 h**	**[149]**
AuCu/Cu-SCA	**EtOH**	**28.0%**	**0.5 M $KHCO_3$**	**-1.0**	**24 h**	**[153]**
Boron-doped Cu catalysts	**C_2H_4**	**52.0%**	**0.1 M KCl**	**-1.1**	**40 h**	**[176]**
N-Doped porous carbon supported Cu	**C_{2+}**	**71.1%**	**0.2 M $KHCO_3$**	**-1.05**	**10 h**	**[179]**

To enhance the stability of electrodes in CO_2RR, various strategies have been investigated. Catalyst stabilization is crucial for improving the performance of copper-based catalysts. Techniques such as particle confinement with Pd atoms [178], graphene oxide wrapping [167], and vertically oriented graphene separation [165], help preserve catalyst morphology and prevent issues like shape changes, coalescence, and agglomeration, thereby increasing morphological stability.

The role of surface-bound organic molecules, particularly ligands used during the colloidal synthesis of nanocatalysts, significantly impacts catalyst stability [180, 181]. While the desorption of ligands can accelerate morphological changes, strongly bound carbene-based ligands have shown potential in stabilizing electrocatalyst morphology, leading to enhanced stability and selective CO formation.

A synergistic interplay between catalyst design and system engineering has been explored to achieve longer periods of stable operation. Studies on shape-controlled nanoparticles have revealed a correlation between morphological transformations and electrocatalytic performance, allowing for the identification of more stable structures. Additionally, establishing a standardized procedure for assessing the stability of CO_2RR electrocatalysts is crucial. This procedure should consider parameters such as electrode type, electrolyte, electrolysis time/potential, and preferred product, enabling straightforward benchmarking of catalyst stability.

2.6 Summary

In the current phase, the production of more reduced hydrocarbons and alcohols faces some challenges.

- The low solubility of CO_2 in electrolytes would limit mass transfer [120]. In most conventional H-cell experiments, current densities are less than 30 mA/cm^2. To achieve considerable current densities, high overpotentials are required to dissociate the double bond between C and O (806 kJ/mol), which leads to a waste of electrical energy [182, 183].
- The critical step for the formation of C_{2+} molecules is the C-C coupling process, which must compete with the formation of the C-H bond and the C-O bond.
- The binding energy between the catalyst and CO intermediate must be moderate. If CO binds strongly to catalysts, the catalysts could be poisoned. If the bond is too weak, CO is easily desorbed, resulting in high selectivity for CO.
- The competing process (hydrogen evolution reaction) is unavoidable in an aqueous system.
- The production rate of CO_2RR must be significantly improved by increasing the number of active sites or the activity of each active site. However, another difficulty may be to find the active sites on the surface of the catalysts [87].
- Furthermore, a significant decrease in catalytic performance was observed in electrocatalysts such as Cu nanoparticles after several hours of testing, which can be attributed to the aggregation of the particles

[168]. Therefore, stability and durability need to be improved for sustainable production [179, 184].

- There are several possible pathways with different intermediates and products, but there is a lack of concrete experimental evidence to prove the correctness of the pathway. In addition, the complexity of the roadmap increases the difficulty of controlling the reaction pathway for the C_2 product [53].
- Another problem is the lack of highly accurate applicable and independent descriptors to determine the activity and selectivity of catalysts. With suitable descriptors, it would be much easier to find one effective catalyst [53, 185].

Overcoming these complex challenges requires the adoption of innovative solutions and the implementation of extensive research to optimize CO_2RR processes. The main objective is to improve the production of multi-carbon products. This endeavour requires the development of efficient catalysts that exhibit improved performance, stability and selectivity. By exploring these areas, we can pave the way for remarkable progress and unlock the full potential of CO_2RR technologies.

In this chapter, a comprehensive scientific investigation was conducted to explore mechanisms and influencing factors that determine the efficiency and selectivity of copper-based catalysts in the electrochemical reduction of carbon dioxide, specifically with a focus on the generation of C_{2+} products. Different types of copper-based catalysts that have shown remarkable efficiency in the electrocatalytic production of multi-carbon products from CO_2 were systematically enumerated and compared. The preparation and refining methods

of copper oxides, copper-containing alloys, and carbon-based copper catalysts were thoroughly analyzed.

Finally, a rigorous evaluation and analysis of future strategies aimed at further improving the efficiency and selectivity of electrochemical CO_2 reduction was conducted. Given the ongoing challenges in this area, three main approaches are explored: PVDC-modified CuO electrodes, microwave-assisted synthesis of CuO electrodes, and Cu-electrodeposited Cu_2O-C_3N_4 electrodes. My proposed research builds on the design and development of innovative catalysts, the optimization of preparation methods and the conduct of in-depth research in both experimental and theoretical simulations. Hydrophobic modifications and CO_2 permeability are studied to optimize proton transfer, while DFT calculations analyze key intermediate binding energies. Surface roughness is adjusted by microwave treatment and electrodeposition to increase active sites and enhance C-C coupling.

Chapter 3. Methodologies

3.1 Introduction

This chapter provides a comprehensive exploration of the experimental and theoretical approaches used to study the fabrication and modification of copper-based electrodes. The chemicals and equipment used in the experiments are described, respectively. The sample preparation procedures are described. The experimental setup and the procedural steps are then presented. The principles underlying the equipment and method used for characterization and analysis.

3.2 Chemicals

The source and specification of chemicals used were listed as follows.

Table 3.1 The chemical used in the experiments.

Chemical name	Specification	Source
Copper (II) oxide	< 50 nm	Sigma Aldrich Co. Ltd
N, N-Dimethylformamide	⩾ 99.5%	Sinopharm Chemical Reagent Co. Ltd
Acetone	⩾ 99.5%	Sinopharm Chemical Reagent Co. Ltd.
Polyvinylidene chloride	-	Macklin Inc.
Polyvinylidene fluoride (HSV900)	-	Arkema Inc.
Copper(II) nitrate trihydrate	99.0 ~ 102%	Sinopharm Chemical Reagent Co. Ltd.

Sodium carbonate	⩾ 99.8%	Sinopharm Chemical Reagent Co. Ltd.
Isopropanol	⩾ 99.7%	Sinopharm Chemical Reagent Co. Ltd.
Melamine	⩾ 99%	Sinopharm Chemical Reagent Co. Ltd.
Copper chloride dihydrate	⩾ 99.0%	Sinopharm Chemical Reagent Co. Ltd.
Sodium hydroxide	⩾ 96.0%	Aladdin Industrial Co. Ltd.
Ascorbic acid	⩾ 99.7%	Sinopharm Chemical Reagent Co. Ltd.
Potassium hydrogen carbonate	⩾ 99.5%	Sinopharm Chemical Reagent Co. Ltd.
Nafion 117 solution	~ 5% in a mixture of lower aliphatic alcohols and water	Aladdin Industrial Co. Ltd.
Dimethyl sulfoxide	⩾ 99.7%	Sinopharm Chemical Reagent Co. Ltd.
Deuterium oxide	99.9%	Sinopharm Chemical Reagent Co. Ltd.
Carbon paper (TGP-H-060)	-	Toray industries, inc.
CO_2	99.999%	Linde plc.
Ar	99.999%	Linde plc.
N_2	99.999%	Linde plc.
Air		Ningbo Nuoan Gas Ltd.

3.3 Equipment

Table 3.2 is a list of the devices used in the experiments. Devices 1-6 are primarily used to characterize the prepared electrocatalyst or electrode. Devices 7 and 8 facilitate the analysis of the gaseous and liquid products produced during the CO_2RR process. And finally, devices 10-16 were used to produce the electrocatalyst or electrode.

Table 3.2 The equipment used in the experiments.

	Equipment	**Equipment model**
1	Field emission scanning electron microscopy	ZEISS GeminiSEM 360
2	Transmission electron microscopy	JEOL JEM-200 microscope
3	X-ray diffraction	Bruker D8 Advance
4	X-ray photoelectron spectroscopy	Shimadzu Axis Supra+
5	Contact angle apparatus	SDC-350
6	Electrochemical workstation	CH Instrument Inc., CHI660e and Gamry, Reference 3000
7	Nuclear magnetic resonance spectrometer	AVANCE NEO 600
8	Gas chromatography	Agilent GC 8890
9	Gas flow meter	Sevenstar, CS200
10	Air dryer oven	Shanghai Yiheng BPG-9156

11	Tube furnace	Shanghai Optics and Fine Mechanics Instillation, SG-GL1200K
12	Heating plate	IKA plate, RCT digital
13	Electronic balance	Mettler toledo, ME104E/204E
14	High-accuracy pH meter	Mettler toledo, FE28-standard
15	Microwave reactor	UWAVE-2000
16	Air flow calibrators	Gilibrator 2-USB Calibrator

3.4 Procedure

3.4.1 Preparation of CuO-polymer electrodes

Copper oxide nanoparticles (CuO NPs) were subjected to acetone ultrasonic cleaning and then rinsed with DI water. Subsequently, the CuO was dried in an oven at 120 °C for 12 hours. 5 mg of CuO NPs were sonicated in 1 mL DMF for 25 minutes [144]. A 50 µL dispersion of the CuO material was coated on both sides of a 1 × 1 cm^2 carbon paper. Then, the coated carbon paper was dried completely at 105 °C. The prepared CuO electrode could be used for electrochemical tests. Under optimal conditions, the amount of CuO on each electrode was about 0.25 mg/cm^2.

To prepare CuO-PVDC electrodes, different volumes (5/10/20/30 µL) of a 5 mg/mL PVDC/DMF solution were dropped on each side of the previously prepared CuO electrodes (Figure 3.1). The cast electrodes were then dried on a hot plate at 80 °C for 1 hour. The polymer loading of the electrodes was adjusted to achieve the target amounts of 25, 50, 100 and 150 $µg/cm^2$, resulting in the

following electrode designations: CuO-PVDC 25, CuO-PVDC 50, CuO-PVDC 100 and CuO-PVDC 150, respectively.

As for the control group, CuO electrodes were coated with different polymers (Nafion, PTFE, PVDF) of 50 µg/cm^2. These control electrodes were labelled CuO-Nafion, CuO-PTFE and CuO-PVDF, respectively.

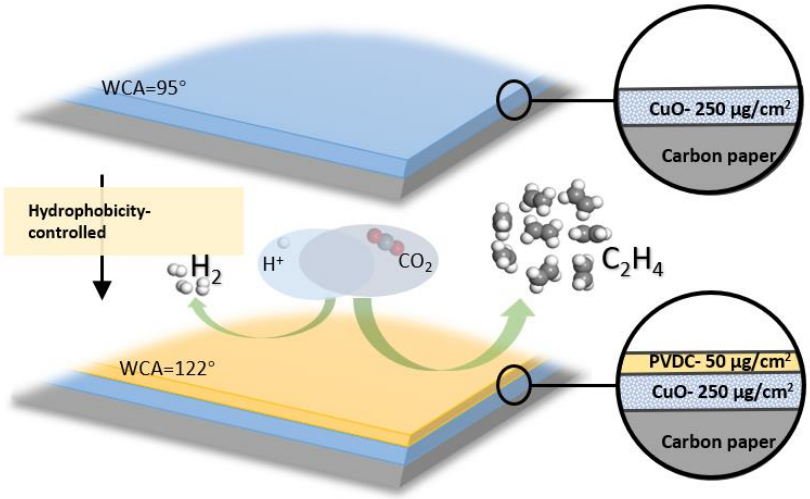

Figure 3.1 Preparation of the CuO-PVDC electrode.

3.4.2 Preparation of CuO and MW-CuO electrodes

A $Cu(NO_3)_2$ solution was first prepared to produce the MW-CuO catalyst. Hydrated copper nitrate in amounts of 0.002, 0.008, 0.016 and 0.021 mol was dissolved in 20 mL of water to prepare the $Cu(NO_3)_2$ solution. In a 100 mL round bottom flask, 15 mL of 1 M Na_2CO_3 solution was heated to 70 °C with constant stirring using a UWAVE-2000 microwave reactor. Then, the $Cu(NO_3)_2$ solution was continuously added to the flask with a peristaltic pump at about 8 mL/min while stirring at 70 °C for 10 minutes. The precipitate obtained was filtered, washed thoroughly with deionized water, dried overnight at 110 °C and then

calcined in air at 300 °C for 4 hours (Figure 3.2). The resulting powder was used for further characterization and experiments. Based on the molar ratio of Cu^{2+} and CO_3^{2-} in the reactants, the obtained copper oxide catalysts were named MW-$CuO_{0.1}$, MW-$CuO_{0.5}$, MW-$CuO_{1.1}$ and MW-$CuO_{1.4}$.

For performance comparison, another set of CuO catalysts was prepared using a similar method, using a water bath heater at the same temperature and stirring speed [186]. The resulting precipitate was washed, dried overnight at 110 °C and then calcined in air at 300 °C for 4 hours. The final CuO samples were labelled as $CuO_{0.1}$, $CuO_{0.5}$, $CuO_{1.1}$ and $CuO_{1.4}$, based on the molar ratio of Cu^{2+} and CO_3^{2-} in the reactants.

To prepare the electrode, a 10 mg CuO catalyst was sonicated in a mixture of 1.92 mL isopropanol and 80 µL Nafion solution for 20 minutes. The resulting dispersion with a volume of 200 µL was dropped onto each side (2 × 2 cm^2) of a carbon paper and dried thoroughly at 110 °C. Then, the resulting CuO electrode was cut into thin slices of 1 × 1 cm^2, with a CuO loading of about 0.25 mg/cm^2. The other electrodes were prepared using the same method, and their names corresponded to the copper oxide catalysts used.

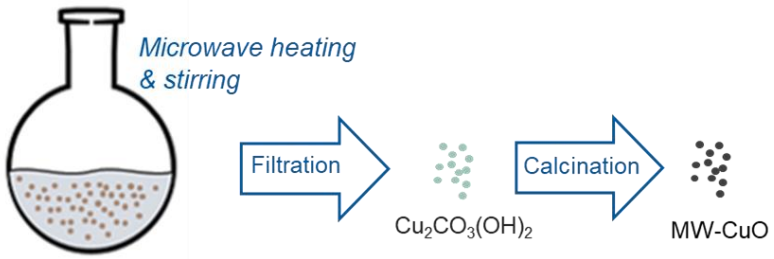

Figure 3.2 Preparation of the MW-CuO catalyst.

3.4.3 Preparation of Cu_2O-C_3N_4 and Cu@Cu_2O-C_3N_4 electrode

The C_3N_4 nanosheets were synthesized in a two-step process. First, melamine was annealed at a temperature of 550 °C for 2 hours in a semi-closed crucible. Subsequently, the resulting material was fired at 520 °C for another hour in an Ar atmosphere [187]. 60 mg of C_3N_4 was dispersed in 30 mL of deionized water (DI), and then 24 mL of $CuCl_2$ solution (0.15 M) was added. This mixture was slowly added dropwise to 36 mL NaOH solution (0.6 M) with constant stirring. Later, 50 mL of ascorbic acid solution (0.06 M) was added to the solution and stirred for 2 hours. The resulting precipitates had an orange colour and were then washed by suction filtration. Finally, the precipitates were dried overnight at 70 °C under vacuum [188, 189]. After grinding, the resulting powder is Cu_2O-C_3N_4. The Cu_2O was prepared using a similar method but without the addition of C_3N_4.

The preparation of Cu_2O-C_3N_4 electrodes starts with the dispersion of 5 mg of the Cu_2O-C_3N_4 catalyst in a solution containing 960 µL of isopropanol and 40 µL of Nafion solution. The resulting mixture is then subjected to ultrasonic treatment for 25 minutes to ensure homogeneous dispersion of the catalyst. Subsequently, 100 µL of the dispersed solution is coated onto a pristine carbon paper electrode. The coated electrode is carefully dried at a temperature of 105 °C to ensure complete evaporation of the solvents. This careful drying process leads to the preparation of the Cu_2O-C_3N_4 electrode, which can be used for subsequent experiments or testing purposes [190].

In the electrodeposition process, the Cu_2O-C_3N_4 electrode was used as the working electrode for the electrodeposition of copper on the electrode produced (Figure 3.3). At the same time, a copper foil electrode and an Ag/AgCl electrode

were used as counter and reference electrodes. The electrolyte consisted of a solution containing 0.01 M $Cu(NO_3)_2$. The electrodeposition process lasted 100 seconds while a constant current density of -2.5 mA/cm^2 was applied [191, 192]. After the deposition process, the Cu@Cu_2O-C_3N_4 electrodes were rinsed with distilled water and then used for electrochemical investigations.

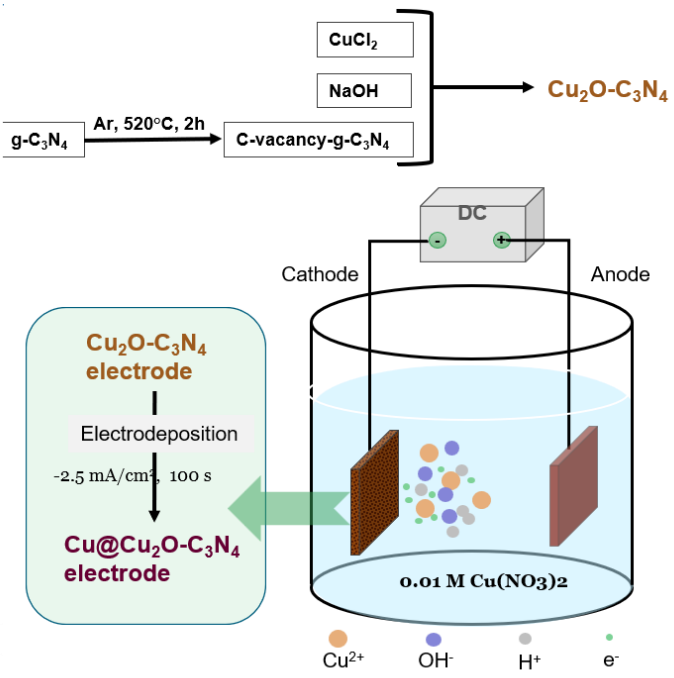

Figure 3.3 Preparation of the Cu@Cu_2O-C_3N_4 electrode.

3.4.4 Electrochemical test

The electrochemical performance test for CO_2 was performed at room temperature and ambient pressure using a conventional 50 mL H cell with a Nafion 117 proton-exchange membrane. Each compartment of the H cell contained 30 mL 0.1 M $KHCO_3$ electrolyte solution. The reference electrode was an Ag/AgCl electrode, while a 2 × 2 cm^2 platinum plate was used on the counter electrode (Figure 3.4). Before the test was performed, the catholyte was saturated

with 99.999% CO_2. Throughout the electrolysis process, a continuous flow of CO_2 was introduced into the catholyte at a rate of 30 mL/min while magnetic stirring was maintained at about 700 rpm. The CHI660e electrochemical workstation from CH Instrument Inc. and the Gamry (Reference 3000) electrochemical workstation were used for the experiment. All potentials were manually adjusted to account for ohmic loss (iRs) using Equation 3.1. After correcting for Ohmic loss, the potentials were converted to a reversible hydrogen electrode scale using Equation 3.2 [193]. After the electrode was prepared, it was subjected to an activation process at -2.4 V vs. RHE for 5 minutes in preparation for the subsequent eCO_2RR. The eCO_2RR was performed at a constant potential for 30 minutes.

$$E_{corrected} = E_{applied} - 85\%\ iR_s \qquad \text{Equation 3.1}$$

where i represents the current in the electrolysis and R_s denotes the solution resistance, which was determined to be approximately 30 Ω)

$$E_{RHE} = E_{Ag/AgCl} + 0.059 \times pH + 0.21 \qquad \text{Equation 3.2}$$

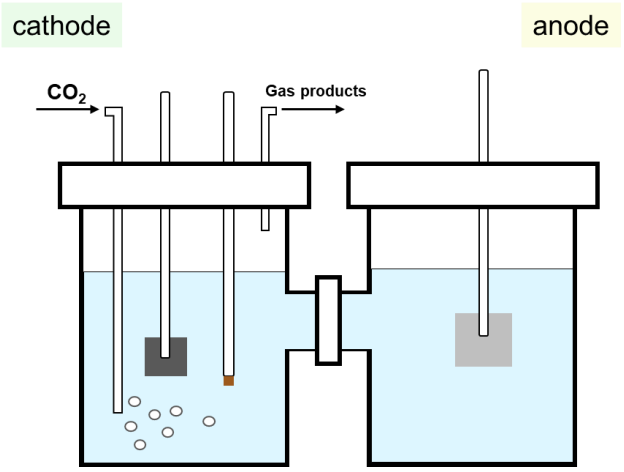

Figure 3.4 H-cell configuration.

After the reaction, gas samples were collected and transferred to a gas chromatography instrument (GC 8890, Agilent) equipped with a thermal conductivity detector (TCD) and two flame ionization detectors (FIDs). The detectors were maintained at a temperature of 275 °C for the FIDs and 250 °C for the TCD, while the oven temperature was set at 60 °C. The concentrations of the gas products were determined by comparison with calibration curves [132, 148, 194, 195].

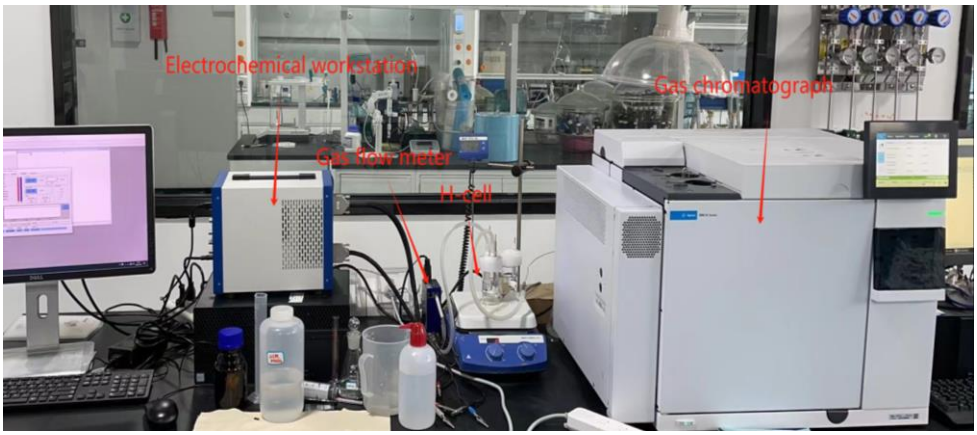

Figure 3.5 Schematic diagram of experimental set-up.

The liquid products were quantified by ^{1}H NMR (Bruker, Avance Neo 600). After 1-2 hours of electrolysis, 500 μL of the electrolyte was mixed with 50 μL DMSO/H_2O (in a volume ratio of 1/2000) and 100 μL D_2O. A presaturation method was used to suppress the water peak and obtain the ^{1}H spectrum. Quantitative analysis of the liquid carbon products was performed using the peak area of DMSO as a reference [196].

Faradaic efficiency (FE) measures the effectiveness of an electrochemical process in producing the desired product. It quantifies the ratio of the electrical charge explicitly used to produce the desired product compared to the total charge transferred during the electrochemical reaction.

$$FE = mnF/It$$ Equation 3.3

Where m is the number of moles of the desired product, n is the number of electrons required to generate per mole of the product (Table 1.1), and F is the Faradaic constant (96485 C/mole electrons). I and t are the current and time, respectively, and their product is the total charge transferred between the electrodes in an experiment.

3.4.5 ECSA measurement

The electrochemically active surface area (ECSA) values of CuO and CuO-PVDC electrodes were determined using the Cottrell equation (Equation 3.4) [197]. $K_3Fe(CN)_6$ was used as the redox probe. A CV measurement was conducted using an electrode (Ag/AgCl) at a scan rate of 10 mV/s within the voltage range of 0.5 to 0 V in Ar-saturated 5 mM $K_3Fe(CN)_6$/ 0.1 M KCl. A chronoamperometry measurement was performed for 1 s at a potential of about 0.25 V, which is more negative than the peak potential in the foregoing CV curve [153].

$$I = \frac{FA\sqrt{D}}{\sqrt{\pi t}}[A]_{bulk}$$ Equation 3.4

Where F is the Faraday constant ($F = 96485\ C/mol$), A is ECSA, D is the diffusion coefficient ($D = 4.34 \times 10^{-6}\ cm^2/s$), $[A]_{bulk}$ is the bulk concentration of $K_3Fe(CN)_6$ ($[A]_{bulk} = 5 \times 10^{-6}\ mol/ml$).

The measurement of double-layer capacitance (C_{dl}) was also used to reveal ECSA. CV curves were conducted in a non-Faradaic region at various scan rates

in CO_2-saturated 0.1 M $KHCO_3$ solution. j_{dl}, calculated to be half of the difference between the anodic and cathodic currents (j_a - j_c) against scan rate, the slope of which is identified with the capacitance of the double layer.

$C_{dl} = \Delta j/v = (j_a - j_c)/2v$ Equation 3.5

Where j_a and j_c are anodic and cathodic current densities, v is the scan rate in mV/s.

3.5 Characterization techniques

3.5.1 Field emission scanning electron microscopy (FESEM)

The Field-Emission Scanning Electron Microscope is an advanced imaging instrument that provides high-resolution analysis of surface properties and morphology in materials. Its primary purpose is to offer detailed visual information about the surface features of a sample. By scanning an electron beam over the surface and measuring the resulting signals, the FESEM generates highly magnified images with exceptional depth of field and resolution. This capability allows researchers to observe microstructural details, surface textures, and nanoscale features of the material under study [198].

The FESEM uses two primary imaging modes: secondary electron imaging and backscattered electron imaging. Secondary electron imaging provides information about the surface morphology and allows researchers to examine the topography and fine structures of the sample. This mode is beneficial for visualizing surface roughness, cracks and other surface features. On the other hand, backscattered electron imaging provides insights into the composition of

the sample and variations in atomic number [199, 200]. By detecting electrons backscattered from the sample, this mode can reveal differences in elemental composition and density within the material.

FESEM images were acquired for the study using the ZEISS GeminiSEM 360 device. FESEM analysis was performed at accelerating voltages of 10 and 15 kV, which determined the energy of the electron beam used for imaging. A careful sample preparation process was carried out to prepare the samples for the SEM images. The material to be analysed was dispersed on a double-sided adhesive, conductive carbon tape, which was then attached to a sample holder.

This deposition process was carried out using the KYKY SBC-12 sputter coater, which deposits a fine layer of gold on the sample. The gold layer acts as a conductive coating that dissipates the charge and minimises the charging effects of the beam during SEM analysis. By combining FESEM images with energy-dispersive X-ray spectroscopy (EDS), both high-resolution images and information about the elemental composition of the samples can be obtained.

3.5.2 Transmission electron microscopy (TEM)

Transmission electron microscopy is an advanced imaging technique that surpasses the capabilities of the SEM by enabling precise examination of materials at the atomic level. In TEM, an electron beam is directed through a thin sample, allowing detailed insights into the atomic arrangement and composition. TEM utilises the wave-particle duality of electrons and uses an electron gun to create a concentrated beam that is precisely focused on the sample using electromagnetic lenses. As the electrons interact with the atoms of

the sample, intricate electron diffraction patterns are created, revealing information about the crystal structure, lattice spacing and orientation of the sample [201]. After exiting the sample, the scattered electrons are further magnified and focussed before impinging on a fluorescent screen or digital detector, resulting in high-resolution images that can resolve atomic-level details. By carefully manipulating the lenses and adjusting the parameters, accurate images can be captured with the TEM (Figure 3.6) [202-204].

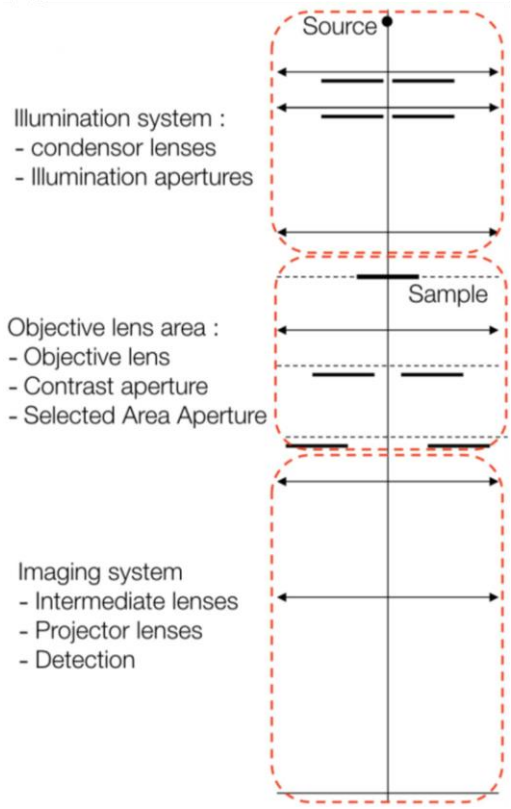

Figure 3.6 General outline of the TEM optic [204].

In this study, TEM images were taken with a JEOL JEM-200 microscope operating at an accelerating voltage of 200 kV. Prior to imaging, the sample powder was dispersed in either ethanol or methanol using ultrasound for 10 minutes. A small amount of the resulting suspension was then placed on a copper grid, which served as a substrate for TEM imaging. This method of sample

preparation ensured that the sample was well dispersed and evenly distributed on the grid, allowing accurate and representative TEM imaging.

3.5.3 X-ray diffraction (XRD)

XRD is a robust analytical method that can be used to determine the properties and crystal structure of a substance. This is achieved by analysing the diffraction pattern [205]. This technique is based on Bragg's law, which describes the constructive interference of X-rays with the distances between the crystal planes (Figure 3.7). By measuring the angles and intensities of the resulting diffraction peaks, valuable information about the crystal lattice, including the dimensions of the unit cell, crystal symmetry and impurities or defects, can be obtained. In XRD analysis, a powdered or single crystal sample is irradiated with a monochromatic X-ray beam, and a detector collects the diffracted X-rays. The resulting diffraction pattern is then analysed to determine the crystal structure and other relevant information about the material [206, 207].

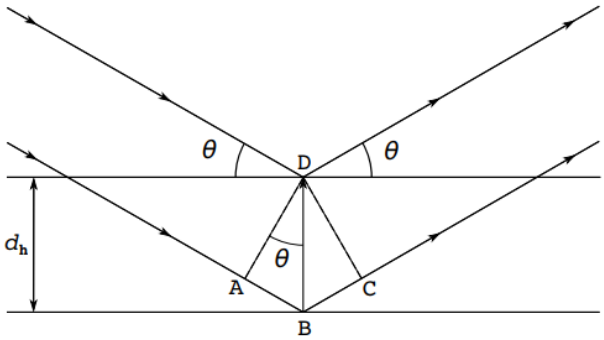

Figure 3.7 Bragg representation of X-ray diffraction by lattice planes with interplanar distance d_h [208].

XRD measurements were performed with a Bruker D8 Advance X-ray diffractometer using monochromatic Cu Kα1 radiation (λ = 1.54056 Å) at 40 kV and 40 mA. The data was collected within the 2θ range of 10−90° with a step size of 0.02°.

3.5.4 X-ray photoelectron spectroscopy (XPS)

X-ray photoelectron spectroscopy is a surface-sensitive analytical technique for determining the elemental composition and chemical state of materials by analysing the energy distribution of photoelectrons emitted from the surface of the material when irradiated with X-rays. This technique provides valuable information about the elemental composition of the elements, the chemical bonding and the oxidation state on the surface of the material. The theory behind XPS is based on the photoelectric effect, in which X-rays excite electrons in the material so that they are emitted from the surface. The kinetic energy and intensity of these emitted electrons are measured to determine their binding energies and relative concentrations, allowing the identification of characteristic peaks corresponding to different elements and chemical states. In XPS analysis, the sample is placed in a vacuum chamber, X-rays of known energy are directed at the surface, and the emitted photoelectrons are collected using an electron energy analyser. The resulting XPS spectrum provides information about the elemental composition and chemical environment of the material surface [209, 210].

In the XPS analysis described, a Shimadzu Axis Supra+ system was used. The system employed a focused, monochromatic Al Kα X-ray source with an energy

of 1486.6 eV for sample excitation. To calibrate the XPS data, the binding energy of the C 1s peak was fixed at 284.6 eV as an internal reference. The experimental curves, including the XPS spectra and other relevant data, were generated using CasaXPS software. It provides various tools and algorithms to analyze the XPS spectra, quantify elemental composition, and determine chemical states.

3.5.5 Contact angle apparatus

The contact angle apparatus serves as a crucial scientific instrument for measuring the contact angle between a liquid droplet and a solid surface, offering insights into the wettability and surface characteristics of the material. Its primary function involves precise measurement of the contact angle at the three-phase interface, where the liquid, solid, and gas phases meet [211]. This enables researchers to analyze and quantify the wetting behaviour of liquids on solid surfaces. The apparatus typically includes a sample stage, a liquid dispenser, an imaging system (such as a high-resolution camera), and image analysis software (Figure 3.8) [212].

The theoretical basis is based on the equilibrium of the interfacial forces at the three-phase contact line, whereby the Young-Laplace equation (Equation 3.6) is usually used to describe the relationship between the contact angle, the interfacial tensions and the curvature of the liquid droplet. The contact angle, which is influenced by surface tension factors, reflects information about the surface energy, roughness and chemistry of the solid material. A high contact angle indicates poor wettability and, therefore, limited spreading of the liquid,

while a low contact angle indicates good wettability and easy spreading of the liquid on the surface [213, 214].

$\Delta p = -\gamma \nabla \cdot \hat{n}$ Equation 3.6

Where Δp is the pressure difference across the fluid interface, γ is the surface tension, $\hat{n}$ is the unit normal pointing out of the surface.

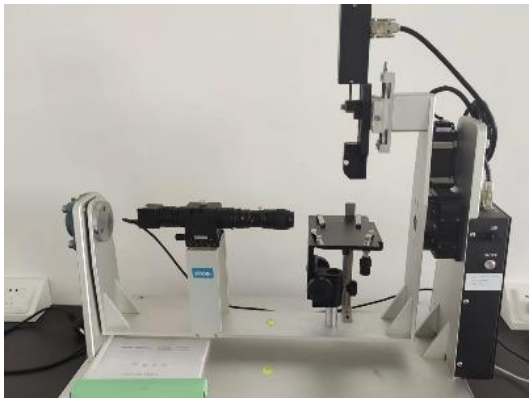

Figure 3.8 Image of the contact angle apparatus.

3.5.6 Electrochemical workstation

The electrochemical workstation, a central tool in electrochemical research, investigates the behaviour of materials during various electrochemical processes. It works by precisely measuring and regulating electrical parameters during experiments. Equipped with multiple channels for potential, current and impedance control, this workstation enables various techniques such as cyclic voltammetry, chronoamperometry, impedance spectroscopy and potentiostatic/galvanostatic measurements. It has its roots in electrochemistry and explores the synergy between electricity and chemical reactions [215-217].

In this study, chronoamperometry and chronopotentiometry were used to analyse the performance of the CO_2RR. Impedance spectroscopy was also used to measure the impedance of the electrochemical system at different frequencies to gain insight into electrical properties such as conductivity, capacitance and the kinetic behaviour of the electrochemical reactions. Cyclic voltammetry was used to investigate the electrochemical activity of the electrode material, the charge transfer processes and the reaction kinetics. By applying different scan rates and measuring the resulting current response, CV allowed the ECSA of the electrode to be determined. In contrast, linear sweep voltammetry is commonly used to measure the limiting current density and potential windows, focussing on the measurement of the kinetic parameters and electrochemical activity of the electrode reaction. Overall, these techniques contribute to a comprehensive understanding of electrochemical systems and help to optimise them.

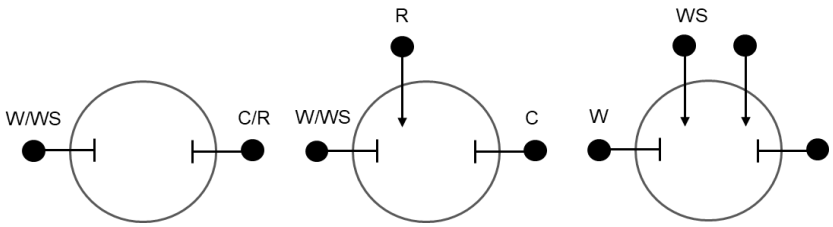

Figure 3.9 Wiring diagram of two -, three - and four-electrode systems.

3.5.7 Gas chromatography (GC)

Gas chromatography is an analytical technique that separates, identifies and quantifies volatile compounds in a sample mixture by utilising the principles of partitioning and selective adsorption. A typical GC system consists of a sample injector, a separation column, a detector and a data acquisition system [218]. The sample is vaporised and introduced into the separation column, which contains

a stationary phase. The mobile phase, usually an inert gas, transports the sample through the column. During this process, various compounds interact with the stationary phase due to their affinity and volatility, leading to their separation. The time it takes for each compound to pass through the column is called the retention time. The detector measures the concentration of each compound as it elutes from the column and produces a chromatogram [219, 220].

In this work, the gas chromatograph system is enhanced with specific detectors to enable comprehensive compound analysis. The configuration includes one methane reformer, two FIDs, and one TCD (Figure 3.10). TCD operates based on the principle of thermal conductivity differences among compounds during sample separation. In this setup, the TCD is specifically used to detect and quantify hydrogen. On the other hand, the FID functions by utilizing the ion flow generated by the combustion of compounds in a flame during sample separation. The FID can detect and quantify several compounds, including carbon monoxide, methane, ethylene, and ethane.

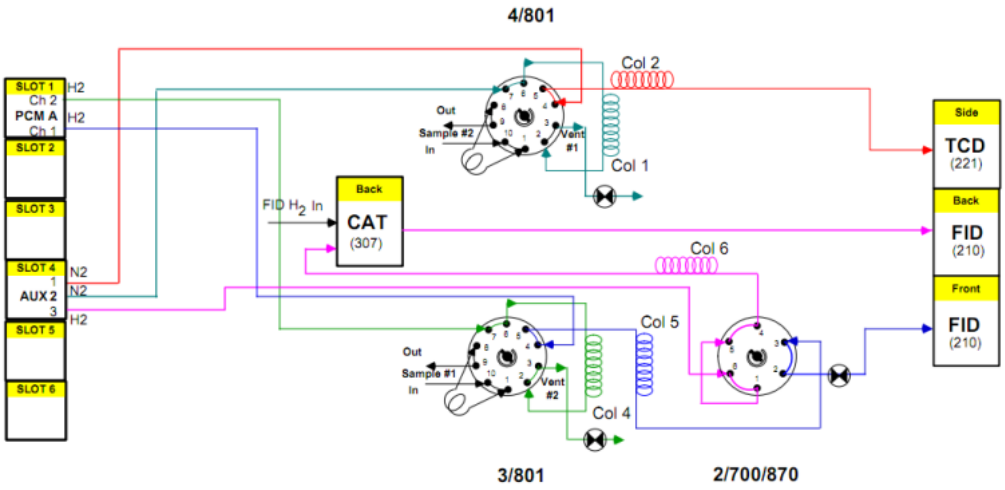

Figure 3.10 Diagram of gas chromatographic configuration used in the experiment.

3.5.8 Nuclear magnetic resonance spectrometer (NMR)

^{1}H-NMR spectroscopy is an analytical technique that utilizes the magnetic properties of hydrogen nuclei to determine the structure and identify organic compounds. The protons absorb and emit energy in the form of electromagnetic radiation by subjecting the hydrogen nuclei to a strong magnetic field and applying a radiofrequency pulse. This emitted radiation is analyzed to provide valuable information about the chemical environment and connectivity of hydrogen atoms in a molecule. The concept of chemical shift reveals the displacement of resonance frequencies due to different chemical environments, while coupling refers to the splitting of NMR signals caused by interactions between neighbouring protons. These principles allow researchers to obtain data on the number of distinct proton environments, their relative positions, and their interactions with neighbouring atoms.

In the electrochemical reduction of CO_2, NMR hydrogen spectroscopy was employed to determine the content of liquid phase products, including formic acid, ethanol, propanol, and other similar compounds. This analytical technique involves analyzing the behaviour of hydrogen atoms in the electrolyte after the reaction. By comparing these signals with those of an internal standard, it becomes possible to quantify the concentration of the liquid phase products.

3.6 Computational method

3.6.1 Density Functional Theory (DFT)

DFT calculations play an essential role in CO_2RR and offer valuable applications and insights. DFT enables structure determination and detection of intermediates, as well as prediction and optimisation of reaction pathways and transition state structures. It facilitates the study of reaction kinetics, including rate constants, activation energies and reactive sites. In addition, DFT helps characterise catalysts by revealing structural, surface adsorption and electronic properties. It helps in the development and improvement of catalysts by evaluating the adsorption energy of the catalyst, the structures of the transition states and the reaction barriers.

In addition, DFT takes solvent effects into account and predicts their influence on reaction rates, selectivity and catalyst activity [158, 176, 221, 222]. The application and importance of DFT calculations in CO_2 electrocatalysis lies in their ability to provide theoretical insights, optimise catalyst performance, and predict experimental results. By integrating experiments and calculations, DFT accelerates the development of CO_2 electrocatalysis and advances research in the field of sustainable energy and carbon reduction.

All calculations in this work were carried out using the Vienna ab initio Simulation Package. The projector-extended wave method was used to describe the core-valence interactions, and the cut-off energy for the plane–wave basis set was 500 eV. The Brillouin zone was sampled using the Monkhorst-Pack scheme with a grid of 3 × 3 × 1 k points. The Cu(111) surface plates were constructed from three layers, with the lower layers fixed and the two upper

layers relaxed, with vacuum layers of at least 15 Å. Only two polymer monomers (PVDC, PVDF and PTFE) were placed over the Cu layers (Figure 3.11). After optimisation, the key intermediates *H, *OCHO and *COOH were placed in three positions above the polymer and the adsorption energy was calculated and recorded.

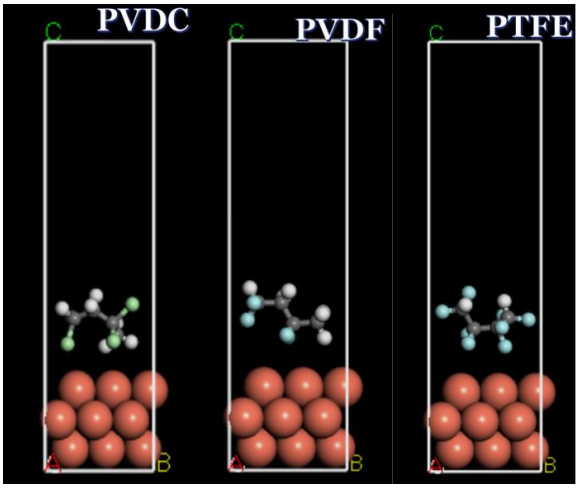

Figure 3.11 Optimized polymer on Cu layers. The corresponding atom to the colour: Red-O, Grey-C, White-H, Blue-F, Green-Cl, Orange-Cu).

Chapter 4. Hydrophobic polymer coated on CuO electrode for improved ethylene production

4.1 Introduction

Renewable energy-driven electrochemical CO_2 reduction is a sustainable approach for CO_2 emission mitigation [223, 224]. Although the current technology is challenging to apply on a large scale, the conversion of CO_2 into value-added products such as CO, HCOOH, CH_4 and C_{2+} products is of great potential, which improves the economics of the process. Ethylene, a lower-carbon product with higher commercial value that could be directly used as a building block in the chemical industry, has become a hot research topic [159, 225]. However, the development of catalysts with high activity and selectivity for the electrochemical production of C_2H_4 remains a challenge due to the complex reaction pathways involved in the eCO_2RR [95, 106, 190].

In recent studies on the electrocatalytic reduction of CO_2 to C_2H_4, some remarkable results have been obtained using copper-based catalysts with different crystal planes, sizes, structures and roughness [226-229]. The CuO-derived Cu electrode showed better performance in CO_2RR to ethylene than a pure Cu electrode. After the lattice oxygen was rapidly removed in the initial phase, the resulting coordination-low, defect-rich and oxygen-rich subsurface sites were able to optimise C-C coupling [230]. When CuO was used as an electrocatalyst, the Faradaic efficiency of ethylene could reach 29.7% at about -1.6 V vs. RHE in 0.2 M $KHCO_3$ electrolyte. Although the C_2H_4 partial current was significantly increased, the inhibition of the hydrogen evolution reaction (FE_{H2} = ~ 50%) remained a challenge [142].

In the conversion of CO_2 to ethylene, protons play a crucial role in the balance of electrons and, thus, in the most critical side reaction, the hydrogen evolution reaction [140]. Research into strategies to reduce HER is necessary. Recently, some studies have paid special attention to the regulation of the microenvironment in Cu-based CO_2RR [231-234]. Modification of polymers is one of the simple and universal methods to suppress hydrogen formation and increase the yield of the target product. Previous modifications with Nafion and PTFE on Cu or CuO electrodes show satisfactory effects in preventing water diffusion (FE_{H2} > 27%) and facilitating CO, CH_4 or HCOOH production but no obvious improvement in ethylene production [235-238].

Coating a CuO electrode with polyvinylidene fluoride increased the local pH on the surface and created a hydrophobic environment, successfully improving the Faraday efficiency of ethylene to 40.6% and suppressing FE_{H2} to about 29%. Nevertheless, the electrical conductivity of the PVDF-modified electrodes was partially sacrificed. The overall energy conversion efficiency was limited, with a total current density of about 15 mA/cm^2 at a relatively high potential of -1.22 V vs. RHE in a 0.5 M $KHCO_3$ electrolyte [144]. Polymer modification holds considerable untapped potential. So far, there have been several applications of PVDC in electrochemical fields to produce activated carbon for high-performance EDLCs or electrolytes for rechargeable batteries, but the possibilities in CO_2RR still need to be explored [239-242].

This study aimed to improve the catalytic activity and selectivity of CuO electrodes for the production of the target product C_2H_4. PVDC was used to form a hydrophobic layer over the CuO electrodes by physical sedimentation. The hydrophobic property of the electrodes was regulated by controlling the amount

of polymer applied. The influence of polymer coating on proton transfer and eCO_2RR was studied with the selectivity and catalytic efficiency.

4.2 Results and discussion

4.2.1 Surface properties of PVDC-modified CuO electrode

The CuO-PVDC electrodes were prepared by drop-casting a PVDC dispersion in DMF onto the CuO electrode. The transmission electron microscopy image shows that the CuO nanoparticles have a cylindrical structure with a length of 100 to 200 nm and a cross-sectional diameter of about 50 nm (see Figure 4.2a), which corresponds to the particles on the bare CuO electrode (Figure 4.1a). The drying process at a high temperature of 105 °C led to a significant agglomeration dispersion of the CuO nanoparticles. This agglomeration led to a partial exposure of the carbon fibres, as shown in Figure 4.1a, e.

Figure 4.1b-d shows that a film is present covering both the CuO particles and the underlying carbon paper. This film acts as a binder and effectively binds the CuO nanoparticles to the carbon paper substrate. For the Cl element referred to in the EDS mapping (Figure 4.1e), this film is the well-distributed hydrophobic polymer PVDC. Moreover, as the loading of PVDC on the CuO electrode increases, the amount of exposed CuO nanoparticles on the surface of the top layer decreases significantly. When the PVDC coating amount reaches 150 $\mu g/cm^2$, a considerable number of catalyst particles are buried under the polymer layer.

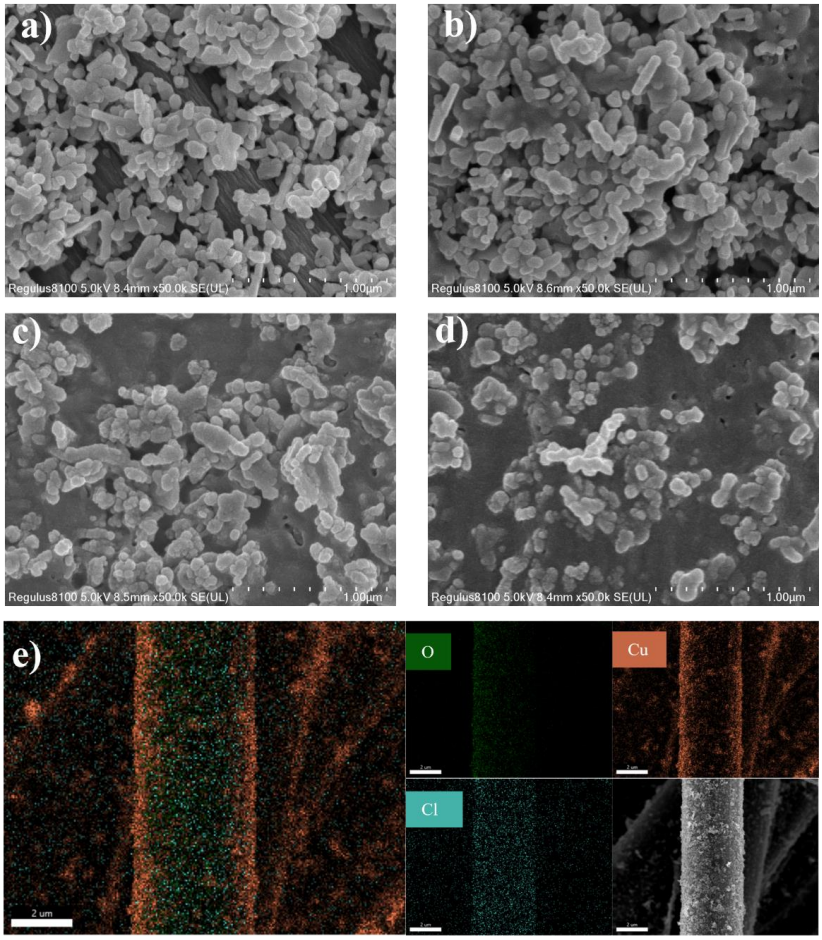

Figure 4.1 SEM images of a) CuO electrode; b) CuO-PVDC 50 electrode; c) CuO-PVDC 100 electrode; d) CuO-PVDC 150 electrode; e) the elemental mapping of CuO-PVDC 100 electrode coating.

The HRTEM image shows enlarged lattice fringes with an interplanar spacing of 0.243 nm, which corresponds to the (111) planes of monoclinic CuO (Figure 4.2b). The crystal phase of the CuO powder was also confirmed by the wide-angle X-ray diffraction, with broad peaks at 35.5 °, 38.7 ° and 48.7 ° corresponding to (002), (111) and (-202) of tenorite CuO (JCPDS#45-0937), respectively (Figure 4.2c). Figure 4.2d shows the XRD patterns of the freshly fabricated electrodes. Due to the small loading amount, the peak of PVDC on the CuO-PVDC electrode is relatively weak, which can be seen by the peak at

42°. The high-intensity peak at 54.5° can be attributed to the carbon paper substrate, respectively[243]. In comparison, distinct peaks at 35.5° and 38.8° appear in the CuO and CuO-PVDC electrodes, which are characteristic of CuO. This is consistent with the observations from the XRD results of the CuO powder and indicates that CuO was successfully deposited on the carbon paper, and the oxidation state of the copper remains unchanged before and after physical vapour deposition and PVDC coating.

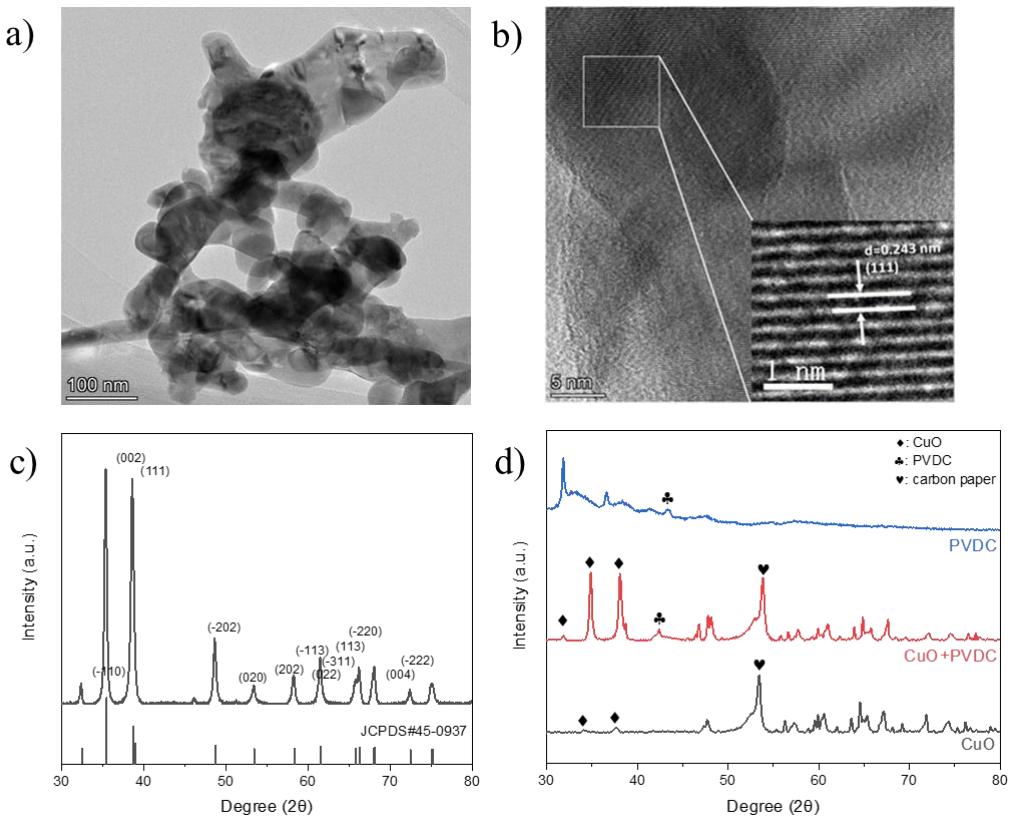

Figure 4.2 a) TEM image of CuO after cleaning, b) HRTEM image with measured lattice distance. c) XRD patterns of CuO powder and d) CuO electrodes with and without PVDC coating.

4.2.2 Electrochemical CO_2RR of PVDC-modified electrodes

To investigate the influence of hydrophobicity on the electrochemical conversion of CO_2 to ethylene, we performed CO_2RR experiments with bare CuO electrodes and CuO electrodes coated with PVDC. The experiments were performed in a CO_2-saturated 0.1 M $KHCO_3$ electrolyte at a fixed potential of -1.19 V vs. RHE (with 85% iR-corrected). Without any polymer modification, the bare CuO electrode exhibited an FE of about 30.9% for C_2H_4 production and ~ 31.8% for H_2 evolution. When the CuO electrodes were coated with various amounts of PVDC, all FE values for H_2 decreased by more than 5%. At the same time, the FE for ethylene production increased by at least 4.5% (Figure 4.3). The change in selectivity showed that the addition of PVDC as a modifier agent significantly weakened the hydrogen evolution reaction and promoted the selective formation of ethylene during the CO_2 reduction process.

The performance of the electrodes varied slightly depending on the amount of PVDC coating. The CuO electrode achieved optimum performance with a PVDC coating of only 50 µg/cm^2. By applying this coating, hydrogen evolution was significantly suppressed, and the FE was reduced from 31.8% to 22.8%. At the same time, the FE_{C2H4} increased from 30.9% to 37.8%, indicating improved ethylene production. Interestingly, when the PVDC coating amount was further increased, there was no clear positive correlation with product selectivity. Instead, it was observed that the inhibitory effect on hydrogen evolution and the promotion of ethylene production were most pronounced when only a tiny amount of PVDC was applied to the electrode. In contrast, excessive loading of PVDC had a suppressive effect on the CO_2 reduction process, indicating an optimal PVDC concentration to achieve the desired performance enhancement.

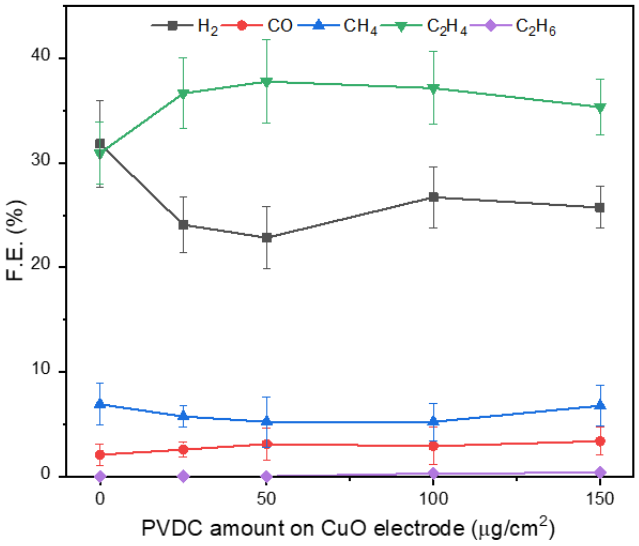

Figure 4.3 Faradaic efficiencies for C_2H_6, C_2H_4, CH_4, CO and H_2 for bare CuO electrode and CuO electrode with various PVDC coating amounts obtained at the fixed potential of -1.19 V vs. RHE in CO_2-saturated 0.1 M $KHCO_3$ solution.

To investigate the influence of the interfacial difference on product selectivity, we performed CO_2 reduction experiments on bare CuO electrodes and CuO electrodes coated with 50 μg/cm^2 PVDC. The experiments were performed at working potentials from -0.89 V to -1.29 V vs. RHE. The bare CuO electrodes showed fluctuating FE of H_2 between 24.8% and 31.8%, with FE_{C2H4} around 30%. Over the entire working potential range, more than 61% of the charges were used to generate gaseous products (Figure 4.4a). After PVDC modification with a dose of 50 μg/cm^2, CO and CH_4 production (FE_{CO+CH4} < 10%) was similar to that observed at the CuO electrode. However, the HER were significantly suppressed, with an FE of only 22.8%, lower than the minimum FE observed with the unmodified CuO electrode at all working potentials.

In addition, the formation of C_2H_4 was significantly increased on the CuO-PVDC electrode, with FEs between 4.7% and 9.3% higher compared to the CuO electrode at the same potential. The observed variations in Faraday efficiency emphasize the sensitivity of the reaction to the properties of the electrode surface. Remarkably, the CuO-PVDC electrode achieved a FE_{C2H4} of 41.4% and a high partial current density for ethylene production of ~6.8 mA/cm^2 at a potential of -0.89 V vs. RHE, surpassing the FE_{C2H4} of the CuO electrode (32.2%). The observed high yield is remarkable and is among the highest reported yields in electrocatalytic CO_2 to C_2H_4 conversion using CuO-derived catalysts (Figure 4.4b and Table 4.1).

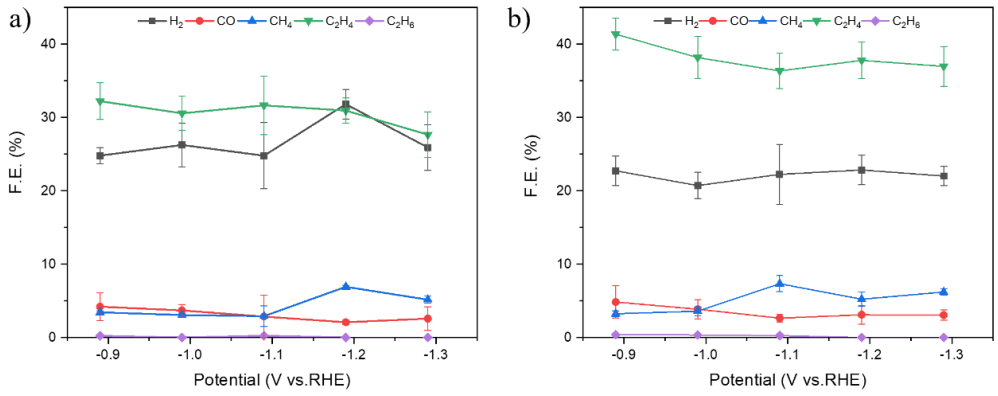

Figure 4.4 The product distribution of a) bare CuO electrode and b) CuO electrode with 50 µg/cm^2 PVDC coating under different working potentials in CO_2-saturated 0.1 M $KHCO_3$ electrolyte (with 85% iR-corrected).

Table 4.1 Comparison of optimized C_2H_4 production using various Cu-based catalysts in H cells.

Electrode	FE_{C2H4}	FE_{H2}	E (V vs. RHE)	$\|j\|_{C2H4}$ (mA/cm^2_{geo})	Electrolyte	Ref.
PVDC modified CuO	41.4%	22.7%	-0.9	6.8	0.1 M $KHCO_3$	This work
Oxide-derived Cu	20%	29.0%	-1.0	2.0	0.5 M $KHCO_3$	[244]
CuO-derived catalyst	29.7%	50.0%	-1.6	~35.6	0.2 M $KHCO_3$	[89]
Mesoporous CuO	33.6%	33.0%	-1.0	~4.2	1.0 M KI	[142]
PVDF modified CuO	40.6%	28.5%	-1.2	~6.1	0.5 M $KHCO_3$	[144]
Cu-on-Cu_3N	39.0%	29.0%	-1.0	~8.5	0.1 M $KHCO_3$	[245]
Copper mesocrystals	27.2%	50.0%	-1.0	~6.8	0.1 M $KHCO_3$	[246]
Prism-shaped Cu	27.8%	32.0%	-1.2	11.8	0.1 M $KHCO_3$	[247]
Copper nanoparticle ensembles	33.2%	34.0%	-0.9	~6.8	0.1 M $KHCO_3$	[248]
Agglomerated Cu Nanocrystals	35.8%	26.4%	-1.0	7.1	0.1 M $KHCO_3$	[177]
Cu_2O films (0.9µm)	40.3%	28.6%	-1.0	10.1	0.1 M $KHCO_3$	[140]
Cu foil	26.0%	22.6%	-1.1	1.5	0.1 M $KHCO_3$	[126]
Cu_2O-derived Cu NP	33.5%	31.0%	-1.1	~12.1	0.1 M $KHCO_3$	[143]
Electrodeposited Cu_2O	25.0%	60.0%	-1.2	~2.3	0.5 M $KHCO_3$	[249]
Anodised copper	38.1%	36.6%	-1.1	7.3	0.1 M $KHCO_3$	[132]
Electroredeposited copper	38.0%	~2.0%	-1.2	22	0.1 M $KHCO_3$	[133]

The influence of polymer coating on ethylene production is considerable. To further investigate the effects of different polymers on the electrochemical

performance of CuO electrodes, a series of comparative tests were carried out with alternative hydrophobic materials, including polytetrafluoroethylene, polyvinylidene fluoride and Nafion. Without the CuO coating, ethylene could not be formed on the bare carbon paper, and more than half of the electrons were involved in the hydrogen evolution reaction (Figure 4.5a). PVDC coating on carbon paper led to a sharp decrease in the Faraday efficiency of CO and CH_4 products, while the FE of H_2 only decreased by 3.5%. A similar change in the selectivity of the products was observed for PVDF and Nafion coatings. It should be noted that the PTFE coating was effective in suppressing hydrogen evolution. However, more charges were consumed to produce CO. Polymer on carbon paper shows no positive catalytic effect on the reduction of CO_2 to ethylene and the suppression of hydrogen evolution.

Nevertheless, a significant shift occurred after the application of polymers to CuO electrodes, leading to improved performance in eCO_2RR. A comparison of Faradaic efficiency at the same potential showed that the polymer-modified electrodes slightly inhibited hydrogen evolution and exhibited an increased ethylene yield (Figure 4.5b). The extent of this increase varied with the different polymers. In particular, CuO electrodes modified with PVDC and Nafion showed a significant increase, improving the ethylene yield from 32.2% to 41.4% and 37.7%, respectively. PVDC continues to be a highly sought-after hydrophobic material, demonstrating its effectiveness.

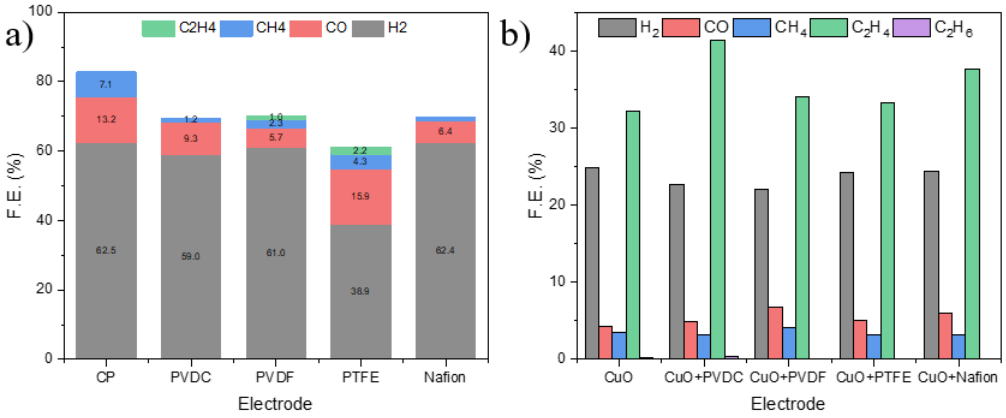

Figure 4.5 Product distribution for a) carbon paper with and without polymer layer (polymer coating amount = ~ 150 µg/cm^2; b) bare CuO electrode and CuO electrode with various polymer coating (coating amount = ~ 50 µg/cm^2) obtained at the fixed potential of -0.89 V vs. RHE in CO_2-saturated 0.1 M $KHCO_3$ solution.

In addition, the effect of PVDC was further tested by changing the coating order by first applying PVDC on carbon paper and then the CuO layer or by dispersing both PVDC and CuO in DMF solution and dripping this mixture on carbon paper. According to the CO_2RR test, the result shows that the coating sequence is also decisive for product distribution. When PVDC and CuO were applied simultaneously on the carbon paper, the catalytic performance of CuO was affected by higher hydrogen evolution (FE = 48.7%) and lower ethylene production (FE = 14.3%). Only when the PVDC layer covered the CuO catalysts, the electrocatalytic performance of the CuO electrode was improved (Figure 4.6). These results prove that the copper species always play the most important role in this electrocatalytic reduction process, and the polymer coating has a synergistic effect on the reaction pathway.

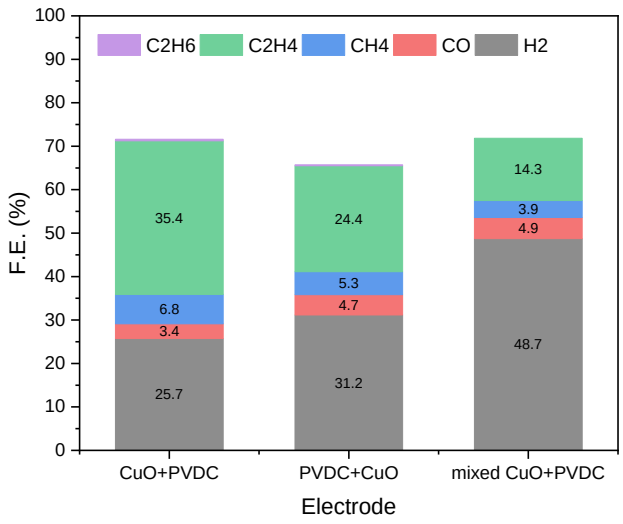

Figure 4.6 CuO electrodes with PVDC layer prepared in different drop-casting order (polymer coating amount = 150 μg/cm^2).

Evolution of electrode species during the CO_2RR

SEM images before and after the 6-hour electrocatalytic reaction could be used to identify the morphological changes on the surface of the electrode (Figure 4.7c-f). When comparing the fresh and spent CuO electrodes, the morphology of the particles changed from a short rod-like shape to spherical particles. For the CuO-PVDC electrode, there is also a similar change in morphology, indicating that the PVDC layer has no obvious effect on protecting the CuO from this type of change during a 6-hour reaction. The atoms with low coordination on the surface quickly transformed into nanoparticles during the stability test, making it difficult to maintain the structure and activity over a long period. As a result, the current density of the stability test decreased [141].

Remarkably, more spherical particles were found on the PVDC-coated electrodes after the reaction than on the bare CuO electrodes, and the decrease

of $|j|_{C2H4}$ on the CuO-PVDC electrode was much better than that of CuO, with $|j|_{C2H4}$ constantly fluctuating from 6.8 to 5 mA/cm^2 on the CuO-PVDC electrode and from 5.8 to 3.2 mA/cm^2 on the CuO electrode (Figure 4.7a-b), which proves that PVDC can act as a binder for the electrocatalysts. In general, four main mechanisms can lead to stability degradation: catalyst poisoning, catalyst delamination, loss of hydrophobicity, and salt/carbonate formation and deposition [59]. The PVDC coating could slow down the decrease in activity by protecting the catalyst and maintaining hydrophobicity.

To verify the evolution of surface copper oxide on the electrodes before and after the 6-hour reaction, we dispersed the particles on the reacted electrode surface in ethanol and prepared samples for HRTEM analysis (Figure 4.8). Large amounts of spherical particles with diameters ranging from 3-10 nm and irregular particles with diameters ranging from 30-100 nm were observed on both the CuO and CuO-PVDC electrodes after the reaction. The lattice spacing of the small particles corresponds to the (111), (200), and (220) crystal planes of copper (Figure 4.8b, e). Similar lattice spacing to Cu_2O and CuO was observed on larger particles (Figure 4.8c, f), requiring further characterization tests to determine the reduction process of CuO.

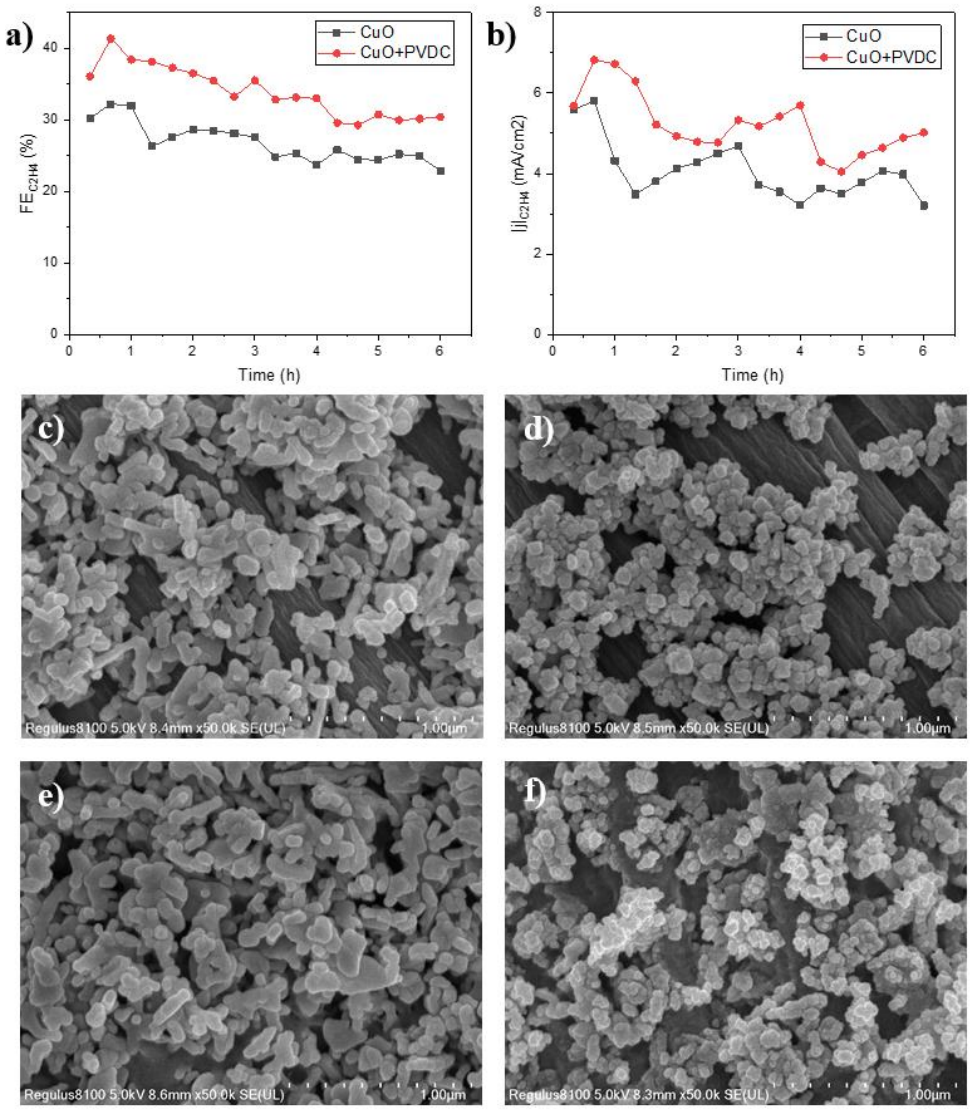

Figure 4.7 a) FE_{C2H4} and b) $|j|_{C2H4}$ of bare CuO and CuO electrodes with 50 µg/cm^2 PVDC coating under long-term operations (two 3h reactions). SEM images of bare CuO electrode c) before CO_2RR and d) after the 6-hour test; SEM images of CuO-PVDC e) before CO_2RR and f) after the 6-hour test.

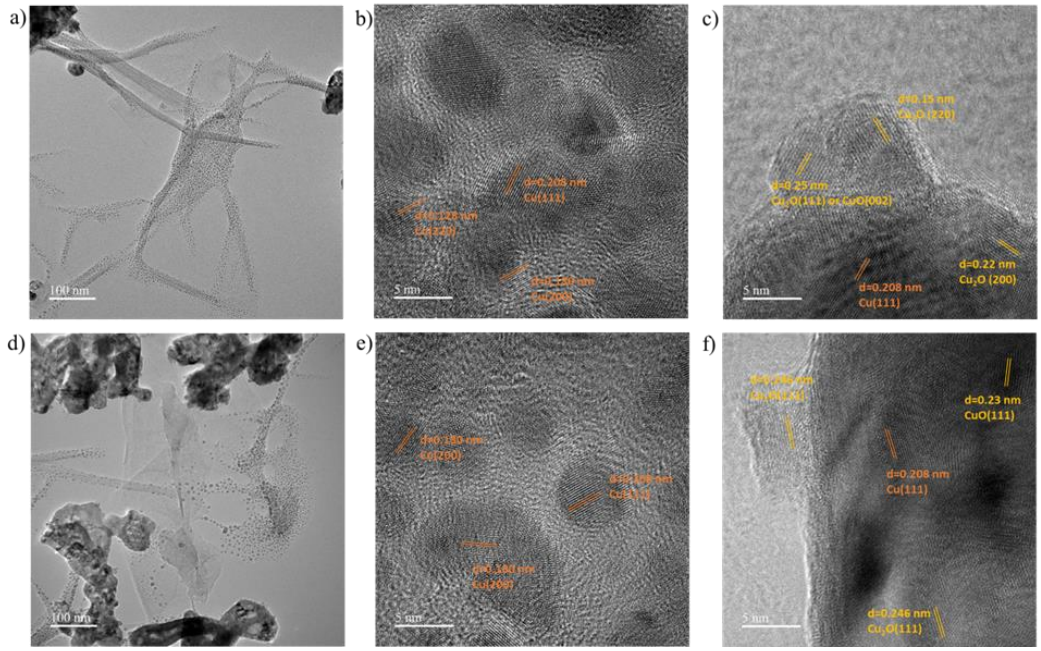

Figure 4.8 HRTEM image with measured lattice distance of the particles on the a-c) CuO electrode; d-f) CuO-PVDC electrode after 6-hour reaction at -0.89 V. After the reaction, the electrodes were immersed in ethanol and ultrasonic treated for a few minutes and then the dispersed solution was prepared for the test.

In addition, XPS analysis was used to analyse the oxidation state of copper on the electrodes before and after a short-term and long-term reaction. The presence of Cu(II) on the freshly prepared CuO and CuO-PVDC electrodes was confirmed by the prominent peak at 933.9 eV. A shift of the peak to 932.8 eV was observed in the Cu 2p spectra after both the 30-minute and 6-hour reactions, indicating the presence of Cu(I) (Figure 4.9a). This phenomenon was further supported by the shift observed in the Cu-LMM spectra (Figure 4.9b). This transition in oxidation state, from Cu^{2+} to Cu^{+}, likely occurred within the first thirty minutes of the reaction, with no further reduction of Cu^{+} to Cu^{0} observed during the six-hour

reaction period. Furthermore, the Cl 2p spectra for CuO-PVDC before and after long-term electrolysis show no peak shift, which is consistent with the SEM results. This indicates that the PVDC coating is stable and would not be easily reduced or fallen off during this reaction (Figure 4.9c).

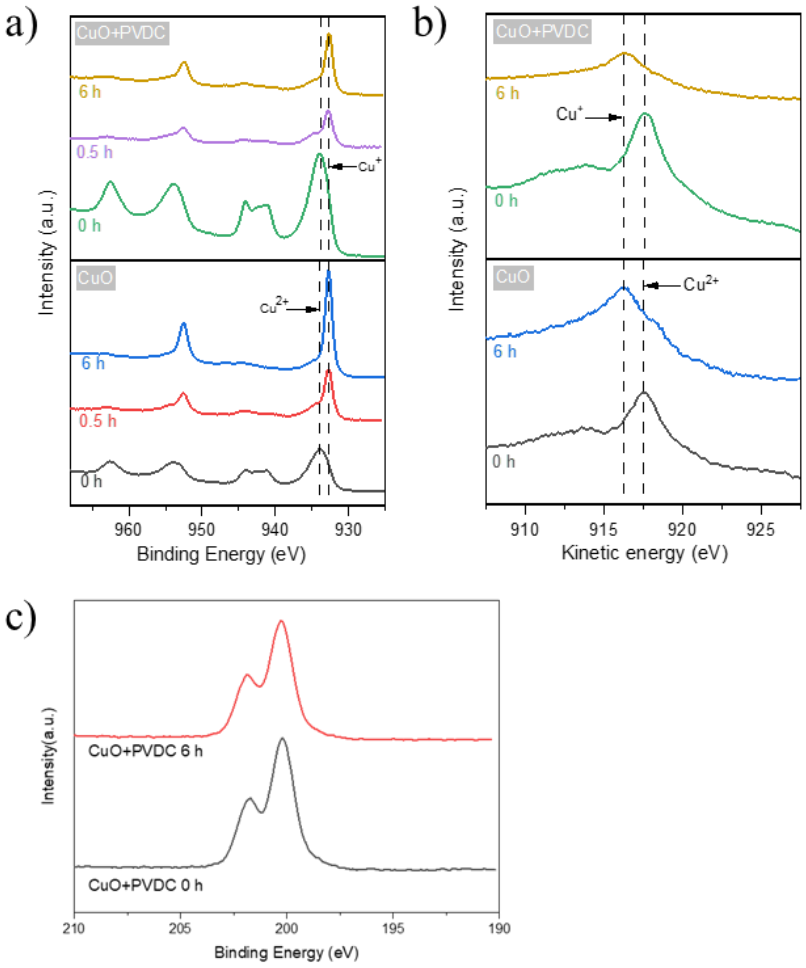

Figure 4.9 High-solution XPS a) Cu 2p; b) Cu LMM; c) Cl 2p.

XRD analysis was used to further confirm the changes in Cu oxidation states during the electrocatalytic process. To mitigate the interference from the carbon paper, the CuO electrode was loaded with twice the amount of CuO and PVDC. Figure 4.10 shows the presence of CuO on the electrode before the reaction. Significant changes in the peak patterns were observed after both the short-term

and long-term reactions. The peaks observed at 43.3° and 50.4° can be attributed to the (111) and (200) crystal phases of copper (JCPDS: 04-0836), respectively. In addition, the peak at 36.4° corresponds to the (111) crystal plane of Cu_2O, suggesting that CuO may have undergone reduction, resulting in a mixture of Cu_2O and Cu, which is not consistent with the results of the XPS analysis. This discrepancy could be due to the limited detection depth of XPS, which is typically less than 10 nm.

Studies on the surface phase of Cu material indicate the coexistence of cathodic reduction and anodic re-oxidation, leading to a dynamic equilibrium due to strong oxidizing species in the electrolyte. The most active species is expected to be metallic Cu, along with some stable Cu^+ species [250, 251]. The relative ratios of Cu^{2+}, Cu^+, and Cu^0 can be estimated based on the peak intensity corresponding to the respective (111) planes (Table 4.2). Interestingly, the Cu^+ amount on the CuO-PVDC electrode is approximately three times higher than that on the unmodified electrode. The observed higher Cu^+ content can be attributed to PVDC's ability to prevent the detachment of active species or regulate the reduction state of copper oxide. This favourable influence may contribute to the enhanced C-C coupling processes, leading to an increased ethylene yield.

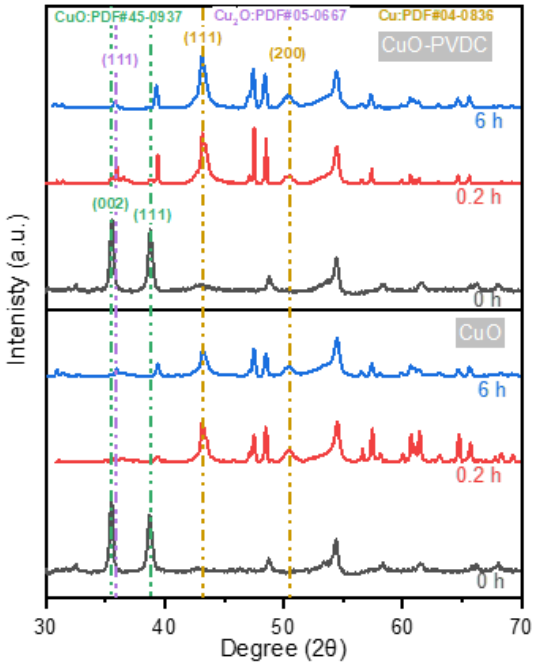

Figure 4.10 XRD patterns of CuO and CuO-PVDC electrodes before and after CO_2RR at -0.89 V vs. RHE.

Table 4.2 Integral area of (111) facet according to XRD patterns.

	CuO	**CuO-PVDC**
Integral area of （111）facet of Cu_2O	27.5	64.3
Integral area of （111）facet of Cu	290.1	244.7
Integral area of （111）facet of CuO	22.4	46.0
The integral area ratio of (111) of Cu /(111) of Cu_2O	10.5	3.8

4.2.3 The influence of coating on electron and proton transfer

The influence of the PVDC coatings on the selectivity of the carbonaceous products was as expected, while the electrical conductivity and porosity of the electrodes were decisive factors for the practical application. It is essential to determine whether hydrophobic materials affect the electrocatalytic properties

and to understand their effects on product distribution. In this context, the effect of PVDC on the electrochemical behaviour was investigated by recording the LSV at the electrodes. The measurements were performed under working conditions and covered a voltage range from 0.5 V to -2 V at a scan rate of 0.01 V/s. Figure 4.11 shows the LSV curves for each pristine CuO electrode and the PVDC-modified electrode. During the first cycle, an irreversible reductive wave between 0.2 V and -1 V vs. RHE was observed. This observation is clear evidence for the reduction of Cu^{2+} to either Cu^{0} or Cu^{+} [144], which is consistent with the results of XPS and XRD analysis.

The overall trends of the curves for all modified CuO electrodes show no significant differences. Within the experimental range and at the same working potential, the PVDC coating increased the total current density only slightly. The electrodes with 25 and 50 µg/cm^2 PVDC coating show a better improvement in current density. However, as the PVDC coating increased further, the increase in current density became less noticeable, and the curves converged to those of the uncoated CuO electrode. A comprehensive analysis of both the current density and Faradaic efficiency for each product suggests that the PVDC modification effectively optimises the partial current density of ethylene while causing a moderate reduction in the partial current density of hydrogen.

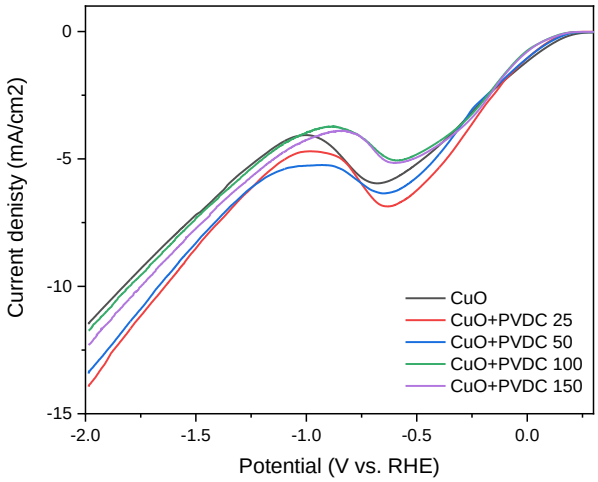

Figure 4.11 LSV of CuO electrodes and CuO with PVDC coating in CO_2-saturated 0.1 M $KHCO_3$ electrolyte at a scan rate of 10 mV/s without iR-corrected.

The LSV of carbon paper and PVDC electrode, as illustrated in Figure 4.12, shows that the coating of PVDC led to the slight increase in current density. The coating of PVDC helps to stabilise the CuO layer on the electrodes. In addition, the PVDC electrode and PVDC-modified CuO electrodes exhibited a negative shift in the onset potential compared to the bare carbon paper and CuO electrodes. This observation indicates that the presence of the PVDC polymer hinders explicitly the transfer of protons from the electrolyte [252].

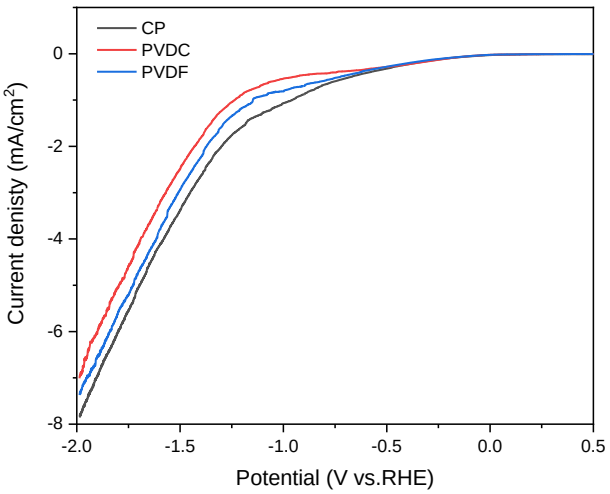

Figure 4.12 LSVs of carbon paper and carbon paper electrode with 150 µg/cm^2 PVDC or PVDF coating in CO_2-saturated 0.1 M $KHCO_3$ electrolyte at a scan rate of 10 mV/s without iR-corrected.

The specific surface area of the electrode is the decisive factor for the electrochemical applications of the nanocatalysts. Unlike an electrode with a flat surface, whose geometric area is almost equal to the electrochemically active area, the ECSAs of CuO electrodes must be determined according to the Cottrell equation, which is supported by C_{dl} [253, 254]. As shown in Table 4.3 and Figure 4.13-14, both the ECSA and the capacitance of the double layer of the CuO electrodes after the reaction are significantly different from those of the unused electrodes, which could be due to the change of active species on the electrodes. As for the electrodes before the reaction, the ECSA of the CuO electrode after hydrophobicity modification (0.432 cm^2) was almost 16% lower than that of the unused CuO electrode (0.501 cm^2), which is consistent with the decrease in the double layer capacitances (C_{dl} = 219.9 µF/cm^2 for the CuO electrode, C_{dl} = 95.7

μF/cm^2 for the CuO-PVDC electrode). Similar trends in the electrodes after the reaction were observed for the ECSA and the C_{dl}. From these results, it can be concluded that the PVDC coating slightly reduces the electrochemically active surface area.

When the ECSA value was used to normalise the current, it reached 244.4 mA/cm^2 for the CuO-PVDC electrode and 208.3 mA/cm^2 for the CuO electrode at a potential of -0.89 V vs. RHE. Considering that the Cu species as electrocatalysts are the primary source of electrochemical activity, it may be that the presence of the PVDC layer on the CuO-PVDC electrode may concentrate copper clusters on the surface, consequently augmenting the overall current density. With C_2H_4 Faradaic efficiencies of 32.2 and 41.4% for the CuO and CuO-PVDC electrodes at -0.89 V, the ECSA-normalized partial current density of ethylene stands at 67.1 and 101.2 mA/cm^2, respectively. This observation indicates that the catalytic activity of CO_2RR to ethylene of the PVDC-modified CuO electrode is inherently a 50.8% increase in comparison to that of the CuO electrode.

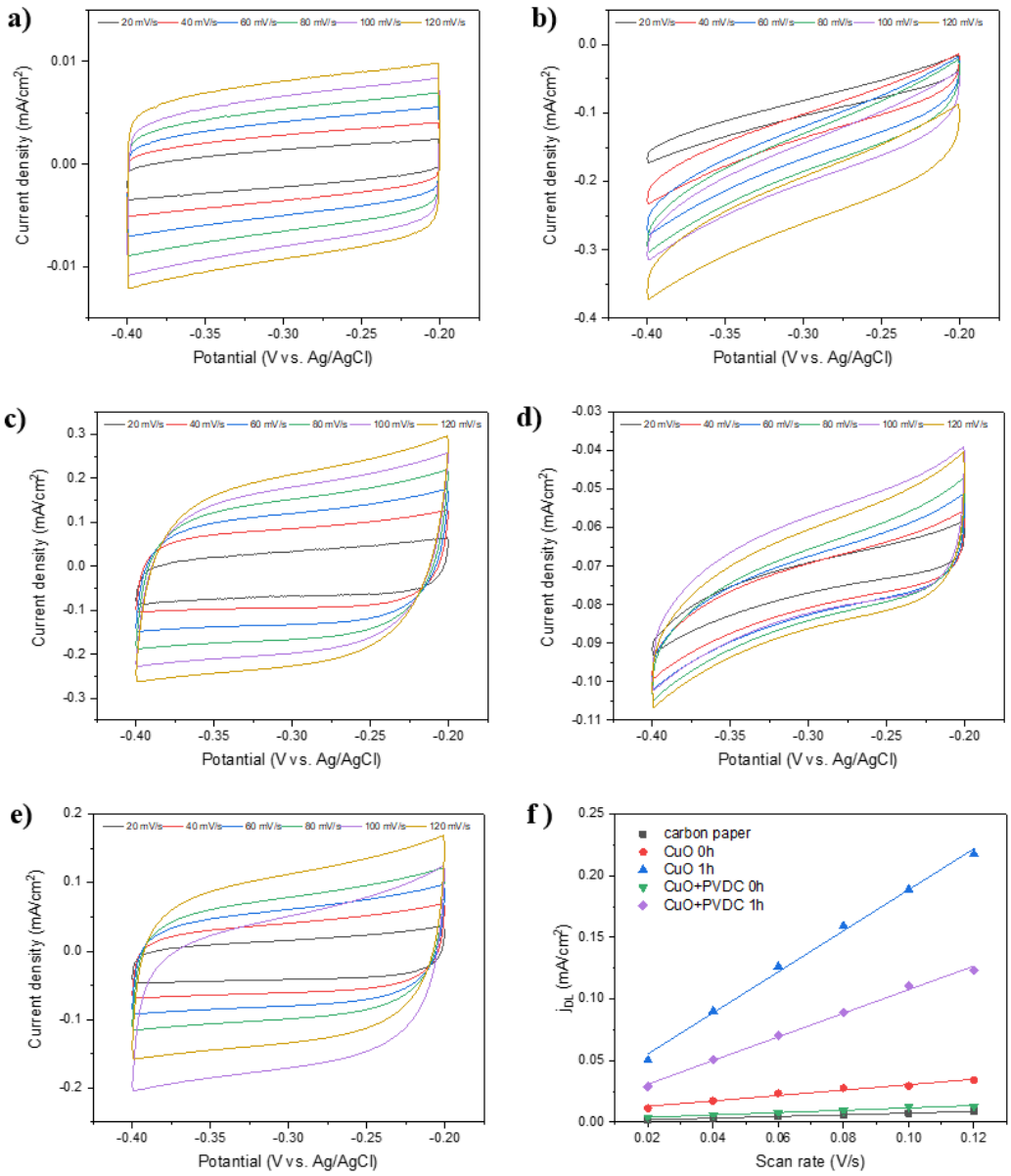

Figure 4.13 CV curves in a non-Faradaic region from -0.4 V to -0.2 V vs Ag/AgCl at various scan rates in CO_2-saturated 0.1 M $KHCO_3$ solution of a) carbon paper, b) pristine CuO electrode, c) CuO electrode after 1-hour reaction, d) pristine CuO-PVDC electrode, and e) CuO-PVDC electrode after 1-hour reaction, f) Plots of double layer current density, j_{dl}, obtained at -0.3 V vs Ag/AgCl against scan rate, the slope of which is identified with the capacitance of double layer.

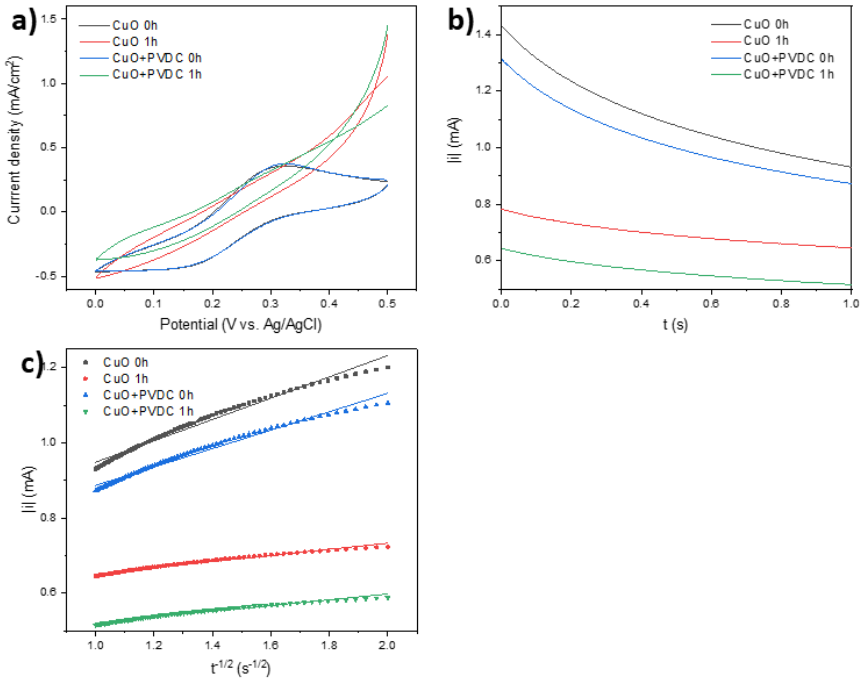

Figure 4.14 a) CV curves of CuO and CuO-PVDC electrodes using a scan rate of 10 mV/s in 5 mM $K_3Fe(CN)_6$/0.1 M KCl; b) constant potential measurement for 1 second at 0.02 V vs. Ag/AgCl on CuO and CuO-PVDC electrodes; c) linearized plot based on the Cottrell equation, the slope of which could be converted to ECSA.

Table 4.3 Double-layer capacitance and electrochemically active surface area of CuO and CuO-PVDC electrodes (PVDC coating amount = 50 μg/cm^2) before and after the reaction.

Electrode	Reaction time（h）	Slope （A*s$^{1/2}$)	$A_{geometric}$ (cm^2)	A_{ECSA} (cm^2)	C_{dl} (μf/cm^2）
CuO	0	2.84E-04	2	0.501	219.9
CuO	1	8.18E-05	2	0.144	1665.1
CuO+PVDC	0	2.45E-04	2	0.432	95.7
CuO+PVDC	1	7.66E-05	2	0.135	959.0

EIS was used to quantify the resistivity of CuO and CuO-PVDC electrodes. As can be seen in Figure 4.15, EIS was measured at - 0.89 V versus RHE and then fitted with a constant phase angle element. The simulated R_s and R_{ct} for these electrodes are listed in Table 4.4. The solution resistances were slightly affected by the position of the electrodes [255]. Here, we mainly focus on the charge transfer resistance. The charge transfer on bare carbon paper was limited, and the polymer even led to an almost double resistance. It is worth highlighting that the PVDC-modified CuO electrodes (< 26.50 Ω) have a lower Rct value than that of bare CuO (29.28 Ω), which correlates well with the behaviour of the LSVs. The charge transfer resistances of the electrodes with different PVDC loading hardly differed. The CuO-PVDC 25 exhibited the lowest charge transfer resistance (24.49 Ω). Since PVDC is not a conductive material, the reduction in resistance could be due to the more stable copper cluster, which means that a small amount of PVDC coating would lead to better conductivity and the PVDC layer could act as a stabiliser of the electrocatalysts on the surface of the electrode during CO_2 reduction.

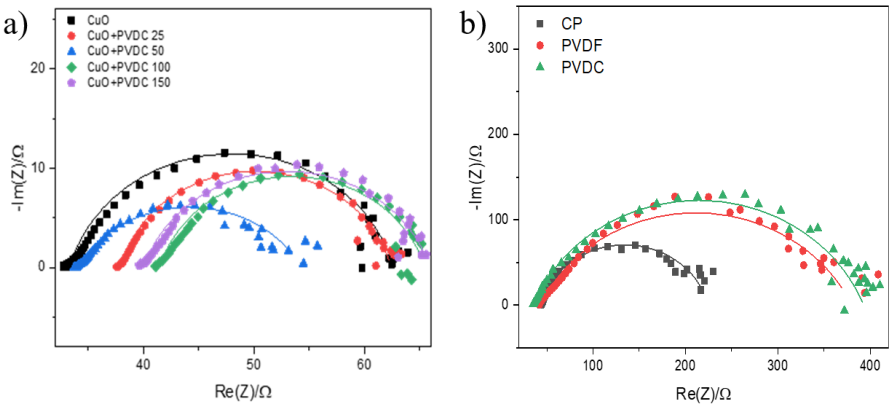

Figure 4.15 EIS of the electrodes taken at -0.89 V vs. RHE in 0.1 M CO_2-saturated $KHCO_3$ electrolyte. The symbols represent the original experimental data, and the lines represent the fitted results.

Table 4.4 Summary of solution resistance and charge transfer resistance obtained from EIS data fitted to a constant phase angle element.

Electrode	R_s (Ω)	R_{ct} (Ω)
CuO	33.33	29.28
CuO+PVDC 25	37.89	24.49
CuO+PVDC 50	34.01	26.10
CuO+PVDC 100	41.44	26.50
CuO+PVDC 150	40.02	25.89
Carbon paper	43.68	181.20
PVDC	35.48	357.50

4.2.4 The influence of coating on HER

The complex reaction pathways of eCO_2RR lead to a number of by-products, such as the formation of hydrogen by HER. To limit the HER without hindering the eCO_2RR to C_2H_4, it is possible to limit the proton transfer by controlling the hydrophobicity of the electrode by coating the electrode with hydrophobic materials. Normally, the hydrophobicity of the electrode surface is characterized by the water contact angle [236, 256-258]. Here, the WCA of the PVDC-modified CuO electrodes was measured at three different positions on the surface. The results in Figure 4.15a show that the CuO-PVDC electrodes are more hydrophobic than the unmodified electrodes. A PVDC layer with a coating of 50 $\mu g/cm^2$ significantly increased the WCA from 94.8 to 122.2 °. The hydrophobicity improved slightly with an increase in the PVDC coating amount. Remarkably, the hydrophobicity of the PVDC-modified electrode (133.0 °)

exceeded that of the PVDF-modified electrode (128.1°) when the same coating amount of 150 µg/cm^2 was applied. In addition, CuO-PVDC 100 achieved similar hydrophobicity to PVDF at a coating amount of 150 µg/cm^2, indicating that the hydrophobic effect of PVDC exceeds that of PVDF.

Figure 4.16b compares the eCO_2RR selectivity between CuO electrodes modified with PVDF and PVDC. Similar suppression of HER and increased ethylene production was observed for the CuO-PVDF electrode, albeit to a lesser extent than for the PVDC-modified electrode with the same coating amount and hydrophobicity. This observation suggests that while the hydrophobicity of the electrode plays a role in influencing H_2 evolution, other factors, such as the specific interaction between the electrode surface and the reactants, the presence of active sites and the catalytic properties of the modified electrode may also contribute to the observed differences in product selectivity.

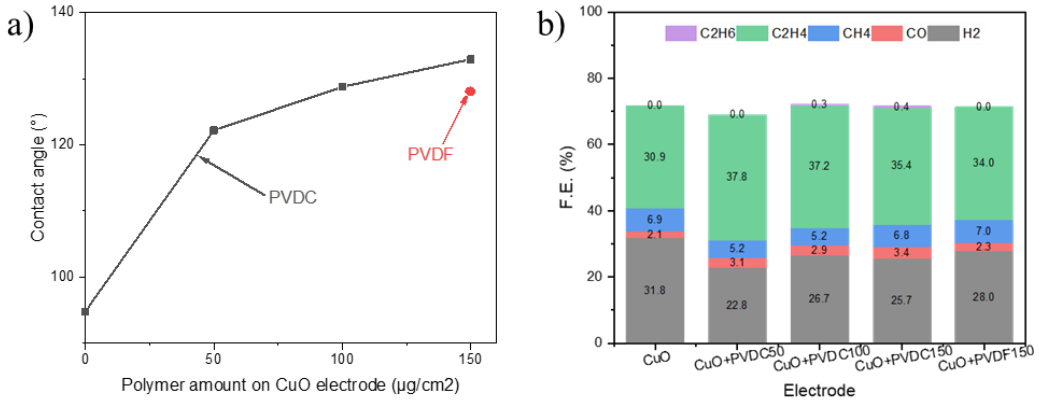

Figure 4.16 a) The water contact angle and b) the performance of bare CuO and CuO electrodes with various amounts of PVDC or PVDF coating modification.

The effect of PVDC on the suppression of HER is shown in Figure 4.17a. The bare CuO electrode exhibits an FE_{H2} of 31.8% with different coating amounts of PVDC. All FEs of H_2 were reduced by more than 5% under the same conditions. In particular, the CuO-PVDC 50 electrode reached its optimum suppression of H_2 evolution by a significant reduction to 22.8%. In addition, the HER study was performed on the CuO and CuO-PVDC 50 electrodes within the working potential range (Figure 4.17b). The bare CuO electrodes showed that the H_2 Faraday efficiency was between 24.8 and 31.8%. After PVDC modification with 50 μg/cm^2, The H_2 efficiency was limited to below 22.8%, which was 2.1-9% lower than that on the untreated CuO electrode. It is noteworthy that at the same coating amount (150 μg/cm^2) or similar hydrophobicity (water contact angle of ~ 128°), the synergistic catalytic effect of PVDC coating on HER suppression (FE_{H2} < 26.7%) and ethylene formation (FE_{C2H4} > 35.4%) was slightly better than that of PVDF coating (FE_{H2} = 28.0%, FE_{C2H4} = 34%) (Figure 4.16b). This phenomenon shows that the characterisation of the polymers is also responsible for the improved ethylene production and the inhibited hydrogen evolution.

There is little doubt that the PVDC modification would improve the product selectivity for ethylene. Although hydrophobicity correlates positively with polymer loading, the increased PVDC coating did not perform better in HER suppression. This could be due to excessively hindered water diffusion on the thicker PVDC layer and insufficient coverage on the thinner PVDC layer. The hydrophobicity induced by 50 μg/cm^2 PVDC was satisfactory and regulated the water diffusion to a certain extent so that HER could be inhibited while sufficient proton transfer for CO_2RR could occur.

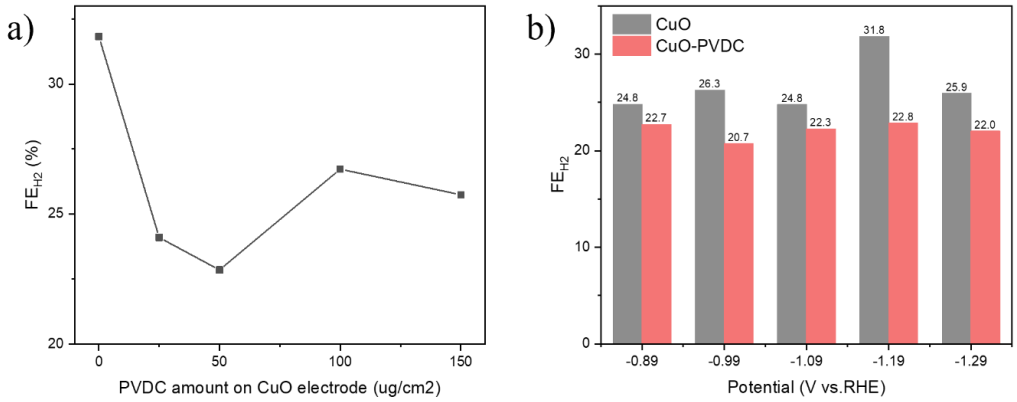

Figure 4.17 Faradaic efficiencies of H_2 for a) bare CuO electrode and CuO electrode with various PVDC coating amounts obtained at the fixed potential of -1.19 V vs. RHE; b) bare CuO electrode and CuO electrode with 50 µg/cm^2 PVDC coating under different working potentials in CO_2-saturated 0.1 M $KHCO_3$ electrolyte (with 85% iR-corrected).

4.2.5 The permeability of CO_2

It is assumed that CO_2 activation is the first step of the reaction. It is crucial to optimise the local CO_2 concentration to an appropriate level so that the surface coverage of *CO_2 and *CO is balanced to promote the production of multi-carbon products. Insufficient CO_2 supply is a common factor inhibiting the reaction [259, 260].

The effect of PVDC on the adsorption of CO_2 can be evaluated by the permeability of CO_2 in the modified electrodes. Here, the current density at the working potential could be used to determine the maximum CO_2 consumption rate. Using the experimental data of the CuO-PVDC 50 electrode as an example, a current density of 10 mA/cm^2 at a potential of -0.75 V vs. RHE was achieved.

Estimating the ratio between electron consumption and carbon dioxide consumption in eCO_2RR is challenging due to the complex reaction pathway and the presence of H_2 by-products. Based on the actual distribution of products, an approximate ratio of 3.5 was determined. The CO_2 consumption rate at the CuO-PVDC 50 electrode is therefore calculated to be 2.97×10^{-8} mol/cm^2·s [237]. The permeability of CO_2 in PVDC is about 0.95 cm^3·mm/m^2·day·atm [261]. The thickness of the PVDC layer is calculated to be 1.65 nm so that the CO_2 flux through the polymer layer corresponds to the theoretical CO_2 consumption rate. These results suggest that CO_2 mass transport is a limiting factor when the thickness of the PVDC layer exceeds 1.65 nm.

In agreement with the SEM, LSV and CO_2RR results, CO_2 transport through the polymer layer becomes more restricted as the PVDC layer becomes thicker, resulting in a lower flux and possibly limiting the overall CO_2 consumption rate. This finding could explain why ethylene production and current density decrease with increasing PVDC coating. Proton transfer is not the only factor influencing the electrochemical performance of electrodes. Permeability to CO_2 is also essential. The particular configuration of CuO-PVDC 50 electrodes provides a favourable balance between proton transfer and CO_2 availability, resulting in efficient CO_2 consumption. The moderate proton transfer rate ensures efficient electrochemical reactions, while the adequate CO_2 supply at the electrode-polymer interface ensures sufficient availability of CO_2 for the reaction. These properties make the CuO electrodes with 50 µg/cm^2 PVDC a promising choice for CO_2 conversion applications.

4.2.6 The adsorption of main intermediates

CO_2 is reduced by multiple proton-electron transfers to intermediates such as *CHO and CO*, which bind to the catalytic metal centre. These intermediates are then subjected to C-C coupling and further hydrogenation to form ethylene (Figure 4.18). DFT calculations implemented in the Vienna Ab-initio Simulation Package package were performed to simulate the adsorption of key intermediates on the surface of unmodified Cu and Cu modified with polymers (PVDC/PVDF/PTFE) [158, 176, 221, 222]. In the reaction pathway, three basic intermediates (*H, *OCHO, *COOH) strongly influence the selectivity of ethylene [262].

For each electrode surface, the intermediates were analysed (Table 4.5). The simulated results show that all these intermediates can be firmly adsorbed on the unmodified Cu electrode and that the modification slightly weakens this adsorption. On the surface of bare Cu, the adsorption energy of *H is much stronger than that of *COOH and *OCHO, resulting in a high FE_{H2}. The adsorption of *H should be moderately weak to control H_2 formation without affecting CO_2RR. Here, PVDC and PVDF-decorated Cu show relatively weak binding with *H compared to the binding on a bare Cu surface. Compared to *OCHO, *COOH is a highly desirable intermediate as it can be easily converted to *CO, allowing C-C coupling to produce ethylene. Although the modification reduces the adsorption of *COOH, it is still much stronger than that of *H, especially on PVDC and PTFE coatings. This result shows that ethylene formation is enhanced after PVDC coating.

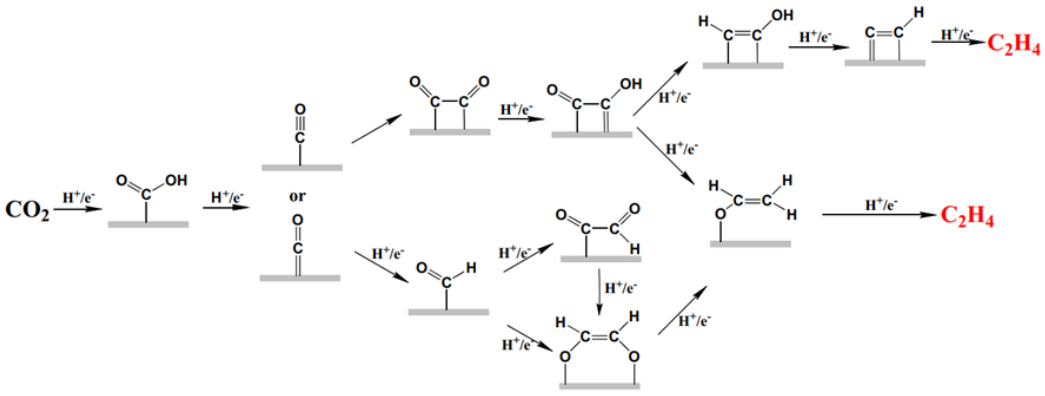

Figure 4.18 Potential reaction pathways for the electrochemical reduction of CO_2 to ethylene.

Table 4.5 Comparison of the adsorption energy of key intermediates to C_2H_4 on polymer-modified copper.

*H adsorption	E_{ad}	*COOH adsorption	E_{ad}	*OCHO adsorption	E_{ad}
Cu-PVDC-*H	-0.009	Cu-PVDC-*COOH	-0.327	Cu-PVDC-*OCHO	-0.819
Cu-PVDF-*H	-0.007	Cu-PVDF-*COOH	-0.079	Cu-PVDF-*OCHO	-0.730
Cu-PTFE-*H	-0.020	Cu-PTFE-*COOH	-0.342	Cu-PTFE-*OCHO	-0.649
Cu- *H	-2.566	Cu- *COOH	-1.954	Cu - *OCHO	-1.705

4.3 Summary

To summarise, the hydrophobicity of CuO electrodes can be controlled by the amount of PVDC coating. CuO electrodes with a PVDC coating of 50 µg/cm^2 exhibit improved conductivity and an optimal synergy between ethylene production and hydrogen suppression. This CuO-PVDC electrode shows favourable performance with FE_{C2H4} = 41.4%, $|j|_{C2H4}$ = 6.8 mA/cm^2, at a low potential of -0.89 V vs. RHE. The catalytic activity of CO_2RR to ethylene of the PVDC-modified CuO electrode is inherently a 50.8% increase in comparison to

that of the CuO electrode. The unique structure of the CuO-PVDC 50 electrode provides a good balance between proton transfer and CO_2 availability, enabling efficient CO_2 consumption. In addition, the PVDC coating increases the amount of Cu^+ and Cu^0 on the electrode surface after the reaction, promoting the C-C coupling process. The results indicate that CuO electrodes with a PVDC coating offer promising advantages in terms of conductivity, CO_2 consumption and catalyst stability, making them a potential candidate for efficient electrocatalytic applications with carbon dioxide.

Chapter 5. Microwave-assisted synthesis of CuO for eCO_2RR to C_{2+} products

5.1 Introduction

Copper catalysts have attracted much attention due to their moderate binding ability to *CO- and *H- intermediates and their potential to generate chemical bonds with high energy density in the formation of C_{2+} products [95, 190]. Compared to metallic Cu, OD-Cu catalysts perform much better in electrochemical CO_2 reduction reactions. The electrocatalytic performance of OD-Cu electrodes with four different preparations, such as thermal annealing and electrodeposition, has been intensively investigated. Among these four other electrodes, the EC-Cu electrode prepared by electrochemical oxidation-reduction cycling of Cu foil shows the highest C_{2+} FE of ~ 56.4%, while $FE_{ethylene}$ reaches ~ 38.1% at -1.0 V vs. RHE in 0.1 M $KHCO_3$ electrolyte. The untreated Cu film shows an FE for C_{2+} of only ~ 36% ($FE_{ethylene}$ = 21.6%) under the same operating conditions, strongly suggesting a better performance of Cu after oxidation treatment [134]. Studies show that CuO is rapidly reduced to a certain percentage of Cu_2O or Cu in the early phase of CO_2ER, which is the main catalytically active species [263].

Most importantly, the adsorption of CO at the Cu^+ site is more stable than the adsorption at the metallic Cu^0 region, which facilitates the dimerisation process. Therefore, the proportion of the Cu^+ site is crucial for the selectivity of multicarbon products [162, 175, 232]. Furthermore, the presence of rich grain boundaries, low coordination sites and oxygen species has been shown to be advantageous for the formation and stabilisation of C-C double bonds [264].

Therefore, optimising the surface structure and controlling the coordination environment are two essential strategies to control further the catalytic activity and selectivity of OD-Cu catalysts [72, 128, 265, 266].

Defect-rich CuO, synthesised by microwave heating, could be a promising electrocatalyst for CO_2RR to multicarbon products. In contrast to conventional heating, microwave heating combines heating mechanisms with a magnetic and electric field. The use of microwave heating for the synthesis of CuO offers several advantages, such as faster reaction rates [267], better control over the size and morphology of the resulting nanoparticles [268] and more efficient use of energy and resources [269]. More importantly, microwaves are non-ionising electromagnetic radiation with a relatively high penetration depth that could significantly accelerate the reaction kinetics, increase the nucleation rate and shorten the synthesis time while potentially causing material stresses, cracks, and, thus, defects [270-272]. The CuO nanoblooms synthesised by the microwave-assisted method have abundant surface oxygen and a large surface area, which have been investigated for their performance in CO oxidation, gas sensing and photocatalysis, as well as their antimicrobial and anticancer properties [186, 273-276].

In this study, CuO was synthesised using different heating methods and used as a catalyst in an electrochemical CO_2 reduction reaction. A CuO catalyst with optimal selectivity and efficiency in CO_2ER was identified by comparing morphology, crystal facets, and electrochemical properties. A series of studies were carried out to investigate the mechanism leading to high C_{2+} product selectivity of the CuO electrodes.

5.2 Results and discussion

5.2.1 Influences of microwave heating on the surface properties of CuO

A simple two-step procedure was developed for the synthesis of MW-CuO catalysts based on previous literature [186]. The synthesis procedure involved mixing a copper salt solution with sodium carbonate at 70 °C with continuous microwave heating to produce the precursor basic copper carbonate. Subsequently, calcination at 300 °C was performed to facilitate the decomposition of the carbonate ions and to obtain the MW-CuO catalysts. A CuO sample was prepared as a control using a similar method but with conventional water bath heating in the first step instead of microwave heating (see details in the Experimental section).

The X-ray diffraction patterns of all samples match those of standard CuO (JCPDS#48-1548). Sharp diffraction peaks at 35.5, 38.7 and 48.7° are observed for all MW-CuO and CuO samples, corresponding to crystal facets (11-1), (111), and (20-2), respectively, indicating that the CuO nanoparticles are well crystallised during calcination (Figure 5.1). The intensities of the main diffraction peaks of the samples are listed in Table 5.1. The high intensity of the (11-1) and (111) peaks indicates that the growth of MW-CuO and CuO occurs preferentially along these two planes.

Scanning electron microscope images of the MW-CuO and conventional CuO nanoparticles are shown in Figure 5.2. The shape of the CuO particles was changed by adjusting the ratio of the reactants Cu^{2+} and CO_3^{2-} during the synthesis process. MW-$CuO_{0.1}$ powder has a fluffy, sea urchin-like morphology with cylindrical villi of 25 to 50 nm in diameter and 200 to 500 nm in length.

MW-$CuO_{0.5}$ has a similar morphology but a more compact appearance. Due to the addition of an excessive amount of copper salt, the morphology of the obtained MW-$CuO_{1.1}$ and MW-$CuO_{1.4}$ differs significantly from that of MW-$CuO_{0.1}$ and MW-$CuO_{0.5}$, resulting in large leaf structures and smooth surfaces that are somewhat randomly distributed. The CuO samples synthesised by heating in a water bath have a comparable morphology to the corresponding MW-CuO samples but are more irregular and have a non-uniform grain size. Figure 5.2 shows that the ratio of reactants has a significant influence on the morphology of the final product, while the heating method in the synthesis process mainly changes the size distribution of the CuO particles.

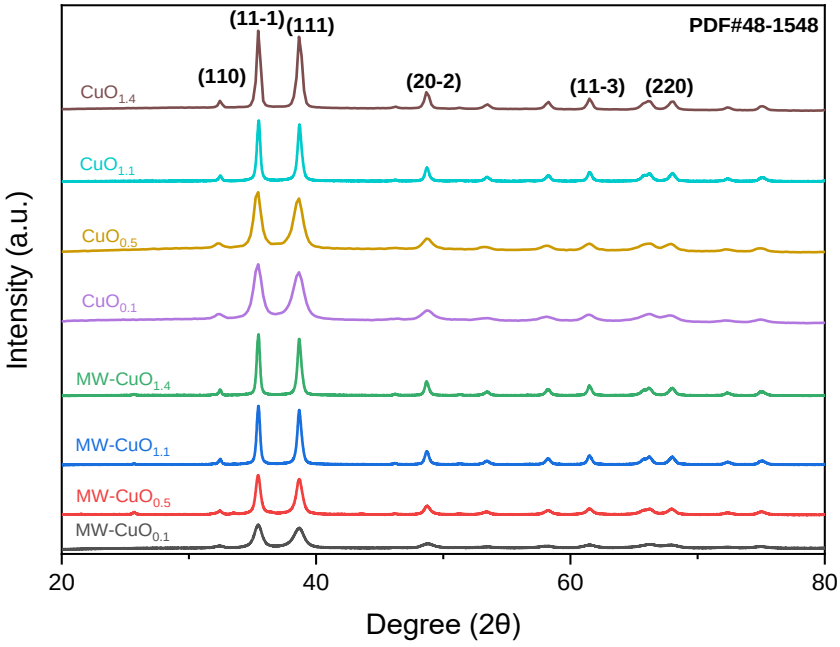

Figure 5.1 XRD partterns of the CuO samples.

Table 5.1 The intensity of the main facets of CuO and MW-CuO.

	MW-$CuO_{0.1}$	**MW-$CuO_{0.5}$**	**MW-$CuO_{1.1}$**	**MW-$CuO_{1.4}$**	**$CuO_{0.1}$**	**$CuO_{0.5}$**	**$CuO_{1.1}$**	**$CuO_{1.4}$**
Intensity of （110）facet	499.3	549.4	546.9	517.9	643.2	597.5	544.2	750.2
Intensity of （11-1）facet	5422.9	6418.4	6931.2	6748.3	8916.5	8243.8	7231.8	10006.8
Intensity of （111）facet	6159.1	7526.2	8008.5	7759.1	9973.0	9603.7	8141.5	11657.3
Intensity of （20-2）facet	1332.8	1679.7	1862.9	1831.2	2081.6	1998.3	1842.1	2609.6
Intensity ratio of (111)/(11-1)	1.14	1.17	1.16	1.15	1.12	1.16	1.13	1.22
Intensity ratio of (111)/(110)	12.34	13.70	14.64	14.98	15.51	16.07	14.96	15.54
Intensity ratio of (111)/20-2)	4.62	4.48	4.30	4.24	4.79	4.81	4.42	4.47

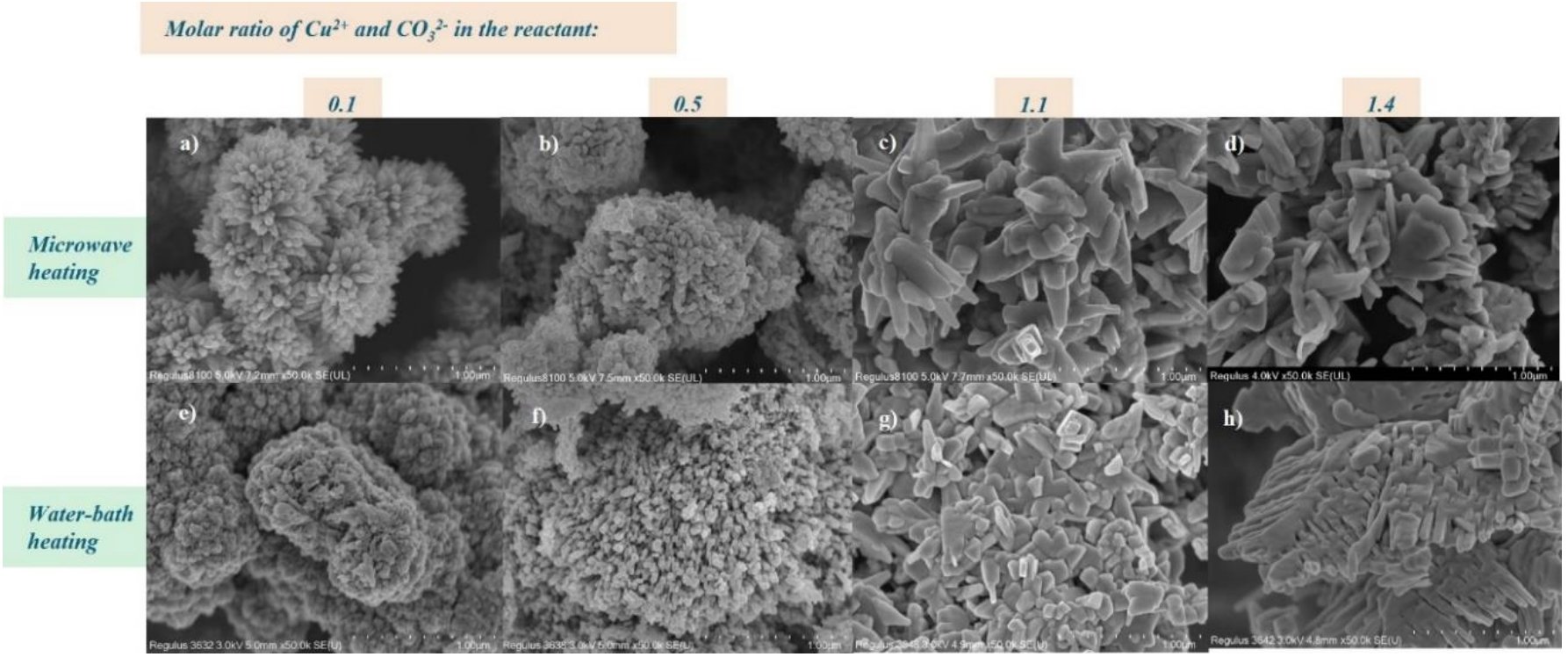

Figure 5.2 SEM images of a) MW-$CuO_{0.1}$; b) MW-$CuO_{0.5}$; c) MW-$CuO_{1.1}$; d) MW-$CuO_{1.4}$; e) $CuO_{0.1}$; f) $CuO_{0.5}$; g) $CuO_{1.1}$; h) $CuO_{1.4}$.

High-resolution transmission electron microscopy was used to further investigate the crystalline structure of CuO with and without microwave treatment (Figure 5.3). The exposed (11-1) facet could be observed on each CuO sample, which is consistent with the results of XRD analysis. The HRTEM images show that the CuO prepared using the water bath method has a uniform lattice orientation with few defects. However, a high density of grain boundaries was observed in the MW-CuO nanoparticles, especially in MW-$CuO_{1.1}$ [277]. In addition, other defects, such as lattice distortions and vacancies, were also found in all MW-CuOs. The similarities and differences in the morphology and crystal facets of the CuO samples indicate that microwave heating affects both nucleation and growth processes and induces defects, and the defect density can be altered by changing the ratio of reactants.

It has been proven that various defects play an essential role in the electrochemical conversion of CO_2 into multi-carbon products. For example, the existence of oxygen vacancies can enhance the adsorption of CO_2 and promote strong binding interactions with intermediates such as *CO and *COH. At the same time, it has a comparatively lowered affinity for $*CH_2$, which leads to the effective production of multi-carbon products [231, 278]. Moreover, as a planar defect, the grain boundary can provide a variety of edge sites and stabilise catalytically active surfaces to regulate the electronic and surface properties and improve the product selectivity of CORR and CO_2RR over C_{2+} products [279-281]. Due to the higher defect density of MW-$CuO_{1.1}$, the defect-rich MW-$CuO_{1.1}$ is expected to be more selective for multi-carbon products as an electrocatalyst.

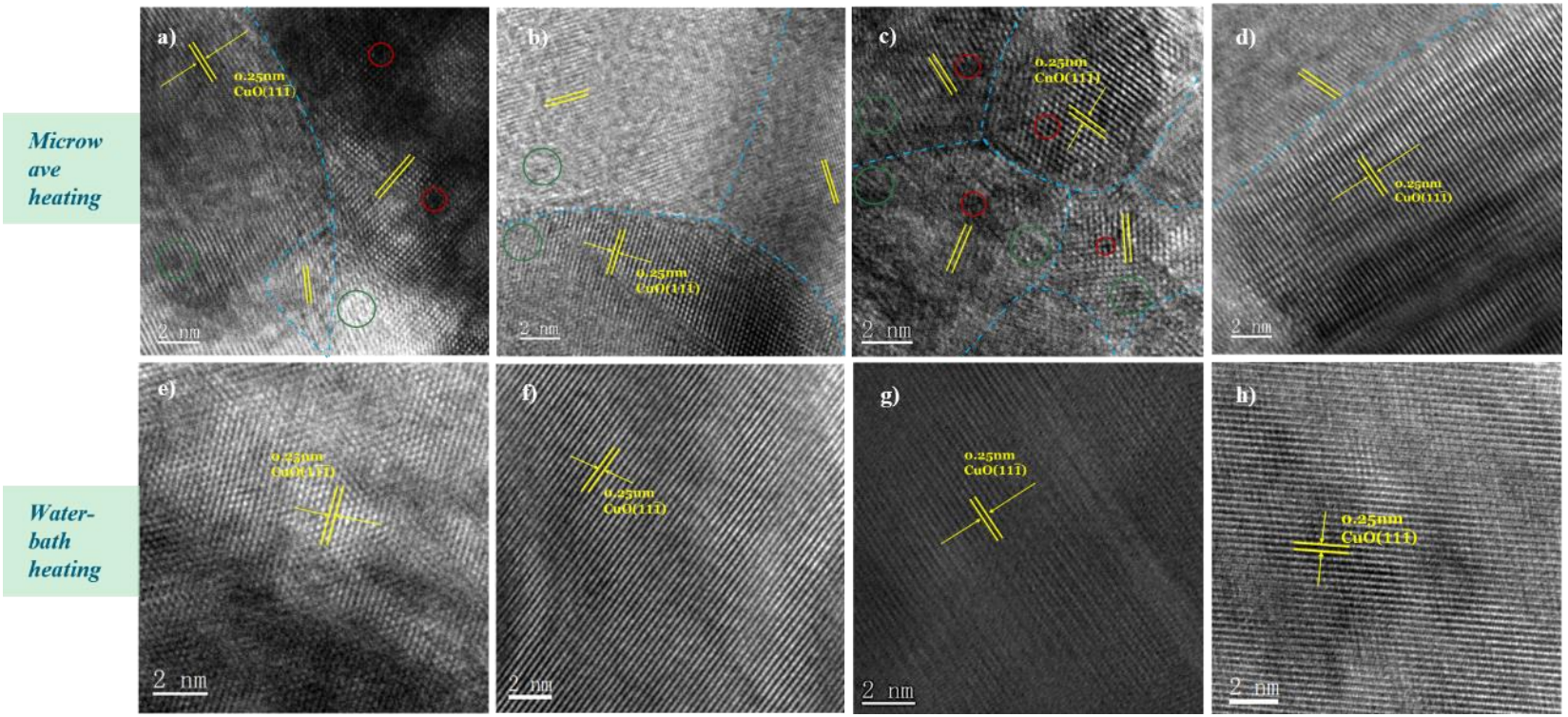

Figure 5.3 HRTEM images of a) MW-$CuO_{0.1}$; b) MW-$CuO_{0.5}$; c) MW-$CuO_{1.1}$; d) MW-$CuO_{1.4}$; e) $CuO_{0.1}$; f) $CuO_{0.5}$; g) $CuO_{1.1}$; h) $CuO_{1.4}$. The blue line presents the grain boundaries, lattice distortion and vacancy marked in the green and red circles, respectively.

5.2.2 CO_2RR of MW-CuO electrodes

The CuO catalysts were dried on purified carbon paper with Nafion as the binder (catalyst loading = ~ 0.25 mg/cm^2), which served as a working electrode in an H-cell with 30 mL CO_2-saturated 0.1 M $KHCO_3$ electrolyte. The electrocatalytic activity of the CuO and MW-CuO electrodes was analysed using cyclic voltammetry. The first two cycles of the cyclic voltammograms for the fresh electrodes are shown in Figure 5.4. The general trends for each electrode are similar. The initial potential of the MW-CuO electrode is close to that of the CuO electrode, indicating no significant difference in proton transfer [252]. All CuO electrodes show irreversible reductive waves between -1.5 and 0.2 V vs. RHE in the first cycle, indicating that Cu^{2+} was reduced to Cu^0 or Cu^+. The current density of the electrodes in the working potential region hardly differs.

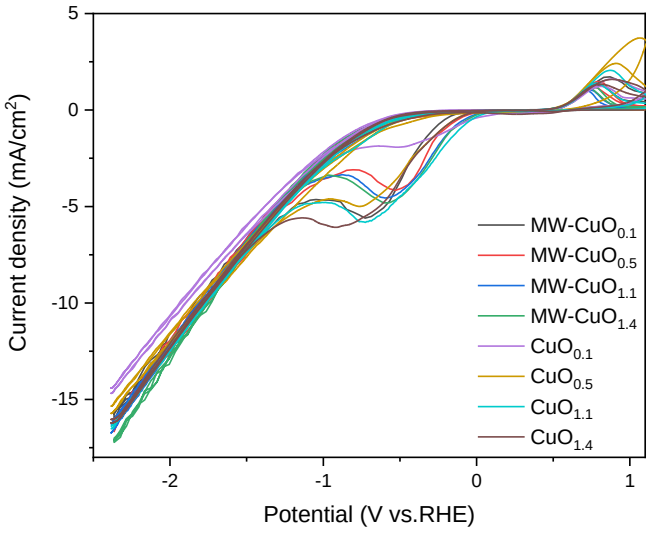

Figure 5.4 CV of MW-CuO and CuO electrodes in CO_2-saturated 0.1 M $KHCO_3$ electrolyte at a scan rate of 10 mV/s without iR correction.

The MW-$CuO_{1.1}$ electrode has the largest active area among all these eight electrodes, and the $CuO_{1.1}$ electrode ranks second, which is crucial for the

catalytic activity (determined by the capacitance of the double layer in Figure 5.5 and Table 5.2). Furthermore, the lower charge transfer resistance observed in $CuO_{1.1}$ and MW-$CuO_{1.1}$, compared to other electrodes, indicates a more efficient and easier electron transfer process. This suggests that these two electrodes have a higher conductivity, which improves their overall electrocatalytic performance.

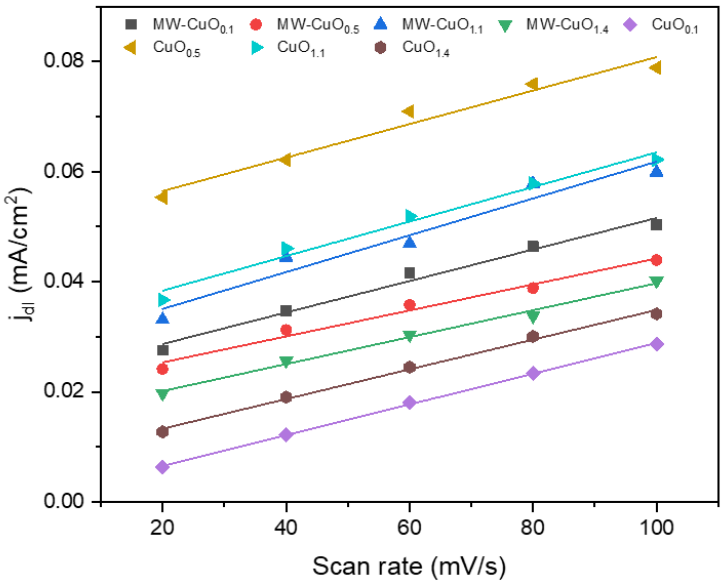

Figure 5.5 Plots of double layer current density, j_{dl} against scan rate, the slope of which is identified with the capacitance of the double layer. The j_{dl} was calculated to be half the difference between the anodic and cathodic currents (i_a - i_c).

Table 5.2 The resistance and double layer capacitance of CuO and MW-CuO electrodes.

Electrode	R_s (Ω)	R_{ct} (Ω)	C_{dl} (μF/cm^2)
MW-$CuO_{0.1}$	39.2	40.2	286.0
MW-$CuO_{0.5}$	38.5	45.4	236.0
MW-$CuO_{1.1}$	35.0	34.3	334.3
MW-$CuO_{1.4}$	34.0	45.9	244.6
$CuO_{0.1}$	34.6	47.9	279.2
$CuO_{0.5}$	40.0	37.1	304.3
$CuO_{1.1}$	39.8	34.9	313.7
$CuO_{1.4}$	39.6	41.0	269.4

The catalytic performance of each CuO electrode was evaluated using the CO_2RR test at a fixed potential of -1.04 V vs. RHE, as shown in Figure 5.6. The total FE for both electrodes is not exactly 100% because some of the charge was consumed in the reduction of CuO to Cu^+ or Cu^0. In addition, the FE of the liquid products was collected after a 1-hour test, while there may be slight variations in the FE of the gaseous products. The results showed that the percentage of multi-carbon products produced was more than 56.7%, with ethylene dominating with an FE of more than 33.2%. The FE of H_2 varied between 19.3 and 28.7%. Among all these CuO electrodes, MW-$CuO_{1.1}$ showed the best performance with 45.1% $FE_{ethylene}$ and 71.9% FE_{C2+}, while $CuO_{1.1}$ was the next most efficient with 35.4% $FE_{ethylene}$ and 64.9% FE_{C2+}. Thus, the 1.1 molar CO_3^{2-} and Cu^{2+} composition in the reactant mixture resulted in CuO with the best

eCO_2RR performance. The better performance of MW-CuO could be due to the numerous defects created by microwave heating.

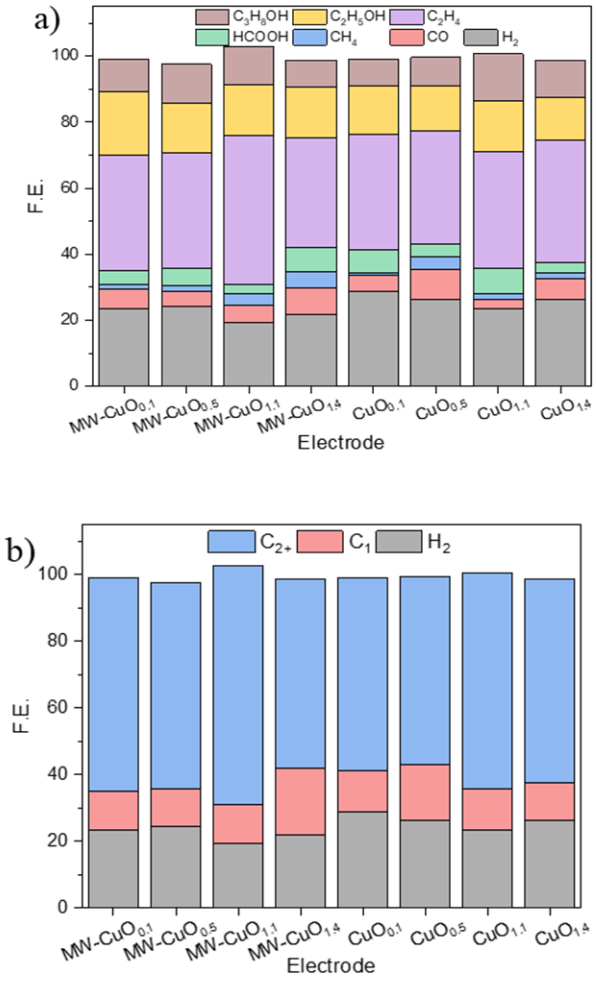

Figure 5.6 The product distribution of MW-CuO electrodes at -1.04 V vs. RHE (with 85% iR-correction).

The catalytic activity and selectivity of MW-$CuO_{1.1}$ and $CuO_{1.1}$ electrodes were investigated (CuO and MW-CuO in the following refer to $CuO_{1.1}$ and MW-$CuO_{1.1}$, respectively). Electrolysis at constant potential was performed for 60 minutes at potentials ranging from -1.14 to -0.94 V vs. RHE (with 85% iR correction). The gas products were quantified during the first 30 minutes of eCO_2RR. The Faradaic efficiencies as a function of voltage at both CuO

electrodes are shown in Figure 5.7a,b. The product distribution appears to be directly related to the working potential. At a more negative potential, the formation of hydrogen increases while CO decreases slightly. CH_4 also increases slightly, while ethanol and propanol decrease. The main product is ethylene, which shows an initial increase and a downward trend. The control experiment shows that CuO synthesised by conventional heating has low selectivity for multi-carbon products (FE_{C2+} = 57.6 ~ 65.7%, $FE_{ethylene}$ = 22.1 ~ 36.1%), while H_2 is the second most produced gas with FE up to 28.4%.

In general, the defects of MW-CuO weaken the competition of the hydrogen evolution reaction and enhance C-C coupling, resulting in a significant improvement in the production of multi-carbon products compared to CuO. The selectivity of the MW-CuO electrode is similar to that of the CuO electrode at low potentials. However, MW-CuO shows a clear superiority in the production of multi-carbon products at a more negative potential. In particular, at a potential of -1.04 V vs. RHE, the CuO electrode shows a total current density of ~ 11.5 mA/cm^2 and FEs for H_2, C_2H_4 and C_{2+} products of 23.4, 35.4 and 64.9%, respectively. Under the same working conditions, the total current density towards CO_2ER of the MW-CuO electrode (~ 15.5 mA/cm^2) is much higher than that of the CuO electrode. The MW-CuO electrode shows only 19.3% for H_2 evolution, while it shows a high FE of 45.1% for ethylene and 71.9% for multi-carbon products.

It should be noted that the high Faradaic efficiency of 71.9% achieved with the MW-CuO electrode for C_{2+} production with the high partial current density of the multi-carbon products (~ 11.2 mA/cm^2) is one of the highest yields for multi-carbon products using oxide-based catalysts (Table 5.3).

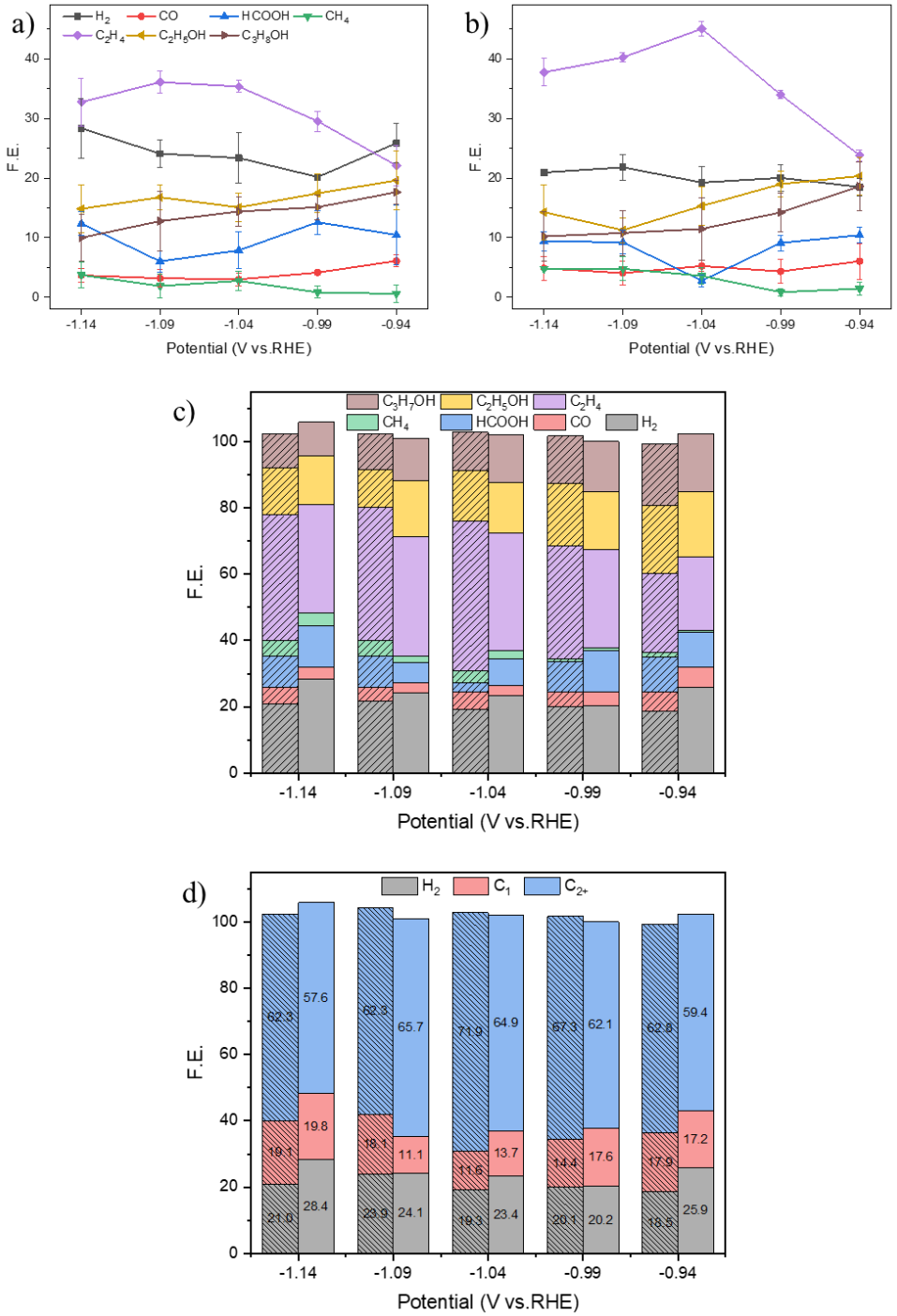

Figure 5.7 The product distribution of a) the CuO electrode, b) the MW-CuO electrode; c,d) the comparison between the $CuO_{1.1}$ electrode (right column with no pattern) and MW-$CuO_{1.1}$ electrode (left column with oblique line) under different working potentials in the CO_2-saturated 0.1 M $KHCO_3$ electrolyte (with 85% iR-corrected).

1

Table 5.3 Comparison of optimized C_{2+} production using various Cu-based catalysts in H-cells.

Electrode	FE_{C2+}	E (V vs. RHE)	Electrolyte	Reference
MW-CuO	71.9%	-1.0	0.1 M $KHCO_3$	This work
Oxide-derived Cu	58.0%	-1.0	0.5 M $KHCO_3$	[244]
Mesoporous CuO	~ 60.0%	-1.0	1.0 M KI	[142]
PVDF modified CuO	~ 49.6%	-1.2	0.5 M $KHCO_3$	[144]
OD Cu	23.5%	-0.8	0.1 M $KHCO_3$	[134]
EC Cu	56.4%	-1.0	0.1 M $KHCO_3$	[134]
OD NWs	45.9%	-1.0	0.1 M $KHCO_3$	[134]
EOD Cu 100s	54.9%	-1.0	0.1 M $KHCO_3$	[134]
HQ-Cu	68.2%	-1.1	0.1 M $KHCO_3$	[135]
Copper mesocrystals	29.4%	-1.0	0.1 M $KHCO_3$	[246]
Copper nanocubes（44 nm）	~ 55.0%	-1.1	0.1 M $KHCO_3$	[228]
Prism-shaped Cu	~ 35.5%	-1.2	0.1 M $KHCO_3$	[247]
Copper nanoparticle ensembles	55.0%	-0.9	0.1 M $KHCO_3$	[248]
Cu foils treated with O_2 plasma 20 W 2 min	~ 61.0%	-0.9	0.1 M $KHCO_3$	[125]
Agglomerated Cu Nanocrystals	60.3%	-1.0	0.1 M $KHCO_3$	[177]
Cu_2O films (0.9 μm)	48.9%	-1.0	0.1 M $KHCO_3$	[140]
Anodized copper	~ 53.0%	-1.1	0.1 M $KHCO_3$	[132]
Electroredeposited copper	54.0%	-1.2	0.1 M $KHCO_3$	[133]
Porous Hollow Copper Microspheres	67.3%	-0.8	0.1 M $KHCO_3$	[136]
Nanosheet structure derived Cu	67.5%	-1.5	0.1 M $KHCO_3$	[137]

5.2.3 Concurrence of Cu^{+} and Cu^{0} during electrolysis

The electrochemical performance provides additional insight into the comparison of the CuO and MW-CuO samples. The curves for the first two cycles for both electrodes are shown in Figure 5.8. In the first cycle, there was an irreversible reductive wave between 0.2 and -1.5 V vs. RHE, which may indicate that Cu^{2+} was reduced to Cu^{0} or Cu^{+} and CuO was not the actual electrocatalyst in the CO_2 reduction reaction [139]. It is noteworthy that the absolute area of the reductive wave is 3.3 for the CuO electrode, while it is 2.4 for the MW-CuO electrode. Since the catalyst loading on the electrode is the same, it could be concluded that the CuO was easier to reduce than the MW-CuO, that a higher proportion of the CuO was reduced, or that the degree of reduction was higher for the particles on the CuO electrode.

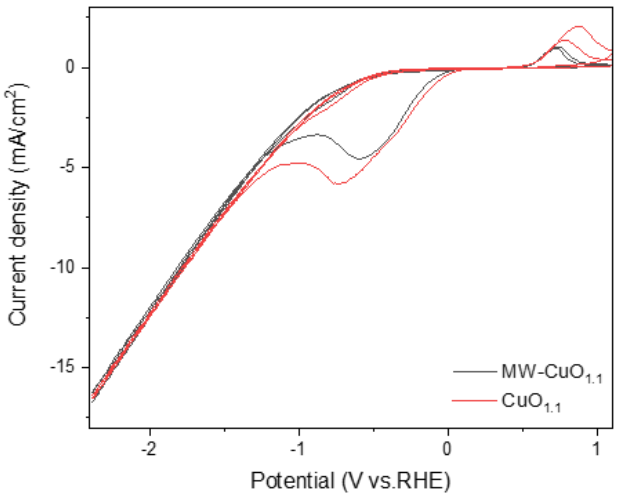

Figure 5.8 CVs of the CuO and MW-CuO electrodes for the first two cycles in CO_2-saturated 0.1 M $KHCO_3$ electrolyte at a scan rate of 10 mV/s without iR-correction.

X-ray photoelectron spectroscopy was used to analyse and characterise the oxidation state of the copper species before and after the reaction. In the Cu 2p 3/2 signals shown in Figure 5.9a, b, the existence of Cu (II) in fresh MW-CuO and CuO catalyst is evidenced by a shoulder at the main peak at 933.5 eV. There is no obvious difference between the CuO and MW-CuO electrodes, indicating that the microwave treatment does not change the valence state of Cu^{2+}. After the 5-minute reaction, the main peaks have shifted to about 932.7 eV, which could be associated with Cu^0 or Cu^+. In the Cu-LMM spectra, the spent electrodes show a peak maximum at ~916 eV, which could be assigned to the Cu^+ species. Due to the small loading amount of CuO on the electrodes, the signal-to-noise ratio is inadequate. The peak could for Cu^0 and Cu^{2+} could hardly be identified.

Furthermore, there is no noticeable difference in the Cu 2p and Cu LMM peaks for MW-CuO electrodes after 5-, 30-, 60-, 120-, and 360-minute reactions (Figure S5b). The chemical phase change should occur in the first 5 minutes of the reaction, which is consistent with the conclusion from the irreversible reductive wave in CV.

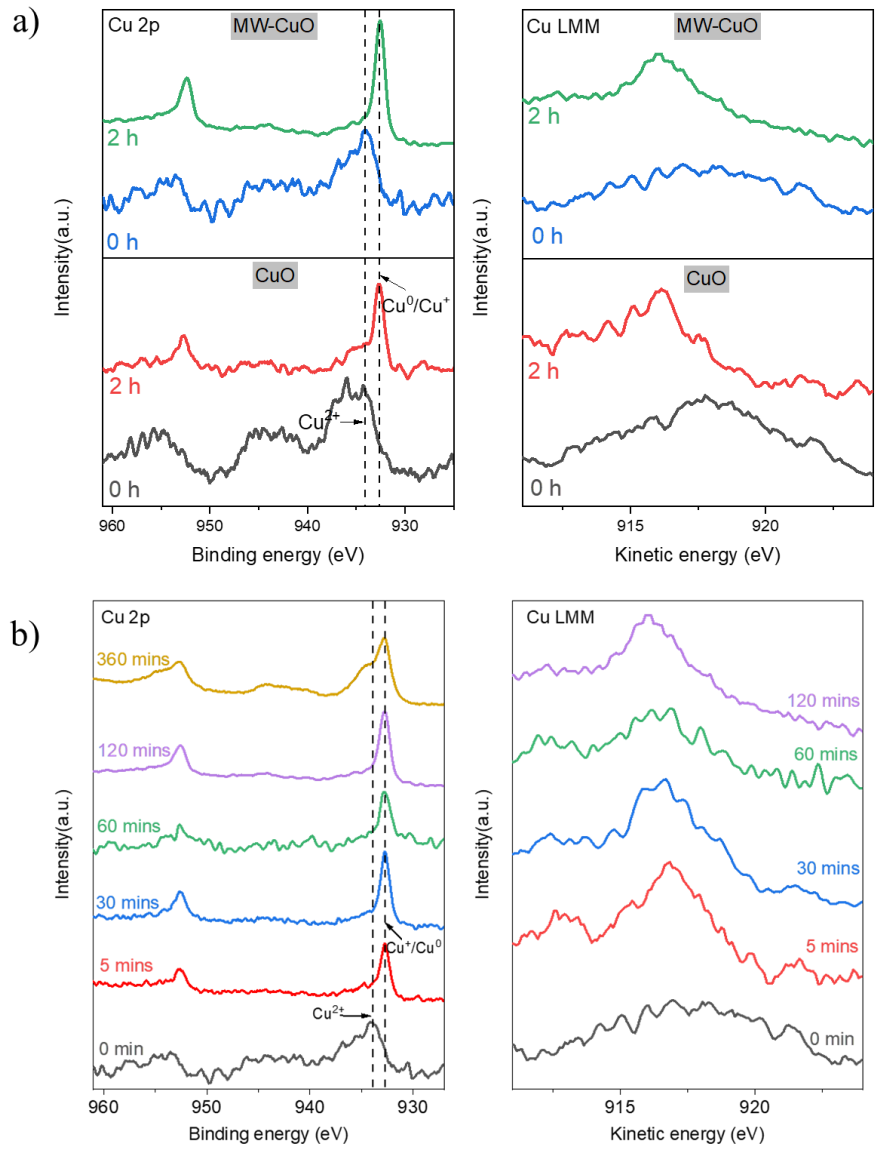

Figure 5.9 The high-resolution XPS Cu 2p and Cu LMM of a) CuO electrode and MW-CuO electrode; b) MW-CuO electrode before and after CO_2RR test at -1.04 V vs. RHE in the CO_2-saturated 0.1 M $KHCO_3$(aq) electrolyte.

Due to the limited detection depth (< 10 nm) of XPS, all electrodes were additionally analysed by XRD before and after the reaction (Figure 5.10). The crystal phase of CuO and MW-CuO remained unchanged in the fresh electrodes. The peaks occurring at 53° can be attributed to the carbon paper. After a 30-

minute CO_2RR test, both electrodes show similar peak shifts. No pattern could be found for CuO, but there are two clear peaks at 43.3 and 50.4° corresponding to (111) and (200) of Cu (PDF#04-0836) and a relatively weak peak at 36.4° corresponding to (111) of Cu_2O (PDF#05-0667), which is consistent with the XPS results. From the above results, it can be concluded that this change of oxidation state from Cu^{2+} to Cu^+ and Cu^0 occurs at the beginning of the reactions at a low working potential. Cu^0 and Cu^+ were the active species and relatively stable, even at a high negative potential during CO_2RR.

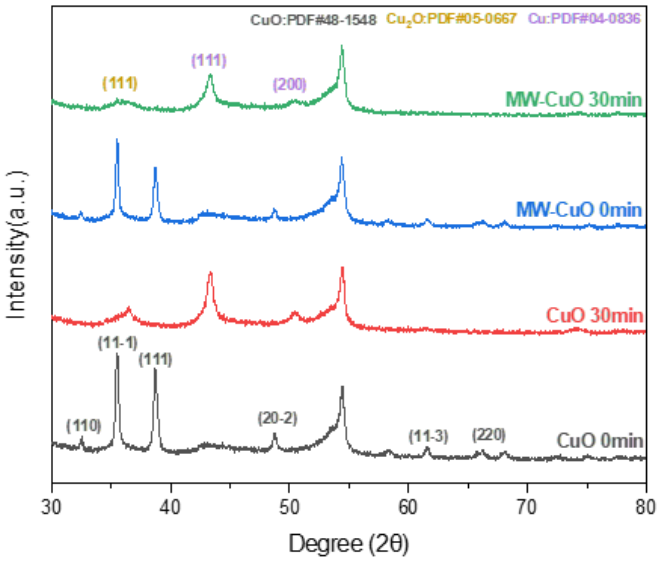

Figure 5.10 XRD of CuO electrode and MW-CuO electrode before and after 0.5-h eCO_2RR at -1.04 V vs. RHE.

The ratio of Cu^0 and Cu^+ plays a pivotal role in dictating the performance of CO_2ER. In this context, both the cathodic voltammetric reductive wave and the cumulative area of XRD serve as instrumental metrics for assessing the reduction degree of CuO. Since all Cu^{2+} was reduced at both electrodes, the absolute area of the reductive wave in the first cycle of CV may illustrate the degree of

reduction. With a minor reductive wave, the degree of reduction was lower at MW-CuO, so the fraction of Cu^+ should be larger than that at the CuO electrode. In addition, the integral area of the main XRD peaks is shown in Table 5.4. Although XRD could not quantify the amount of Cu^0 and Cu^+ on the electrodes, the ratio could be roughly judged. The ratio (111) of Cu_2O / (111) of Cu is 0.5 for the CuO electrode and 0.74 for MW-CuO, which suggests that more Cu^+ could be found on the MW-CuO electrode compared to the CuO electrode.

The coexistence of Cu^0 and Cu^+ at the electrode has proven to be favourable for the production of multicarbon products. The ratio of Cu^0 and Cu^+ exhibited variation between the CuO electrode and the MW-CuO electrode, providing a potential explanation for the disparity in product selectivity. The carbon atoms within *CO intermediates adhering to Cu^+ and Cu^0 surfaces exhibit disparate charges. This electrostatic disparity between the two carbon atoms enhances the dimerization process. The collaborative interaction between Cu^+ and Cu^0 on a CuO surface assumes a pivotal role in fostering the generation of C_{2+} products. The higher ratio of Cu^+ and Cu^0 (0.74:1) elucidates the better selectivity of the multicarbon products with the MW-CuO as an electrocatalyst.

Table 5.4 Integral area of the main facets of CuO and MW-CuO electrodes after 30 minutes' reaction.

	CuO	**MW-CuO**
Integral area of （111）facet of Cu_2O	315.46	289.38
Integral area of （111）facet of Cu	632.78	392.79
Integral area of （200）facet of Cu	77.48	64.53
Integral area of (111)/(200) of Cu	8.17	6.09
The integral area ratio of (111) of Cu_2O /(111) of Cu	0.50	0.74

5.2.4 Evolution of the catalyst morphology

A 6-hour stability test was performed at -1.04 V vs. RHE using the current interruption correction method (Figure 5.11). The Faradaic efficiency of H_2 increased for both the MW-CuO and CuO electrodes with a similar trend in current densities, while $FE_{ethylene}$ decreased by over 10% during the 5-hour reaction. It should be noted that the partial current density of ethylene is relatively stable for both electrodes. In addition, more charges are used for the production of CH_4, which would decompose into graphitic carbon and cause poisoning of the active site [61, 178].

Among the carbonaceous products, the selectivity of methane increased from 1.9 to 11.1% for the CuO electrode and from 4.3 to 6.7% for the MW-CuO electrode, while the selectivity of the carbonaceous products gradually decreased from 83.9 to 71.8% for CuO and from 85.1 to 80.5% for the MW-CuO electrode. More charges are used to produce CH_4, which may decompose into graphitic carbon and cause poisoning of the active site[178]. Defects have been found to play a dual role: they promote the formation of C_2H_4 while concurrently inhibiting the generation of CH_4, all the while enhancing the overall stability of the catalyst[61]. The change in product distribution shows that the low tendency of methane formation on the MW-CuO electrode prevents the deactivation of the catalysts, which partially explains why the production of the multicarbon product on the MW-CuO electrode continues for longer.

Apart from catalyst poisoning, the loss of activity in electrochemical CO_2 reduction can be attributed to catalyst degradation, surface fouling, changes in

electrolyte composition and structural changes [58]. To investigate this further, the SEM images of the electrodes before and after a certain reaction time are shown in Figure 5.12. Obviously, changes in the morphology and distribution of all catalysts were observed after CO_2 electrolysis at −1.04 V vs. RHE for two hours. The CuO particles were buried under the Nafion layer on the surface of the freshly prepared MW-CuO electrode. The catalysts on the electrode were spherical and well-distributed after the reaction. After a 5-minute eCO_2RR test at -1.04 V, uniformly distributed nanoclusters are found on the carbon paper. These nanoclusters are a mixture of Cu and Cu_2O, averaging 61.3 nm in size and consisting of 10.9 nm nanoparticles. These clusters continue to grow as the reaction progresses (Figures 5.12a-d and Table 5.5). After 6 hours, the clusters on the MW-CuO electrode have smaller and more uniform sizes (d = 270.33 ± 74.66 nm) than those on the CuO electrode (d = 327.95 ± 145.71 nm) (Figure 5.12e-h).

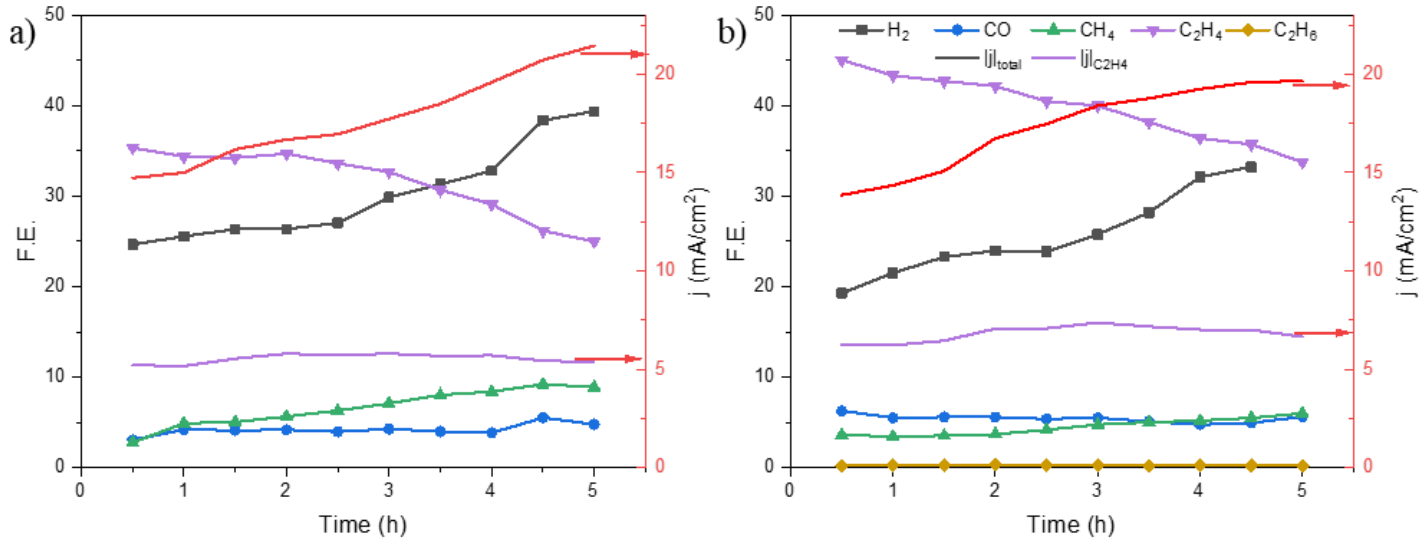

Figure 5.11 FE, $|j|_{C2H4}$ and $|j|_{total}$ of a) CuO electrode and b) MW-CuO electrode at the potential of -1.04 V with current interrupt correction under long-term operation.

Although the size of the nanoparticles on the CuO electrode is similar to that on the MW-CuO electrode, the growth of the clusters varies. At the same working potential, the growth of clusters on the MW-CuO electrode is slower, and the MW-CuO electrode exhibits a more uniform cluster density. These results indicate that the differences in the electrocatalytic activity of MW-CuO and CuO electrodes are due to the influence of microwaves on the nucleation and crystal growth process. The reduction and reconstruction at the beginning of the reaction lead to the formation of Cu^{+}, which effectively promotes the C-C coupling process, but the continuous agglomeration leads to a loss of activity and aggravates the hydrogen evolution reaction.

Table 5.5 The size of particles and clusters on the reacted CuO and MW-CuO electrodes.

Reaction time / Electrode		30 min	120 min	360 min
CuO	**Size of particles (nm)**	12.12 ± 2.72	10.46 ± 2.61	-
	Size of clusters (nm)	52.47 ± 13.67	63.71 ± 18.42	327.95 ± 145.71
MW-CuO	**Size of particles (nm)**	12.77 ± 2.36	13.54 ± 4.03	-
	Size of clusters (nm)	43.74 ± 9.33	60.06 ± 15.31	270.33 ± 74.66

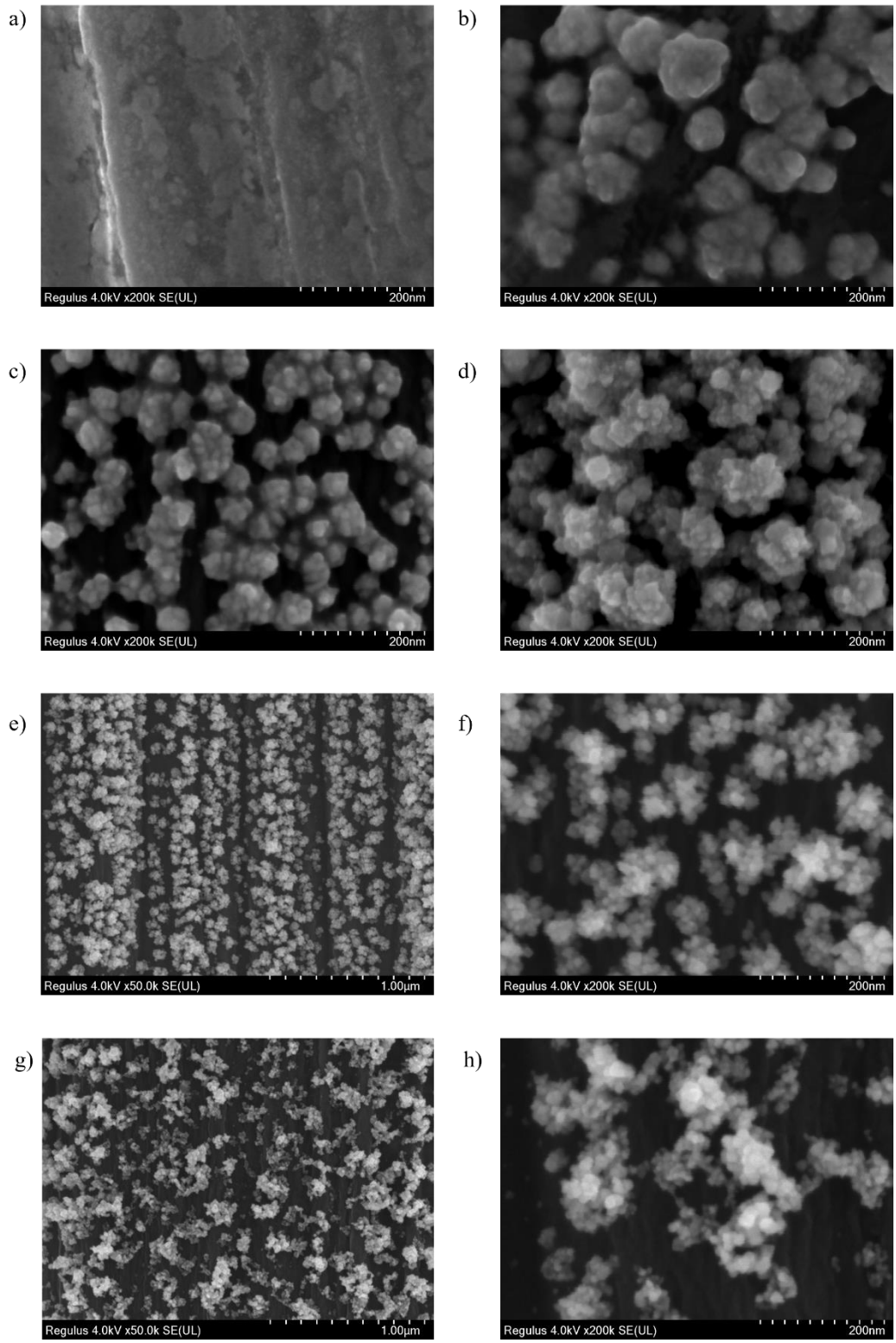

Figure 5.12 SEM of MW-CuO electrode after CO_2RR at -1.04 V for a) 0 minutes; b) 5 minutes; c) 30 minutes; and d) 120 minutes; CuO electrode after CO_2RR at -1.04 V for e, f) 30 minutes; g, h) 120 minutes.

5.2.5 Loss of defect sites

Defect sites such as vacancies and grain boundaries on copper-based electrocatalysts are considered essential for the reduction of CO_2 to higher C_2 and C_3 molecules, as they are very effective in stabilising C_1 and C_2 intermediates and trimerising them to C_3 compounds such as n-propanol. The grain boundaries were confirmed on the MW-CuO particles before the reaction (Figure 5.3). It is also hypothesised that CuO or Cu_2O nanoparticles are reduced and reconstructed in situ during the eCO_2RR test, resulting in numerous lattice distortions (3D volume defects) and oxygen vacancies.

The oxygen vacancies could be observed according to the elemental O 1s spectrum (Figure 5.13). The peak at binding energies at 531.6 eV (red line) corresponds to defect O. The high-intensity defect peaks observed in the electrode are indicative of a significant presence of defect sites, predominantly oxygen vacancies [282]. These materials with smaller particle sizes demonstrate characteristics of low oxygen coordination [231]. The oxygen vacancy phenomenon is detected not only in the pristine MW-CuO electrode but also in both electrodes post-reaction, suggesting the introduction of oxygen vacancies during sample preparation and their potential formation during the electrode reduction and reconstruction processes. Oxygen vacancies on catalyst surfaces significantly enhance CO_2RR by increasing CO_2 adsorption, modifying the catalyst's electronic structure, facilitating electron transfer, and directing the reaction towards desired products like ethylene [278]. This conclusion further corroborates the significance of defects for achieving outstanding performance of MW-CuO electrodes.

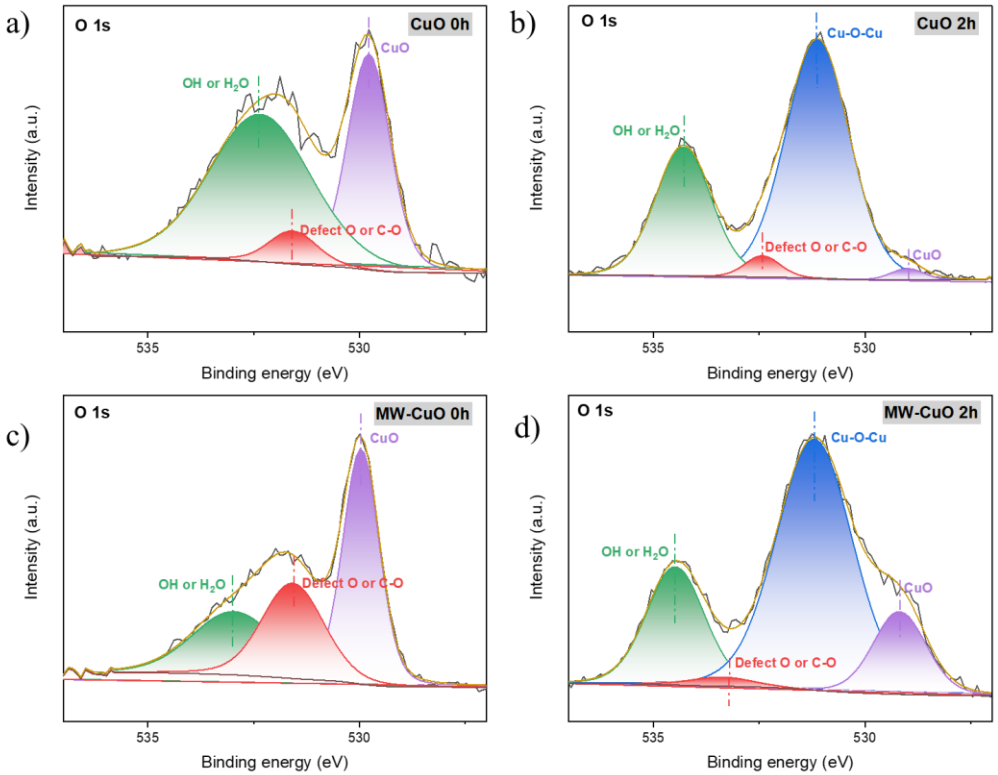

Figure 5.13 O 1s for CuO electrode a) before and b) after reaction and MW-CuO electrode c) before and d) after 1-hour reaction at -0.89 V vs. RHE in the CO2-saturated 0.1 M $KHCO_3$(aq) electrolyte.

The defect sites related to the reduction of CuO can be identified by their voltammetric properties in Figure 5.14 [177, 247]. The reduction peaks at ~ 0 and ~ -0.25 V vs. RHE were assigned to the reduction of oxidised Cu defect sites. The integrated charge value of these defect peaks was plotted in Table 5.6 and represents the density of defect sites. The density of defect sites on the MW-CuO electrode was twice that of the CuO electrode after 5 min of CO_2RR at -1.04 V (Figure 5.14a), while the FEs of C_{2+} products for the CuO and MW-CuO electrodes were 65.1 and 71.9%, respectively, confirming the significant role of defect sites in the promotion of C_{2+} products [283]. This result indicates that the

dense Cu nanocluster aggregation can form abundant surface defects, which is beneficial for the production of multi-carbon products. Another result was a continuous decrease in the integrated area of the reduction peak during CO_2RR. For the CuO electrode after 30 minutes of CO_2RR and the MW-CuO electrode after 90 minutes of CO_2RR, no reduction peaks could be detected in the corresponding region, indicating the loss of defect sites.

In addition, the distinct reduction peaks at ~ 0.5 and ~ 0.25 V could be related to the reduction of Cu^{2+} to Cu^{+} and Cu^{+} to Cu^{0}, respectively. The integrated charge value of the peaks is directly related to the electrochemically active surface areas of the electrodes [284].

From the cyclic voltammograms of the electrodes before and after the reaction over a period of time in Figure 5.14b-c, the active surface area of the CuO electrode continued to decrease after 5 minutes of CO_2RR, while the decrease in ECSA for the MW-CuO electrode was less during the first 90 minutes. The agglomeration of catalyst particles or surface impurities could cause the loss of ECSA. In addition, this decrease could cause the decreasing FE of ethylene during the long-term test. The defect sites could be blocked or poisoned by the growth of nanoclusters, leading to a decrease in the yield of ethylene and other multi-carbon products by about 25%.

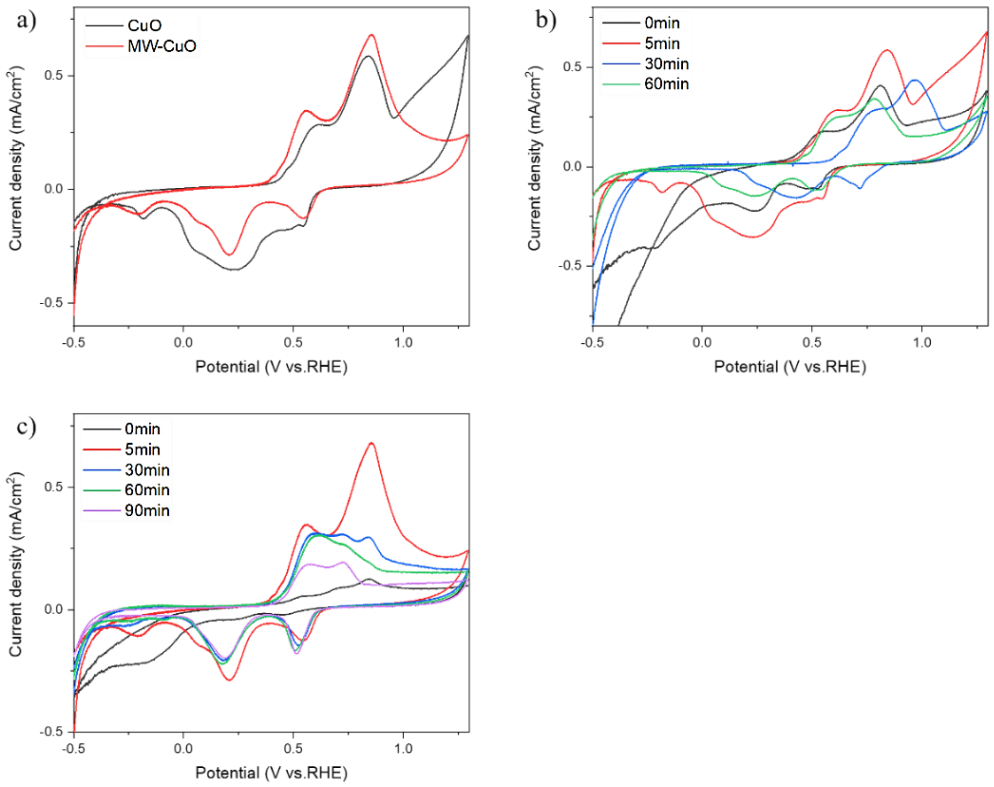

Figure 5.14 a) CVs of CuO and MW-CuO electrodes after a 5-min CO_2RR reaction; b) CuO and c) MW-CuO electrodes before and after CO_2RR reaction for a certain period in 0.1 M $KHCO_3$ (saturated with N_2) at the scan rate of 10 mV/s.

Table 5.6 The area of reduction peak at ~ -0.25 V vs. RHE for electrodes after the CO_2RR test at -1.04 V for a certain period.

	0min	**5min**	**30min**	**60min**	**90min**
CuO	0.00441	0.00393	0	0	0
MW-CuO	0.01047	0.00503	0.0019	0.00115	0

5.2.6 Reaction mechanisms of CO_2 reduction

There are several possible reaction pathways to the C_{2+} products, with C−C coupling being a crucial step. In this work, the presence of Cu^0 and Cu^+ in the spent CuO and MW-CuO electrodes was confirmed, with a higher Cu^+/Cu^0 ratio found on the MW-CuO electrode than on the CuO electrode. Before the reaction, the MW-CuO was rich in defects, such as grain boundaries. During in situ reduction and reconstruction of CuO nanoparticles, defect sites form on staggered lattices in which Cu atoms have low coordination. These defect sites serve as nucleation sites for oxide, leading to the occurrence of Cu^+ species along the grain boundaries of Cu [285].

In recent theoretical studies on the CO_2 reduction process on Cu^+/Cu^0, it has been suggested that the rate-limiting step is the dimerisation of CO, which can be facilitated by increasing the coverage of *CO species. Since the adsorption of *CO and *H on the Cu_2O (111) facets was calculated to be relatively strong and the desorption of C_2H_4 to be weak, the higher proportion of Cu^+ on the MW-CuO electrode should lead to better selectivity for ethylene compared to the CuO electrode [286]. In addition, the opposite charges of the carbon atoms in the *CO intermediates bound to Cu^0 and Cu^+ create an electrostatic attraction that further promotes dimerisation [286-288]. The introduction of GBs into Cu^0 and Cu^+ should further enhance the C-C coupling process, as the Cu^+/Cu^0 interfaces are thermodynamically more favourable for the formation of *CO species. Therefore, rapid and uniform microwave heating should promote the nucleation and growth of MW-CuO nanoparticles and induce the formation of defects. These defects are crucial for the stabilisation of the C_1 intermediate and improve the electrocatalytic selectivity for multi-carbon products in eCO_2RR.

5.3 Summary

In summary, this study shows that the application of microwave heating in the synthesis of CuO can lead to a GB-rich CuO product with improved electrocatalytic activity and selectivity for C_{2+} products in the electrochemical reduction of CO_2. The mass ratio of the precursors determines the morphology and size of the resulting CuO nanoparticles during the nucleation and crystal growth process. With the optimal Cu^{2+} and CO_3^{2-} feed ratio of 1.1:1, the MW-CuO achieved 71.9% FE of C_{2+} products and 45.1% FE of ethylene, while the current density reached about 15.5 mA/cm^2 at a potential of -1.04 V vs. RHE. Compared to the CuO electrode, more Cu(I) was found on the MW-CuO electrode. The synergistic effect of Cu_2O and defect sites could be the reason for the increased formation of multi-carbon products. The practical synthesis approach developed in this study offers a promising strategy for the development of efficient and selective electrocatalysts for the conversion of CO_2 to C_{2+} products.

Chapter 6. Cu-electrodeposition modified electrodes for eCO$_2$RR to C$_{2+}$ products

6.1 Introduction

The optimisation of C-C coupling to achieve high activity and selectivity for multi-carbon products while suppressing the formation of undesired by-products is crucial for the commercial viability of CO_2RR [259, 289]. In recent years, electrodeposition technology has shown enormous potential for the production of electrodes [290-292]. Electrodeposition involves the deposition of metals or alloys on the surface of an electrode to produce the desired structures and properties [192]. By manipulating the deposition conditions such as current density, deposition time and electrolyte composition, the morphology, crystalline structure, and chemical composition of the electrode can be precisely controlled [293-296].

Pulse electrodeposition (P-ED) has been used for copper coatings on carbon paper. The resulting copper electrodes show high faradaic efficiency for methane (85% at −2.8 V vs. SCE). The improved activity can be attributed to increased active sites, a rough surface, and a loose structure that facilitates CO_2 access to the sub-layers of the copper coatings [297]. C_{2+} products can also be obtained with electrosynthetic Cu catalysts under controlled deposition conditions. The high-density copper nanoplatelet synthesised by electrodeposition on copper foil has predominantly Cu(200) facets. The copper nanoplatelet has a high partial current density of − 9.6 mA/cm^2 compared to C_2 products [298]. Electrodeposition is often used for the production of electrodes, effectively

achieving the desired performance [196, 258, 299, 300]. However, it is rarely used as a technique for modifying electrodes [191].

In this study, electrodeposition was used to modify the Cu_2O-C_3N_4 electrodes. The influence of electrodeposition on the catalyst activity and selectivity of the catalyst was investigated, with the aim of improving the overall efficiency of CO_2 conversion and facilitating the selective synthesis of multi-carbon products. Besides, the degradation of the electrode and the effect of the substrate on the electrodeposition process were investigated.

6.2 Results and discussion

6.2.1 The characterization of Cu_2O-C_3N_4

SEM analysis revealed the morphology and nanostructure of the C_3N_4, Cu_2O and Cu_2O-C_3N_4 samples. The pure C_3N_4 exhibits a loosely layered structure, while the pure Cu_2O shows a well-defined cubic structure with a size of several tens to several hundred nanometers (Figure 6.1a, b). The in-situ formation of Cu_2O cubes on the C_3N_4 nanosheets by chemical reduction is shown in Figure 6.1c. The synthesised Cu_2O in the Cu_2O-C_3N_4 heterojunction has a similar morphology and size as the pure Cu_2O. However, due to the small amount of C_3N_4, it is difficult to identify it using SEM images. Therefore, element mapping was performed, as shown in Figure 6.1d and Table 6.1, which shows the uniform distribution of the individual elements.

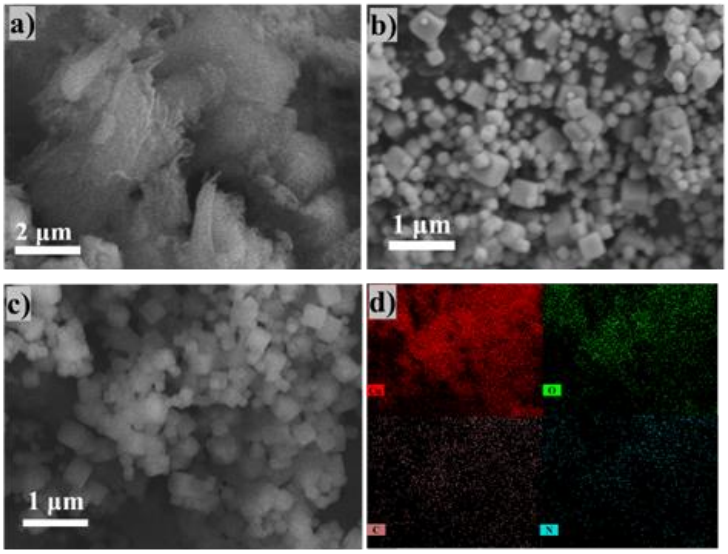

Figure 6.1 SEM images of a) C_3N_4, b) Cu_2O and c) Cu_2O-C_3N_4 powder; d) SEM-EDS mapping.

Table 6.1 The element content in the prepared sample obtained by the SEM-EDS.

Sample	Element (Atomic%)			
	Cu	O	C	N
C_3N_4	-	-	43.8	56.2
Cu_2O	62.6	37.4	-	-
Cu_2O-C_3N_4	38.2	20.0	29.1	12.7

In order to gain a deeper understanding of the structural properties of Cu_2O-C_3N_4, a thorough investigation was carried out using high-resolution transmission electron microscopy. Figure 6.2a shows the presence of both C_3N_4 and Cu_2O. Given the relatively low content of C_3N_4, it is very likely that it is partially enveloped by the cubic Cu_2O particles. It is noteworthy that distinct lattice fringes were observed in Cu_2O-C_3N_4, as shown in Figure 6.2b. These fringes were attributed to the (111) facet of Cu_2O based on the measured distance between the planes.

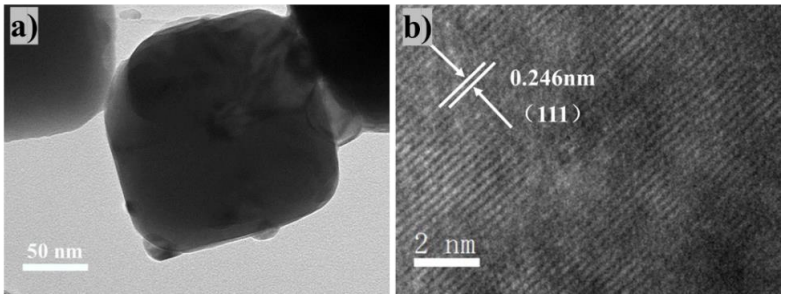

Figure 6.2 a) TEM images of Cu_2O-C_3N_4; b) high-resolution TEM image of the selected area.

X-ray diffraction measurements also confirmed that the Cu_2O-C_3N_4 nanoparticles consist of a mixture of Cu_2O and C_3N_4 (Figure 6.3). It is noteworthy that both the C_3N_4 nanosheet and Cu_2O-C_3N_4 sample patterns have a characteristic diffraction peak at 27.0°, which corresponds to the C_3N_4 crystal structure (JCPDS #87-1526). In addition, the other diffraction peaks of Cu_2O-C_3N_4 samples correspond to those of Cu_2O, dominated by the (111) crystal face of Cu_2O at 36.4° (JCPDS #05-0667). This confirms the successful synthesis of the Cu_2O-C_3N_4 composite without any impurity phases.

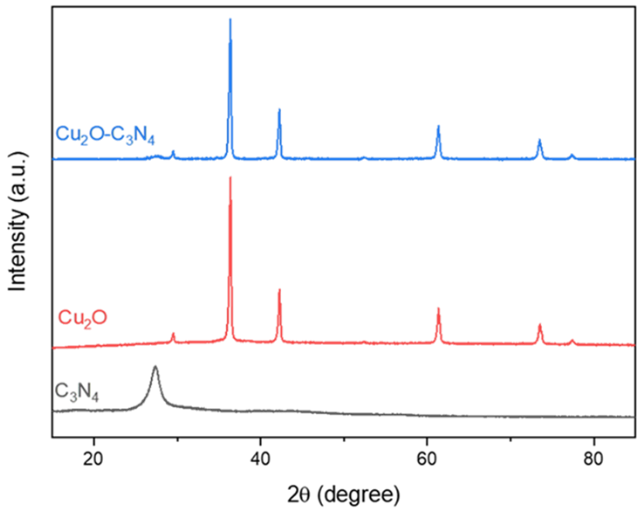

Figure 6.3 XRD pattern of Cu_2O, C_3N_4 and Cu_2O-C_3N_4.

X-ray photoelectron spectroscopy was used to investigate the valence state of copper in the Cu_2O-C_3N_4 catalyst (Figure 6.4). The discovery of a prominent peak at 931.6 eV provided strong evidence for the existence of Cu(I) in the recently synthesised Cu_2O-C_3N_4 catalyst (Figure 6.4d). This finding was further supported by the Auger spectrum of copper (Figure 6.4e). When the Cu 2p peaks are deconvoluted, a small peak at a higher binding energy of 933.7 eV indicates the presence of Cu(II) species [285]. While the Cu(I) species dominates, the small amount of Cu(II) observed could be due to oxidation of the sample prior to testing or insufficient amounts of ascorbic acid during Cu_2O-C_3N_4 synthesis, resulting in incomplete reduction of the copper hydroxide.

The elemental O 1s spectrum could be fitted into three different peaks at binding energies of 530.3, 531.0, and 532.1 eV, corresponding respectively to the lattice oxygen (O_2-) in the Cu_2O phase, the defect O and the O- species adsorbed on the surface with an affinity to bind with hydrogen (Figure 6.4b) [254, 301]. In addition, the XPS peaks of C 1s and N 1s in the sample are in excellent agreement with those of C_3N_4, confirming the presence of C_3N_4 in the Cu_2O-C_3N_4 composite (Figure 6.4a, c) [187]

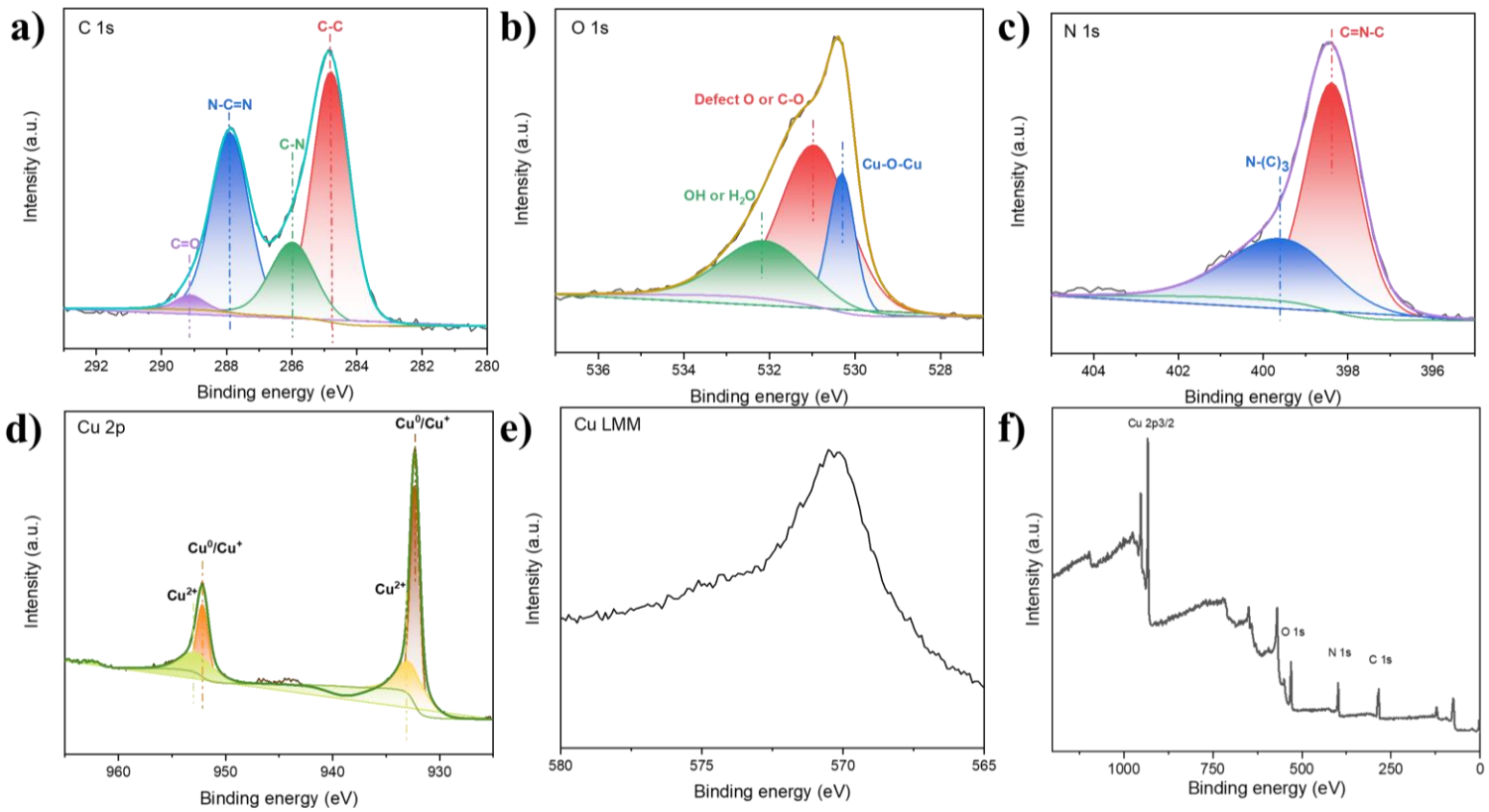

Figure 6.4 High-resolution XPS spectra of Cu_2O-C_3N_4.

6.2.2 The characteristics of the Cu@Cu_2O-C_3N_4 electrodes

The Cu_2O-C_3N_4 catalyst was processed into a Cu_2O-C_3N_4 electrode. The Cu electrodeposition was carried out on the Cu_2O-C_3N_4 electrode in a 0.01 M $Cu(NO_3)_2$ solution at a current density of -2.5 mA/cm^2. The electrodeposited electrode was named Cu@Cu_2O-C_3N_4. SEM-EDS was used to characterise the morphological changes and elemental distribution on the electrode surface before and after electrodeposition. No change in the particles on the Cu_2O-C_3N_4 electrode surface was observed, which corresponds to the state before coating (Figure 6.5a). The Nafion layer acts as a binder that holds the particles to the surface of the carbon paper. Red or black "tufts" grow on the orange-red electrode surface during the deposition process. Figure 6.5b shows that copper branches with a diameter of less than 100 nm grow on the electrode surface, completely covering the underlying Cu_2O-C_3N_4. Compared with the original electrodes, the electrodeposited electrode yields a three-dimensional hierarchical structure, which could facilitate rapid electron and mass transfer and enhance catalytic performance[191, 302-304].

SEM-EDS analysis shows that after electrodeposition, the atomic ratio of copper to oxygen on the electrode surface decreases from 2.03 to 1.62, while the ratio of carbon to nitrogen remains relatively unchanged (Table 6.2). Based on the decrease in the copper-to-oxygen ratio and the colour of the "clumps" on the Cu@Cu_2O-C_3N_4 electrode surface, it can be deduced that the material deposited on the electrode surface is probably a mixture of CuO and Cu.

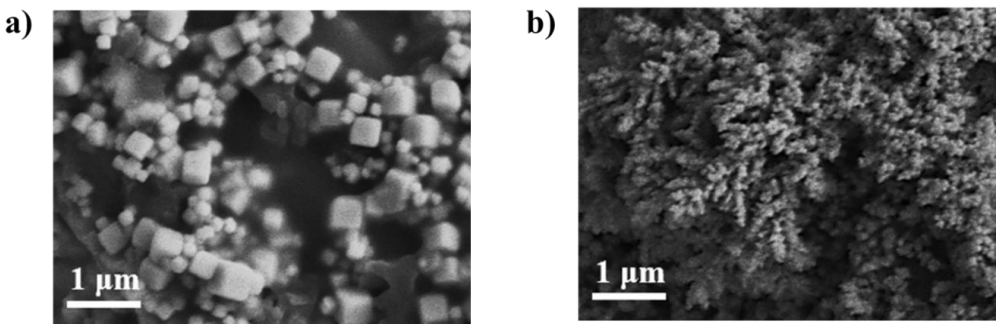

Figure 6.5 SEM images of a) Cu_2O-C_3N_4 electrode and b) Cu@Cu_2O-C_3N_4 electrode.

XPS measurements were carried out to gain deeper insights into the chemical state of the surface copper (Figure 6.6a). For the Cu_2O-C_3N_4 electrode, the Cu 2p 3/2 binding energy was measured at 932.7 eV, a range consistent with that expected for Cu^0 and Cu^+. The modified Auger parameter, referred to as α', provides valuable information about the electronic structure of the copper species and its bonding properties. It can be calculated by the combined kinetic energy of the Cu LMM Auger electron and the binding energy of the Cu 2p3/2 photoelectron. The α' value for the pristine Cu_2O-C_3N_4 electrode was 1849.2 eV, indicating the presence of copper as Cu^+ [305]. In particular, the XPS spectra of the Cu_2O-C_3N_4 electrode indicated the presence of Cu^{2+}, as indicated by the peak at about 935.5 eV. This is probably due to accidental exposure to air during transport of the sample to the XPS spectrometer, as no feature of CuO was found in the XRD pattern (Figure 6.6b).

The semi-quantitative analysis of copper in different valence states is based on the peak matching of Cu 2p. After the electrodeposition of Cu, three types of valence copper occur simultaneously in the electrode, of which Cu^0 takes up a significant proportion (Table 6.3). The crystal phase of Cu (JCPDS#04-0836) with a peak at 43.3° was also confirmed by X-ray diffraction. However, no

characteristic peak of CuO was found on the electrode after electrodeposition. Excluding the effect of electrode oxidation, the divalent copper on the electrode surface could have been formed by rapid oxidation of electrodeposited copper in copper nitrate solution, and only the top layer of Cu was oxidised, which is consistent with the XPS and SEM results. These results suggest that elemental copper is deposited on the surface of Cu_2O-C_3N_4 during electrodeposition, with some of the surface copper being oxidised to CuO.

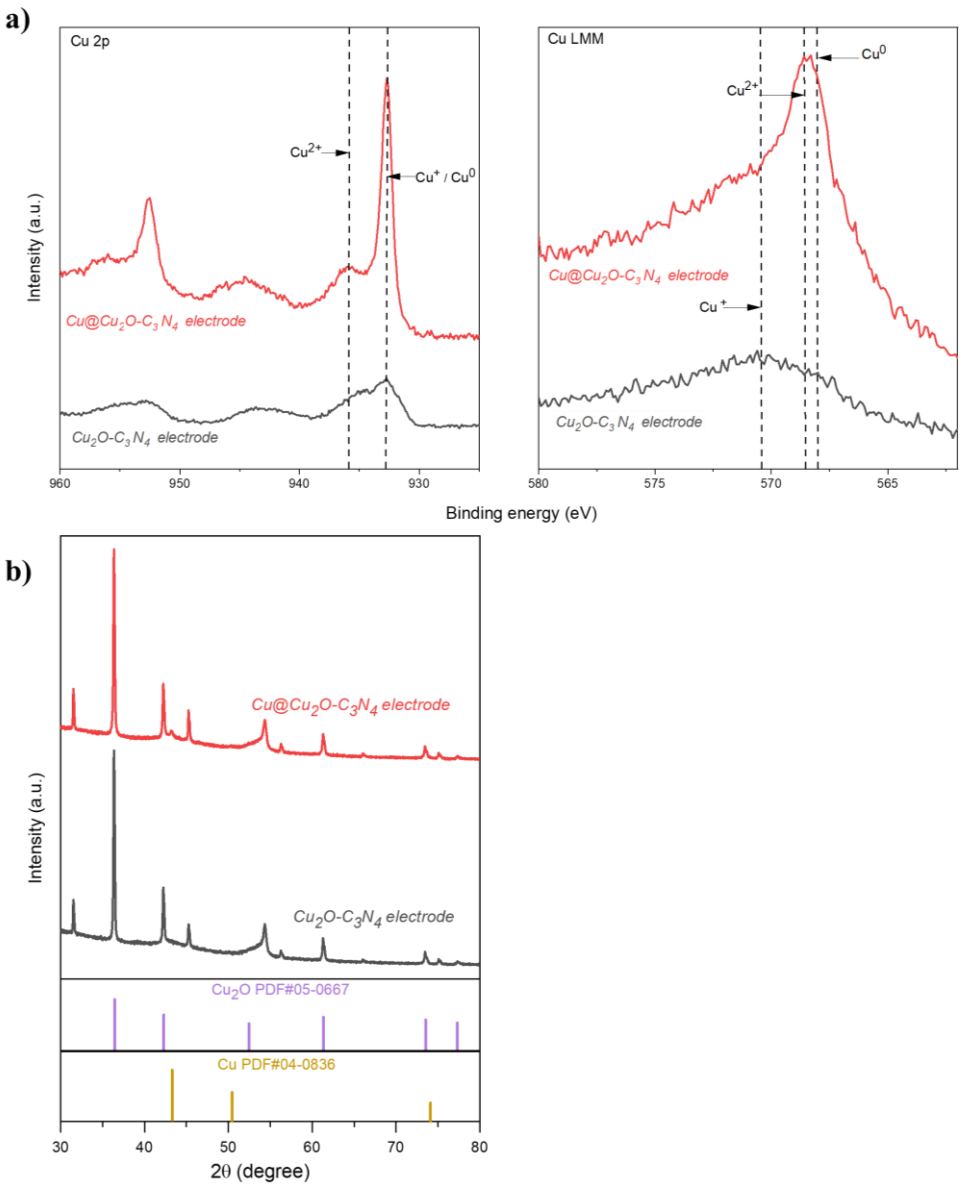

Figure 6.6 a) XPS Cu 2p and LMM; b) XRD for pristine electrodes.

The influence of electrodeposition on the activity and selectivity of CO_2RR at the Cu_2O-C_3N_4 electrode was investigated. Constant potential electrolysis was carried out for 30 minutes using potentials from -1.09 to -0.89 V vs. RHE in a CO_2-saturated 0.1 M $KHCO_3$ solution (Figure 6.7). For the pristine Cu_2O-C_3N_4 electrode, the predominant products obtained over the range of potentials investigated were H_2 and C_2H_4. Remarkably, the faradaic efficiency of H_2 initially decreased from 34.2 to 22.2% when more negative potentials were applied, while the FE of ethylene continued to increase and eventually reached around 30.2% when a potential of -1.09 V vs. RHE was used. It is worth noting that a significant portion of the total charges, about 28.1%, was used to generate the single carbon products CO, HCOOH and CH_4, indicating a limited selectivity of the Cu_2O-C_3N_4 electrode.

The Cu@Cu_2O-C_3N_4 electrode shows a significant improvement in selectivity compared to the Cu_2O-C_3N_4 electrode, particularly in the production of C_{2+} carbon products, especially ethylene, with a higher faradaic efficiency (Figure 6.7). Electrodeposited Cu significantly increases the faradaic efficiency of multi-carbon products, from 46.0% for Cu_2O-C_3N_4 to 64.0% for Cu@Cu_2O-C_3N_4 at -1.04 V vs. RHE. The FE for C_2H_4 reaches 36.1% for Cu@Cu_2O-C_3N_4, compared to 28.7% for Cu_2O-C_3N_4. In addition, the electrodeposited Cu shifts the product distribution, reducing the proportion of one-carbon products and emphasizing the potential to produce C_{2+} products.

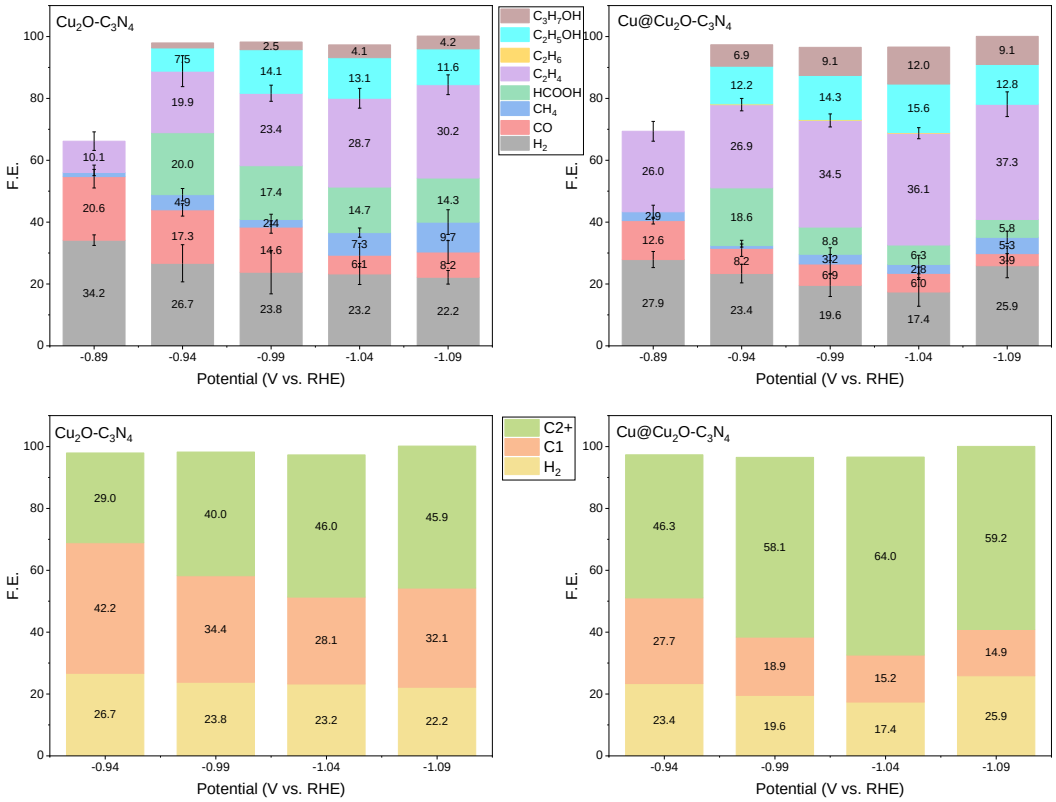

Figure 6.7 The product distribution under different working potentials (with current interrupt-corrected).

The comparison of the current density (|j|) further underpins the favourable effects of electrodeposition (Figure 6.8a, b). The total current density for the $Cu@Cu_2O$-C_3N_4 electrode has more than doubled at the working potential. The partial current density for multi-carbon products also shows a significant improvement. For example, the Cu_2O-C_3N_4 electrode shows $|j|_{ethylene}$ = 1.2 mA/cm^2 at -0.99 V vs RHE, while the $Cu@Cu_2O$-C_3N_4 electrode shows $|j|_{ethylene}$ = 5.0 mA/cm^2, which is more than a fourfold increase. Under this working condition, the $|j|_{C2+}$ increases from 2.1 to 8.3 mA/cm^2. In addition, the increased catalytic activity at the $Cu@Cu_2O$-C_3N_4 electrode remains constant over the entire potential range investigated, and the current density for multi-carbon

products reaches a maximum value of 12.7 mA/cm^2 ($|j|_{ethylene}$ = 7.2 mA/cm^2) at -1.04 V vs. RHE.

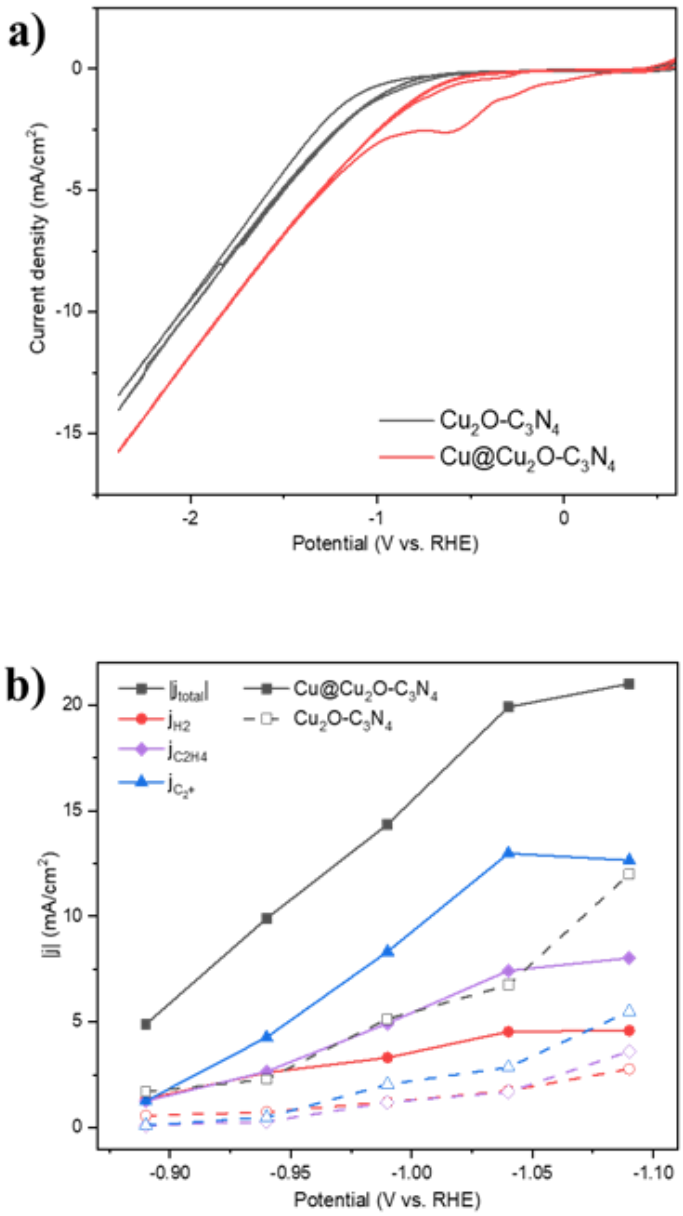

Figure 6.8 a) Cyclic voltammograms of electrodes in CO_2-saturated 0.1 M $KHCO_3$ electrolyte at a scan rate of 40 mV/s without iR correction; b) the total and partial current density of H_2, C_2H_4 and C_{2+} products for both electrodes.

6.2.3 Active sites

Significant differences can be observed on the surface of the electrodes before and after the reaction. The particles on the Cu_2O-C_3N_4 electrode turn into nanoscale particles after one hour of eCO_2RR and show a uniform distribution on the surface of the carbon fibre (Figure 6.9b). The electrodeposited electrode also shows similar changes after the reaction but with relatively uneven particle sizes and distributions, with some spherical particles exceeding 100 nm (Figure 6.9e). EDS analysis shows a significant reduction in copper content on both electrode surfaces after the reaction, with the Cu_2O-C_3N_4 electrode showing a more significant reduction (Table 6.2). This indicates surface reconstruction and partial detachment of copper from the electrode, indicating a probable reduction of copper oxide during the reaction.

Table 6.2 The element content in the electrodes as determined by SEM-EDS.

Electrode	Element (Atomic%)				
	Cu	O	C	N	F
a) Cu_2O-C_3N_4 before reaction	39.7	19.6	26.2	5.0	9.5
b) Cu_2O-C_3N_4 after 1-hour reaction	19.2	18.7	39.3	3.8	13.4
c) Cu_2O-C_3N_4 after 3-hour reaction	2.1	4.9	87.8	2.4	1.3
d) Cu@Cu_2O-C_3N_4 before reaction	34.8	21.5	27.5	7.7	8.6
e) Cu@Cu_2O-C_3N_4 after 1-hour reaction	29.5	17.3	32.7	4.3	16.2
f) Cu@Cu_2O-C_3N_4 after 3-hour reaction	1.2	4.2	92.4	1.8	0.5

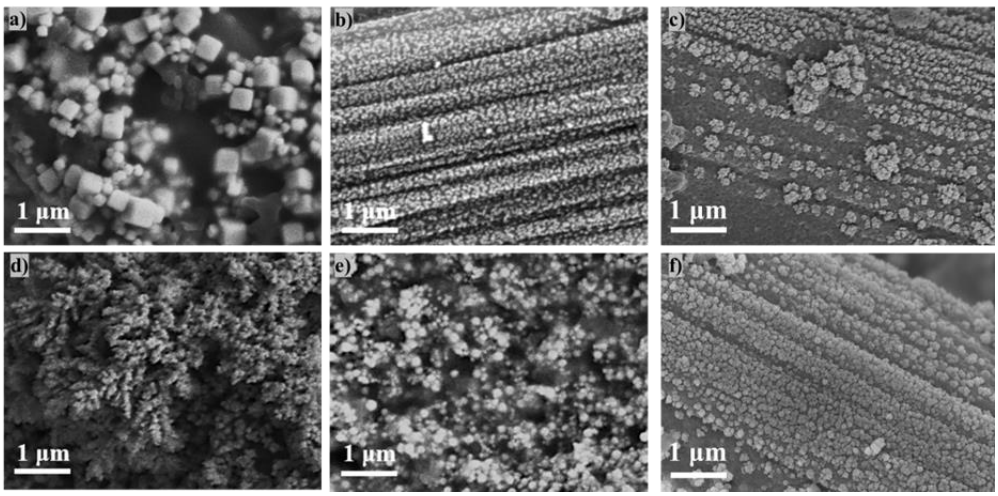

Figure 6.9 SEM images of Cu_2O-C_3N_4 electrodes a) before, after b) 1-hour and c) 3-hour reaction and Cu@Cu_2O-C_3N_4 electrodes d) before, after e) 1-hour and f) 3-hour reaction.

In order to determine the actual active species in the reaction, the XPS measurements for the electrodes were carried out according to eCO_2RR (Figure 6.10). Both the Cu_2O-C_3N_4 and Cu@Cu_2O-C_3N_4 electrodes appeared to have been reduced to a mixture of Cu^+ and Cu^0, as shown by the main peak at 568.0 eV and a smaller matched peak at 570.5 eV in the Cu LMM, which is consistent with the properties of metallic Cu and Cu^+. This result is confirmed by the XRD pattern, which shows that the characteristic peak of Cu_2O decreases significantly after the reaction while the characteristic peak of zero-valent copper becomes clearer (Figure 6.10a). Therefore, Cu^{2+} and Cu^+ on the Cu_2O-C_3N_4 and Cu@Cu_2O-C_3N_4 electrode were reduced to a mixture consisting mainly of metallic Cu, together with a small amount of Cu^+, which probably originated from the unreacted Cu_2O and the reduced CuO during eCO_2RR.

After peak matching of Cu 2p 3/2, the ratio of Cu^+ and Cu^0 is calculated to be 0.83 and 1.13 for the Cu_2O-C_3N_4 and Cu@Cu_2O-C_3N_4 electrodes after the 1-

hour reaction (Table 6.3). It has been shown that the presence of Cu^+ facilitates the adsorption and reaction of CO_2 molecules [264, 285]. In addition, an appropriate ratio of monovalent and zero-valent copper can promote the C-C coupling process and favour the formation of multi-carbon products [263]. The performance of the electrodes indicates that more multi-carbon products are produced at a Cu^+ to Cu^0 ratio of 1.13 compared to methane. This indicates an enhanced C-C coupling process leading to the formation of more carbon-containing products such as C_2H_4 and C_2H_5OH.

Table 6.3 The proportion of each copper valence state on the electrode before and after the reaction according to the fitting peak for XPS Cu 2p 3/2.

Electrode	Peak concentration %			Cu^+/Cu^0
	Cu^0	Cu^+	Cu^{2+}	
a) Cu_2O-C_3N_4 before reaction	0	31.7	35.2	-
b) Cu_2O-C_3N_4 after 1-hour reaction	19.2	16.0	25.3	0.83
c) Cu_2O-C_3N_4 after 3-hour reaction	19.9	23.9	15.2	1.20
d) Cu@Cu_2O-C_3N_4 before reaction	28.8	23.0	11.3	0.80
e) Cu@Cu_2O-C_3N_4 after 1-hour reaction	19.0	21.5	19.7	1.13
f) Cu@Cu_2O-C_3N_4 after 3-hour reaction	20.1	27.7	9.82	1.38

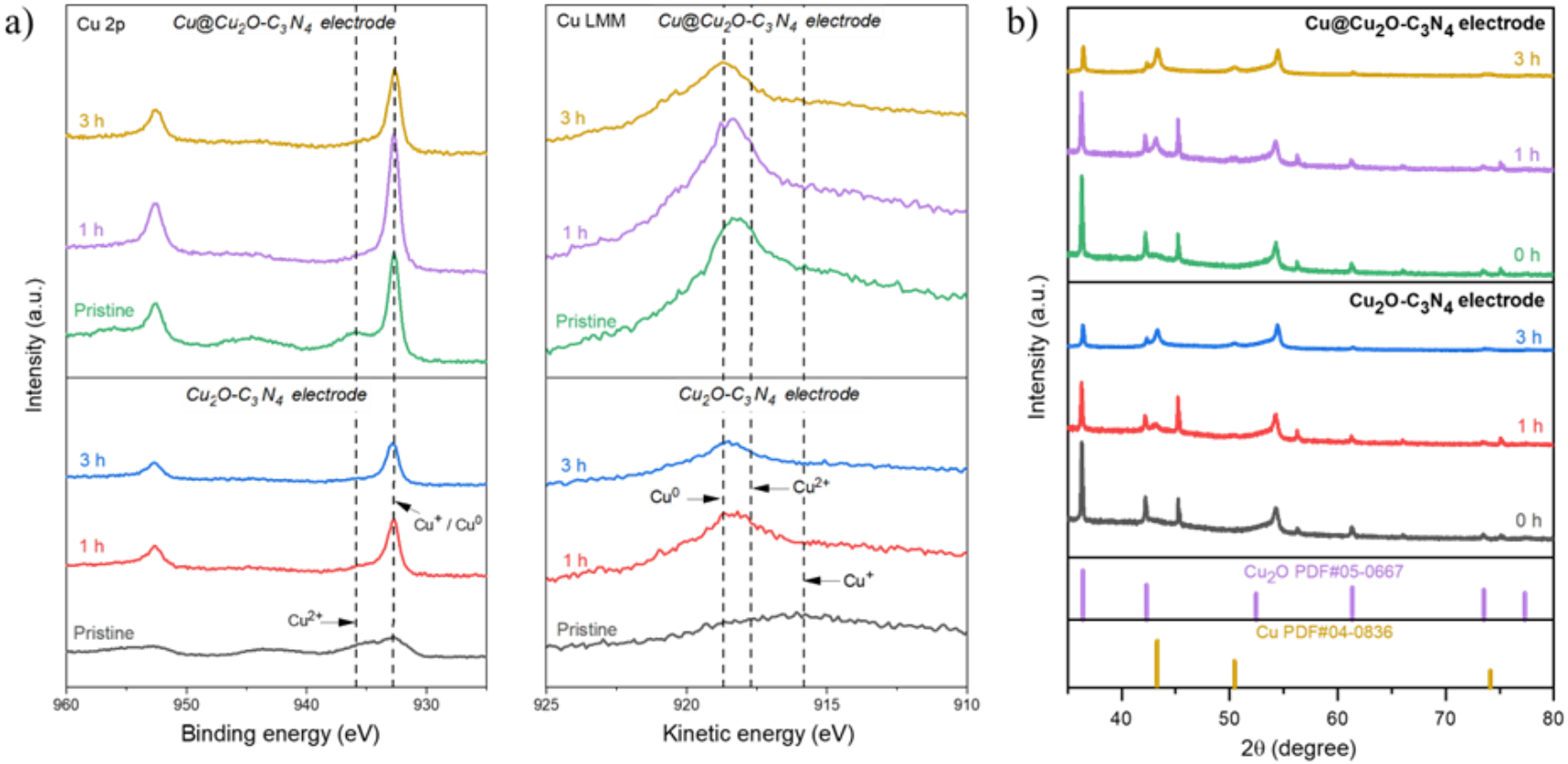
a)
Cu 2p
Cu@Cu2O-C3N4 electrode
3 h
1 h
Pristine
Intensity (a.u.)
Cu2O-C3N4 electrode
3 h
1 h
Pristine
Cu+ / Cu0
Cu2+
960
950
940
930
Binding energy (eV)
Cu LMM
Cu@Cu2O-C3N4 electrode
3 h
1 h
Pristine
Cu2O-C3N4 electrode
3 h
Cu0
Cu2+
1 h
Cu+
Pristine
925
920
915
910
Kinetic energy (eV)
b)
Cu@Cu2O-C3N4 electrode
3 h
1 h
0 h
Cu2O-C3N4 electrode
3 h
1 h
0 h
Intensity (a.u.)
Cu2O PDF#05-0667
Cu PDF#04-0836
40
50
60
70
80
2θ (degree)

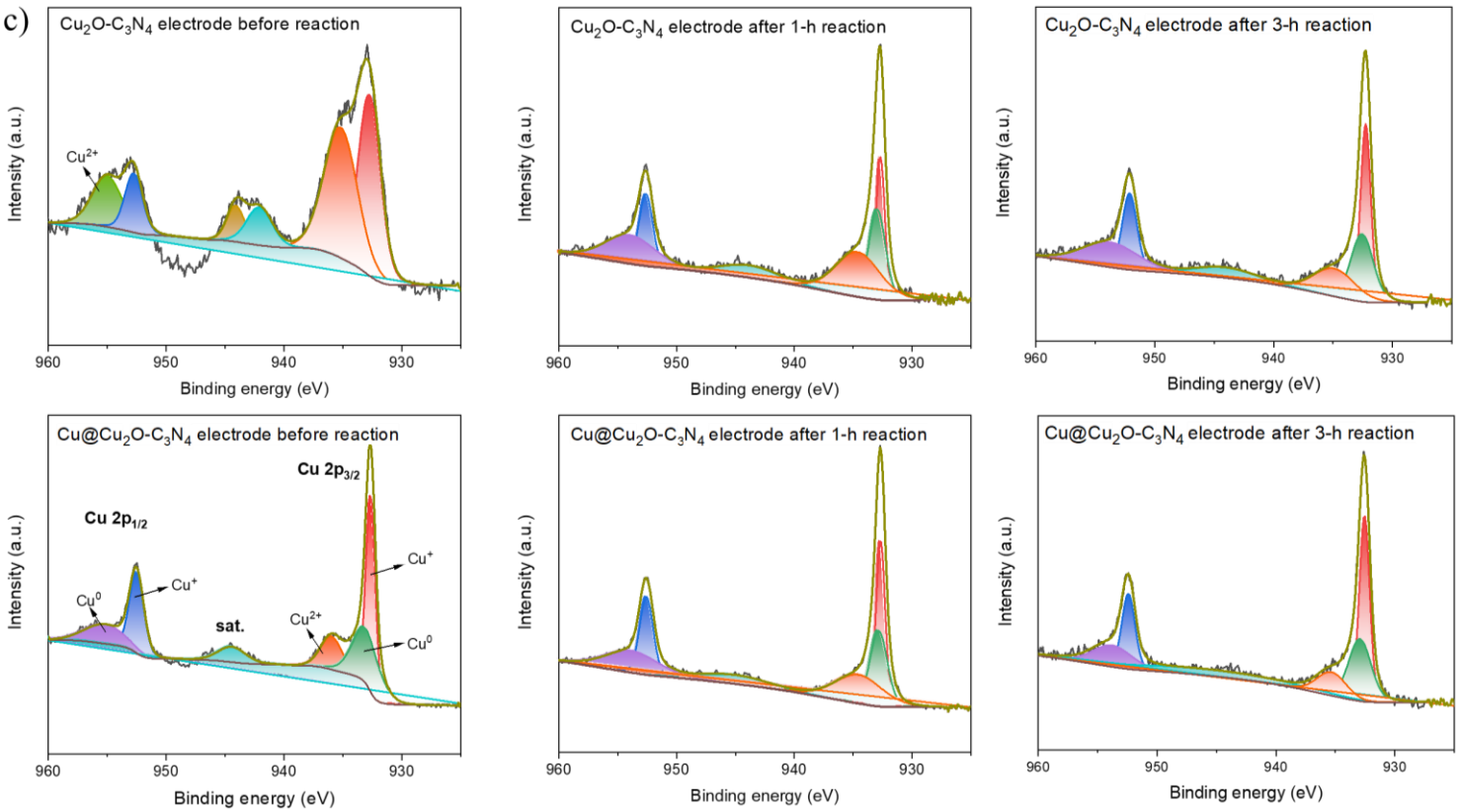

Figure 6.10 a) XPS Cu 2p and LMM; b) XRD pattern; c) the fitted Cu 2p for pristine electrodes and electrodes after 1-hour eCO_2RR at -1.04 V vs. RHE. Different colours correspond to different valence peaks of copper.

The electrochemically active surface of the electrode can be assessed by measuring the double-layer capacitance of the catalyst [195, 306]. Here, the electrodeposition process leads to a 0.5-fold increase in the electrochemically active sites on the electrode surface (Figure 6.11a-c). The formation of additional active sites can be attributed to the metal deposition and the restructuring of the surface during electrodeposition. The increased number of active sites has a positive effect on the activity and efficiency of the catalytic reactions and increases the activity over time.

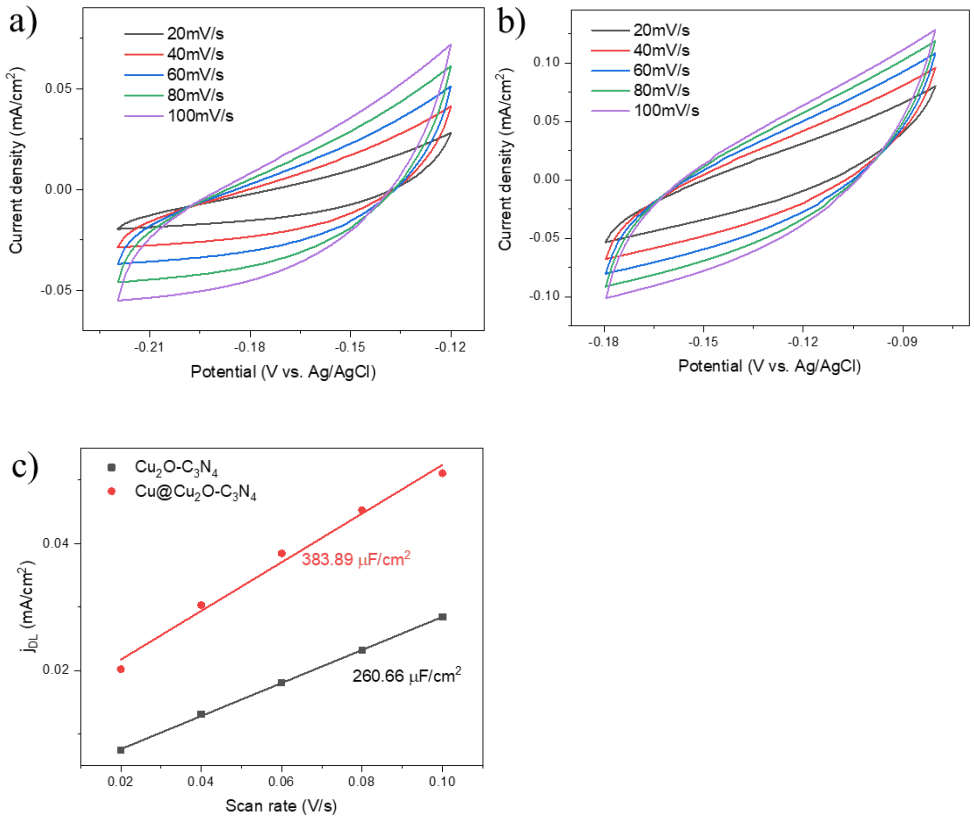

Figure 6.11 a, b) CV curves in a non-Faradaic region at various scan rates in CO_2-saturated 0.1 M $KHCO_3$ solution of electrodes after a 10-minute reaction; c) plots of double layer current density, j_{dl} against scan rate, the slope of which is identified with the capacitance of double layer.

In addition, the $Cu@Cu_2O-C_3N_4$ electrode shows a significantly lower charge transfer resistance of 31.1 Ω compared to the $Cu_2O-C_3N_4$ electrode, which has a resistance of 52.3 Ω (Figure 6.12). The reduction in resistance can be attributed to the better electronic conductivity of the metal deposit. This, in turn, leads to a lower onset potential and a lower applied potential. As a result, the electron transfer in $Cu@Cu_2O-C_3N_4$ from the bulk to the electrode surface is facilitated compared to the pristine electrodes [307]. The enhanced electron and ion transfer processes increase the activity of CO_2RR.

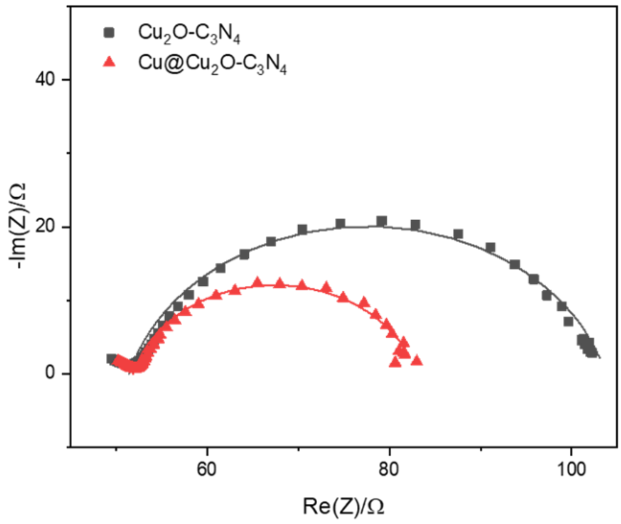

Figure 6.12 EIS of the electrodes taken at -0.99 V vs. RHE. The symbols represent the original experimental data, and the lines represent the fitted results.

6.2.4 Electrode deactivation

In addition, the 6-hour stability tests show the continued stability of the partial current density for ethylene, indicating a significant and stable increase in the

catalytic activity of the electrodeposited electrode (Figure 6.13a, b). The FEs of CO and CH_4 are relatively stable for both electrodes. As the reaction progresses, both the current density and the hydrogen production increase in a similar manner.

The primary consideration for electrode deactivation lies in the changes in the surface material. Comparing the electrodes after 1- and 3-hour reactions reveals that while the size and morphology of the particles remain unchanged, there is evident agglomeration, as shown in Figure 6.9c, f. Additionally, SEM-EDS analysis indicates significant differences in elemental distribution, as detailed in Table 6.2. In particular, the carbon content steadily increases throughout the entire reaction process. Initially, the atomic proportion of carbon on the electrode is 26.2 and 27.5% for Cu_2O-C_3N_4 and Cu@Cu_2O-C_3N_4, respectively. However, there is a significant increase between the first and third hours. After 3 hours of reaction, the atomic compositions of carbon on the Cu_2O-C_3N_4 and Cu@Cu_2O-C_3N_4 electrodes reach 87.8 and 92.4%, respectively. On the contrary, the ratios of copper, oxygen, and nitrogen decrease.

XRD and XPS tests were conducted on the Cu_2O-C_3N_4 and Cu@Cu_2O-C_3N_4 electrodes after 3 hours of reaction (Figure 6.10a, b). Compared to electrodes tested after 1 hour of reaction, the XPS peak for copper on the surface of the electrode remained similar after 3 hours, albeit with weakened signals. Peak fitting results from the Cu 2p spectrum indicate a notable increase in the Cu^+/Cu^0 ratio as the reaction progresses (Figure 6.10c and Table 6.3). XRD spectra also show a gradual decrease in characteristic peak signals for copper, while those for cuprous oxide diminish over the course of the reaction and the proportion of metallic copper increases. This result contrasts with the XPS findings, possibly

due to differences in the testing depth between the two methods, suggesting an overall increase in the proportion of metallic copper on the electrode with Cu^+ concentration being higher at the surface. The results indicate the presence of copper material detachment from the electrode during the reaction, and the variation in Cu^+/Cu^0 ratio on the electrode surface also affects the selectivity of CO_2 reduction.

To further investigate the deactivation processes of the electrode during prolonged operation, linear sweep voltammetry was performed on the electrode every hour (Figure 6.13c, d). The double-layer capacitance, the solution resistance, and the charge transfer resistance were measured at each interval (Figure 6.13g, h). During a three-hour reaction period without changing the cathodic electrolyte, both R_s and R_{ct} gradually decreased. The LSV plots also showed an increase in current density at the same potential as the reaction time progressed.

In the electrocatalytic reduction of carbon dioxide at constant potential, the compensated current did not fully follow the trend of gradual increase due to the use of current interruption compensation. However, with increasing current density, the availability of protons is higher than that of CO_2, resulting in HER gradually dominating.

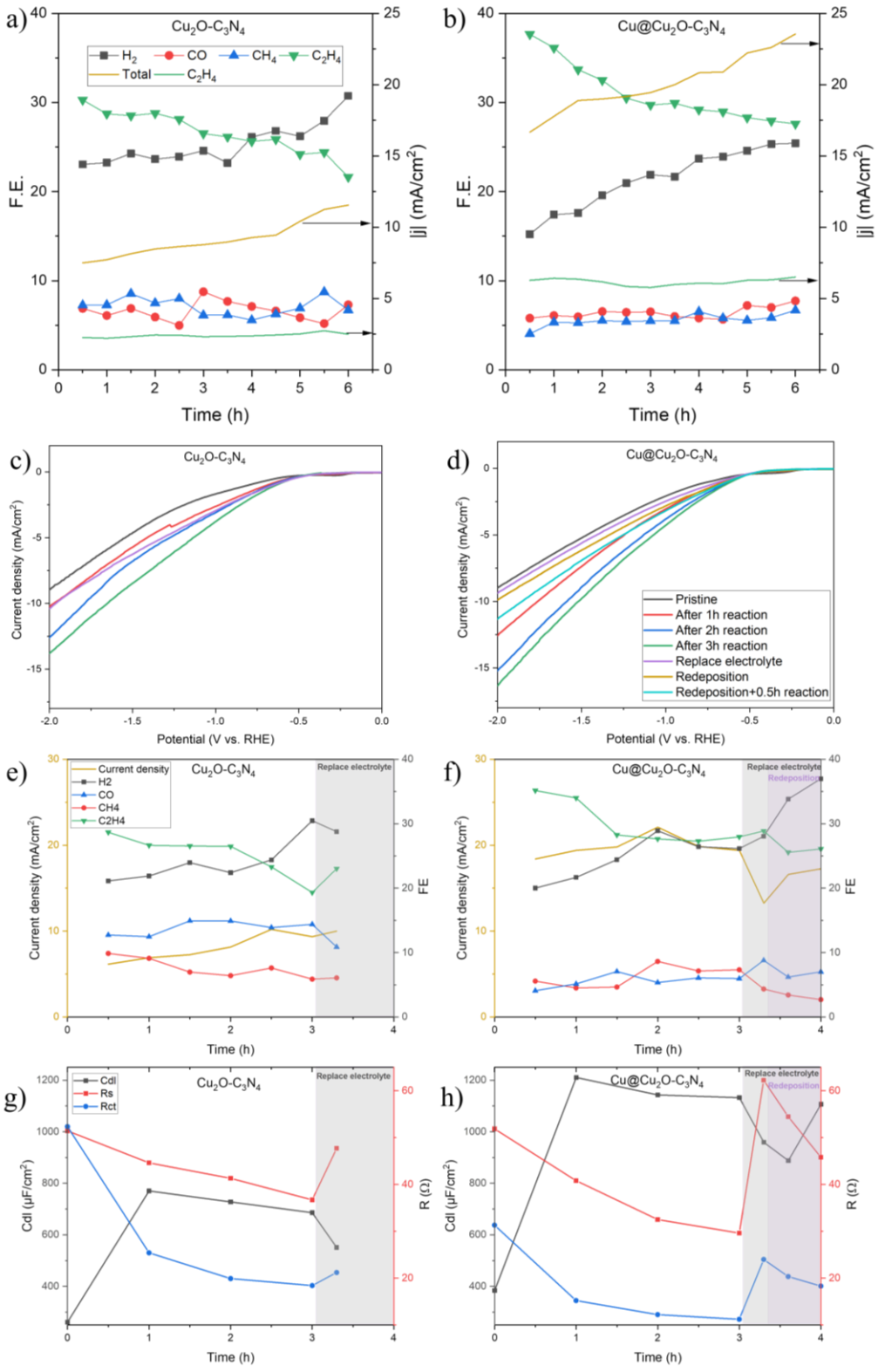

Figure 6.13 Stability test, LSV, C_{dl} and resistance for Cu_2O-C_3N_4 electrode and Cu@Cu_2O-C_3N_4 electrode after each hour reaction at the potential of -1.65 V vs. RHE, replacing electrolyte and redeposition.

The double-layer capacitance reflects changes in the number of active sites on the electrode surface. As can be seen in Figure 6.13g, h, the number of active sites initially increased during the reaction, followed by a gradual decrease. The initial increase in active sites was related to reduction and restructuring processes on the electrode surface. However, as the reactions progressed, factors such as carbon deposition on the electrode surface and deactivation due to poisoning of the active sites led to a gradual decrease in active sites [61]. This affected the dynamics of the chemical reaction and intensified the hydrogen evolution reaction. This phenomenon was partially alleviated after the electrode solution was replaced.

Furthermore, the performance of the electrode redeposition after a three-hour reaction shows that secondary electrodeposition increased the number of active sites but did not significantly contribute to the recovery of ethylene efficiency. Instead, it further increased the efficiency of hydrogen evolution. This result suggests that the reduction in the deactivation of active sites cannot be compensated by simply increasing the number of sites by electrodeposition again. The reason for this could be the formation of a dense deposition layer on the electrode surface after redeposition, which in turn hinders the adsorption and desorption processes of CO_2 molecules.

6.2.5 Cu electrodeposition on different electrodes

To investigate the influence of electrodeposition on the electrochemistry and intrinsic properties of Cu_2O and C_3N_4 in more detail, we performed a series of control experiments. Electrochemical deposition was performed under identical

conditions (0.01 M $Cu(NO_3)_2$, -2.5 mA/cm^2, 100 s) on carbon paper, C_3N_4, Cu_2O and Cu_2O-C_3N_4 electrodes, resulting in electrodes labelled Cu, Cu@C_3N_4, Cu@Cu_2O and Cu@Cu_2O-C_3N_4, respectively.

Electrochemical tests were then carried out with these electrodes. The cyclic voltammetry diagrams show a significant increase in current density at the working potential after electrodeposition (Figure 6.14a). As with the Cu@Cu_2O-C_3N_4 electrode, a reduction wave between -1 and 0 V vs. RHE was observed after electrodeposition, indicating an early-stage reduction reaction on the electrode surface. The electrodeposition of Cu significantly changed the product distribution, resulting in a decreased Faradaic efficiency of hydrogen and a remarkable increase in the Faradaic efficiency of ethylene (Figure 6.14b). Furthermore, electrodeposition significantly increased the C_2H_4/CH_4 ratio of the electrode, indicating that during the electrochemical CO_2 reduction process, sufficient concentrations of key intermediates such as *CHO and *CO, adsorb onto the electrode surface, facilitating C-C coupling and subsequent hydrogenation, ultimately leading to the production of ethylene (Figure 6.14c) [308]. The control experiments show that Cu deposition enhances the activity of the electrochemical CO_2 reduction reaction across different electrodes and modulates the selectivity.

Both C_3N_4 and Cu_2O have been shown to support the electrodeposition of Cu, leading to a higher current density and a higher proportion of C_2H_4/CH_4 in the gas products, endowing the resulting electrodes with increased reaction activity and selectivity. Studies show that substrate choice significantly shapes the structure and morphology of electrodeposited materials [309]. Differing electrode roughness leads to diverse growth patterns [310]. Higher roughness

electrodes can offer more active sites and a larger surface area, promoting better adsorption and reaction kinetics. The presence of C_3N_4 enhances the surface roughness of the electrode, creating more sites for growth. Besides, Cu_2O plays a vital role in modulating the Cu^+/Cu^0 ratio on the electrode surface during the reaction, thereby facilitating C-C coupling. The synergy between C_3N_4 and Cu_2O further emphasizes this advantage.

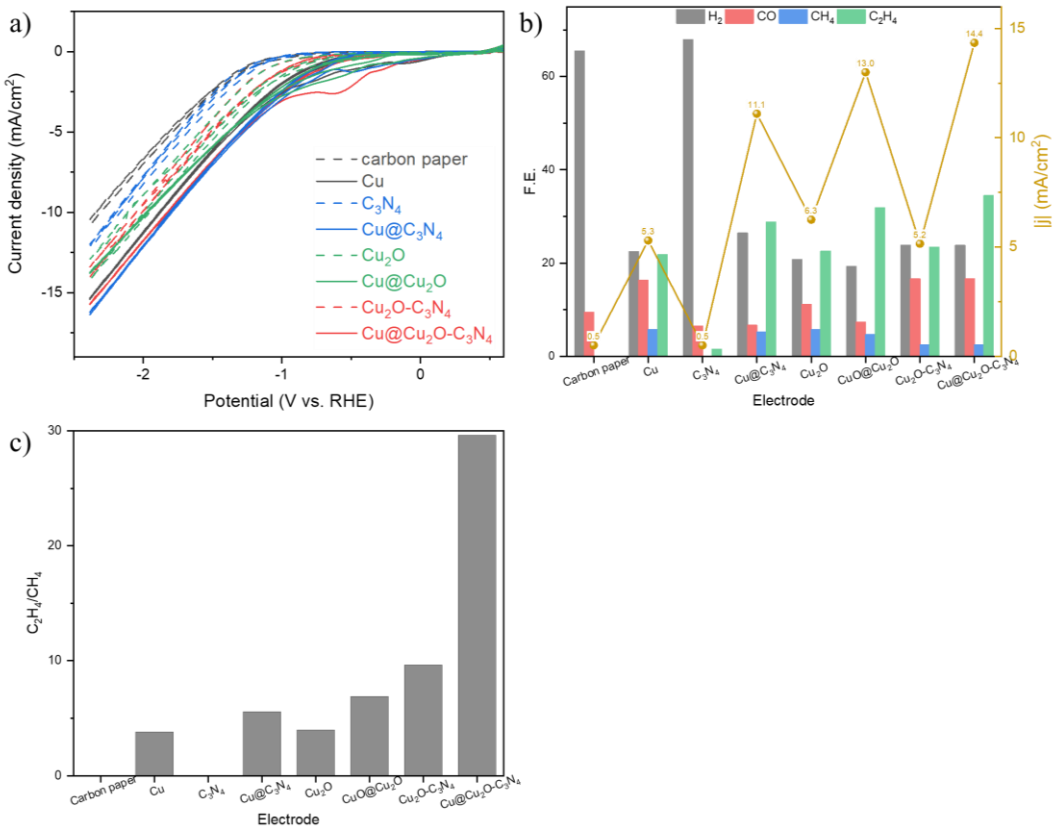

Figure 6.14 a) CV at the scan rate of 40 mV/s; b) the gaseous product distribution; and c) the ratio of C_2H_4/CH_4 of the electrodes before and after deposition at the potential of -0.99 V vs. RHE.

6.3 Summary

In summary, Cu was successfully deposited on the Cu_2O-C_3N_4 electrode, and the top layer of Cu was oxidised into CuO. The 3D dendritic structure of the electrodeposited copper increases the electrochemically active sites and decreases the charge transfer resistance, thereby improving the catalytic activity and efficiency of the electrode. After electrodeposition, the current density shows a remarkable four-fold improvement for multi-carbon products, reaching a peak value of 12.7 mA/cm^2 ($|j|_{ethylene}$ = 7.2 mA/cm^2) at -1.04 V vs. RHE. Moreover, during the CO_2RR process, the Cu substance on the electrode undergoes reduction and reconstruction, with the electrodeposited copper protecting the underlying Cu_2O layer. The high Cu^+/Cu^0 ratio on the electrode surface contributes to an increased product ratio of C_2H_4/CH_4. Moreover, an investigation into electrode deactivation unveiled carbon deposition as the primary culprit. Importantly, physical properties such as the roughness of the Cu_2O-C_3N_4 electrode facilitate the electrodeposition process. These findings hold significance for the development of efficient electrochemical reaction catalysts.

Chapter 7. Conclusions and recommendations for future work

7.1 Conclusions

This work provides a comprehensive review of recent advances in various types of Cu-based electrocatalysts for CO_2RR. The mechanisms of CO_2RR to multi-carbon products, including reaction pathways and factors critical to the reaction, are summarised. The mini-review provides a better understanding of the progress and advancement in this research field and highlights the challenges and prospects for further improvement of CO_2RR efficiency (Chapter 2). In addition, the influence of CuO synthesis conditions and the ratio of starting materials on the morphology, size and defects of CuO is investigated in this thesis (Chapter 5). Two different surface modification techniques, polymer coating (Chapter 4) and electrodeposition (Chapter 6) are applied to Cu-based electrodes with different objectives. Mechanistic insights are gained through simulations and electrode characterisation. The intricate relationship between electrode properties and electrochemical performance is illustrated by the improved electrochemical conversion efficiency of CO_2 to multi-carbon products.

In the first experimental work of this dissertation, control over proton transfer on the CuO electrode surface was achieved by tuning the surface hydrophobicity using the low-cost and hydrophobic polymer PVDC. A modest 50 µg/cm^2 PVDC coating exhibited optimised hydrophobicity (WCA = 122°), which effectively suppressed the hydrogen evolution reaction while facilitating the conversion of CO_2 to ethylene (FE = 41.4% at -0.89 V vs. RHE). Comparative tests and

calculations have shown that the PVDC modification remarkably balances proton transfer and CO_2 availability, preserves conductivity and improves selectivity and stability. Furthermore, the improved C-C coupling process is also attributed to the increased presence of Cu^+ active species on the CuO-PVDC surface.

Besides, the mechanism of CuO growth was demonstrated using precursors with different mass ratios both with and without microwave heating. Microwave-assisted synthesised CuO (MW-CuO) exhibited a higher defect site density and significantly increased grain boundaries than conventionally produced CuO. At an optimal reactant ratio, MW-CuO exhibited superior catalytic performance and achieved a remarkable FE of C_{2+} products (71.9% at -1.04 V vs. RHE, yielding a partial current density of about 11.2 mA/cm^2). This performance, which is among the highest reported for OD-Cu catalysts, results from an appropriate ratio of Cu(I) and Cu species and defective surface features. Microwave heating during catalyst preparation induces surface defects, which increases the CO_2RR selectivity for multi-carbon products, emphasizing the sustainable approach to catalyst preparation.

Another modification strategy was demonstrated: electrodeposition on the Cu_2O-C_3N_4 electrode, resulting in an intriguing 3D dendritic Cu structure that significantly increases the catalytic activity. Electrochemical analysis revealed a fourfold increase in current density for multicarbon products after electrodeposition, peaking at 12.7 mA/cm^2 (with $|j|_{ethylene}$ = 7.2 mA/cm^2) at -1.04 V vs. RHE. The restructuring of Cu species during eCO_2RR resulted in a high Cu^+/Cu^0 ratio on the Cu@Cu_2O-C_3N_4 electrode, which correlates with enhanced C-C coupling as evidenced by higher product ratios of C_2H_4/CH_4. The

electrodeposition increased the electrochemically active sites by 1.5 times, while the charge transfer resistance was reduced by 0.4-fold. Moreover, an investigation into electrode deactivation unveiled carbon deposition as the primary culprit. Importantly, physical properties such as the roughness of the Cu_2O-C_3N_4 electrode facilitate the electrodeposition process. Electrodeposition as a modification method has also been shown to be effective on other electrodes.

Overall, PVDC coating on CuO electrode controls proton transfer, achieving optimal hydrophobicity and suppressing H_2 evolution while facilitating high ethylene yield. Additionally, microwave heating generates CuO with abundant grain boundaries, resulting in a high density of defect sites and an excellent performance in the production of C_{2+} products. The Cu-electrodeposited electrode exhibits a 4-fold increase in the current density for C_{2+} species. The accelerated C-C coupling, attributed to a higher Cu^+/Cu^0 ratio, is observed, although electrode deactivation primarily stems from carbon deposition, with rough substrates aiding Cu electrodeposition and contributing to the observed 3D dendrite structure. These works offer universal strategies to enhance the efficiency of electrochemical reduction of CO_2 for multi-carbon product generation, advancing our comprehension of the reaction mechanisms involved.

7.2 Recommendations for future work

Future research should focus on high-throughput screening, active site regulation, sustainable synthesis and stability testing to drive progress in efficient CO_2RR towards multi-carbon products. Detailed recommendations on this topic are provided below:

1. Real-time insights into the changes in the catalyst

Variations in the Cu^0/Cu^+ ratio, which reflect the oxidation states of the surface, have been shown to influence catalytic activity and selectivity during CO_2RR. However, the optimal ratio for the desired CO_2RR results appears to depend on factors such as the reaction conditions, the morphology of the catalyst, and the nature of the active sites involved. The integration of advanced characterisation techniques and theoretical calculations is essential to unravel these complex relationships.

In future work, in-situ spectroscopy, operando studies, and high-resolution microscopy will provide real-time insights into the changes in electrodes. The activation and deactivation processes of electrodes can be better explained through a combination of experiments and theoretical calculations.

2. New electrode materials

While efficient catalysts exist for the conversion of eCO_2RR to CO, the integration of CO-affine materials with copper-based electrodes, such as metal oxides or carbides, is promising. This integration improves the selective adsorption of CO, which is particularly important to drive the C-C coupling process and consequently promote the preferential formation of C_{2+} products. In addition, a strategic focus on structural design is critical to improving the

electrode interface and transfer performance. Here, in the second work of the microwave-assisted synthesis of CuO, the increased concentration of *CO may further enhance the C-C coupling process. Thus, the introduction of conductive additives, nanostructures or heterostructures into the defect-rich CuO may offer opportunities to optimise the performance of copper-based electrodes in CO_2RR.

3. Long-term stability

Long-term stability is a critical factor in assessing the practical feasibility of electrode materials in continuous CO_2 reduction reactions. Monitoring changes in structural integrity and catalytic performance through extended durability testing under realistic operating conditions helps to identify potential problems such as catalyst aggregation, surface passivation or chemical transformation. To maintain stability and prevent degradation of electrodes in the CO_2 reduction reaction, managing carbon-containing byproducts is crucial. Strategies such as regular cleaning, catalyst regeneration, and the use of sacrificial electrodes can effectively mitigate electrode contamination. Additionally, modifying electrode surfaces, optimizing operating conditions, and employing selective capture methods can further enhance stability by reducing the accumulation of carbonaceous species. By integrating these approaches, the stability and efficiency of CO_2RR electrodes can be improved, enabling sustainable conversion into valuable products.

Reference

[1] X. Huang, S. Yang, W. Jiang, M. Ding, Y. Wang, M. Sun, S. Zhang, Enhanced east–west climatic contrast in northern China under past global warming: Evidence from paleovegetation records and numerical simulations, Quaternary Science Reviews, 320 (2023) 108353.

[2] J. Sousa, I. Soares, The effect of demand response on CO2 Emissions in the Iberian electricity market – Combining economic and environmental perspectives, Energy and Climate Change, 4 (2023) 100093.

[3] H. Song, G. Hou, S. Xu, CO2 emissions in China under electricity substitution: Influencing factors and decoupling effects, Urban Climate, 47 (2023) 101365.

[4] N. Saqib, M. Radulescu, M. Usman, D. Balsalobre-Lorente, T. Cilan, Environmental technology, economic complexity, renewable electricity, environmental taxes and CO2 emissions: Implications for low-carbon future in G-10 bloc, Heliyon, 9 (2023) e16457.

[5] M.T. Kartal, U.K. Pata, Ö. Depren, S. Erdogan, Effectiveness of nuclear and renewable electricity generation on CO2 emissions: Daily-based analysis for the major nuclear power generating countries, Journal of Cleaner Production, 426 (2023) 139121.

[6] M. Jiang, B. Wang, Y. Hao, S. Chen, Y. Wen, Z. Yang, Quantification of CO2 emissions in transportation: An empirical analysis by modal shift from road to waterway transport in Zhejiang, China, Transport Policy, 145 (2024) 177-186.

[7] Q. Qiao, H. Eskandari, H. Saadatmand, M.A. Sahraei, An interpretable multi-stage forecasting framework for energy consumption and CO2 emissions for the transportation sector, Energy, 286 (2024).

[8] F. Jawadi, P. Rozin, D. Bourghelle, Insights into CO2 emissions in Europe in the context of COVID-19: A panel data analysis, International Economics, 173 (2023) 164-174.

[9] W. Zhang, T. Zhang, S. Wang, H. Li, CO2 emission spillover effects in the digital transformation of China's manufacturing industry and its inter-industry differences, Energy Reports, 10 (2023) 520-534.

[10] A. Shen, J. Zhang, Technologies for CO2 emission reduction and low-carbon development in primary aluminum industry in China: A review, Renewable and Sustainable Energy Reviews, 189 (2024) 113965.

[11] B. Jiang, D. Xia, Toward carbon neutrality in China: A national wide carbon flow tracing and the CO2 emission control strategies for CO2-intensive industries, Science of The Total Environment, 879 (2023) 163009.

[12] Z. Saadaoui, T. Boufateh, Z. Jiao, On the transmission of oil supply and demand shocks to CO2 emissions in the US by considering uncertainty: A time-varying perspective, Resources Policy, 85 (2023).

[13] G. Colucci, D. Lerede, M. Nicoli, L. Savoldi, A dynamic accounting method for CO2 emissions to assess the penetration of low-carbon fuels: application to the TEMOA-Italy energy system optimization model, Applied Energy, 352 (2023).

[14] P. Huang, F. Zhao, B. Zhou, K. Xu, Active microeukaryotes hold clues of effects of global warming on benthic diversity and connectivity in the coastal sediments, Ecological Indicators, 158 (2024) 111316.

[15] J. Zhang, P. Huang, Different uncertainty in tropical oceanic and land precipitation sensitivities under global warming, Atmospheric Research, 292 (2023) 106850.

[16] C.E. Richards, H.L. Gauch, J.M. Allwood, International risk of food insecurity and mass mortality in a runaway global warming scenario, Futures, 150 (2023) 103173.

[17] Y. Meng, K. Duan, P. Shi, W. Shang, S. Li, Y. Cheng, L. Xing, R. Chen, J. He, Sensitive temperature changes on the Tibetan Plateau in response to global warming, Atmospheric Research, 294 (2023) 106948.

[18] J.-L. Chen, S.-C. Kang, A.D. Wu, D.-D. Hu, Impacts of 1.5 ℃ global warming on hydrological conditions of navigation along the Northern Sea Route and Northwest Passage, Advances in Climate Change Research, (2023).

[19] K. Guesmi, P. Makrychoriti, S. Spyrou, The relationship between climate risk, climate policy uncertainty, and CO2 emissions: Empirical evidence from the US, Journal of Economic Behavior & Organization, 212 (2023) 610-628.

[20] G. Grolleau, C. Weber, The effect of inflation on CO2 emissions: An analysis over the period 1970–2020, Ecological Economics, 217 (2024).

[21] M. Wang, M.R. Hossain, K. Si Mohammed, J. Cifuentes-Faura, X. Cai, Heterogenous Effects of Circular Economy, Green energy and Globalization on CO2 emissions: Policy based analysis for sustainable development, Renewable Energy, 211 (2023) 789-801.

[22] IEA, CO2 Emissions in 2022, https://www.iea.org/reports/co2-emissions-in-2022, 2023.

[23] E. García-Bordejé, R. González-Olmos, Advances in process intensification of direct air CO2 capture with chemical conversion, Progress in Energy and Combustion Science, 100 (2024) 101132.

[24] Y. Luo, X. Yue, H. Zhang, X. Liu, Z. Wu, Recent advances in energy efficiency optimization methods for plasma CO2 conversion, Science of The Total Environment, 906 (2024) 167486.

[25] D.P.H. Tran, M.-T. Pham, X.-T. Bui, Y.-F. Wang, S.-J. You, CeO2 as a photocatalytic material for CO2 conversion: A review, Solar Energy, 240 (2022) 443-466.

[26] Y. Sun, Y. Zhao, Y. Zhou, L. Wang, Z. Wang, J. Qi, D. Fu, P. Zhang, K. Zhao, Engineering the micro-structure for reducing energy consumption in CO2 capture and catalytic conversion process, Materials Today Energy, 37 (2023) 101397.

[27] A. Islam, A. Malek, S.H. Teo, H.M. Marwani, M.M. Rahman, A.M. Asiri, M.A.R. Khan, Y.H. Taufiq-Yap, M.R. Awual, Smart materials for CO2 conversion into renewable fuels and emission reduction, Sustain Mater Techno, 37 (2023) e00636.

[28] Q. Li, Y.X. Ouyang, S.H. Lu, X.W. Bai, Y.H. Zhang, L. Shi, C.Y. Ling, J.L. Wang, Perspective on theoretical methods and modeling relating to electro-catalysis processes, Chem Commun, 56 (2020) 9937-9949.

[29] D. Adu, D. Jianguo, R.O. Darko, E. Baffour G, S.N. Asomani, Overcoming CO2 emission from energy generation by renewable hydropower – The role of pump as turbine, Energy Reports, 9 (2023) 114-118.

[30] M.A. Zambrano-Monserrate, Clean energy production index and CO2 emissions in OECD countries, Science of The Total Environment, 907 (2024).

[31] C. Du, X. Wang, W. Chen, S. Feng, J. Wen, Y.A. Wu, CO2 transformation to multicarbon products by photocatalysis and electrocatalysis, Mater Today Adv, 6 (2020) 100071.

[32] M. Kuang, G. Zheng, Interfacial microenvironments for carbon dioxide electro-upgrading to multicarbon products, Chem Catalysis, 3 (2023) 100565.

[33] L. Fan, C. Xia, F.Q. Yang, J. Wang, H.T. Wang, Y.Y. Lu, Strategies in catalysts and electrolyzer design for electrochemical CO2 reduction toward C2+ products, Sci Adv, 6 (2020).

[34] X. Ji, H. Guo, Y. Xue, Y. Huang, S. Zhang, Microenvironment: An efficient avenue for converting CO2 to high-value compounds, Renewable and Sustainable Energy Reviews, 188 (2023) 113809.

[35] T. Jaster, A. Gawel, D. Siegmund, J. Holzmann, H. Lohmann, E. Klemm, U.-P. Apfel, Electrochemical CO2 reduction toward multicarbon alcohols - The microscopic world of catalysts & process conditions, iScience, 25 (2022) 104010.

[36] H. Xie, T. Wang, J. Liang, Q. Li, S. Sun, Cu-based nanocatalysts for electrochemical reduction of CO2, Nano Today, 21 (2018) 41-54.

[37] M. Nath, H. Singh, A. Saxena, Progress of transition metal chalcogenides as efficient electrocatalysts for energy conversion, Current Opinion in Electrochemistry, 34 (2022) 100993.

[38] A. Prajapati, N.C. Kani, J.A. Gauthier, R. Sartape, J. Xie, I. Bessa, M.T. Galante, S.L. Leung, M.H.S. Andrade, R.T. Somich, M.V. Rebouças, G.T. Hutras, N. Diniz, M.R. Singh, CO2-free high-purity ethylene from electroreduction of CO2 with 4% solar-to-ethylene and 10% solar-to-carbon efficiencies, Cell Reports Physical Science, 3 (2022) 101053.

[39] S. Hu, B. Pang, L. Zhang, Q. Feng, P. Zhang, Y. Ding, X. Zhu, W. Yang, Enhancing puncture voltage of La0.8Sr0.2Ga0.8Mg0.2O3-δ solid electrolyte membrane by improving CO2 reduction kinetics, Journal of Power Sources, 556 (2023) 232482.

[40] A.S. Varela, The importance of pH in controlling the selectivity of the electrochemical CO2 reduction, Curr Opin Green Sust, 26 (2020) 100371.

[41] A. Hermawan, T. Amrillah, V.N. Alviani, J. Raharjo, Z.W. Seh, N. Tsuchiya, Upcycling air pollutants to fuels and chemicals via electrochemical reduction technology, Journal of Environmental Management, 334 (2023) 117477.

[42] J. Fernández-González, M. Rumayor, A. Domínguez-Ramos, Á. Irabien, CO2 electroreduction: Sustainability analysis of the renewable synthetic natural gas, International Journal of Greenhouse Gas Control, 114 (2022) 103549.

[43] P. Samani, Synergies and gaps between circularity assessment and Life Cycle Assessment (LCA), Science of The Total Environment, 903 (2023) 166611.

[44] G. Falcone, A. Fazari, G. Vono, G. Gulisano, A. Strano, Application of the LCA approach to the citrus production chain – A systematic review, Cleaner Environmental Systems, 12 (2024) 100156.

[45] A. Dervishaj, K. Gudmundsson, From LCA to circular design: A comparative study of digital tools for the built environment, Resources, Conservation and Recycling, 200 (2024) 107291.

[46] V. Bisinella, S. Schmidt, A.S. Varling, D. Laner, T.H. Christensen, Waste LCA and the future, Waste Management, 174 (2024) 53-75.

[47] X.-x. Wang, Y.-h. Duan, J.-f. Zhang, Y.-s. Tan, Catalytic conversion of CO2 into high value-added hydrocarbons over tandem catalyst, Journal of Fuel Chemistry and Technology, 50 (2022) 538-563.

[48] E. Ruiz-López, J. Gandara-Loe, F. Baena-Moreno, T.R. Reina, J.A. Odriozola, Electrocatalytic CO2 conversion to C2 products: Catalysts design,

market perspectives and techno-economic aspects, Renewable and Sustainable Energy Reviews, 161 (2022) 112329.

[49] M.A. Rudolph, P. Isbrücker, R. Schomäcker, Bifunctional catalysts for the conversion of CO2 into value-added products – distance as a design parameter for new catalysts, Catal Sci Technol, 13 (2023) 3469-3482.

[50] L. Zhang, I. Merino-Garcia, J. Albo, C.M. Sánchez-Sánchez, Electrochemical CO2 reduction reaction on cost-effective oxide-derived copper and transition metal–nitrogen–carbon catalysts, Current Opinion in Electrochemistry, 23 (2020) 65-73.

[51] B. Ligt, E.J.M. Hensen, M. Costa Figueiredo, Electrochemical interfaces during CO2 reduction on copper electrodes, Current Opinion in Electrochemistry, 41 (2023).

[52] B. Sun, M. Dai, S. Cai, H. Cheng, K. Song, Y. Yu, H. Hu, Challenges and strategies towards copper-based catalysts for enhanced electrochemical CO2 reduction to multi-carbon products, Fuel, 332 (2023).

[53] Y. Zheng, A. Vasileff, X. Zhou, Y. Jiao, M. Jaroniec, S.Z. Qiao, Understanding the Roadmap for Electrochemical Reduction of CO2 to Multi-Carbon Oxygenates and Hydrocarbons on Copper-Based Catalysts, J Am Chem Soc, 141 (2019) 7646-7659.

[54] Q. Zhou, W. Zhang, M. Qiu, Y. Yu, Role of oxygen in copper-based catalysts for carbon dioxide electrochemical reduction, Materials Today Physics, 20 (2021).

[55] Z. Guo, H. Zhu, G. Yang, A. Wu, Q. Chen, Z. Yan, K. Loon Fow, H. Do, J.D. Hirst, T. Wu, M. Xu, Synergistic engineering of heteronuclear Ni-Ag dual-

atom catalysts for high-efficiency CO2 electroreduction with nearly 100% CO selectivity, Chemical Engineering Journal, 476 (2023).

[56] X. Mao, R. Guo, Q. Chen, H. Zhu, H. Li, Z. Yan, Z. Guo, T. Wu, Recent Advances in Graphitic Carbon Nitride Based Electro-Catalysts for CO(2) Reduction Reactions, Molecules, 28 (2023) 3292.

[57] A.R. Woldu, Z. Huang, P. Zhao, L. Hu, D. Astruc, Electrochemical CO2 reduction (CO2RR) to multi-carbon products over copper-based catalysts, Coordin Chem Rev, 454 (2022).

[58] S. Popovic, M. Smiljanic, P. Jovanovic, J. Vavra, R. Buonsanti, N. Hodnik, Stability and Degradation Mechanisms of Copper-Based Catalysts for Electrochemical CO(2) Reduction, Angew Chem Int Ed Engl, 59 (2020) 14736-14746.

[59] K. Van Daele, B. De Mot, M. Pupo, N. Daems, D. Pant, R. Kortlever, T. Breugelmans, Sn-Based Electrocatalyst Stability: A Crucial Piece to the Puzzle for the Electrochemical CO2 Reduction toward Formic Acid, Acs Energy Lett, 6 (2021) 4317-4327.

[60] P. Grosse, D. Gao, F. Scholten, I. Sinev, H. Mistry, B. Roldan Cuenya, Dynamic Changes in the Structure, Chemical State and Catalytic Selectivity of Cu Nanocubes during CO2 Electroreduction: Size and Support Effects, Angewandte Chemie International Edition, 57 (2018) 6192-6197.

[61] K. Xiang, F. Zhu, Y. Liu, Y. Pan, X. Wang, X. Yan, H. Liu, A strategy to eliminate carbon deposition on a copper electrode in order to enhance its stability in CO2RR catalysis by introducing crystal defects, Electrochemistry Communications, 102 (2019) 72-77.

[62] A. Engelbrecht, C. Uhlig, O. Stark, M. Hämmerle, G. Schmid, E. Magori, K. Wiesner-Fleischer, M. Fleischer, R. Moos, On the Electrochemical CO2Reduction at Copper Sheet Electrodes with Enhanced Long-Term Stability by Pulsed Electrolysis, Journal of The Electrochemical Society, 165 (2018) J3059-J3068.

[63] C. Xiao, J. Zhang, Architectural Design for Enhanced C2 Product Selectivity in Electrochemical CO2 Reduction Using Cu-Based Catalysts: A Review, Acs Nano, 15 (2021) 7975-8000.

[64] D. Ren, B.S.-H. Ang, B.S. Yeo, Tuning the Selectivity of Carbon Dioxide Electroreduction toward Ethanol on Oxide-Derived CuxZn Catalysts, Acs Catal, 6 (2016) 8239-8247.

[65] T.-C. Chou, C.-C. Chang, H.-L. Yu, W.-Y. Yu, C.-L. Dong, J.-J. Velasco-Vélez, C.-H. Chuang, L.-C. Chen, J.-F. Lee, J.-M. Chen, H.-L. Wu, Controlling the Oxidation State of the Cu Electrode and Reaction Intermediates for Electrochemical CO2 Reduction to Ethylene, Journal of the American Chemical Society, 142 (2020) 2857-2867.

[66] A. Bagger, W. Ju, A.S. Varela, P. Strasser, J. Rossmeisl, Electrochemical CO2 Reduction: Classifying Cu Facets, Acs Catal, 9 (2019) 7894-7899.

[67] D.T. Whipple, E.C. Finke, P.J.A. Kenis, Microfluidic Reactor for the Electrochemical Reduction of Carbon Dioxide: The Effect of pH, Electrochemical and Solid-State Letters, 13 (2010).

[68] B. Deng, M. Huang, X. Zhao, S. Mou, F. Dong, Interfacial Electrolyte Effects on Electrocatalytic CO2 Reduction, Acs Catal, 12 (2021) 331-362.

[69] P.P. Sharma, X.D. Zhou, Electrocatalytic conversion of carbon dioxide to fuels: a review on the interaction between CO2 and the liquid electrolyte, Wires Energy Environ, 6 (2017).

[70] B. Zhang, J. Zhang, M. Hua, Q. Wan, Z. Su, X. Tan, L. Liu, F. Zhang, G. Chen, D. Tan, X. Cheng, B. Han, L. Zheng, G. Mo, Highly Electrocatalytic Ethylene Production from CO2 on Nanodefective Cu Nanosheets, Journal of the American Chemical Society, 142 (2020) 13606-13613.

[71] A.J. Garza, A.T. Bell, M. Head-Gordon, Mechanism of CO2 Reduction at Copper Surfaces: Pathways to C2 Products, Acs Catal, 8 (2018) 1490-1499.

[72] S. Liu, B. Zhang, L. Zhang, J. Sun, Rational design strategies of Cu-based electrocatalysts for CO2 electroreduction to C2 products, J Energy Chem, 71 (2022) 63-82.

[73] Z. Li, H. Yang, W. Cheng, L. Tian, Recent progress of in situ/operando characterization techniques for electrocatalytic energy conversion reaction, Chinese Chemical Letters, (2023) 109237.

[74] J. Kim, D. Lee, C. Nam, J. Chung, B. Koo, N. Kim, J. Lim, Energy material analysis via in-situ/operando scanning transmission x-ray microscopy: A review, Journal of Electron Spectroscopy and Related Phenomena, 266 (2023) 147337.

[75] D. Mendoza, S.-T. Dong, B. Lassalle-Kaiser, In situ/operando X-ray spectroscopy applied to electrocatalytic CO2 reduction: Status and perspectives, Current Opinion in Colloid & Interface Science, 61 (2022) 101635.

[76] X. Gong, Z. Chen, L. Zhu, Y. Ye, Using ambient pressure X-ray photoelectron spectroscopy to characterize electrode/electrolyte interfaces in situ and operando, in: K. Wandelt, G. Bussetti (Eds.) Encyclopedia of Solid-Liquid Interfaces (First Edition), Elsevier, Oxford, 2024, pp. 266-282.

[77] M. Chen, D. Liu, L. Qiao, P. Zhou, J. Feng, K.W. Ng, Q. Liu, S. Wang, H. Pan, In-situ/operando Raman techniques for in-depth understanding on electrocatalysis, Chemical Engineering Journal, 461 (2023) 141939.

[78] F. Zhou, X. Fang, Y. Zhang, W. Yang, W. Zhou, H. Zhou, Q. Liu, J. Wu, F. Qi, Y. Shen, Synergetic effects of Cu cluster-doped g-C3N4 with multiple active sites for CO2 reduction to C2 products: A DFT study, Fuel, 353 (2023) 129202.

[79] N.K. Singh, P. Kumar, A. Yadav, V.C. Srivastava, Multi-doped borophene catalysts with engineered defects for CO2 reduction: A DFT study, Journal of Colloid and Interface Science, 654 (2024) 895-905.

[80] M.G. Sandoval, J. Walia, M.S.E. Houache, Y. Abu-Lebdeh, P. Berini, R. Faccio, A. Weck, CO2 adsorption and activation on Ag(111) surfaces in the presence of surface charge density: A static gas phase DFT study, Applied Surface Science, 610 (2023) 155498.

[81] T. Liu, G. Song, X. Liu, Z. Chen, Y. Shen, Q. Wang, Z. Peng, G. Wang, Insights into the mechanism in electrochemical CO2 reduction over single-atom copper alloy catalysts: A DFT study, iScience, 26 (2023) 107953.

[82] Y. Song, Y. Guo, J. Chen, M. Yuan, K. Dong, Deep learning assisted high throughput screening of ionic liquid electrolytes for NRR and CO2RR, Journal of Environmental Chemical Engineering, 11 (2023) 110556.

[83] J.Y. Lok, W.-H. Tsai, I.C. Cheng, A hybrid machine learning-genetic algorithm (ML-GA) model to predict optimal process parameters of nanoporous Cu for CO2 reduction, Materials Today Energy, 36 (2023) 101352.

[84] Y. Liu, Q. Ge, T. Wang, K. Li, Y. Deng, W. You, L. Xie, L. Zhang, Investigating the impact of pretreatment strategies on photocatalyst for accurate

CO2RR productivity quantification: A machine learning approach, Chemical Engineering Journal, 473 (2023) 145255.

[85] H.L. Liu, Y.T. Zhu, J.M. Ma, Z.C. Zhang, W.P. Hu, Recent Advances in Atomic-Level Engineering of Nanostructured Catalysts for Electrochemical CO2 Reduction, Adv Funct Mater, 30 (2020).

[86] L. Sun, V. Reddu, A.C. Fisher, X. Wang, Electrocatalytic reduction of carbon dioxide: opportunities with heterogeneous molecular catalysts, Energ Environ Sci, 13 (2020) 374-403.

[87] Z.W. Seh, J. Kibsgaard, C.F. Dickens, I. Chorkendorff, J.K. Norskov, T.F. Jaramillo, Combining theory and experiment in electrocatalysis: Insights into materials design, Science, 355 (2017).

[88] A.C. Pérez-Sequera, M.A. Díaz-Pérez, J.C. Serrano-Ruiz, Recent Advances in the Electroreduction of CO2 over Heteroatom-Doped Carbon Materials, Catalysts, 10 (2020).

[89] Y. Pang, T. Burdyny, C.-T. Dinh, M.G. Kibria, J.Z. Fan, M. Liu, E.H. Sargent, D. Sinton, Joint tuning of nanostructured Cu-oxide morphology and local electrolyte programs high-rate CO2 reduction to C2H4, Green Chem, 19 (2017) 4023-4030.

[90] Q. Zhu, J. Ma, X. Kang, X. Sun, H. Liu, J. Hu, Z. Liu, B. Han, Efficient Reduction of CO2 into Formic Acid on a Lead or Tin Electrode using an Ionic Liquid Catholyte Mixture, Angew Chem Int Ed Engl, 55 (2016) 9012-9016.

[91] S. Xu, S. Li, W. Yao, D. Dong, K. Xie, Direct electrolysis of CO2 using an oxygen-ion conducting solid oxide electrolyzer based on $La_{0.75}Sr_{0.25}Cr_{0.5}Mn_{0.5}O_{3-\delta}$ electrode, Journal of Power Sources, 230 (2013) 115-121.

[92] S. Pérez-Rodríguez, F. Barreras, E. Pastor, M.J. Lázaro, Electrochemical reactors for CO 2 reduction: From acid media to gas phase, International Journal of Hydrogen Energy, 41 (2016) 19756-19765.

[93] D.A. Salvatore, D.M. Weekes, J. He, K.E. Dettelbach, Y.C. Li, T.E. Mallouk, C.P. Berlinguette, Electrolysis of Gaseous CO2 to CO in a Flow Cell with a Bipolar Membrane, Acs Energy Lett, 3 (2017) 149-154.

[94] R.A. Tufa, D. Chanda, M. Ma, D. Aili, T.B. Demissie, J. Vaes, Q. Li, S. Liu, D. Pant, Towards highly efficient electrochemical CO2 reduction: Cell designs, membranes and electrocatalysts, Applied Energy, 277 (2020).

[95] A.M. Liu, M.F. Gao, X.F. Ren, F.N. Meng, Y.N. Yang, L.G. Gao, Q.Y. Yang, T.L. Ma, Current progress in electrocatalytic carbon dioxide reduction to fuels on heterogeneous catalysts, J Mater Chem A, 8 (2020) 3541-3562.

[96] T. Zheng, K. Jiang, H. Wang, Recent Advances in Electrochemical CO2-to - CO Conversion on Heterogeneous Catalysts, Advanced materials (Weinheim), 30 (2018) 1802066-n/a.

[97] W. Ma, S. Xie, X.-G. Zhang, F. Sun, J. Kang, Z. Jiang, Q. Zhang, D.-Y. Wu, Y. Wang, Promoting electrocatalytic CO2 reduction to formate via sulfur-boosting water activation on indium surfaces, Nature communications, 10 (2019) 892-892.

[98] L. Xue, Q.-Y. Fan, Y. Zhao, Y. Liu, H. Zhang, M. Sun, Y. Wang, S. Zeng, Ultralow Ag-assisted carbon–carbon coupling mechanism on Cu-based catalysts for electrocatalytic CO2 reduction, J Energy Chem, 82 (2023) 414-422.

[99] S.A. Ali, I. Sadiq, T. Ahmad, Deep insight of CO2 reduction reaction mechanism through experimental and theoretical anticipations, Materials Today Sustainability, 24 (2023).

[100] Q. Lu, F. Jiao, Electrochemical CO2 reduction: Electrocatalyst, reaction mechanism, and process engineering, Nano Energy, 29 (2016) 439-456.

[101] T. Liu, G. Song, X. Liu, Z. Chen, Y. Shen, Q. Wang, Z. Peng, G. Wang, Insights into the mechanism in electrochemical CO2 reduction over single-atom copper alloy catalysts: A DFT study, iScience, 26 (2023).

[102] N. Han, P. Ding, L. He, Y. Li, Y. Li, Promises of Main Group Metal–Based Nanostructured Materials for Electrochemical CO2 Reduction to Formate, Adv Energy Mater, 10 (2019).

[103] J.H. Montoya, C. Shi, K. Chan, J.K. Nørskov, Theoretical Insights into a CO Dimerization Mechanism in CO2 Electroreduction, The Journal of Physical Chemistry Letters, 6 (2015) 2032-2037.

[104] M. Li, Y. Hu, T. Wu, A. Sumboja, D. Geng, How to enhance the C2 products selectivity of copper-based catalysts towards electrochemical CO2 reduction?—A review, Materials Today, 67 (2023) 320-343.

[105] D.M. Fernandes, A.F. Peixoto, C. Freire, Nitrogen-doped metal-free carbon catalysts for (electro)chemical CO2 conversion and valorisation, Dalton Trans, 48 (2019) 13508-13528.

[106] S. Nitopi, E. Bertheussen, S.B. Scott, X. Liu, A.K. Engstfeld, S. Horch, B. Seger, I.E.L. Stephens, K. Chan, C. Hahn, J.K. Norskov, T.F. Jaramillo, I. Chorkendorff, Progress and Perspectives of Electrochemical CO2 Reduction on Copper in Aqueous Electrolyte, Chem Rev, 119 (2019) 7610-7672.

[107] J. He, N.J.J. Johnson, A. Huang, C.P. Berlinguette, Electrocatalytic Alloys for CO2 Reduction, ChemSusChem, 11 (2018) 48-57.

[108] H. Shen, Q. Sun, Cu Atomic Chain Supported on Graphene Nanoribbon for Effective Conversion of CO2 to Ethanol, Chemphyschem, 21 (2020) 1768-1774.

[109] A.R. Heenan, A.T. Marshall, Impact of electrode geometry and operating conditions on the activity and selectivity of the electrochemical CO2 reduction reaction, Electrochimica Acta, 468 (2023).

[110] K. Li, S. Zou, J. Zhang, Y. Huang, L. He, X. Feng, Superhydrophobicity-Enabled Efficient Electrocatalytic CO2 Reduction at a High Temperature, Acs Catal, (2023) 9346-9351.

[111] J.-B. Vennekötter, T. Scheuermann, R. Sengpiel, M. Wessling, The electrolyte matters: Stable systems for high rate electrochemical CO2 reduction, J Co2 Util, 32 (2019) 202-213.

[112] Y. Ji, A. Guan, G. Zheng, Copper-based catalysts for electrochemical carbon monoxide reduction, Cell Reports Physical Science, 3 (2022).

[113] T. Chen, J. Hu, K. Wang, K. Wang, W. Zhang, H. Xie, G. Gan, J. Shi, Oxygen vacancies in oxide-derived EGaIn enhance CO2 electrochemical reduction to CO in organic electrolyte, Applied Surface Science, 612 (2023).

[114] S. Ma, Y. Lu, H. Yao, Q. Liu, Z. Li, Enhancing the process of CO2 reduction reaction by using CTAB to construct contact ion pair in Li-CO2 battery, Chinese Chemical Letters, 33 (2022) 2933-2936.

[115] L.M. Aeshala, R.G. Uppaluri, A. Verma, Effect of cationic and anionic solid polymer electrolyte on direct electrochemical reduction of gaseous CO2 to fuel, J Co2 Util, 3-4 (2013) 49-55.

[116] J. Wu, W. Li, K. Liu, A. Kucernak, H. Liu, L. Chai, M. Liu, Cation effects on electrochemical CO2 reduction reaction, Next Energy, 1 (2023).

[117] S. Lu, Y. Wang, H. Xiang, H. Lei, B.B. Xu, L. Xing, E.H. Yu, T.X. Liu, Mass transfer effect to electrochemical reduction of CO2: Electrode, electrocatalyst and electrolyte, Journal of Energy Storage, 52 (2022).

[118] S. Liang, N. Altaf, L. Huang, Y. Gao, Q. Wang, Electrolytic cell design for electrochemical CO2 reduction, J Co2 Util, 35 (2020) 90-105.

[119] W. Xi, P. Yang, M. Jiang, X. Wang, H. Zhou, J. Duan, M. Ratova, D. Wu, Electrochemical CO2 reduction coupled with alternative oxidation reactions: Electrocatalysts, electrolytes, and electrolyzers, Applied Catalysis B: Environmental, 341 (2024).

[120] F.L. Lu, H.H. Bao, Y.Y. Mi, Y.F. Liu, J.Q. Sun, X.Y. Peng, Y. Qiu, L.C. Zhuo, X.J. Liu, J. Luo, Electrochemical CO2 reduction: from nanoclusters to single atom catalysts, Sustain Energ Fuels, 4 (2020) 1012-1028.

[121] F.P. García de Arquer, C.-T. Dinh, A. Ozden, J. Wicks, C. McCallum, A.R. Kirmani, D.-H. Nam, C. Gabardo, A. Seifitokaldani, X. Wang, Y.C. Li, F. Li, J. Edwards, L.J. Richter, S.J. Thorpe, D. Sinton, E.H. Sargent, CO2 electrolysis to multicarbon products at activities greater than 1 A cm−2, Science (American Association for the Advancement of Science), 367 (2020) 661-666.

[122] M. Jia, S. Hong, T.S. Wu, X. Li, Y.L. Soo, Z. Sun, Single Sb sites for efficient electrochemical CO2 reduction, Chem Commun (Camb), 55 (2019) 12024-12027.

[123] M. Liu, Y. Pang, B. Zhang, P. De Luna, O. Voznyy, J. Xu, X. Zheng, C.T. Dinh, F. Fan, C. Cao, F.P. de Arquer, T.S. Safaei, A. Mepham, A. Klinkova, E. Kumacheva, T. Filleter, D. Sinton, S.O. Kelley, E.H. Sargent, Enhanced electrocatalytic CO(2) reduction via field-induced reagent concentration, Nature, 537 (2016) 382-386.

[124] K. Kamiya, Selective single-atom electrocatalysts: a review with a focus on metal-doped covalent triazine frameworks, Chem Sci, 11 (2020) 8339-8349.

[125] H. Mistry, A.S. Varela, C.S. Bonifacio, I. Zegkinoglou, I. Sinev, Y.W. Choi, K. Kisslinger, E.A. Stach, J.C. Yang, P. Strasser, B.R. Cuenya, Highly selective plasma-activated copper catalysts for carbon dioxide reduction to ethylene, Nat Commun, 7 (2016) 12123.

[126] K.P. Kuhl, E.R. Cave, D.N. Abram, T.F. Jaramillo, New insights into the electrochemical reduction of carbon dioxide on metallic copper surfaces, Energ Environ Sci, 5 (2012).

[127] Y. Zhong, S. Wang, M. Li, J. Ma, S. Song, A. Kumar, H. Duan, Y. Kuang, X. Sun, Rational design of copper-based electrocatalysts and electrochemical systems for CO2 reduction: From active sites engineering to mass transfer dynamics, Materials Today Physics, 18 (2021).

[128] W. Ye, X. Guo, T. Ma, A review on electrochemical synthesized copper-based catalysts for electrochemical reduction of CO2 to C2+ products, Chemical Engineering Journal, 414 (2021).

[129] R. Reske, H. Mistry, F. Behafarid, B. Roldan Cuenya, P. Strasser, Particle size effects in the catalytic electroreduction of CO(2) on Cu nanoparticles, J Am Chem Soc, 136 (2014) 6978-6986.

[130] Y. Hori, I. Takahashi, O. Koga, N. Hoshi, Electrochemical reduction of carbon dioxide at various series of copper single crystal electrodes, Journal of Molecular Catalysis A: Chemical, 199 (2003) 39-47.

[131] Z. Chen, T. Wang, B. Liu, D. Cheng, C. Hu, G. Zhang, W. Zhu, H. Wang, Z.J. Zhao, J. Gong, Grain-Boundary-Rich Copper for Efficient Solar-Driven

Electrochemical CO2 Reduction to Ethylene and Ethanol, J Am Chem Soc, 142 (2020) 6878-6883.

[132] S.Y. Lee, H. Jung, N.K. Kim, H.S. Oh, B.K. Min, Y.J. Hwang, Mixed Copper States in Anodized Cu Electrocatalyst for Stable and Selective Ethylene Production from CO2 Reduction, J Am Chem Soc, 140 (2018) 8681-8689.

[133] P. De Luna, R. Quintero-Bermudez, C.-T. Dinh, M.B. Ross, O.S. Bushuyev, P. Todorović, T. Regier, S.O. Kelley, P. Yang, E.H. Sargent, Catalyst electro-redeposition controls morphology and oxidation state for selective carbon dioxide reduction, Nat Catal, 1 (2018) 103-110.

[134] Y. Lum, B. Yue, P. Lobaccaro, A.T. Bell, J.W. Ager, Optimizing C–C Coupling on Oxide-Derived Copper Catalysts for Electrochemical CO2 Reduction, The Journal of Physical Chemistry C, 121 (2017) 14191-14203.

[135] Q. Lei, H. Zhu, K. Song, N. Wei, L. Liu, D. Zhang, J. Yin, X. Dong, K. Yao, N. Wang, X. Li, B. Davaasuren, J. Wang, Y. Han, Investigating the Origin of Enhanced C(2+) Selectivity in Oxide-/Hydroxide-Derived Copper Electrodes during CO(2) Electroreduction, J Am Chem Soc, 142 (2020) 4213-4222.

[136] J. Liu, J. Fu, Y. Zhou, W. Zhu, L.P. Jiang, Y. Lin, Controlled Synthesis of EDTA-Modified Porous Hollow Copper Microspheres for High-Efficiency Conversion of CO(2) to Multicarbon Products, Nano Lett, 20 (2020) 4823-4828.

[137] Y. Fu, Q. Xie, L. Wu, J. Luo, Crystal facet effect induced by different pretreatment of Cu2O nanowire electrode for enhanced electrochemical CO2 reduction to C2+ products, Chinese Journal of Catalysis, 43 (2022) 1066-1073.

[138] R.F. Zarandi, B. Rezaei, H.S. Ghaziaskar, A.A. Ensafi, Electrochemical reduction of CO2 to ethanol using copper nanofoam electrode and 1-butyl-3-

methyl-imidazolium bromide as the homogeneous co-catalyst, Journal of Environmental Chemical Engineering, 7 (2019).

[139] D. Chi, H. Yang, Y. Du, T. Lv, G. Sui, H. Wang, J. Lu, Morphology-controlled CuO nanoparticles for electroreduction of CO2 to ethanol, RSC Adv., 4 (2014) 37329-37332.

[140] D. Ren, Y. Deng, A.D. Handoko, C.S. Chen, S. Malkhandi, B.S. Yeo, Selective Electrochemical Reduction of Carbon Dioxide to Ethylene and Ethanol on Copper(I) Oxide Catalysts, Acs Catal, 5 (2015) 2814-2821.

[141] D. Gao, I. Sinev, F. Scholten, R.M. Aran-Ais, N.J. Divins, K. Kvashnina, J. Timoshenko, B. Roldan Cuenya, Selective CO(2) Electroreduction to Ethylene and Multicarbon Alcohols via Electrolyte-Driven Nanostructuring, Angew Chem Int Ed Engl, 58 (2019) 17047-17053.

[142] P. Liu, H. Liu, S. Zhang, J. Wang, C. Wang, Significant role of reconstructed character on CuO-derived catalyst for enhanced electrocatalytic reduction of CO2 to multicarbon products, Electrochimica Acta, 354 (2020) 136753.

[143] R. Kas, R. Kortlever, A. Milbrat, M.T. Koper, G. Mul, J. Baltrusaitis, Electrochemical CO2 reduction on Cu2O-derived copper nanoparticles: controlling the catalytic selectivity of hydrocarbons, Phys Chem Chem Phys, 16 (2014) 12194-12201.

[144] H.-Q. Liang, S. Zhao, X.-M. Hu, M. Ceccato, T. Skrydstrup, K. Daasbjerg, Hydrophobic Copper Interfaces Boost Electroreduction of Carbon Dioxide to Ethylene in Water, Acs Catal, 11 (2021) 958-966.

[145] M.G. Kibria, C.T. Dinh, A. Seifitokaldani, P. De Luna, T. Burdyny, R. Quintero-Bermudez, M.B. Ross, O.S. Bushuyev, F.P. García de Arquer, P. Yang,

D. Sinton, E.H. Sargent, A Surface Reconstruction Route to High Productivity and Selectivity in CO2 Electroreduction toward C2+ Hydrocarbons, Adv Mater, 30 (2018).

[146] T.T.H. Hoang, S. Verma, S. Ma, T.T. Fister, J. Timoshenko, A.I. Frenkel, P.J.A. Kenis, A.A. Gewirth, Nanoporous Copper-Silver Alloys by Additive-Controlled Electrodeposition for the Selective Electroreduction of CO2 to Ethylene and Ethanol, J Am Chem Soc, 140 (2018) 5791-5797.

[147] S. Lee, G. Park, J. Lee, Importance of Ag–Cu Biphasic Boundaries for Selective Electrochemical Reduction of CO2 to Ethanol, Acs Catal, 7 (2017) 8594-8604.

[148] L. Hou, J. Han, C. Wang, Y. Zhang, Y. Wang, Z. Bai, Y. Gu, Y. Gao, X. Yan, Ag nanoparticle embedded Cu nanoporous hybrid arrays for the selective electrocatalytic reduction of CO2 towards ethylene, Inorganic Chemistry Frontiers, 7 (2020) 2097-2106.

[149] L.R.L. Ting, O. Piqué, S.Y. Lim, M. Tanhaei, F. Calle-Vallejo, B.S. Yeo, Enhancing CO2 Electroreduction to Ethanol on Copper–Silver Composites by Opening an Alternative Catalytic Pathway, Acs Catal, 10 (2020) 4059-4069.

[150] Y.C. Li, Z. Wang, T. Yuan, D.H. Nam, M. Luo, J. Wicks, B. Chen, J. Li, F. Li, F.P.G. de Arquer, Y. Wang, C.T. Dinh, O. Voznyy, D. Sinton, E.H. Sargent, Binding Site Diversity Promotes CO2 Electroreduction to Ethanol, J Am Chem Soc, 141 (2019) 8584-8591.

[151] F. Jia, X. Yu, L. Zhang, Enhanced selectivity for the electrochemical reduction of CO2 to alcohols in aqueous solution with nanostructured Cu–Au alloy as catalyst, Journal of Power Sources, 252 (2014) 85-89.

[152] C.G. Morales-Guio, E.R. Cave, S.A. Nitopi, J.T. Feaster, L. Wang, K.P. Kuhl, A. Jackson, N.C. Johnson, D.N. Abram, T. Hatsukade, C. Hahn, T.F. Jaramillo, Improved CO2 reduction activity towards C2+ alcohols on a tandem gold on copper electrocatalyst, Nat Catal, 1 (2018) 764-771.

[153] S. Shen, X. Peng, L. Song, Y. Qiu, C. Li, L. Zhuo, J. He, J. Ren, X. Liu, J. Luo, AuCu Alloy Nanoparticle Embedded Cu Submicrocone Arrays for Selective Conversion of CO2 to Ethanol, Small, 15 (2019) e1902229.

[154] B.-B. Zhang, Y.-H. Wang, S.-M. Xu, K. Chen, Y.-G. Yang, Q.-H. Kong, Tuning nanocavities of Au@Cu2O yolk–shell nanoparticles for highly selective electroreduction of CO2 to ethanol at low potential, RSC Advances, 10 (2020) 19192-19198.

[155] F.Y. Zhang, T. Sheng, N. Tian, L. Liu, C. Xiao, B.A. Lu, B.B. Xu, Z.Y. Zhou, S.G. Sun, Cu overlayers on tetrahexahedral Pd nanocrystals with high-index facets for CO2 electroreduction to alcohols, Chem Commun (Camb), 53 (2017) 8085-8088.

[156] X. Zhi, Y. Jiao, Y. Zheng, A. Vasileff, S.-Z. Qiao, Selectivity roadmap for electrochemical CO2 reduction on copper-based alloy catalysts, Nano Energy, 71 (2020).

[157] M. Luo, Z. Wang, Y.C. Li, J. Li, F. Li, Y. Lum, D.-H. Nam, B. Chen, J. Wicks, A. Xu, T. Zhuang, W.R. Leow, X. Wang, C.-T. Dinh, Y. Wang, Y. Wang, D. Sinton, E.H. Sargent, Hydroxide promotes carbon dioxide electroreduction to ethanol on copper via tuning of adsorbed hydrogen, Nature Communications, 10 (2019).

[158] X. Zhang, C. Liu, Y. Zhao, L. Li, Y. Chen, F. Raziq, L. Qiao, S.-X. Guo, C. Wang, G.G. Wallace, A.M. Bond, J. Zhang, Atomic nickel cluster decorated

defect-rich copper for enhanced C2 product selectivity in electrocatalytic CO2 reduction, Applied Catalysis B: Environmental, 291 (2021).

[159] V.K. Abdelkader-Fernández, D.M. Fernandes, C. Freire, Carbon-based electrocatalysts for CO2 electroreduction produced via MOF, biomass, and other precursors carbonization: A review, J Co2 Util, 42 (2020) 101350.

[160] Z.X. Song, L. Zhang, K. Doyle-Davis, X.Z. Fu, J.L. Luo, X.L. Sun, Recent Advances in MOF-Derived Single Atom Catalysts for Electrochemical Applications, Adv Energy Mater, (2020).

[161] X. Sun, R. Wang, S. Ould-Chikh, D. Osadchii, G. Li, A. Aguilar, J.-l. Hazemann, F. Kapteijn, J. Gascon, Structure-activity relationships in metal organic framework derived mesoporous nitrogen-doped carbon containing atomically dispersed iron sites for CO2 electrochemical reduction, Journal of Catalysis, 378 (2019) 320-330.

[162] K. Zhao, Y. Liu, X. Quan, S. Chen, H. Yu, CO2 Electroreduction at Low Overpotential on Oxide-Derived Cu/Carbons Fabricated from Metal Organic Framework, ACS Appl Mater Interfaces, 9 (2017) 5302-5311.

[163] X. Huang, Z. Yin, S. Wu, X. Qi, Q. He, Q. Zhang, Q. Yan, F. Boey, H. Zhang, Graphene-based materials: synthesis, characterization, properties, and applications, Small, 7 (2011) 1876-1902.

[164] Y. Song, R. Peng, D.K. Hensley, P.V. Bonnesen, L. Liang, Z. Wu, H.M. Meyer, M. Chi, C. Ma, B.G. Sumpter, A.J. Rondinone, High-Selectivity Electrochemical Conversion of CO2to Ethanol using a Copper Nanoparticle/N-Doped Graphene Electrode, ChemistrySelect, 1 (2016) 6055-6061.

[165] Y. Zhang, K. Li, M. Chen, J. Wang, J. Liu, Y. Zhang, Cu/Cu2O Nanoparticles Supported on Vertically ZIF-L-Coated Nitrogen-Doped Graphene

Nanosheets for Electroreduction of CO2 to Ethanol, ACS Applied Nano Materials, 3 (2019) 257-263.

[166] X. Wang, Z. Wang, F.P. García de Arquer, C.-T. Dinh, A. Ozden, Y.C. Li, D.-H. Nam, J. Li, Y.-S. Liu, J. Wicks, Z. Chen, M. Chi, B. Chen, Y. Wang, J. Tam, J.Y. Howe, A. Proppe, P. Todorović, F. Li, T.-T. Zhuang, C.M. Gabardo, A.R. Kirmani, C. McCallum, S.-F. Hung, Y. Lum, M. Luo, Y. Min, A. Xu, C.P. O'Brien, B. Stephen, B. Sun, A.H. Ip, L.J. Richter, S.O. Kelley, D. Sinton, E.H. Sargent, Efficient electrically powered CO2-to-ethanol via suppression of deoxygenation, Nature Energy, 5 (2020) 478-486.

[167] J. Yuan, M.-P. Yang, W.-Y. Zhi, H. Wang, H. Wang, J.-X. Lu, Efficient electrochemical reduction of CO2 to ethanol on Cu nanoparticles decorated on N-doped graphene oxide catalysts, J Co2 Util, 33 (2019) 452-460.

[168] Z. Li, Y. Yang, Z. Yin, X. Wei, H. Peng, K. Lyu, F. Wei, L. Xiao, G. Wang, H.D. Abruña, J. Lu, L. Zhuang, Interface-Enhanced Catalytic Selectivity on the C2 Products of CO2 Electroreduction, Acs Catal, (2021) 2473-2482.

[169] P. Li, L. Liu, W. An, H. Wang, H. Guo, Y. Liang, W. Cui, Ultrathin porous g-C3N4 nanosheets modified with AuCu alloy nanoparticles and C-C coupling photothermal catalytic reduction of CO to ethanol, Applied Catalysis B: Environmental, 266 (2020).

[170] M. Wu, X. Dong, W. Chen, A. Chen, C. Zhu, G. Feng, G. Li, Y. Song, W. Wei, Y. Sun, Investigating the Effect of the Initial Valence States of Copper on CO2 Electroreduction, Chemelectrochem, 8 (2021) 3366-3370.

[171] J.-N. Lu, J. Liu, L. Zhang, L.-Z. Dong, S.-L. Li, Y.-Q. Lan, Crystalline mixed-valence copper supramolecular isomers for electroreduction of CO2 to hydrocarbons, J Mater Chem A, 9 (2021) 23477-23484.

[172] P. Qi, L. Zhao, Z. Deng, H. Sun, H. Li, Q. Liu, X. Li, Y. Lian, J. Cheng, J. Guo, Y. Cui, Y. Peng, Revisiting the Grain and Valence Effect of Oxide-Derived Copper on Electrocatalytic CO2 Reduction Using Single Crystal Cu(111) Foils, The Journal of Physical Chemistry Letters, 12 (2021) 3941-3950.

[173] P. Wang, S. Meng, B. Zhang, M. He, P. Li, C. Yang, G. Li, Z. Li, Sub-1 nm Cu2O Nanosheets for the Electrochemical CO2 Reduction and Valence State–Activity Relationship, Journal of the American Chemical Society, 145 (2023) 26133-26143.

[174] H. Jung, S.Y. Lee, C.W. Lee, M.K. Cho, D.H. Won, C. Kim, H.S. Oh, B.K. Min, Y.J. Hwang, Electrochemical Fragmentation of Cu2O Nanoparticles Enhancing Selective C-C Coupling from CO2 Reduction Reaction, J Am Chem Soc, 141 (2019) 4624-4633.

[175] J. Kim, W. Choi, J.W. Park, C. Kim, M. Kim, H. Song, Branched Copper Oxide Nanoparticles Induce Highly Selective Ethylene Production by Electrochemical Carbon Dioxide Reduction, J Am Chem Soc, 141 (2019) 6986-6994.

[176] Y. Zhou, F. Che, M. Liu, C. Zou, Z. Liang, P. De Luna, H. Yuan, J. Li, Z. Wang, H. Xie, H. Li, P. Chen, E. Bladt, R. Quintero-Bermudez, T.K. Sham, S. Bals, J. Hofkens, D. Sinton, G. Chen, E.H. Sargent, Dopant-induced electron localization drives CO(2) reduction to C(2) hydrocarbons, Nat Chem, 10 (2018) 974-980.

[177] D. Ren, N.T. Wong, A.D. Handoko, Y. Huang, B.S. Yeo, Mechanistic Insights into the Enhanced Activity and Stability of Agglomerated Cu Nanocrystals for the Electrochemical Reduction of Carbon Dioxide to n-Propanol, J Phys Chem Lett, 7 (2016) 20-24.

[178] Z. Weng, X. Zhang, Y. Wu, S. Huo, J. Jiang, W. Liu, G. He, Y. Liang, H. Wang, Self-Cleaning Catalyst Electrodes for Stabilized CO2 Reduction to Hydrocarbons, Angewandte Chemie International Edition, 56 (2017) 13135-13139.

[179] H. Han, Y. Noh, Y. Kim, S. Park, W. Yoon, D. Jang, S.M. Choi, W.B. Kim, Selective electrochemical CO2 conversion to multicarbon alcohols on highly efficient N-doped porous carbon-supported Cu catalysts, Green Chem, 22 (2020) 71-84.

[180] J. Xiao, T. Zhang, Q. Wang, Metal–organic framework derived single-atom catalysts for CO2 conversion to methanol, Curr Opin Green Sust, 37 (2022) 100660.

[181] X. Xie, X. Zhang, M. Xie, L. Xiong, H. Sun, Y. Lu, Q. Mu, M.H. Rummeli, J. Xu, S. Li, J. Zhong, Z. Deng, B. Ma, T. Cheng, W.A. Goddard, Y. Peng, Au-activated N motifs in non-coherent cupric porphyrin metal organic frameworks for promoting and stabilizing ethylene production, Nature Communications, 13 (2022).

[182] M.R. Li, S. Garg, X.X. Chang, L. Ge, L.Y. Li, M. Konarova, T.E. Rufford, V. Rudolph, G. Wang, Toward Excellence of Transition Metal-Based Catalysts for CO(2)Electrochemical Reduction: An Overview of Strategies and Rationales, Small Methods, 4 (2020).

[183] X. Zhang, J. Li, Y.Y. Li, Y. Jung, Y. Kuang, G. Zhu, Y. Liang, H. Dai, Selective and High Current CO2 Electro-Reduction to Multicarbon Products in Near-Neutral KCl Electrolytes, J Am Chem Soc, (2021).

[184] H.P. Yang, X.D. Wang, Q. Hu, X.Y. Chai, X.Z. Ren, Q.L. Zhang, J.H. Liu, C.X. He, Recent Progress in Self-Supported Catalysts for CO2 Electrochemical Reduction, Small Methods, 4 (2020).

[185] A. Wagner, C.D. Sahm, E. Reisner, Towards molecular understanding of local chemical environment effects in electro- and photocatalytic CO2 reduction, Nat Catal, 3 (2020) 775-786.

[186] H. Peng, Y. Liu, Y. Guo, J. Zhang, L. Zhang, S. Zhou, X. Xu, W. Liu, N. Zhang, X. Wang, Treating Copper(II) Oxide Nanoflowers with Hydrogen Peroxide: A Novel and Facile Strategy To Prepare High-Performance Copper(II) Oxide Nanosheets with Exposed (1 1 0) Facets, ChemCatChem, 8 (2016) 3714-3719.

[187] S. Li, G. Dong, R. Hailili, L. Yang, Y. Li, F. Wang, Y. Zeng, C. Wang, Effective photocatalytic H2O2 production under visible light irradiation at g-C3N4 modulated by carbon vacancies, Applied Catalysis B: Environmental, 190 (2016) 26-35.

[188] S. Mahzoon, M. Haghighi, M. Nowee, H. Zeinalzadeh, Sonoprecipitation design of novel efficient all-solid Z-Scheme Cu(OH)2/Cu2O/C3N4 nanophotocatalyst applied in water splitting for H2 production: Synergetic effect of Cu-Based cocatalyst (Cu(OH)2) and electron mediator (Cu), Solar Energy Materials and Solar Cells, 219 (2021).

[189] L. Vivas, I. Chi-Duran, J. Enríquez, N. Barraza, D.P. Singh, Ascorbic acid based controlled growth of various Cu and Cu2O nanostructures, Materials Research Express, 6 (2019).

[190] Z. Yan, T. Wu, Highly Selective Electrochemical CO(2) Reduction to C(2) Products on a g-C(3)N(4)-Supported Copper-Based Catalyst, Int J Mol Sci, 23 (2022) 14381.

[191] J. Liu, P. Li, J. Bi, Q. Zhu, B. Han, Design and Preparation of Electrocatalysts by Electrodeposition for CO2 Reduction, Chemistry – A European Journal, 28 (2022).

[192] I.S. Brandt, M.A. Tumelero, S. Pelegrini, G. Zangari, A.A. Pasa, Electrodeposition of Cu2O: growth, properties, and applications, Journal of Solid State Electrochemistry, 21 (2017) 1999-2020.

[193] H. Yuan, Z. Liu, S. Sang, X. Wang, Dynamic re-construction of sulfur tailored Cu2O for efficient electrochemical CO2 reduction to formate over a wide potential window, Applied Surface Science, 613 (2023).

[194] O.A. Baturina, Q. Lu, M.A. Padilla, L. Xin, W. Li, A. Serov, K. Artyushkova, P. Atanassov, F. Xu, A. Epshteyn, T. Brintlinger, M. Schuette, G.E. Collins, CO2 Electroreduction to Hydrocarbons on Carbon-Supported Cu Nanoparticles, Acs Catal, 4 (2014) 3682-3695.

[195] S. Zhao, Z. Tang, S. Guo, M. Han, C. Zhu, Y. Zhou, L. Bai, J. Gao, H. Huang, Y. Li, Y. Liu, Z. Kang, Enhanced Activity for CO2 Electroreduction on a Highly Active and Stable Ternary Au-CDots-C3N4 Electrocatalyst, Acs Catal, 8 (2017) 188-197.

[196] K. Jiang, R.B. Sandberg, A.J. Akey, X. Liu, D.C. Bell, J.K. Nørskov, K. Chan, H. Wang, Metal ion cycling of Cu foil for selective C–C coupling in electrochemical CO2 reduction, Nat Catal, 1 (2018) 111-119.

[197] K. Ngamchuea, S. Eloul, K. Tschulik, R.G. Compton, Planar diffusion to macro disc electrodes—what electrode size is required for the Cottrell and

Randles-Sevcik equations to apply quantitatively?, Journal of Solid State Electrochemistry, 18 (2014) 3251-3257.

[198] M. Abd Mutalib, M.A. Rahman, M.H.D. Othman, A.F. Ismail, J. Jaafar, Chapter 9 - Scanning Electron Microscopy (SEM) and Energy-Dispersive X-Ray (EDX) Spectroscopy, in: N. Hilal, A.F. Ismail, T. Matsuura, D. Oatley-Radcliffe (Eds.) Membrane Characterization, Elsevier2017, pp. 161-179.

[199] D. Brabazon, A. Raffer, Chapter 3 - Advanced characterization techniques for nanostructures, in: W. Ahmed, M.J. Jackson (Eds.) Emerging Nanotechnologies for Manufacturing (Second Edition), William Andrew Publishing, Boston, 2015, pp. 53-85.

[200] T. Allen, S. Rutherford, S. Murray, S. Reipert, M. Goldberg, Chapter 33 - Field Emission Scanning Electron Microscopy and Visualization of the Cell Interior, in: J.E. Celis (Ed.) Cell Biology (Third Edition), Academic Press, Burlington, 2006, pp. 325-333.

[201] H. Rostamabadi, S.R. Falsafi, S.M. Jafari, Chapter Two - Transmission electron microscopy (TEM) of nanoencapsulated food ingredients, in: S.M. Jafari (Ed.) Characterization of Nanoencapsulated Food Ingredients, Academic Press2020, pp. 53-82.

[202] W. Zhou, Y.H. Ikuhara, Z. Zheng, K. Wang, B. Cao, J. Chen, 17 - Transmission electron microscopy (TEM) studies of functional nanomaterials, in: V.K. Tewary, Y. Zhang (Eds.) Modeling, Characterization, and Production of Nanomaterials (Second Edition), Woodhead Publishing2023, pp. 467-512.

[203] C.Y. Tang, Z. Yang, Chapter 8 - Transmission Electron Microscopy (TEM), in: N. Hilal, A.F. Ismail, T. Matsuura, D. Oatley-Radcliffe (Eds.) Membrane Characterization, Elsevier2017, pp. 145-159.

[204] F. Houdellier, Chapter One - Characterization of nanomaterials properties using FE-TEM, in: M. Hÿch, P.W. Hawkes (Eds.) Advances in Imaging and Electron Physics, Elsevier2023, pp. 1-105.

[205] A. Ahmad, M. Pervaiz, S. Ramzan, M.Z. Kiyani, A. Khan, I. Ahmad, A.M. Asiri, 9 - Role of XRD for nanomaterial analysis, in: F. Verpoort, I. Ahmad, A. Ahmad, A. Khan, C.Y. Chee (Eds.) Nanomedicine Manufacturing and Applications, Elsevier2021, pp. 149-161.

[206] J.P.R. de Villiers, L. Lu, Chapter 3 - Quantitative XRD analysis and evaluation of iron ore, sinter, and pellets, in: L. Lu (Ed.) Iron Ore (Second Edition), Woodhead Publishing2022, pp. 109-126.

[207] T. Akitsu, Chapter 2 - Using XRD technique for model composite and related materials, in: H. Song, T.A. Nguyen, G. Yasin, N.B. Singh, R.K. Gupta (Eds.) Nanotechnology in the Automotive Industry, Elsevier2022, pp. 15-35.

[208] A. Dibenedetto, M. Aresta, Single Crystal and Powder XRD Techniques: An Overview, Germany: De Gruyter, Germany, 2013, pp. 1-1.

[209] H. Bluhm, 4 - X-ray photoelectron spectroscopy (XPS) for in situ characterization of thin film growth, in: G. Koster, G. Rijnders (Eds.) In Situ Characterization of Thin Film Growth, Woodhead Publishing2011, pp. 75-98.

[210] M. Aziz, A.F. Ismail, Chapter 5 - X-Ray Photoelectron Spectroscopy (XPS), in: N. Hilal, A.F. Ismail, T. Matsuura, D. Oatley-Radcliffe (Eds.) Membrane Characterization, Elsevier2017, pp. 81-93.

[211] A. Fabien, G. Lefebvre, E. Badens, B. Calvignac, D. Chaudanson, A. Ranguis, C. Crampon, Contact angle of ethanol, water, and their mixtures on stainless steel surfaces in dense carbon dioxide, Journal of Colloid and Interface Science, 655 (2024) 535-545.

[212] F. Wang, M. Xiang, W. Yang, Effects of contact angle hysteresis on frosting and defrosting characteristics on vertical superhydrophobic surfaces, Applied Thermal Engineering, 236 (2024) 121881.

[213] Z. Ye, M. Mizutani, Apparent contact angle of curved and structured surfaces, Colloids and Surfaces A: Physicochemical and Engineering Aspects, 677 (2023) 132337.

[214] J.-i. Saito, M. Monbernier, Relationship between the contact angle of pure Cu and its alloys owing to liquid Na and electronic states at the interface, Surfaces and Interfaces, 41 (2023) 103248.

[215] R. Shawabkeh, A. Al-Absi, M. Shamlooh, M. Khaled, I.A. Hussein, Chapter 6 - Electrochemical reduction of carbon dioxide to hydrocarbons: techniques and methods, in: M. Khalid, S.A. Dharaskar, M. Sillanpää, H. Siddiqui (Eds.) Emerging Carbon Capture Technologies, Elsevier2022, pp. 161-191.

[216] T.W. Quadri, O.E. Fayemi, L.O. Olasunkanmi, E.E. Ebenso, Chapter 15 - Survey of different electrochemical and analytical techniques for corrosion measurements, in: J. Aslam, C. Verma, C. Mustansar Hussain (Eds.) Electrochemical and Analytical Techniques for Sustainable Corrosion Monitoring, Elsevier2023, pp. 293-323.

[217] R.P. Lamsal, D. Beauchemin, Chapter 11 - Electrochemical techniques, in: D. Beauchemin (Ed.) Sample Introduction Systems in ICPMS and ICPOES, Elsevier, Amsterdam, 2020, pp. 533-559.

[218] K. Robards, D. Ryan, Chapter 4 - Gas chromatography, in: K. Robards, D. Ryan (Eds.) Principles and Practice of Modern Chromatographic Methods (Second Edition), Academic Press2022, pp. 145-245.

[219] C.F. Poole, Chapter 12 - Conventional detectors for gas chromatography, in: C.F. Poole (Ed.) Gas Chromatography (Second Edition), Elsevier, Amsterdam, 2021, pp. 343-369.

[220] L.M. Blumberg, Chapter 2 - Theory of gas chromatography, in: C.F. Poole (Ed.) Gas Chromatography (Second Edition), Elsevier, Amsterdam, 2021, pp. 19-97.

[221] M.S. Xie, B.Y. Xia, Y. Li, Y. Yan, Y. Yang, Q. Sun, S.H. Chan, A. Fisher, X. Wang, Amino acid modified copper electrodes for the enhanced selective electroreduction of carbon dioxide towards hydrocarbons, Energ Environ Sci, 9 (2016) 1687-1695.

[222] H. Xiao, T. Cheng, W.A. Goddard, 3rd, Atomistic Mechanisms Underlying Selectivities in C(1) and C(2) Products from Electrochemical Reduction of CO on Cu(111), J Am Chem Soc, 139 (2017) 130-136.

[223] X. Zhang, Y. Geng, S. Shao, J. Wilson, X. Song, W. You, China's non-fossil energy development and its 2030 CO2 reduction targets: The role of urbanization, Applied Energy, 261 (2020).

[224] R. Chai, Y. Liu, J. Wang, Q. Liu, Z. Rui, CO2 utilization and sequestration in Reservoir: Effects and mechanisms of CO2 electrochemical reduction, Applied Energy, 323 (2022).

[225] S. Pacala, Stabilization Wedges: Solving the Climate Problem for the Next 50 Years with Current Technologies, Science (American Association for the Advancement of Science), 305 (2004) 968-972.

[226] Y. Huang, A.D. Handoko, P. Hirunsit, B.S. Yeo, Electrochemical Reduction of CO2 Using Copper Single-Crystal Surfaces: Effects of CO*

Coverage on the Selective Formation of Ethylene, Acs Catal, 7 (2017) 1749-1756.

[227] C. Hahn, T. Hatsukade, Y.G. Kim, A. Vailionis, J.H. Baricuatro, D.C. Higgins, S.A. Nitopi, M.P. Soriaga, T.F. Jaramillo, Engineering Cu surfaces for the electrocatalytic conversion of CO(2): Controlling selectivity toward oxygenates and hydrocarbons, Proc Natl Acad Sci U S A, 114 (2017) 5918-5923.

[228] A. Loiudice, P. Lobaccaro, E.A. Kamali, T. Thao, B.H. Huang, J.W. Ager, R. Buonsanti, Tailoring Copper Nanocrystals towards C2 Products in Electrochemical CO2 Reduction, Angew Chem Int Ed Engl, 55 (2016) 5789-5792.

[229] M. Ye, T. Shao, J. Liu, C. Li, B. Song, S. Liu, Phase engineering of Cu@Cu2O core-shell nanospheres for boosting tandem electrochemical CO2 reduction to C2+ products, Applied Surface Science, 622 (2023).

[230] F. Cavalca, R. Ferragut, S. Aghion, A. Eilert, O. Diaz-Morales, C. Liu, A.L. Koh, T.W. Hansen, L.G.M. Pettersson, A. Nilsson, Nature and Distribution of Stable Subsurface Oxygen in Copper Electrodes During Electrochemical CO2 Reduction, The Journal of Physical Chemistry C, 121 (2017) 25003-25009.

[231] S. Qiao, Y. Chen, Y. Tang, J. Yuan, J. Shen, D. Zhang, Y. Du, Z. Li, D. Yuan, H. Tang, C. Liu, Oxygen vacancy–rich Cu2O@Cu with a hydrophobic microenvironment for highly selective CC coupling to generate C2H4, Chemical Engineering Journal, 454 (2023) 140321.

[232] H. Liu, Y. Su, Z. Liu, H. Chuai, S. Zhang, X. Ma, Tailoring microenvironment for enhanced electrochemical CO2 reduction on ultrathin tin oxide derived nanosheets, Nano Energy, 105 (2023) 108031.

[233] J.Y. Maeng, S.Y. Hwang, C.K. Rhee, Y. Sohn, Electrochemical CO2 reduction over surface-modified Cd-based electrodes and reaction paths for long-chain hydrocarbons, Applied Surface Science, 631 (2023).

[234] H. Chen, Z. Wang, X. Wei, S. Liu, P. Guo, P. Han, H. Wang, J. Zhang, X. Lu, B. Wei, Promotion of electrochemical CO2 reduction to ethylene on phosphorus-doped copper nanocrystals with stable Cuδ+ sites, Applied Surface Science, 544 (2021).

[235] Z. Cai, Y. Zhang, Y. Zhao, Y. Wu, W. Xu, X. Wen, Y. Zhong, Y. Zhang, W. Liu, H. Wang, Y. Kuang, X. Sun, Selectivity regulation of CO2 electroreduction through contact interface engineering on superwetting Cu nanoarray electrodes, Nano Research, 12 (2018) 345-349.

[236] M. Wang, L. Wan, J. Luo, Promoting CO2 electroreduction on CuO nanowires with a hydrophobic Nafion overlayer, Nanoscale, 13 (2021) 3588-3593.

[237] H. Pan, C.J. Barile, Electrochemical CO2 reduction to methane with remarkably high Faradaic efficiency in the presence of a proton permeable membrane, Energ Environ Sci, 13 (2020) 3567-3578.

[238] L. Zhao, Z. Yuan, B. Ma, X. Ding, Y. Tian, X. Yang, Regulation of three-dimensional hydrophobic state of copper dendrite adjusts the distribution of liquid products from electrochemical reduction of CO2, Applied Surface Science, 628 (2023).

[239] B. Xu, F. Wu, S. Chen, Z. Zhou, G. Cao, Y. Yang, High-capacitance carbon electrode prepared by PVDC carbonization for aqueous EDLCs, Electrochimica acta, 54 (2009) 2185-2189.

[240] Y.-J. Kim, Y. Masutzawa, S. Ozaki, M. Endo, M.S. Dresselhaus, PVDC-based carbon material by chemical activation and its application to nonaqueous EDLC, Journal of the Electrochemical Society, 151 (2004) E199-E205.

[241] D. Hambali, Z. Osman, L. Othman, K.B.M. Isa, N. Harudin, Magnesium (II) bis(trifluoromethanesulfonimide) doped PVdC-co-AN gel polymer electrolytes for rechargeable batteries, Journal of polymer research, 27 (2020).

[242] D. Hambali, N.H. Zainol, L. Othman, K.B. Md Isa, Z. Osman, Magnesium ion-conducting gel polymer electrolytes based on poly(vinylidene chloride-co-acrylonitrile) (PVdC-co-AN): a comparative study between magnesium trifluoromethanesulfonate (MgTf2) and magnesium bis(trifluoromethanesulfonimide) (Mg(TFSI)2), Ionics, 25 (2019) 1187-1198.

[243] Junyi.Wu, <聚偏氟乙烯树脂的应用和聚合进展.pdf>, Organo-Fluorine Industry, 1 (2008) 26.

[244] A. Zahid, A. Shah, I. Shah, Oxide Derived Copper for Electrochemical Reduction of CO(2) to C(2+) Products, Nanomaterials (Basel), 12 (2022) 1380.

[245] Z.Q. Liang, T.T. Zhuang, A. Seifitokaldani, J. Li, C.W. Huang, C.S. Tan, Y. Li, P. De Luna, C.T. Dinh, Y. Hu, Q. Xiao, P.L. Hsieh, Y. Wang, F. Li, R. Quintero-Bermudez, Y. Zhou, P. Chen, Y. Pang, S.C. Lo, L.J. Chen, H. Tan, Z. Xu, S. Zhao, D. Sinton, E.H. Sargent, Copper-on-nitride enhances the stable electrosynthesis of multi-carbon products from CO2, Nat Commun, 9 (2018) 3828.

[246] C.S. Chen, A.D. Handoko, J.H. Wan, L. Ma, D. Ren, B.S. Yeo, Stable and selective electrochemical reduction of carbon dioxide to ethylene on copper mesocrystals, Catal Sci Technol, 5 (2015) 161-168.

[247] H.S. Jeon, S. Kunze, F. Scholten, B. Roldan Cuenya, Prism-Shaped Cu Nanocatalysts for Electrochemical CO2 Reduction to Ethylene, Acs Catal, 8 (2017) 531-535.

[248] D. Kim, C.S. Kley, Y. Li, P. Yang, Copper nanoparticle ensembles for selective electroreduction of CO2 to C2-C3 products, Proc Natl Acad Sci U S A, 114 (2017) 10560-10565.

[249] D. Kim, S. Lee, J.D. Ocon, B. Jeong, J.K. Lee, J. Lee, Insights into an autonomously formed oxygen-evacuated Cu2O electrode for the selective production of C2H4 from CO2, Phys Chem Chem Phys, 17 (2015) 824-830.

[250] S. Mu, H. Lu, Q. Wu, L. Li, R. Zhao, C. Long, C. Cui, Hydroxyl radicals dominate reoxidation of oxide-derived Cu in electrochemical CO2 reduction, Nat Commun, 13 (2022) 3694.

[251] C. Chen, X. Yan, Y. Wu, S. Liu, X. Zhang, X. Sun, Q. Zhu, H. Wu, B. Han, Boosting the Productivity of Electrochemical CO2 Reduction to Multi-Carbon Products by Enhancing CO2 Diffusion through a Porous Organic Cage, Angewandte Chemie International Edition, 61 (2022).

[252] R.P. Gautam, Y.T. Lee, G.L. Herman, C.M. Moreno, E.C.M. Tse, C.J. Barile, Controlling Proton and Electron Transfer Rates to Enhance the Activity of an Oxygen Reduction Electrocatalyst, Angew Chem Int Ed Engl, 57 (2018) 13480-13483.

[253] D. Voiry, M. Chhowalla, Y. Gogotsi, N.A. Kotov, Y. Li, R.M. Penner, R.E. Schaak, P.S. Weiss, Best Practices for Reporting Electrocatalytic Performance of Nanomaterials, Acs Nano, 12 (2018) 9635-9638.

[254] R.S. Kanase, K.B. Lee, M. Arunachalam, R.P. Sivasankaran, J. Oh, S.H. Kang, Nanostructure engineering of Cu electrocatalyst for the selective

C2+ hydrocarbons in electrochemical CO2 reduction, Applied Surface Science, 584 (2022).

[255] L. Yu, Z. Ren, Systematic study of the influence of iR compensation on water electrolysis, Materials Today Physics, 14 (2020).

[256] Z. Wang, T. Li, Q. Wang, A. Guan, N. Cao, A.M. Al-Enizi, L. Zhang, L. Qian, G. Zheng, Hydrophobically made Ag nanoclusters with enhanced performance for CO2 aqueous electroreduction, Journal of Power Sources, 476 (2020).

[257] P. Yue, Q. Fu, J. Li, L. Zhang, L. Xing, Z. Kang, Q. Liao, X. Zhu, Triple-phase electrocatalysis for the enhanced CO2 reduction to HCOOH on a hydrophobic surface, Chemical Engineering Journal, 405 (2021).

[258] D. Wakerley, S. Lamaison, F. Ozanam, N. Menguy, D. Mercier, P. Marcus, M. Fontecave, V. Mougel, Bio-inspired hydrophobicity promotes CO2 reduction on a Cu surface, Nat Mater, 18 (2019) 1222-1227.

[259] H. Song, J.T. Song, B. Kim, Y.C. Tan, J. Oh, Activation of C2H4 reaction pathways in electrochemical CO2 reduction under low CO2 partial pressure, Applied Catalysis B: Environmental, 272 (2020).

[260] X. She, T. Zhang, Z. Li, H. Li, H. Xu, J. Wu, Tandem Electrodes for Carbon Dioxide Reduction into C2+ Products at Simultaneously High Production Efficiency and Rate, Cell Reports Physical Science, 1 (2020).

[261] T. Al-Ati, J.H. Hotchkiss, The Role of Packaging Film Permselectivity in Modified Atmosphere Packaging, Journal of Agricultural and Food Chemistry, 51 (2003) 4133-4138.

[262] Y. Quan, J. Zhu, G. Zheng, Electrocatalytic Reactions for Converting CO2 to Value‐Added Products, Small Science, 1 (2021).

[263] J.-J. Velasco-Vélez, T. Jones, D. Gao, E. Carbonio, R. Arrigo, C.-J. Hsu, Y.-C. Huang, C.-L. Dong, J.-M. Chen, J.-F. Lee, P. Strasser, B. Roldan Cuenya, R. Schlögl, A. Knop-Gericke, C.-H. Chuang, The Role of the Copper Oxidation State in the Electrocatalytic Reduction of CO2 into Valuable Hydrocarbons, ACS Sustainable Chemistry & Engineering, 7 (2018) 1485-1492.

[264] R.M. Arán-Ais, F. Scholten, S. Kunze, R. Rizo, B. Roldan Cuenya, The role of in situ generated morphological motifs and Cu(i) species in C2+ product selectivity during CO2 pulsed electroreduction, Nature Energy, 5 (2020) 317-325.

[265] Z. Lyu, S. Zhu, M. Xie, Y. Zhang, Z. Chen, R. Chen, M. Tian, M. Chi, M. Shao, Y. Xia, Controlling the Surface Oxidation of Cu Nanowires Improves Their Catalytic Selectivity and Stability toward C(2+) Products in CO(2) Reduction, Angew Chem Int Ed Engl, 60 (2021) 1909-1915.

[266] S. Wang, T. Kou, S.E. Baker, E.B. Duoss, Y. Li, Recent progress in electrochemical reduction of CO2 by oxide-derived copper catalysts, Materials Today Nano, 12 (2020) 100096.

[267] J.-S.C. Sung Hwa Jhung, Sang-Eon Park, Paul M. Forster, Gérard Férey, and Anthony K. Cheetham, Template-Free Synthesis of the Nanoporous Nickel Phosphate VSB-5 under Microwave Irradiation, Chemistry of Materials, 16 (8) (2004) 1394-1396.

[268] I. Bilecka, M. Niederberger, Microwave chemistry for inorganic nanomaterials synthesis, Nanoscale, 2 (2010).

[269] J.M.K. M. Antonia Herrero, and C. Oliver Kappe, Nonthermal Microwave Effects Revisited: On the Importance of Internal Temperature Monitoring and

Agitation in Microwave Chemistry, The Journal of Organic Chemistry, 73 (2008) 36-47.

[270] R. Krishnan, S.N. Shibu, D. Poelman, A.K. Badyal, A.K. Kunti, H.C. Swart, S.G. Menon, Recent advances in microwave synthesis for photoluminescence and photocatalysis, Materials Today Communications, 32 (2022) 103890.

[271] M.L. Moreira, V.M. Longo, W. Avansi, M.M. Ferrer, J. Andrés, V.R. Mastelaro, J.A. Varela, É. Longo, Quantum Mechanics Insight into the Microwave Nucleation of SrTiO3 Nanospheres, The Journal of Physical Chemistry C, 116 (2012) 24792-24808.

[272] D. Dallinger, C.O. Kappe, Microwave-Assisted Synthesis in Water as Solvent, Chem Rev, 107 (2007) 2563-2591.

[273] K. Kannan, D. Radhika, S. Vijayalakshmi, K.K. Sadasivuni, A. A. Ojiaku, U. Verma, Facile fabrication of CuO nanoparticles via microwave-assisted method: photocatalytic, antimicrobial and anticancer enhancing performance, International Journal of Environmental Analytical Chemistry, 102 (2022) 1095-1108.

[274] D.P. Volanti, D. Keyson, L.S. Cavalcante, A.Z. Simões, M.R. Joya, E. Longo, J.A. Varela, P.S. Pizani, A.G. Souza, Synthesis and characterization of CuO flower-nanostructure processing by a domestic hydrothermal microwave, Journal of Alloys and Compounds, 459 (2008) 537-542.

[275] J.-Z.X. Hui Wang, Jun-Jie Zhu*, Hong-Yuan Chen, Preparation of CuO nanoparticles by microwave irradiation, Journal of Crystal Growth 244 (2002) 88-94.

[276] J. Zeng, K. Bejtka, G. Di Martino, A. Sacco, M. Castellino, M. Re Fiorentin, F. Risplendi, M.A. Farkhondehfal, S. Hernández, G. Cicero, C.F. Pirri, A. Chiodoni, Microwave-Assisted Synthesis of Copper-Based Electrocatalysts for Converting Carbon Dioxide to Tunable Syngas, Chemelectrochem, 7 (2020) 229-238.

[277] Z.Y. Wang L, Zeng Z, Zhou H, He J, Liu P, Chen M, Han J, Srolovitz DJ, Teng J, Guo Y, Yang G, Kong D, Ma E, Hu Y, Yin B, Huang X, Zhang Z, Zhu T, Han X., Tracking the sliding of grain boundaries at the atomic scale, Science, 375(6586) (2022) 1261-1265.

[278] Z. Gu, N. Yang, P. Han, M. Kuang, B. Mei, Z. Jiang, J. Zhong, L. Li, G. Zheng, Oxygen Vacancy Tuning toward Efficient Electrocatalytic CO2 Reduction to C2H4, Small Methods, 3 (2019) 1800449.

[279] X. Feng, K. Jiang, S. Fan, M.W. Kanan, Grain-boundary-dependent CO2 electroreduction activity, J Am Chem Soc, 137 (2015) 4606-4609.

[280] X. Feng, K. Jiang, S. Fan, M.W. Kanan, A Direct Grain-Boundary-Activity Correlation for CO Electroreduction on Cu Nanoparticles, ACS Cent Sci, 2 (2016) 169-174.

[281] A. Verdaguer-Casadevall, C.W. Li, T.P. Johansson, S.B. Scott, J.T. McKeown, M. Kumar, I.E. Stephens, M.W. Kanan, I. Chorkendorff, Probing the Active Surface Sites for CO Reduction on Oxide-Derived Copper Electrocatalysts, J Am Chem Soc, 137 (2015) 9808-9811.

[282] A. Macedo Andrade, Z. Liu, S. Grewal, A.J. Nelson, Z. Nasef, G. Diaz, M.H. Lee, MOF-derived Co/Cu-embedded N-doped carbon for trifunctional ORR/OER/HER catalysis in alkaline media, Dalton T, 50 (2021) 5473-5482.

[283] X. Yan, L. Zhuang, Z. Zhu, X. Yao, Defect engineering and characterization of active sites for efficient electrocatalysis, Nanoscale, 13 (2021) 3327-3345.

[284] W. Tang, A.A. Peterson, A.S. Varela, Z.P. Jovanov, L. Bech, W.J. Durand, S. Dahl, J.K. Norskov, I. Chorkendorff, The importance of surface morphology in controlling the selectivity of polycrystalline copper for CO2 electroreduction, Phys Chem Chem Phys, 14 (2012) 76-81.

[285] J. Zhang, Y. Wang, Z. Li, S. Xia, R. Cai, L. Ma, T. Zhang, J. Ackley, S. Yang, Y. Wu, J. Wu, Grain Boundary-Derived Cu(+) /Cu(0) Interfaces in CuO Nanosheets for Low Overpotential Carbon Dioxide Electroreduction to Ethylene, Adv Sci (Weinh), 9 (2022) e2200454.

[286] Y. Chen, Z. Fan, J. Wang, C. Ling, W. Niu, Z. Huang, G. Liu, B. Chen, Z. Lai, X. Liu, B. Li, Y. Zong, L. Gu, J. Wang, X. Wang, H. Zhang, Ethylene Selectivity in Electrocatalytic CO2 Reduction on Cu Nanomaterials: A Crystal Phase-Dependent Study, J Am Chem Soc, 142 (2020) 12760-12766.

[287] H. Xiao, W.A. Goddard, 3rd, T. Cheng, Y. Liu, Cu metal embedded in oxidized matrix catalyst to promote CO(2) activation and CO dimerization for electrochemical reduction of CO(2), Proc Natl Acad Sci U S A, 114 (2017) 6685-6688.

[288] H. Li, T. Liu, P. Wei, L. Lin, D. Gao, G. Wang, X. Bao, High-Rate CO(2) Electroreduction to C(2+) Products over a Copper-Copper Iodide Catalyst, Angew Chem Int Ed Engl, 60 (2021) 14329-14333.

[289] C. Liu, X.-D. Zhang, J.-M. Huang, M.-X. Guan, M. Xu, Z.-Y. Gu, In Situ Reconstruction of Cu–N Coordinated MOFs to Generate Dispersive Cu/Cu2O

Nanoclusters for Selective Electroreduction of CO2 to C2H4, Acs Catal, 12 (2022) 15230-15240.

[290] J.L. Bott-Neto, T.S. Martins, O.N. Oliveira Jr, F. Marken, Controlled electrodeposition of brookite TiO2 for photoelectroanalysis at printed carbon electrodes, Applied Surface Science, 640 (2023).

[291] Z. Chen, X. Zhao, R. Lu, R. Hong, X. Yang, Electrodeposition of polypyrrole as binder-free and high mass-loading electrodes for flexible supercapacitors, Synthetic Metals, 296 (2023).

[292] Z. Geng, Z. Cui, Y. Liu, Y. Zhang, L. Wan, N. Gao, J. Liu, H. Li, Electrodeposition ZnO/BDD film as a supercapacitor electrode, Diamond and Related Materials, 140 (2023).

[293] W. Jiang, F. Zhu, Y. Chen, J. Li, W. Cheng, J. Liu, Fabrication of NiCoP-Fe3O4 composite electrode for water electrolysis by magnetically controlled scanning electrodeposition, Journal of Alloys and Compounds, 962 (2023).

[294] X. Yang, Z. Han, J. Song, P. Hu, F. Teng, Novel application of electrochemical test for the controllable electrodeposition of Cu2O and metallic Cu film, Journal of Alloys and Compounds, 970 (2024).

[295] I.A. Poimenidis, M. Lykaki, N. Papakosta, P.A. Loukakos, N. Kallithrakas Kontos, M. Konsolakis, One-step electrodeposition of NiS heterostructures on nickel foam electrodes for hydrogen evolution reaction: On the impact of thiourea content, Results in Chemistry, 6 (2023).

[296] K. Zhan, F. Li, J. Liu, J. Cao, Z. Wang, B. Zhao, Preparation and mechanism of Cu-GO laminated composite films with high thermal conductivity by intermediate nickel and silver layers via electrodeposition and ultrasonic spraying method, Surface and Coatings Technology, 472 (2023) 129960.

[297] Y.-L. Qiu, H.-X. Zhong, T.-T. Zhang, W.-B. Xu, X.-F. Li, H.-M. Zhang, Copper Electrode Fabricated via Pulse Electrodeposition: Toward High Methane Selectivity and Activity for CO2 Electroreduction, Acs Catal, 7 (2017) 6302-6310.

[298] S. Ajmal, Y. Yang, M.A. Tahir, K. Li, A.-U.-R. Bacha, I. Nabi, Y. Liu, T. Wang, L. Zhang, Boosting C2 products in electrochemical CO2 reduction over highly dense copper nanoplates, Catal Sci Technol, 10 (2020) 4562-4570.

[299] Y. Wang, Z. Wang, C.-T. Dinh, J. Li, A. Ozden, M. Golam Kibria, A. Seifitokaldani, C.-S. Tan, C.M. Gabardo, M. Luo, H. Zhou, F. Li, Y. Lum, C. McCallum, Y. Xu, M. Liu, A. Proppe, A. Johnston, P. Todorovic, T.-T. Zhuang, D. Sinton, S.O. Kelley, E.H. Sargent, Catalyst synthesis under CO2 electroreduction favours faceting and promotes renewable fuels electrosynthesis, Nat Catal, 3 (2019) 98-106.

[300] T.T.H. Hoang, S. Ma, J.I. Gold, P.J.A. Kenis, A.A. Gewirth, Nanoporous Copper Films by Additive-Controlled Electrodeposition: CO2 Reduction Catalysis, Acs Catal, 7 (2017) 3313-3321.

[301] Q. Wan, J. Zhang, B. Zhang, D. Tan, L. Yao, L. Zheng, F. Zhang, L. Liu, X. Cheng, B. Han, Boron-doped CuO nanobundles for electroreduction of carbon dioxide to ethylene, Green Chem, 22 (2020) 2750-2754.

[302] Z. Aribou, N. Khemmou, R. Allah Belakhmima, I. Chaouki, M. Ebn Touhami, R. Touir, S. Bakkali, Effect of polymer additive on structural and morphological properties of Cu-electrodeposition from an acid sulfate electrolyte: Experimental and theoretical studies, Journal of Electroanalytical Chemistry, 946 (2023).

[303] F. Li, W. Wang, J. Cao, J. Liu, K. Zhan, S. You, Z. Wang, B. Zhao, Fabrication of Cu-GO layered composites with enhanced thermal conductivity by ultrasonic spraying and electrodeposition, Journal of Materials Research and Technology, 24 (2023) 2442-2457.

[304] X. Li, Z. Zhang, Z. Zhang, J. Kou, M. Wu, M. Zhao, R. Qiao, Z. Ding, Z. Zhang, F. Liu, X. Yang, D. Zou, X. Wang, P. Gao, Y. Fu, E. Wang, K. Liu, Production of single-crystal Cu plates by electrodeposition on high-index Cu foils, Science Bulletin, 68 (2023) 1611-1615.

[305] H. Zhang, H.-R. Tan, S. Jaenicke, G.-K. Chuah, Highly efficient and robust Cu catalyst for non-oxidative dehydrogenation of ethanol to acetaldehyde and hydrogen, Journal of Catalysis, 389 (2020) 19-28.

[306] P.-P. Guo, Z.-H. He, S.-Y. Yang, W. Wang, K. Wang, C.-C. Li, Y.-Y. Wei, Z.-T. Liu, B. Han, Electrocatalytic CO2 reduction to ethylene over ZrO2/Cu-Cu2O catalysts in aqueous electrolytes, Green Chem, 24 (2022) 1527-1533.

[307] Y. Cui, Y. Cheng, C. Yang, Y. Su, D. Yao, B. Liufu, J. Li, Y. Fang, S. Liu, Z. Zhong, X. Wang, Y. Song, Z. Li, High-Performance Electrocatalytic CO2 Reduction for CO Generation Using Hydrophobic Porous Carbon Supported Au, ACS Sustainable Chemistry & Engineering, 11 (2023) 11229-11238.

[308] Q. Chen, H. Zhu, Z. Guo, Z. Yan, G. Yang, Y. Zheng, Y. Xing, H. Yin, T. Wu, Enhanced electrochemical reduction of CO2 to ethylene using boosted hydrophobicity of polyvinyl dichloride - coated CuO electrodes, Journal of Alloys and Compounds, 991 (2024).

[309] I.S. Brandt, V.C. Zoldan, V. Stenger, C.C. Plá Cid, A.A. Pasa, T.J. Oliveira, F.D.A. Aarão Reis, Substrate effects and diffusion dominated roughening in Cu2O electrodeposition, Journal of Applied Physics, 118 (2015).

[310] Z. Zeng, P. Barai, S.-Y. Lee, J. Yang, X. Zhang, W. Zheng, Y.-S. Liu, K.C. Bustillo, P. Ercius, J. Guo, Y. Cui, V. Srinivasan, H. Zheng, Electrode roughness dependent electrodeposition of sodium at the nanoscale, Nano Energy, 72 (2020).